BIREFRINGENT AND DIFFRACTIVE DEVICES FOR IMPLEMENTING MULTI–GBIT/S TRANSMISSION SYSTEMS USING VISIBLE WDM OVER SI–POF TECHNOLOGY

Universidad
Carlos III de Madrid

TESIS DOCTORAL

Birefringent and Diffractive Devices for Implementing Multi−Gbit/s Transmission Systems using Visible WDM over SI−POF Technology

Autor: Plinio Jesús PINZÓN CASTILLO

Directoras: Carmen VÁZQUEZ GARCÍA

Isabel PÉREZ GARCILÓPEZ

Departamento de Tecnología Electrónica

Leganés, _____ de ________________ de 2015

TESIS DOCTORAL

Título:

Birefringent and Diffractive Devices for Implementing Multi−Gbit/s Transmission Systems using Visible WDM over SI−POF Technology

Autor: Plinio Jesús PINZÓN CASTILLO

Directoras: Carmen VÁZQUEZ GARCÍA

Isabel PÉREZ GARCILÓPEZ

Tribunal:	**Firma:**
Presidente:	
Vocal:	
Secretario:	

Calificación:

Leganés, _____ de ___________________ de 2015

Agradecimientos

Este trabajo es fruto de seis años de trabajo, esfuerzo y mucha dedicación. En este tiempo he aprendido que todos somos capaces de hacer grandes cosas siempre que tengamos personas que nos apoyen incondicionalmente, que confíen en nosotros y que estén siempre presentes. En este sentido, tengo a muchos que agradecer.

Es muy fácil aventurarse cuando sabes que pase lo que pase estarás bien, es por esto que en primer lugar querría agradecer a mis padres (Plinio y Silvia) y a mi hermano (Javier). Por ustedes soy quien soy y estoy donde estoy, Muchas Gracias. Además, quiero dedicarle este trabajo a mi sobrina Aurora. ¡Espero que te motive!

Eva, tengo mucho que agradecerte. Me has ayudado en los momentos más difíciles. Y créeme que me has hecho madurar mucho. Más allá de ser solo novia, eres quien me ha motivado a ser mejor día a día. Obviamente, agradezco infinitamente a tus padres, al Sr. Pero y la Sra. Gloria, por confiar en mí y hacerme sentir en como casa. Y a todos los buenos amigos que te rodean (Lerdas, Club selecto y claro a Pablo).

Hay dos personas que son directamente responsables de que esté aquí. Félix, un amigo que siempre me ha motivado a que siga mi camino. Y Salvador, un profesor, compañero y amigo que me ha dado los mejores consejos y mucho apoyo. Muchas gracias a ambos.

Tengo mucho que agradecer a mis directoras Carmen e Isabel. Vosotras han apostado y confiado en mí desde el primer momento. Y han sabido como orientarme y motivarme para sacar siempre lo mejor de mí. Os agradezco todo el trabajo, esfuerzo y dedicación que han puesto en el desarrollo de este trabajo.

Algunas veces no es necesario saber cómo hacer las cosas, si no saber quién sabe y claro preguntar. En este sentido quiero agradecer a mis compañeros del Grupo de Displays y Aplicaciones Fotónicas (GDAF) que con su sabiduría y experiencia han supuesto un constante apoyo y ayuda para conseguir mis objetivos. En especial a José Manuel Sánchez Pena, que como corresponsable del grupo ha tenido una participación muy importante en el trabajo realizado y en mi formación.

Querría agradecer al resto de compañeros del Departamento de Tecnología Electrónica que con su calidad humana, profesionalidad y buen trato me han ayudado a lo largo de estos años y han servido de ejemplo para mí. Especial mención a Óscar y Marimar en la Secretaría del

Departamento por sus gestiones, atención y simpatía. Y a Emilio, por el interés especial que siempre ha demostrado.

Igualmente quiero agradecer a los doctores Kevin Heggarty y Bruno Fracasso por el cálido recibimiento y los invaluables comentarios otorgados durante mi estancia en Telecom Bretagne, Brest, Francia. Así como a Hani y a Maina por hacer mi estancia muy agradable.

Y mi mayor agradecimiento va para los miembros de esas reuniones de trabajo darías en la cafetería, 10:30 am, donde se tratan los temas más serios y trascendentales. En especial a los señores doctores David Sánchez, Pedro Contreras, Juan Carlos y Braulio, que aburrido seria todo sin ustedes. A Javi, Fran y Alberto, ver que no soy el único padeciendo motiva mucho XD. Lo mismo le digo Luis Jorge, Robinson, Don Guille, Don Julio y a mi compatriota Carlos Boya, este camino ha sido muy llevadero gracias a todos ustedes. Y no me puedo olvidar de Dani, gracias por tu disposición constante de ayudar. También tengo que agradecer a los que no están pero son miembros VIP, Carlos Marcos y David Barrios. Y por supuesto a Yolanda, que le da un toque muy especial a la hora del café.

Agradezco también a los que se incorporan al turno de las 14:30, Virginia, Ricardo y Vicente, vosotros saben muy bien que la más mínima demora en la hora de la comida tiene graves consecuencias, tenéis una gran responsabilidad. El mundo os lo agradece.

Pedro Debora, te mereces una mención muy especial como compañero de residencia, piso y despacho. Eres un hermano y alguien en quien puedo confiar. Igualmente agradezco a José Isidro y a Mariajo, porque los buenos compañeros son muy importantes.

En estas últimas líneas, agradezco a mis amigos eternos. San Roque, donde crecí y Calle el Agua donde pase la mejor adolescencia. Ruth, Lili y Alys, gracias por estar siempre presentes y por perdonar mis largas ausencias. A mis amigos de la UTP, Yader, Nando, Elizabeth, Lia, Ivonne, Linda, Villegas, Desiderio y claro a Fulgencio, gracias por hacerme sentir que el tiempo no ha pasado. Jilka, te agradezco todo tu apoyo. Y finalmente a ti Jennifer, gracias por todos consejos y todas esas discusiones llenas de mucho ingenio.

Tengo a muchas personas más que mencionar. A todos ustedes/vosotros mi mayor reconocimiento y gratitud.

> “*Muchas cosas se reputan imposibles antes de haberse realizado.*”
>
> *Plinio el Viejo*

Content

Chapter I:

Chapter II:

Chapter III:

Chapter IV:

Chapter V:

Chapter VI:

Chapter VII:

Chapter VIII:

Appendices:

List of Figures

List of Tables

Acronyms List

Acronym (Acrónimo)	English Term (Término en Inglés)	Spanish Term (Término en Castellano)
2D	Two–Dimensional	Bidimensional
3D	Three–Dimensional	Tridimensional
ADAS	Advanced Driver Assistance Systems	Sistemas Avanzados de Asistencia al Conductor
ADC	Analog–to–Digital Converter	Convertidor Analógico a Digital
AMLCD	Active Matrix Liquid Crystal Displays	Pantalla de Cristal Líquido de Matriz Activa
AR	Anti–Reflection	Anti−reflectante
AWG	Arrayed Waveguide Gratings	Agrupación de Guías de Onda
BER	Bit Error Rate	Tasa de Error de Bit
BF	Birefringent Filter	Filtro Birrefringente
BMW	Bavarian Motor Works (car manufacturer)	Bavarian Motor Works (fabricante de automóviles)
BRL	Back−Reflection Loss	Pérdidas por Reflexión
CA	Clear Aperture	Apertura
CAP	Carrier−less Amplitude Phase Modulation	Modulación de Fase y Amplitud sin Portadora
CCD	Charge Coupled Devices	Dispositivo de Carga Acoplada
CD	Chromatic Dispersion	Dispersión Cromática
CEMDATIC	Center for Advanced Materials and Devices for ICT	Centro de Materiales y Dispositivos Avanzados para las TIC
CTA	Crosstalk Attenuation	Atenuación de Diafonía
DAC	Digital–to–Analog Converter	Convertidor de Digital a Analógico
DeMux	Demultiplexer	Demultiplexor

DFT	Discrete Fourier Transform	Transformada de Fourier Discreta
DMT	Discrete Multitone Modulation	Modulación por Multitono Discreto
DSL	Digital Subscriber Lines	Línea de Suscripción Digital
DWDM	Dense Wavelength Division Multiplexing	Multiplexación en Longitud de Onda Densa
EFL	Effective Focal Length	Distancia Focal Efectiva
EO	Electro–Optical	Electro–Óptico
FEC	Forward Error Correction	Corrección de Errores hacia Adelante
FED	Field Emission Displays	Pantalla de Emisión de Campo
FFT	Fast Fourier Transform	Transformada de Fourier Rápida
FIR	Finite Impulse Response	Respuesta Finita al Impulso
FPGA	Field Programmable Gate Array	Arreglo de Compuertas de Campo Programable
FSR	Free Spectral Range	Rango Espectral Libre
FTTS	Fiber–To–The–Screen	Fibra hasta la Pantalla
FWHM	Full Width Half Maximum	Ancho de Banda a Mitad del Máximo de Potencia
FWM	Four Wave Mixing	Mezcla de Cuatro Ondas
GA	Genetic Algorithm	Algoritmo Genético
GDAF	Displays and Photonics Applications Group	Grupo de Displays y Aplicaciones Fotónicas
GI	Graded–Index	Índice Gradual
GI−POF	Graded–Index Polymer Optical Fiber	Fibra Óptica de Plástico de Índice Gradual
GOF	Glass Optical Fiber	Fibra Óptica de Vidrio/Sílice
GRIN	Gradient–Index Lens	Lente de Índice Gradual
HD	High Definition	Alta Definición
HN	Homogeneous Nematic LC Cell	Célula de CL Nemática Homogénea
ICT	Information and	Tecnologías de la Información y las

	Communications Technology	Comunicaciones
IDFT	Inverse Discrete Fourier Transform	Transformada de Fourier Discreta Inversa
IFE	In Flight–Entertainment	Entretenimiento en Vuelo
IFG	Inter–Frame Gap	Espacio entre Tramas
IL	Insertion Loss	Perdidas de Inserción
IPG	Inter−Packet Gap	Espacio entre Paquetes
IPTV	Internet Protocol Television	Televisión por Protocolo de Internet
IR	Infrared	Infrarrojo
ISI	Inter−Symbol Interference	Interferencia entre Símbolos
ISP	Internet Service Provider	Proveedor de Servicios de Internet
ITO	Indium Tin Oxide	Óxido de Indio Estaño
L	Length	Longitud
LAN	Local Area Network	Red de Área Local
LC	Liquid Crystal	Cristal Líquido
LC–OR	Liquid Crystal Optical Router	Encaminador Óptico de Cristal Líquido
LCTF	Liquid Crystal Tunable Filter	Filtro Sintonizable de Cristal Líquido
LD	Laser Diode	Diodo Láser
LED	Light–Emitting Diode	Diodo Emisor de Luz
$LiNbO_3$	Lithium Niobate	Niobato de Litio
LP	Linear Polarizer	Polarizador Lineal
LProg	Linear Programming	Programación Lineal
MC	Media Converter	Convertidor de Medio
MEMS	Micro Electro Mechanical Systems	Sistemas Micro–Electromecánicos
MLCC	Multi−Level Coset Coding	Codificación Multinivel por Cosets
MOST	Media Oriented Systems Transport	Sistemas de Transporte Orientado al Medio

MUT/WAT	Military University of Technology in Warsaw	Universidad Militar de Tecnología en Varsovia
Mux	Multiplexer	Multiplexor
MZI	Mach−Zehnder Interferometer	Interferómetro Mach–Zehnder
MZRRI	Mach–Zehnder Ring–Resonator Interferometer	Interferómetro Mach–Zehnder con Resonador en Anillo
NA	Numerical Aperture	Apertura Numérica
NIR	Near Infrared	Infrarrojo Cercano
NLC	Nematic Liquid Crystal	Cristal Líquido Nemático
NProg	Nonlinear Programming	Programación No–Lineal
NRZ	Non Return to Zero	No Retorno a Cero
OF	Optical Filter	Filtro Óptico
OLED	Organic Light Emitting Diode	Diodo Emisor de Luz Orgánico
OOK	On−Off Keying	Manipulación Encendido–Apagado (Modulación Binaria Sencilla)
PAM	Pulse Amplitude–Modulation	Modulación por Amplitud de Pulsos
PBS	Polarizing Beam Splitter	Divisor de Haz Polarizado
PC	Personal Computers	Ordenador Personal
PD	Monitor Photodiode	Fotodiodo Monitor
PDL	Polarization Dependent Loss	Pérdidas Dependientes de la Polarización
PDP	Plasma Display Panels	Pantalla de Plasma
PHDER	Errored Headers Rate	Tasa de Error en Cabeceras
PHY	Physical Layer	Capa Física
PMMA	Polymethyl Methacrylate	Polimetil Metacrilato
POF	Polymer Optical Fiber	Fibra Óptica de Plástico
PolConv	Polarization Converter	Convertidor de Polarización
PR	Polarization Rotator	Rotador de la Polarización
QAM	Quadrature Amplitude Modulation	Modulación de Amplitud en Cuadratura

QProg	Programming (QP)	Programación Cuadrática
R	Data Rate	Tasa de Datos
R−WSS	Reconfigurable Wavelength Selective Switch	Conmutador Selectivo en Longitud de Onda Reconfigurable
RMS	Root Mean Square	Media Cuadrática
RMSE	Root Mean Square Error	Error Cuadrático Medio
RR	Ring Resonator	Resonador en Anillo
SI	Step–Index	Salto de Índice
SI−POF	Step–Index Polymer Optical Fiber	Fibra Óptica de Plástico de Salto de Índice
SNR	Signal to Noise Ratio	Relación Señal–Ruido
SNR decod	Signal to Noise Ratio After Equalization	Relación Señal–Ruido tras Ecualizar
SOA	Semiconductor Optical Amplifiers	Amplificador Óptico de Semiconductor
SPM	Self Phase Modulation	Modulación de Autofase
ST	Straight Tip Connectors	Conectores de Punta Recta
TCP/IP	Transmission Control Protocol e Internet Protocol	Protocolo de Control de Transmisión y Protocolo de Internet
TeO_2	Paratellurite	Dióxido de Telutio (Peratelurita)
TF	Tunable Filter	Filtro Sintonizable
TFEL	Thin−Film Electroluminescent	Electroluminiscente de Capa Delgada
TN	Twisted Nematic LC Cell	Célula de CL Nemática Torsionada
TPA	Two–Photon Absorption Phenomenon	Absorción de Dos Fotones
UC3M	Carlos III University of Madrid	Universidad Carlos III de Madrid
UPM	Polytechnic University of Madrid	Universidad Politécnica de Madrid
VFD	Vacuum Fluorescent Displays	Pantalla de Fluorescencia en Vacío
VIS	Visible Spectrum	Espectro Visible

VOA	Variable Optical Attenuator	Atenuador Óptico Variable
WDM	Wavelength Division Multiplexing	Multiplexación por División en Longitud de Onda
WSS	Wavelength Selective Switches	Conmutador Selectivo en Longitud de Onda
XPM	Cross Phase Modulation	Modulación de Fase Cruzada

Chapter I:

Introduction

1.1. Motivation

Today, the volume of data transmitted by short−range networks, especially by In−Home networks, both to the Internet Service Provider (ISP) and between different terminals, is increasing beyond the Gbit/s, exceeding the capabilities of current networking technologies such as copper and wireless **[1]**. This is due to the fast growth of new multimedia services like IPTV, multi−room/multivision configurations, high−definition (HD) TV, three−dimensional visual information (3D) or remote "face−to−face communication", among others **[2]**.

On the other hand, energy conservation is gaining increasing interest in our society in recent years. There is growing consensus on the necessity to put energy conservation at the top of the research agenda, as one of the most compelling and critical issues. The energy consumption of computers and network equipment is becoming a significant part of the global energy consumption **[3]**. As the coverage of Information and Communications Technology (ICT) is spreading rapidly worldwide, the energy consumption and carbon footprint of ICTs are also increasing fast, since more equipment and components for networks and communications are being deployed annually **[4]**. The energy−efficient optical network is a new concept, which is being investigated in recent years. Minimizing energy consumption of optical networks can be generically addressed at four levels: component, transmission, network, and application **[4]**, **[5]**.

In recent years, polymer optical fiber (POF) has been proposed, and recognized, as one of the most promising transmission media for implementing high speed and low cost short−range communication networks **[1]**. Specifically, in scenarios such as Local Area Networks (LANs), In−Home and Office networks **[6]**, as well as in Automotive **[7]** and Avionic multimedia buses, or in Data Center connections **[8]**, due to its potential low cost and transmission capacity. Nowadays, POF technology is an excellent choice to implement high−speed short−range networks and it is replacing step by step copper based technology, such as twisted pair, coax cable, power−line and Ethernet Cat−5. An historical evolution of the most important milestones related to the POF development can be found in **[9]** and **[10]**.

It has been shown that POFs have multiple applications in sensor systems at low or competitive cost compared to the established conventional technologies. POF based sensors have important applications in structural health monitoring, biomedicine, environmental and biochemical areas **[11]**. Optical fiber sensor networks are evolving rapidly. They are used because of the inert nature of optical fibers allowing no electromagnetic interference and safe applications in inflammable atmospheres; other relevant characteristics are their low weights and wide bandwidths as a transmission medium. In any case, it is very interesting to have specific components such as optical routers and switches for selecting a certain path in a sensing network with no optical to electrical and electrical to optical conversions **[12]**.

POF application in the automotive field has been particularly successful. Since the vehicle bus standard called Media Oriented Systems Transport (MOST) was first introduced by BMW in 2001, POF has displaced copper in the passenger compartment for multimedia applications and today, MOST technology is used by almost all major car manufacturers in the world **[13]**. In addition, POF is also used in protocols designed to support the rapidly growing number of sensors, actuators and electronic control units within cars. Up to date, a number of different in–car networks for multimedia and security applications have been developed.

MOST networks are based on ring topologies, as shown in **Fig. 1.1**. In those kinds of networks, bypass optical switches are used to improve the system availability, by giving an alternative optical path when an Electronic Control Unit (ECU) shuts down **[14]**. Besides, the introductions of Y−couplers allow the simple analysis of the network performance, just by plugging in a diagnostic tool without opening and influencing the network. In a similar way, Plug-in sockets allow the extension of the network, simplifying the offer of extra equipment or the installation and deinstallation of after-market or mobile devices **[15]**.

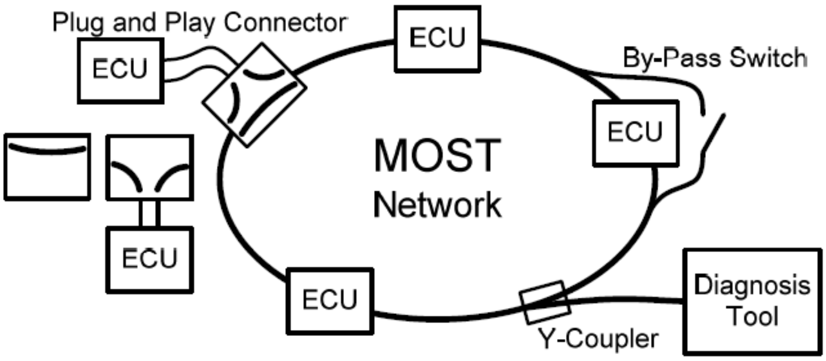

Fig. 1.1: Optical bypass protection switching in a MOST Network, where each ECU represents an Automotive Electronic Control Unit [15].

Avionics networks can also be considered an example of short range communication as its size is limited to a maximum length of 100 meters. The requirement of faster communication systems in the range of 100Mbps– 1Gbps, immune to electromagnetic radiation, initiated in the nineties the migration of avionics data buses from copper to fiber based networks **[16]**. These first systems based on glass fibers, demonstrated a high reliability which has steadily increased the use of optical data links in commercial aircraft over the last decade, culminating with the launch of the 787 Dreamliner airplane by The Boeing Company introducing the 3rd generation of airborne fiber optics communication networks **[17]** and with the introduction in the Flydubai B737 of Lumexis fiber–to–the–screen (FTTS) In flight–entertainment (IFE) systems **[18]**. The ease of installation and lower costs of multimode fibers excited the interest of the avionic industry in polymer fibers as it is possible to realize a high speed, short range fiber optic link for data communication at relatively low cost using commercial off–the–shelf components. POF can meet requirements to compete in the replacement by fiber of the aircraft data links that are now based on low–speed low–cost copper, especially on IFE systems. The use of visible light has also obvious advantages for failure detection and maintenance.

Among the different POF types, the step index POF (SI−POF) with a 980 μm core diameter of polymethyl–methacrylate (PMMA) and numerical aperture (*NA*) of ~0.5 offers several advantages, especially in the short−range scenarios listed above, due to its potential low cost associated with its easiness of installation, splicing and connecting. This is due to the fact that SI−POF has higher dimensions, larger *NA* and larger critical curvature radius in comparison with other POF types, as the graded index POF (GI−POF), and glass optical fibers (GOFs). Moreover, SI−POF is more flexible and ductile, making it easier to handle, even by people without specialized training.

However, SI−POF bandwidth is still significantly lower than that of GI−POFs and GOFs (monomode and multimode). This is because; SI−POF suffers from high modal dispersion due to its large *NA*, limiting its bandwidth distance product to ~50 MHz × 100 m **[19]**. And it is only used in the visible spectrum range (VIS), where it can provide acceptable attenuation (e.g. ~0.17 dB/m at 650 nm) **[20]**. The limited bandwidth and high attenuation hamper the desired integration of multiple broadband services into a common SI−POF access for In−building/home network or in the different short−range scenarios.

Overcoming the bandwidth limitation of such fibers requires the development of techniques oriented to extend the capabilities of SI−POF networks to attend the consumer's demand for multimedia services in short−range networks. Different efficient modulation and equalizing schemes for SI−POF networks have been proposed and implemented **[21]**, with excellent results. And because of this, the Gbit/s transmission capacity of SI–POF links has been widely demonstrated in recent years **[19]**, using single channel based systems (typically at 650 nm).

But SI–POF's data transmission capacity needs a greater exploitation to meet user requirements for higher–data rates with a low power consumption and low cost. This generates an interest in the development of new systems for Multi–Gbit/s transmission over SI–POF, including new transmitters and receivers, and in new standards based on SI–POF **[1]**, **[7]**.

At this point, and after exploiting the capabilities of a single channel transmission, visible wavelength division multiplexing (WDM) is being proposed as a promising solution to expand the data transmission capacity of SI−POF based systems, transmitting more than one wavelength over one single fiber, see **Fig. 1.2**. Most recent results related to visible WDM over SI−POF (using offline processing techniques) reveals the great potential of this technology **[22]**, **[23]**, **[24]**.

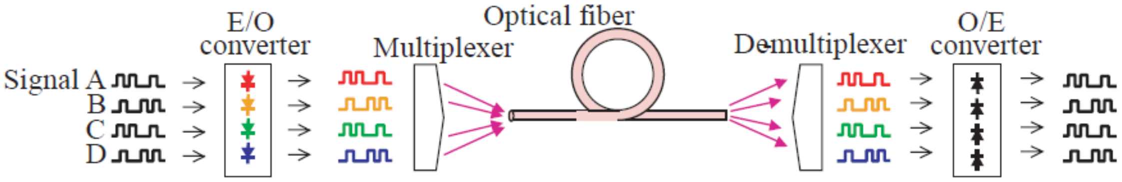

Fig. 1.2: Wavelength division multiplexing basic scheme [25].

In the case of automotive and avionic industry, SI−POF WDM schemes can be used to assign specific wavelengths to the different systems (e.g. ADAS, On-Board Diagnostics, Infotainment ...) and transmit them over a single high-speed bus, which would reduce the number of connections or links in the system, as shown in **Fig. 1.3**. In this kind of schemes, different optical devices such as Routers and Wavelength Selective Switches can be used to add advanced functionalities to the network, further reducing the number of connections.

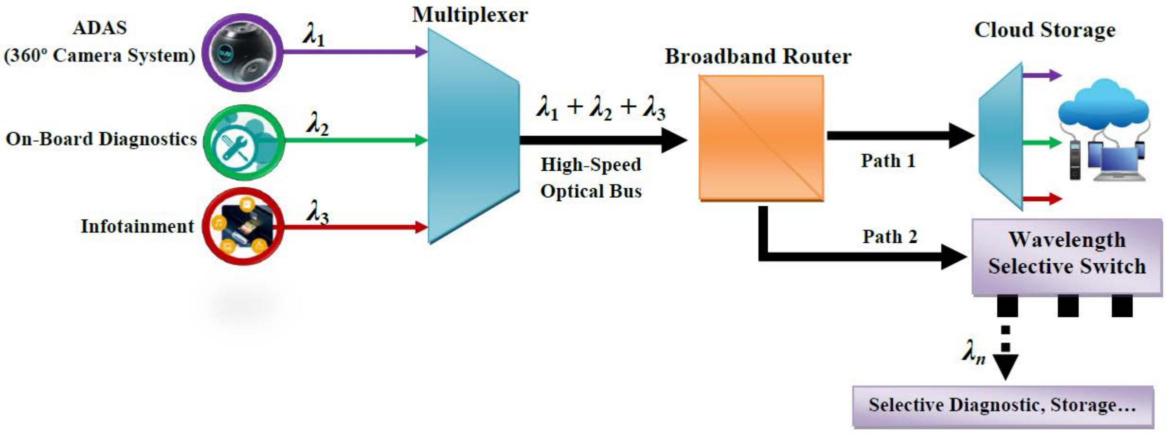

Fig. 1.3: High-Speed multifunction SI−POF network based on a WDM scheme.

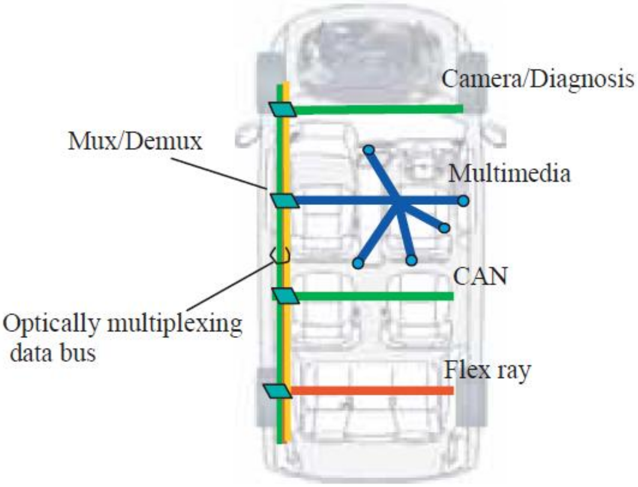

Fig. 1.4: Basic concept of automotive multi−protocol communication using WDM [25].

On the other hand, the sharing of the communication line by several signals that do not interfere with each other is a promising approach for unifying the various communication standards. Some authors believe that systems based on WDM, such as that shown in **Fig. 1.4**, where each protocol is transmitted at a specific wavelength, is the most suitable solution **[25]**.

But there are some constrains that must be addressed in order to perform the same (or similar) capabilities as in the case of GOFs based WDM approaches. For example, SI−POF is only used in the VIS range (400 to 700 nm) which is extremely wide if compared with C− and L−bands (1530 – 1565 nm and 1565 – 1625 nm, respectively) used in silica−based WDM. In a similar way, the channels' spectral bandwidth, numerical aperture and diameter of SI−POF systems are too large when compared to GOF and GI−POF, which is translated into millions of propagating modes. That is why many of the optical devices, such as Filters, Switches, Interleavers, Routers, Multiplexers and Demultiplexers, used in GOF based WDM systems are not usable with SI−POF and those that could be used require a complete redesign.

Optical devices are indispensable for the development of the future high speed short−range communication networks **[6]** and in many sensors applications **[12]**, **[26]**. However, the different requirements, or needs, imposed by the visible WDM SI−POF technology, must be carefully considered on their designs. Optical devices for SI−POF technology should have:

- Reconfiguration or tuning capability, since no standard channels are defined.
- The capability of handling channels with large spectral bandwidths, since laser diodes, LDs, and light emitting diodes, LEDs, are used.
- The capability of accepts highly divergent beams, since SI−POF is an object with 1 mm of height and 0.5 *NA*.
- Low insertion losses, in order to avoid or reduce the power penalty in the transmission capacity of WDM based SI−POF systems **[27]**.

Obviously, one single technology cannot fulfil all these requirements, the appropriate technology for each optical device or application (e.g. filtering, switching, interleaving, routing, multiplexing and demultiplexing) should be chosen depending on the network type, topology and specific needs. In this work, novel optical devices for SI−POF applications are developed. They can be classified into two groups: reconfigurable devices and low loss devices.

Among the different technologies used for implementing optical devices, those based on liquid crystals (LC) are a very interesting choice for designing reconfigurable devices because they do not have mobile parts for reconfiguration, need low excitation voltages and have low power consumption. Current applications of LC devices in WDM GOF networks are multiple (in the infrared range, IR), but not in the VIS range for WDM SI−POF networks **[28]**.

The Group of Displays and Photonics Applications (GDAF), of the Carlos III University of Madrid (UC3M), has been active working in the design, manufacturing and characterization of LC devices for optical communications networks and POF applications. This and the useful advantages of LC technology, as well as the rapid growth of the SI−POF networks have motivated the development of new LC based devices especially designed to implement SI−POF networks based on visible WDM systems. The LC devices presented in this work have been classified as: reconfigurable wavelength selective devices (filters, interleavers and switches) and reconfigurable routers.

Those LC devices are fundamental to implement the future networks based on visible WDM over SI−POF, mainly due to their versatility and reconfiguration capacity, and because they can be mass produced with low cost (mainly because LCs are a mature technology) and with compact designs (even with the bulk optics technology used).

The operation temperature range of SI–POF and LCs based technologies is a determinant factor in the development and implementation of their potential applications. SI–POF optimum temperature characteristics are ensured in the temperature range from –40ºC through +80ºC. However, the temperature limit may be enhanced to 125 °C – 135 °C with the use of a modified polyethylene or an elastomer with polyolefin coating **[11]**. In the case of LCs, industrial, non–automotive transportation and military sectors, among others, often require LC displays that can operate in extreme temperature environments. Typically, standard LC display modules provide a temperature range of 0°C to +50°C. However, several display manufacturers offer extreme temperature models with operating temperatures of –40°C to +85°C. There is also a wide selection of standard versions that range from –20°C to +70°C **[29]**, even with an upper temperature between +60º and +100ºC. **[30]**. **Table 1.1** lists the temperature requirements for various applications compatible with SI–POF and LCs based technologies.

TABLE 1.1. TEMPERATURE REQUIREMENTS FOR VARIOUS APPLICATIONS COMPATIBLE WITH SI–POF AND LCS BASED TECHNOLOGIES.

Application	Acceptable temperature range	References
Home Networking	–20 to +70º	**[31]**
Industrial Networking	–20 to +85º	**[32]**
Automotive	–40 to +85ºC	**[33]**
Aircraft (high–speed, high definition cabin management, multimedia, and in–flight entertainment systems)	–55 to +85º, or +150º	**[34]**
Structural Health Monitoring	–20°C to +60°C	**[35]**

On the other hand, for a WDM system implementation, two key devices, multiplexer (Mux) and demultiplexer (DeMux) are indispensable to combine and to separate the different transmitted wavelength channels, see **Fig. 1.2**. However, most Muxes/DeMuxes for GOFs **[36]**, **[37]**, **[38]**, or for GI−POF with low *NA* and diameter **[39]**, are not suitable for SI–POFs **[40]**. This is due to the wider spectral range and spectral bandwidths used for visible WDM over SI–POFs **[41]**, and the SI–POF multimodal nature and physical characteristics, which produces beams in the free space with a large diameter and divergence.

A limitation of visible WDM links over SI–POF is the power budget reduction due to the current Muxes/DeMuxes high insertion losses (*ILs*), limiting the transmission capacity of each channel in comparison with single channel systems, for the same transmitted power. Most of the SI–POF based Mux/DeMux prototypes reported in literature have been developed on the basis of interference filters, prisms and diffraction gratings, with *ILs* much higher than 5 dB. Therefore, for visible WDM over SI−POF becoming a reality, the development of Mux/DeMux devices with low−loss and multiple channels is required. Some authors set the insertion loss per channel to 5 dB as a reasonable value, for a real increase in the link capacity using WDM SI−POF. This has motivated the design and implementation of low loss Muxes/DeMuxes based on Diffraction Gratings with *IL* of less than 4.5 dB and more than 3 channels.

Finally, one of the most important motivations of this work is to demonstrate the possibility of increasing the transmission capacity of actual single channel links based on SI−POF using the visible WDM approach over SI−POF technology.

1.2. Objectives

New optical devices are indispensable for the development of the future SI−POF high speed short−range communication networks and as well as in many sensors applications based on SI−POFs. These devices are not well established to date due to the physical and multimodal characteristics of the SI−POF technology as well as the characteristics of the SI−POF visible WDM systems. Therefore, the main objective that has been established for this research work is to develop new optical components based primarily on liquid crystals and diffractive elements for applications in advanced optical communication systems with plastic optical fibers, ensuring an optimized power consumption to reduce the carbon footprint of ICTs. This objective is addressed through the following four specific objectives:

Objective 1: Designing and testing new reconfigurable optical devices based on birefringent elements for implementing advanced SI−POF systems based on visible WDM. These systems include schemes for protection and recovering applications and sensing systems.

Objective 2: Designing and testing new low–loss Mux/DeMux devices based on diffractive elements for implementing energy efficient WDM data transmission systems over SI–POF technology.

Objective 3: To implement a real–time Multi–Gbit/s Ethernet data transmission system over SI–POF technology in a bidirectional and error free link of up to 50 m that can improve the performance, in terms of data–rate by length, of those systems that transmit a single channel.

Objective 4: To contribute to minimize the energy consumption of optical networks at the component and transmission level, by using low power consumption technologies and low insertion losses devices, respectively.

1.3. Content of the Work

The structure of the document is described below.

Chapter 2 is devoted to a brief introduction to the nematic LC materials and cells used in this work. This chapter presents also a new experimental approach for the fast measurement of arbitrary nematic liquid crystal (TN) cells. Its effectiveness is demonstrated with the characterization of two different nematic LC cells. This characterization method is a very useful tool for the design of LC devices presented in the following chapters (**Chapter 3** and **Chapter 4**).

Chapter 3 is divided in four main sections; and each one is dedicated to a different type of Wavelength Selective device, based on birefringent structures using LCs, for visible WDM SI–POF networks. The first section presents a tunable optical filter based on a Lyot structure using high birefringence LCs. The second section describes a novel proposal of reconfigurable wavelength selective switch based on the previous described LC tunable filter. The third section describes a novel and useful method for the synthesis of asymmetric flattop birefringent interleavers based on digital filters design and a Genetic Algorithm based optimization. And finally, in the last section, the transfer function of three types of birefringent filters (Lyot, Solc and Arbitrary), are analyzed and compared in the visible range for WDM SI–POF networks.

Chapter 4 refers to two reconfigurable LC devices designed to route optical signals in the visible range, called reconfigurable routers. The first one is a reconfigurable optical router with control of output power level and the second one is a reconfigurable broadband router with low thermal dependence. The latter represents a very innovative design regarding the different proposals of routers based on LCs previously reported.

The **Chapter 5** is dedicated to the design and implementation of low loss Mux/DeMux devices, based on Planar Diffraction Gratings, for visible WDM SI−POF networks. The devices presented in this chapter are key components for the efficient implementation of visible WDM SI−POF networks. The designs are easy to implement, are compact, have multiple channels, have low *ILs* and high adjacent crosstalk attenuation (*CTA*) and are at the level, or above, of the current state−of−the−art.

In **Chapter 6**, the implementation of a real−time bidirectional link for Multi−Gbit/s Ethernet transmission over 50 m of SI−POF using a 5−channel visible WDM system is presented. It is based on fully integrated media converters for 1 Gbit/s transmission over SI−POF and the low loss Muxes/DeMuxes designed on **Chapter 5**. The experimental results presented in this chapter, and the analyses done over the system, demonstrate the functionality of the visible WDM SI−POF link. This scheme allows obtaining a real improvement in the performance of commercial and experimental transmission systems. It has the potential for reaching real−time data rates of up to 5 Gbit/s over 50 m of SI−POF in a bidirectional scheme, with better energy efficiency than current proposals.

The main conclusions and contributions of this work and future research tasks are given in **Chapter 7**. And finally, the **Chapter 8** presents a Spanish resume of this work.

1.4. Acknowledgements

The present research work has been supported by the following Spanish projects:

- SINFOTON−CM: Sensores e Instrumentación en Tecnologías Fotónicas, Ref: S2013/MIT–2790–SINFOTON–CM, Comunidad de Madrid − Consejería de Educación Dir. General de Universidades e Investigación, 2014–2016.
- Nuevas Técnicas Fotónicas de Transmisión, Monitorización y Sensado en Redes de Banda Ancha de Bajo Consumo, Ref: TEC2012–37983–C03–02, CICYT (Ministerio de Economía y Competitividad), 2013–2015.
- FACTOTEM−II−CM: Fotónica Aplicada a la Creación de Tecnologías Ópticas y su Transferencia a Empresas Madrileñas−II, Ref: S2009/ESP–1781), CAM (Comunidad de Madrid), 2010–2013.
- Nuevas Técnicas de Conmutación y Sensado en Redes Ópticas, Ref: TEC2009–14718–C03–03, CICYT (Ministerio de Ciencia e Innovación), 2010–2013.

- Ayudas Técnicas Integradas para Discapacidades Visuales, Transportables y Accesibles, Ref: CCG10–UC3M/TIC–4787, Comunidad de Madrid − UC3M, 2011.

Additional financial support has been obtained from the ICT COST Action IC−1208: Integrating devices and materials: a challenge for new instrumentation in ICT, and the European project BONE: Building the Future Optical Network in Europe (FP7−ICT−216863) carried out during the VII Framework Program of the European Union.

Some of the results obtained in **Chapter 5** related to the manufacturing of diffraction grating prototypes and the ray tracings based simulations were obtained during the research stays in the Optic Department of Telecom Bretagne of Brest (France) from June to August 2012 and from June to July 2013. Mobility actions of Research Vicechancellor at University Carlos III of Madrid in 2012 and 2013 are acknowledged for funding these research stays in Brest (France).

I would also like to acknowledge to the Military University of Technology (MUT/WAT) in Warsaw and the Polytechnic University of Madrid (CEMDATIC−UPM) for supplying the LC devices. And I would also like to thank to the staff of the Displays and Photonics Application Group (GDAF) group for their support.

1.5. References

[1] E. Dai, “Home Networking bandwidth growth needs and POF,” in *IEEE* 802.3 *GEPOF Study Group Meeting*, October 2014.

[2] Y. Shi, E. Tangdiongga, A. Koonen, A. Bluschke, P. Rietzsch, J. Montalvo, M. De Laat, G. Van Den Hoven and B. Huiszoon, “Plastic-optical-fiber-based in-home optical networks,” *IEEE Communications Magazine,* vol. 52, nº 6, pp. 186-193, 2014.

[3] W. Vereecken, L. Deboosere, D. Colle, B. Vermeulen, M. Pickavet, B. Dhoedt and P. Demeester, “Energy efficiency in telecommunication networks,” in *European Conference on Networks and Optical Communications & Optical Cabling and Infrastructure (NOC)*, 2008.

[4] Y. Zhang, P. Chowdhury, M. Tornatore and B. Mukherjee, “Energy Efficiency in Telecom Optical Networks,” *IEEE Communications Surveys & Tutorials,* vol. 12, nº 4, pp. 441-458, 2010.

[5] R. S. Tucker, “Green Optical Communications—Part I: Energy Limitations in Transport,” *IEEE Journal of Selected Topics in Quantum Electronics,* vol. 17, nº 2, pp. 245-260, 2011.

[6] I. Mollers, D. Jager, R. Gaudino, A. Nocivelli, H. Kragl, O. Ziemann, N. Weber, T. Koonen, C. Lezzi, A. Bluschke and S. Randel, “Plastic optical fiber technology for reliable home networking: overview and results of the EU project pof-all,” *IEEE Communications Magazine,* vol. 47, nº 8, pp. 58-68, 2009.

[7] M. R. Co., “Plastic Optical Fiber (POF) technology for Automotive, Home network systems,” in *IEEE* 802.3 *GEPOF Study Group meeting*, May 2014.

[8] R. Kruglov, J. Vinogradov, S. Loquai, O. Ziemann, C.-A. Bunge, T. Hager and U. Strauss, “21.4 Gb/s discrete multitone transmission over 50-m SI-POF employing 6-channel WDM,” in *Optical Fiber Communications Conference and Exhibition (OFC)*, March 2014.

[9] P. Polishuk, “Plastic optical fibers branch out,” *IEEE Communications Magazine,* vol. 44, nº 9, pp. 140-148, 2006.

[10] A. Berganza, Estudio and Caracterización de las Fibras Ópticas de Plástico Multinúcleo, Bilbao: Universidad del Pais Vasco (EHU), 2013.

[11] L. Bilro, N. Alberto, J. L. Pinto and R. Nogueira, “Optical Sensors Based on Plastic Fibers,” *Sensors,* vol. 12, nº 9, pp. 12184-12207, 2012.

[12] C. Vazquez, J. M. S. Pena, S. E. Vargas, A. L. Aranda and I. Perez, “Optical router for optical fiber sensor networks based on a liquid crystal cell,” *IEEE Sensors Journal,* vol. 3, nº 4, pp. 513-518, 2003.

[13] M. Cooperation, “Appendix D: Frame Structure and Boundary (informative),” in *MOST Specification Rev.* 3.0 *E*2, MOST Cooperation, July 2010, pp. 211-215.

[14] P. C. Lallana and C. Vázquez, “Plug and Play Connector for Automotive POF Networks,” in *e-PhotoneONe/COST* 291 *Summer School*, Brest (France), 2007.

[15] T. Kibler, S. Poferl, G. Böck, H.-P. Huber and E. Zeeb, “Optical Data Buses for Automotive Applications,” *Journal of Lightwave Technology,* vol. 22, nº 9, pp. 2184-2199, 2004.

[16] D. Anderson and M. Beranek, “777 optical LAN technology review,” in *Electronic Components & Technology Conference,* 1998. 48*th IEEE* , 1998.

[17] Boeing, “Boeing 787 Dreamliner,” [En línea]. Available: http://www.boeing.com/commercial/787/. [Último acceso: 25 June 2015].

[18] Lumexis, “Lumexis FTTS® IFE Systems,” [En línea]. Available: http://lumexis.com/. [Último acceso: 25 June 2015].

[19] C. Okonkwo, E. Tangdiongga, H. Yang, D. Visani, S. Loquai, R. Kruglov, B. Charbonnier, M. Ouzzif, I. Greiss, O. Ziemann, R. Gaudino and A. Koonen, “Recent Results From the EU POF-PLUS Project: Multi-Gigabit Transmission Over 1 mm Core Diameter Plastic Optical Fibers,” *Journal of Lightwave Technology,* vol. 29, nº 2, pp. 186-193, 2011.

[20] O. Ziemann, J. Krauser, P. Zamzow and W. Daum, POF Handbook: Optical Short Range Transmission Systems, 2nd Edition ed., Springer, 2008.

[21] J. Siuzdak and G. Stepniak, “Efficiency of various modulation types in Step Index Polymer Optical Fiber,” in *Proc. SPIE* 9290*, Photonics Applications in Astronomy, Communications, Industry, and High-Energy Physics Experiments*, 2014.

[22] M. Jončić, R. Kruglov, M. Haupt, R. Caspary, J. Vinogradov and U. H. P. Fischer, “Four-Channel WDM Transmission Over 50 m SI-POF at 14.77 Gb/s Using DMT Modulation,” *IEEE Photonics Technology Letter,* vol. 26, pp. 1328-1331, 2014.

[23] R. Kruglov, J. Vinogradov, S. Loquai, O. Ziemann, C.-A. Bunge, T. Hager and U. Strauss, “21.4 Gb/s Discrete Multitone Transmission over 50-m SI-POF employing 6-channel WDM,” in *OFC*, San Francisco, California United States, 2014.

[24] U. H. P. Fischer, S. Höll, M. Haupt and M. Joncic, “Polymeric demultiplexer component for wavelength division multiplex communication systems using polymer fibers,” in *SPIE* 9368, San Francisco CA, 2015.

[25] M. Kagami, “Visible Optical Fiber Communication: Review,” *R&D Review of Toyota CRDL,* vol. 20, nº 2, 2005.

[26] A. Tapetado, P. Pinzón, J. Zubia and C. Vázquez, “Polymer Optical Fiber Temperature Sensor With Dual-Wavelength Compensation of Power Fluctuations,” *Journal of Lightwave Technology,* vol. 33, nº 13, pp. 2716-2723, 2015.

[27] O. Ziemann and L. Bartkiv, “POF-WDM, the Truth,” in *Proc.* 20*nd POF conference*, Bilbao, 2011.

[28] J. Beeckman, K. Neyts and P. J. M. Vanbrabant, “Liquid-crystal photonic applications,” *Optical Engineering,* vol. 50, nº 8, p. 081202, 2011.

[29] G. Roos, “Selecting LCD Modules for Extreme Temperatures,” Hearst Electronic Products, 02 12 2014. [En línea]. Available: http://www.digikey.com/es/articles/techzone/2014/dec/selecting-lcd-modules-for-extreme-temperatures. [Último acceso: 09 09 2015].

[30] G. Meier, E. Sackmann and J. G. Grabmaier, Applications of Liquid Crystals, Springer Science & Business Media, 2012.

[31] N. Schunk, K. Panzer, E. Baur, W. Kuhlmann, K. Streubel, R. Wirth and C. Kamutsch, “IEEE1394b POF transmission system 500Mbit/s versus 50m 0.3NA POF,” in *ICPOF*, Amsterdam, 2001.

[32] O. Ciordia, C. Esteban, C. Pardo and R. Pérez de Aranda, “Commercial Silicon for Gigabit Communication over SI-POF,” in *Proc.* 22*nd POF conference*, Buzios, 2013.

[33] O. Schoenfeld, K. Panzer, J. Wittl and H. Essl, “Transceivers for in-car optical buses,” in *ICPOF*, Chiba, 1999.

[34] C. I. Technologies, “Cabin Management Systems: Data Bus and Video Cables, Rev. 010115-POD,” 2015. [En línea]. Available: http://www.carlisleit.com/sites/default/files/resources/documents/CabinManagementSystems.pdf. [Último acceso: 09 September 2015].

[35] B. Glisic and D. Inaudi, Fibre Optic Methods for Structural Health Monitoring, John Wiley & Sons, 2008.

[36] T. Fukushima and T. Sakamoto, “A 7×6 optical fiber grating demultiplexer-multiposition switch for 0.64-0.88 μm band,” *J. Lightw. Technol.,* vol. 14, nº 5, p. 867–872, May 1996.

[37] W. J. Tomlinson III, “Wavelength division multiplexer”. U.S. Patente 4.111.524, September 1978.

[38] A. A. M. Kok, A. M. S. Musa, A. Borreman, M. B. J. Diemeer and A. Driessen, “Completely multimode arrayed waveguide grating-based wavelength demultiplexer,” in *IEEE Region* 8 *EUROCON* 2003*, Computer as a Tool*, Ljubljana, Slovenia , 2003.

[39] H. P. A. van den Boom, W. Li, P. K. van Bennekom, I. T. Monroy and G. -D. Khoe, “High-capacity transmission over polymer optical fiber,” *IEEE Journal of Selected Topics in Quantum Electronics,* vol. 7, nº 3, pp. 461 - 470, May/Jun 2001.

[40] J. M. Senior and S. D. Cusworth, “Devices for wavelength multiplexing and demultiplexing,” *IEE Proceedings - Optoelectronics,* vol. 136, nº 3, pp. 183-203, 1989.

[41] M. Joncic, M. Haupt and U. Fischer, “Standardization Proposal for Spectral Grid for VIS WDM Applications over SI-POF,” in *Proceedings of POF Congress*, Atlanta, 2012.

Chapter II:

Optical Modeling of Nematic Liquid Crystal Devices

This chapter presents a novel experimental approach for the fast measurement of nematic LC (NLC) cells' manufacturing parameters and its phase delay (retardation) wavelength dependence **[1]**. All the parameters can be obtained simultaneously, with few measurements and without the need of applying control voltages or analytical conditions. The chapter starts with a brief introduction to the type of LC devices used in this work: Homogeneous nematic (HN) and Twisted nematic (TN). First, a review of the main properties of nematic Liquid Crystal (NLC) materials and the models used to represent the dependence of its birefringence with the wavelength (dispersion) and the temperature are presented. Then, the basic configurations of NLC cells, such as HN and TN, and their respective optical transmission models, based on Jones Matrices, are detailed. After this introduction, the novel experimental approach for the fast measurement of arbitrary TN cells' manufacturing parameters (arbitrary TN cells include HN cells) is described. This method allows determining the rubbing angle, the twist angle and its sense, as well as the retardation dispersion of the LC cell. The characterization method and the results presented in this chapter are used on the design of the LC optical devices for SI−POF networks presented in **Chapter 3** and **Chapter 4**.

2.1. Introduction to Liquid Crystals

Liquid Crystals (LCs) are materials that exhibit several intermediate states between liquid and solid states. These intermediate states are called mesophases and the molecules that favour the formation of mesophases are called mesogenic groups **[2]**. LCs are called "lyotropics", when the different phases are obtained by varying their concentration in a solvent, and "thermotropics", when the different phases exist at a certain temperature (T) range, $T_m < T < T_C$, where T_m is the temperature of melting from solid state into a mesophase, and T_C the is clearing temperature, which represents the temperature when the liquid crystal transforms into an isotropic liquid. Thermotropic LCs can be composed by rod−like molecules, called calamitic molecules, or by flat−shaped molecules, called discotic molecules. The thermotropic LCs formed by calamitic molecules are the most used in many displays and photonic applications because of their excellent electro−optical properties **[3]**.

The rod−like shape of the calamitic molecules makes them to be in parallel, but with the freedom to move with respect to their long axis. The direction of the average orientation of the LC long axis, or *c*−axis for short, is represented by the director vector **n** **[4]**, as shown in **Fig. 2.1a**. This arrangement produces anisotropy in all major physical properties of the LC. This means that many of the physical properties of the LC molecules are different depending on the direction considered.

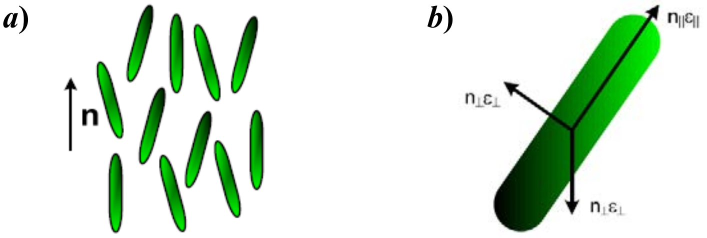

Fig. 2.1: Liquid Crystal Molecules: *a*) Calamitic molecules orientation, *b*) uniaxial molecule of thermotropic liquid crystals [5].

Physical parameters of interest in electro−optical applications are: the dielectric permittivity (ε) and the refractive index (n). These properties cannot be represented by a scalar, since they have different values in each of the three axes of the molecules, due to the LC anisotropy **[6]**. Most LC molecules are uniaxial as shown in **Fig. 2.1b**. The components of ε and n parallel to the LC *c*−axis are represented by $\varepsilon_{\parallel}$ and $n_{\parallel}$, and the components perpendicular to the *c*−axis are represented by $\varepsilon_{\perp}$ and $n_{\perp}$, respectively. The anisotropy sign is defined by the difference between the parallel and perpendicular components.

Dielectric anisotropy ($\Delta\varepsilon = \varepsilon_{\parallel} - \varepsilon_{\perp}$) may be positive or negative. If an electric field (**E**) is applied over the LC and $\Delta\varepsilon$ is positive, the molecules try to be oriented parallel to **E**; while if $\Delta\varepsilon$ is negative, the molecules try to be oriented perpendicular to **E**, as shown in **Fig. 2.2a** and **Fig. 2.2b**, respectively. Therefore, the director vector, **n**, of the LC *c*–axis can be modified by applying an external **E**, which allows the electro–optical modulation of devices based on these materials **[7]**.

In the case of the optical anisotropy, which is also called birefringence ($\Delta n = n_{\parallel} - n_{\perp}$), $n_{\parallel}$ is called extraordinary index (n_e), because it is located parallel to the *c*–axis of the molecule, and $n_{\perp}$ is called ordinary index (n_o). It is important to note that in all LCs Δn is positive since $n_e > n_o$.

When polarized light is incident on the LC, it is decomposed in two orthogonal waves. One is the extraordinary wave that vibrates parallel to the *c*–axis of the molecule, with refractive index n_e. And the other is the ordinary wave that vibrates perpendicular to the *c*–axis of the molecule, with refractive index n_o. Then, there is a phase shift, also called retardation (Γ), between the waves, since they travel over paths with different refractive indices, and without any interference as they have opposite polarizations. The result is a variation of the polarization state of the light passing through the LC.

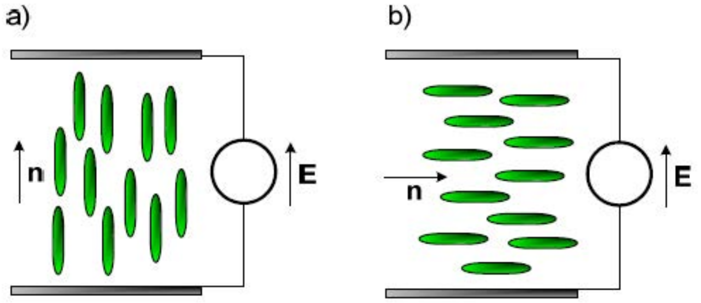

Fig. 2.2: Molecular reorientation due to the electric field: *a*) positive dielectric anisotropy and *b*) negative dielectric anisotropy [5].

2.1.1. Classification of Thermotropic Liquid Crystals (LCs)

In 1922, Georges Friedel classified the thermotropic LCs with calamitic molecules, by their symmetry, into three different groups or mesophases: nematic (N), Cholesteric (N*) and Smectic (Sm).

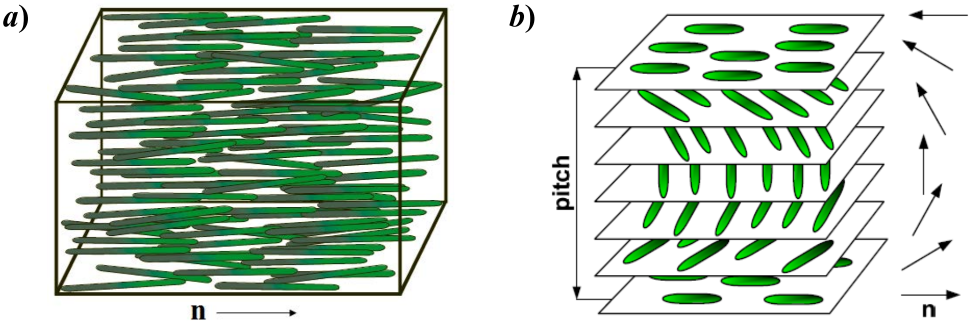

Fig. 2.3: Arrangement of molecules in the: *a*) nematic mesophase (N) *b*) cholesteric mesophase (N*) [5].

The nematic mesophase (N) is the less orderly. The centers of gravity of the molecules show no positional order, as in the liquid phase, but they tend to point in the same direction (defined by **n**), as it is shown in **Fig. 2.3a**. This mesophase is the most used in display systems and in many photonics applications. Its typical response times are in the millisecond range, or less **[8]**, and the molecular orientation can be easily controlled with an electric field of low amplitude **[6]**. Therefore, it is the specific type of LCs used in this work.

The cholesteric mesophase (N*), also called chiral nematic phase, presents a helical structure as that shown in **Fig. 2.3b**. In this phase, the molecules are arranged in parallel planes and each of these planes shows the same characteristics as the nematic phase. The **n** of each plane rotates describing a helix around the perpendicular axis with a period defined by the pitch. Cholesteric LCs are often used as dopants in mixtures of nematic materials for twist purposes.

The smectic phases (Sm) are numerous. The best known are the mesophases smectic A (SmA), smectic C (SmC) and smectic chiral C (SmC*).

2.1.2. Birefringence Modeling of Nematic Liquid Crystals (NLCs)

In the optical frequency regime, which is in the range of $10^{-14}s^{-1}$, the refractive index is generally used to describe wave propagation in the optical medium. While the dielectric constants are used to explain the molecular reorientation of LCs under the influence of a low frequency electric field (**E**).

The refractive indices n_e and n_o are mainly determined by the LC molecular structure, the wavelength (λ) and temperature (T) of operation. The dependence of the refractive index with λ is called dispersion and is expressed as $n(\lambda)$; and as a general rule, as λ increases, n_e and n_o decrease. The variation with T is different because as T increases, n_e decreases, but n_o can increases or decreases depending on the crossover temperature (T_o) of the LC material. T_o is defined as the transition temperature where $\partial n_o/\partial T = 0$ **[9]**.

Different physical models have been developed to describe the dependence of the LC refractive indices with the wavelength (e.g. the single−band model, the three−band model and the Cauchy model) and with the temperature (e.g. the Vuks model).

2.1.2.1. Birefringence dispersion: Extended Cauchy model

The Cauchy model is a very general and useful model because it is not only applicable to simple LC compounds; it is also applicable to LC mixtures. Besides, it also allows a good approximation of the dispersion of LC materials with low and high birefringence. The extended Cauchy equations are expressed as:

$$n_e(\lambda) = A_e + \frac{B_e}{\lambda^2} + \frac{C_e}{\lambda^4} \tag{2.1}$$

$$n_o(\lambda) = A_o + \frac{B_o}{\lambda^2} + \frac{C_o}{\lambda^4} \tag{2.2}$$

where A_e, A_o, B_e, B_o, C_e and C_o are called Cauchy coefficients. In (2.1) and (2.2) is clearly shown that as λ increases the LC refractive indices decrease. For large values of λ, i.e. infrared and millimeter waves, these equations are reduced to the constant terms A_e and A_o, which depend only of T. Therefore, in these regions the refractive indices are independent of λ, but the effects of other phenomena, as the molecular absorption and vibrations, increase.

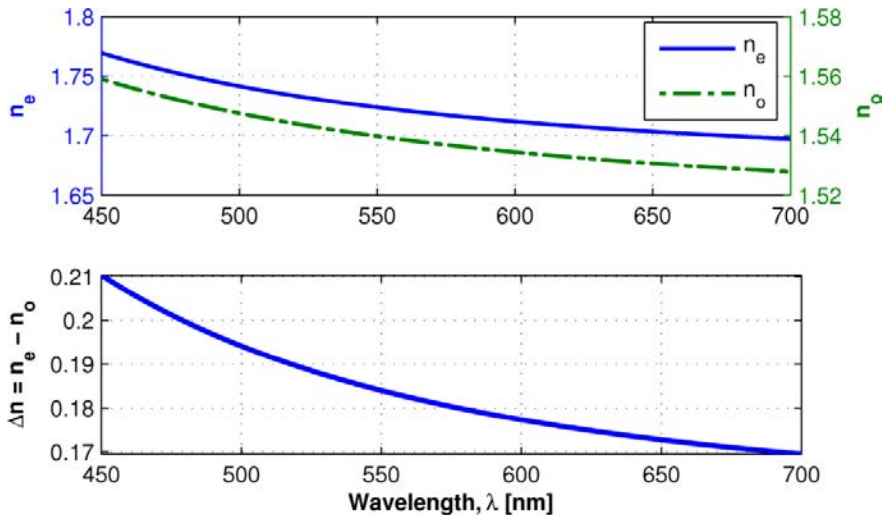

Fig. 2.4: Dispersion of the refractive indices and birefringence of the LC compound 5CB simulated with the Cauchy equations.

The Cauchy coefficients of some common compounds and mixtures of LCs are reported in **[9]**. These coefficients are shown in **Table 2.1**. They are calculated by fitting (2.1) and (2.2) to the experimental refractive indices of at least three wavelengths.

TABLE 2.1: CAUCHY COEFFICIENTS OF SOME COMPOUNDS AND MIXTURES OF LC AT 25 °C.

LC Material	n_e			n_o		
	A_e	B_e	C_e	A_o	B_o	C_o
MCL−9200−000	1.5382	0.0073	$4.00\text{x}10^{-5}$	1.4600	0.0058	$3.95\text{x}10^{-17}$
MCL−9200−100	1.5720	0.0111	$4.00\text{x}10^{-5}$	1.4740	0.0063	$6.04\text{x}10^{-18}$
MCL−6608	1.5359	0.0070	$4.02\text{x}10^{-17}$	1.4609	0.0050	$3.29\text{x}10^{-17}$
TL−216	1.6772	0.0155	0.0011	1.4989	0.0079	0.0001
E44	1.7282	0.0121	0.0027	1.5006	0.0091	0.0001
E7	1.6933	0.0078	0.0028	1.4990	0.0072	0.0003
5CB	1.6708	0.0081	0.0024	1.5139	0.0052	0.0008
5PCH	1.5801	0.0073	0.0003	1.4718	0.0049	0.0002
MLC−6241−000	1.5397	0.0075	$1.03\text{x}10^{-5}$	1.4601	0.0054	$3.15\text{x}10^{-17}$

In this work, the modeling of the LC dispersion is done by using the extended Cauchy equations, taking as theoretical reference the coefficients shown in **Table 2.1**. As an example, the **Fig. 2.4** shows the dispersion of the ordinary and extraordinary refractive indices and the resulting birefringence of the LC compound 5CB.

2.1.2.2. Temperature dependence: Vuks equations based model

As previously mentioned, the temperature also plays an important role in the variations of the LC refractive indices. As T increases, n_e behaves differently from n_o. For example, the derivative of n_e (i.e., $\partial n_e/\partial T$) is always negative. However, $\partial n_o/\partial T$ changes from negative to positive as T exceeds the crossover temperature T_o **[9]**, **[10]**. A good model for describing the effect of the T over the refractive indices of LCs is presented by **[10]**. It is based on the Vuks equations and it is given by:

$$n_e(T) \approx A - BT + \frac{2(\Delta n)_o}{3}(1 - T/T_C)^{\beta}, \tag{2.3}$$

$$n_o(T) \approx A - BT - \frac{(\Delta n)_o}{3}(1 - T/T_C)^{\beta}, \tag{2.4}$$

This model has four fitting parameters, where A and B describe the average refractive index as a function of the temperature, $\langle n(T)\rangle = A - B(T)$, while the exponent β is a material constant, $(\Delta n)_o$ is the LC birefringence in the crystalline state (at T = 0 K), that define birefringence (Δn) at the temperature of operation, and T_C is the LC clearing temperature. The **Table 2.2** shows the fitting parameters of the $\langle n(T)\rangle$ and Δn for the 5CB material at 546 nm, 589 nm, and 633 nm **[10]**. Then, the **Fig. 2.5** shows the variation of the refractive indices and the birefringence of the 5CB at 633 nm for T under T_C.

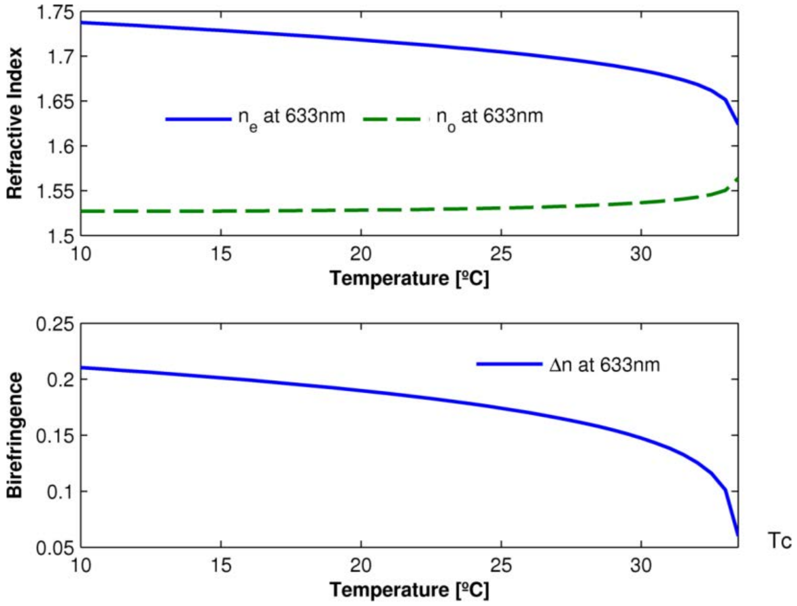

Fig. 2.5: Variation of the refractive indices and birefringence of the 5CB LC material for temperatures between 10º and T_C = 306.6º.

TABLE 2.2. FITTING PARAMETERS FOR THE AVERAGE REFRACTIVE INDEX $<n(T)>$ AND BIREFRINGENCE Δn OF 5CB AT $\lambda = 546$, 589, AND 633 nm. 5CB HAS $T_C = 306.6°$.

λ [nm]	$<n(T)>$		$\Delta n(T)$	
	A	$B(K^{-1})$	$(\Delta n)_o$	β
546	1.7751	5.81×10^{-4}	0.3594	0.1862
589	1.7674	5.79×10^{-4}	0.3505	0.1889
633	1.7601	5.75×10^{-4}	0.3389	0.1855

2.2. Basic Configurations of Nematic LC Devices

Due to the LCs nature, they are filled into cells in order to implement LC devices. The general structure of a LC cell is shown in **Fig. 2.6.** A LC cell consists of a thin layer of LC material sandwiched between two transparent glass substrates. The thickness of the LC layer (*d*) is kept uniform by using small spacers made of plastic microspheres or glass fibers. Transparent electrodes, usually of Indium Tin Oxide (ITO), are placed inside the substrates in order to apply the electric field (**E**) **[11]**. The structure shown in **Fig. 2.6** includes a pair of linear polarizers to controlling light transmission through the LC cell depending on **E**.

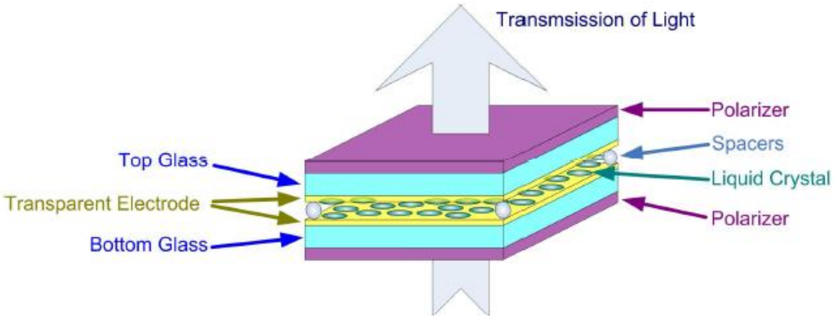

Fig. 2.6: Typical structure of a nematic LC cell between linear polarizers. This scheme includes an input and an output polarizer (analyzer) in order to controlling light transmission [12].

In the previous section, it was mentioned that the NLC molecules are oriented in the same direction, but this is not entirely true. If the NLC is inserted between two substrates, such as glasses, all the molecules will not be oriented in the same direction throughout the volume; they will do it by region, forming what is called micro−domains. There are two ways to achieve that the molecules to be oriented uniformly between the glass substrates. The first has already been explained in the previous section, and it consists in to apply an **E**. This is known as the Freedericksz effect **[13]**. The second option consists in to anchor and hold the LC molecules that are closest to the walls of the glass by a suitable mechanical or chemical treatment, using an alignment layer. With this method it is achieved that the molecules fixed to the glass surfaces influence the orientation of other neighbouring molecules **[13]**. Depending on the anchoring, the molecules can be oriented in two configurations: homogeneous and homeotropic.

When the c–axis direction of the molecules is parallel to the surface of the glass, it is called homogeneous alignment. This anchoring can be obtained by mechanical or chemical means. On the other hand, when the c–axis direction is perpendicular to the glass surface, it is called homeotropic alignment. This anchoring can only be achieved by chemical means. LC devices with different configurations can be manufactured depending on the alignment type in each of the surfaces and the LC material with which the cell is filled. The following briefly describes the two configurations of NLC cells used in this work.

2.2.1. Homogeneous nematic (HN) LC Cells

Homogeneous nematic LC cells (HN), also known as Freedericksz devices **[14]**, consist of a uniform layer of NLC, with thickness d_H, that is content between two transparent substrates, with homogeneous alignment and the same alignment direction in both surfaces.

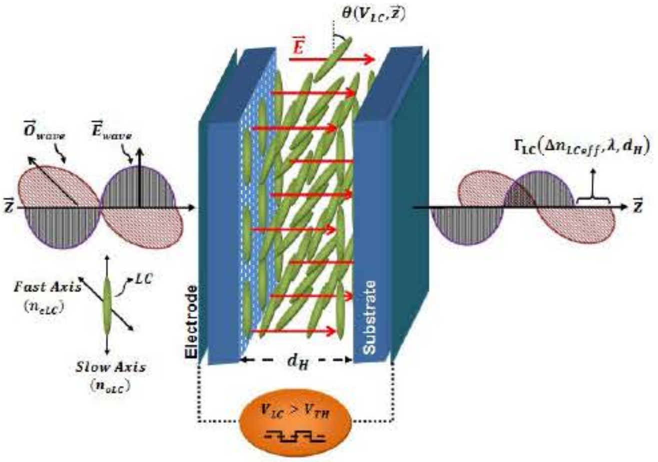

Fig. 2.7: Structure and operation of a homogeneous nematic LC cell.

2.2.1.1. *Freedericksz effect*

Under the effect of an electric field (**E**), with normal direction to the surface of the cell, the c–axes of the LC molecules are reoriented in the direction of **E**, with a tilt angle θ, relative to the surface of the cell, as shown in **Fig. 2.7**, only if $\varepsilon_{\parallel} > \varepsilon_{\perp}$ (positive dielectric anisotropy). The Freedericksz effect was first observed in 1933 and it is the basis of most of the electro–optic effects currently used in LC applications.

The minimum value of voltage (V) which produces an increment in the tilt angle θ is defined as the threshold voltage (V_{th}) **[15]**. V_{th} is determined by the LC splay constant k_{11} and its dielectric anisotropy and it is given by:

$$V_{th} = \pi \sqrt{\frac{k_{11}}{\varepsilon_o\left(\varepsilon_{\parallel} - \varepsilon_{\perp}\right)}} \tag{2.5}$$

where ε_o is the vacuum permittivity.

The distribution of θ is a function of the applied voltage V and the distance in the z direction. For high precision calculations, it is necessary to know the exact profile of $\theta(V,z)$, but to describe the behaviour of the device is sufficient to know the maximum tilt angle, θ_m, as a function of applied voltage. θ_m happens at a distance $d_H/2$ **[14]**. Just above the threshold voltage, the squared maximum tilt angle θ_m^2 (V) is linear, and is given by:

$$\theta_m^2(V) = \frac{4(V - V_{th})}{V_{th}\left(\frac{k_{33}}{k_{11}} + \frac{\varepsilon\text{[redacted]}}{\varepsilon_\perp}\right)} \tag{2.6}$$

where k_{33} is the LC bend constant. Equation (2.6) is incorrect for $V>>V_{th}$ due to approximations taken into account in its deduction **[16]**. In **[16]** one can find a detailed derivation of the accurate profile of $\theta(V,z)$. **Fig. 2.8** shows a graph with the relation of θ_m with the voltage applied to a HN cell of 5CB material.

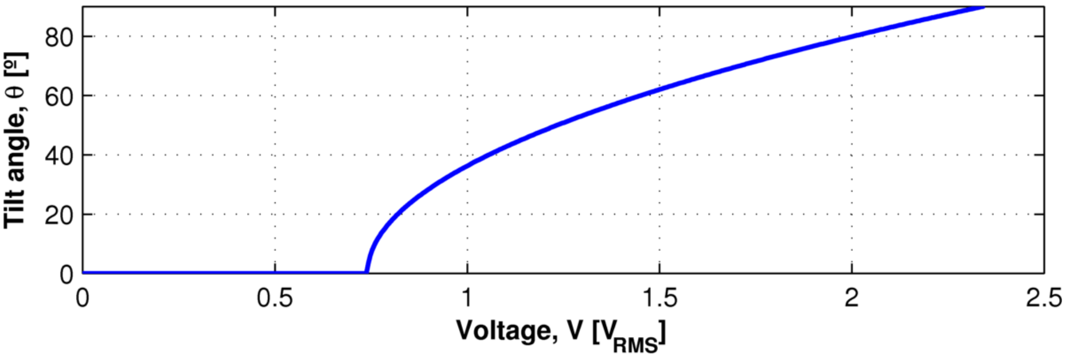

Fig. 2.8: Dependence of the maximum tilt angle with the applied voltage of a HN LC cell of 5CB material with λ = 515 nm, T = 25º, k_{11} = 6.4 pN (splay elastic constant), k_{22} = 3 pN (twist elastic constant), k_{33} = 10 pN (bend elastic constant), $\varepsilon_\parallel$ = 19.7 and $\varepsilon_\perp$ = 6.7.

2.2.1.2. *Electrically controlled phase delay (Γ)*

Therefore, HN cells are retarder plates with electrically controlled delay (or retardation). When $V < V_{th}$ ($\theta = 0º$), a HN cell with thickness d_H and birefringence Δn, produces a phase delay (Γ) between the polarization components of a incident light beam which travels normal to the cell surface, with wavelength λ, that is given by:

$$\Gamma = 2\pi \frac{\Delta n d_H}{\lambda} \tag{2.7}$$

However, when $V > V_{th}$ ($0º < \theta < 90º$) the polarization component that travels over the c–axis of the LC molecules sees an effective refractive index given by:

$$n_{ew}(V) = \frac{n_e n_o}{\sqrt{n_o^2 \cos^2(\theta_m) + n_e^2 \sin^2(\theta_m)}} \tag{2.8}$$

This generates an effective birefringence ($\Delta n_{eff} = n_{ew} - n_o$) and an electrically controlled delay (Γ_{eff}) that is expressed as:

$$\Gamma_{eff} = 2\pi \frac{\Delta n_{eff} d_H}{\lambda} \tag{2.9}$$

A detailed solutions of $n_{ew}(V,z)$ and $\Gamma(V,z)$ can be found in **[16]**. It is important to note that throughout this work the term retardation is often used to refer the phase delay.

2.2.2. Twisted nematic (TN) LC Cells

Twisted nematic LC cells (TN), consist of a uniform layer of NLC that is content between two transparent substrates, with homogeneous alignment in each surface and a twist angle between their alignment directions, as shown **Fig. 2.9**.

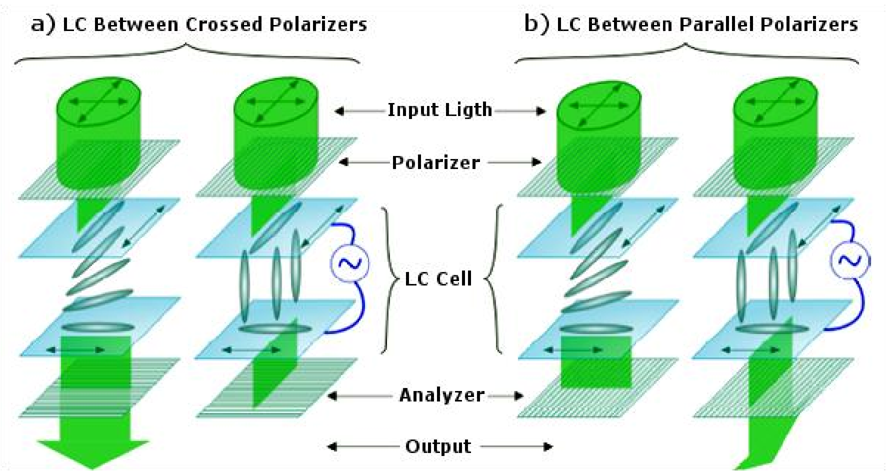

Fig. 2.9: Representation of a TN cell operation between: *a*) crossed polarizers, *b*) parallel polarizers [12].

This arrangement produces a twist structure in LC molecules between both surfaces, which acts as an optical wave–guide and rotates the polarization of the input beam. In order to facilitate the twist, the nematic material is often doped with a small amount of cholesteric LC and a small pre–tilt angle is allowed on the surfaces where the molecules are anchored.

The most common TN cell is the 90º–twisted and its operation between parallel and crossed linear polarizers (LPs) is shown in **Fig. 2.9**. In this type of cells, the twisted structure of the LC molecules performs a 90º twist through the thickness of the LC cell (PolRot cell). In this case, when a linearly polarized light passes through a TN cell, its polarization state is continuously rotated and finally it goes out at 90º from the incoming direction. This only occurs while Mauguin condition is satisfied **[17]**:

$$d\Delta n \gg$$ [redacted] (2.10)

If a voltage, V, greater than the threshold voltage, V_{th}, is applied to the cell, the LC molecules reorient. When voltage is greater enough ($V \gg V_{th}$), the LC molecules are aligned parallel to the electric field, that is, their molecular axes are perpendicular to the glass substrate plane, and the polarization rotation disappears. The voltage driven to the cell for obtaining a complete molecular reorientation is known as switching voltage, V_{SW}. Thus, light transmission is controlled by the voltage applied to the TN cell, lower voltages induce less polarization shifts. Taking into account the TN behaviour, the light passing through a TN cell, placed between polarizers, can be electrically controlled.

2.3. Optical Modeling with Jones Matrices

LC devices are usually modeled with Mueller **[18]** calculus, manipulating Stokes vectors and Mueller matrices, or with Jones calculus **[16]**, manipulating Jones vectors and matrices. Unlike a Mueller matrix, which is suitable for all kinds of optical systems, a Jones matrix can only be applied to a non−depolarizing optical system. Then, the Mueller matrix based models of LC devices provide a more accurate representation of the polarization state of the transmitted light than the Jones matrix based models. However, Jones matrix based models generally provides a good compromise between physical adequacy and accuracy with computational efficiency and optimization facilities in the theoretical model **[19]**. Moreover, the characterization methods that use Jones matrix models are less complex and require fewer measurements (less input polarization states), so they are widely used **[20]**, **[21]**, **[22]**, **[23]**, **[24]**.

2.3.1. Jones Calculus of Retarder Plates

Light propagation through a birefringent crystal (e.g. retarder plate or HN cell) consists of the linear superposition of two orthogonal waves, which travels over a fast (*f*) and a slow (*s*) axis. In the Jones Matrix modeling of a retarder plate it is assumed that the material has uniaxial birefringence, that the retarder plate is designed so that the optical axis (*c*−axis) is parallel to the surface and the dispersion of the material is neglected, moreover it is assumed that there is no reflection in the material surface and that the incident beam is entirety transmitted through the birefringent medium **[16]**. Then, the light transformation due to its passing through a retarder plate is modeled as:

$$\begin{pmatrix} V_x' \\ V_y' \end{pmatrix} = R(-\alpha) W_o R(\alpha) \begin{pmatrix} V_x \\ V_y \end{pmatrix} \tag{2.11}$$

where V_x and V_y are the polarization components of the input beam in the *xy* plane, $R(\alpha)$ is the rotation matrix of the *fs*−plane respect the *xy*−plane, given by (2.12), which represents the azimuth angle (α) of the retarder plate, W_o is the Jones matrix of the retarder plate, given by (2.13), and V_x’

and V_y' are the polarization components of the transmitted beam in the *xy* plane. The detailed deduction of this expression can be found in **[16]**.

$$R(\alpha)=\begin{pmatrix} \cos\alpha & \sin\alpha \\ -\sin\alpha & \cos\alpha \end{pmatrix} \tag{2.12}$$

$$W_o = e^{-i\varphi}\begin{pmatrix} e^{-i\Gamma/2} & 0 \\ 0 & e^{i\Gamma/2} \end{pmatrix} \tag{2.13}$$

The phase factor $e^{(-i\varphi)}$ of (2.13) can be neglected if the interference effects are not important, or are not observable. Retarder plates are characterized by their phase delay, Γ, their azimuth angle, *α*, and its transfer function matrix, *W*, which is represented by the product of the three matrices, obtaining:

$$W = R(-\alpha)W_oR(\alpha) \tag{2.14}$$

The passing of a light beam through a retarder plate can be described mathematically as a unitary transformation. Therefore many of the properties of the incident vector remain invariable; one of those properties is the orthogonality. If the polarization states of two beams are mutually orthogonal, they will remain orthogonal after passing through any retarder plate.

2.3.2. Jones Matrix of Linear Polarizers (LPs)

If the absolute phase delay is neglected, the representations of linear polarizers with the transmission axis parallel to the *x*− and *y*−axis, respectively, are given by:

$$P_{xo} = \begin{pmatrix} 1 & 0 \\ 0 & 0 \end{pmatrix} \quad and \quad P_{yo} = \begin{pmatrix} 0 & 0 \\ 0 & 1 \end{pmatrix} \tag{2.15}$$

Then, the characteristic transfer matrix of a linear polarizer with azimuth angle *α*, from the *x*−axis, can be defined as:

$$P_x = R(-\alpha)P_{xo}R(\alpha) \tag{2.16}$$

It is important to note that, in order to determine the effect of a stack of retarder plates and polarizers on the polarization state of an incident beam, the transfer matrix of each element must be written in reverse order. Then, the Jones vector of the output beam is obtained by the multiplication of the matrixes in sequence.

2.3.3. Jones Matrix of HN and TN cells

The operation of a HN cell and a retarder plate (H) are the same. Then, in this work, the characteristic transfer matrix of a HN cell, or retarder plate H, with azimuth angle α_H will be expressed as:

$$W_H(\alpha_H) = R^{-1}(\alpha_H) \times \begin{bmatrix} e^{-i\frac{\Gamma_H}{2}} & 0 \\ 0 & e^{i\frac{\Gamma_H}{2}} \end{bmatrix} \times R(\alpha_H) \qquad (2.17)$$

where $R(\alpha_H)$ is the rotation matrix of the c–axis orientation angle respect to the x–axis, see **Fig. 2.10b**, and Γ_H is the phase delay of a HN cell with thickness d_H, from (2.9).

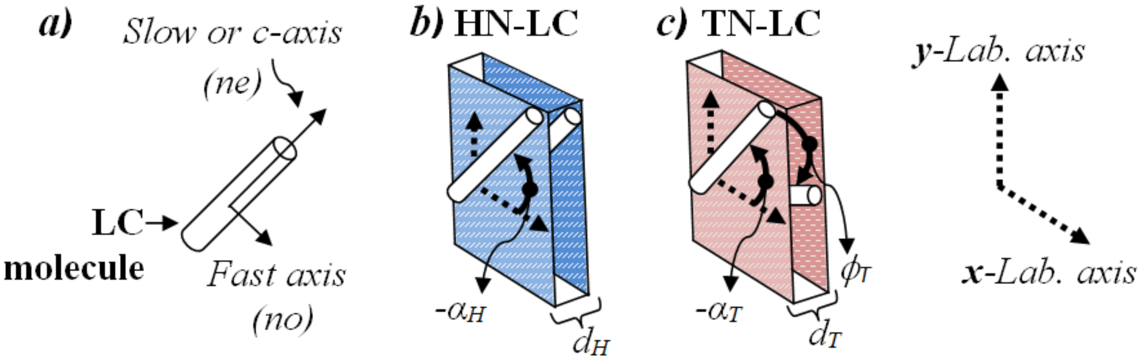

Fig. 2.10: Nematic LC cells representation: a) nematic LC molecule, b) homogeneous nematic LC cell (HN) c) twisted nematic LC cell (TN).

On the other hand, TN cells can be modeled as a stack of N HN layers, each one with a constant α_H varying in a total twist angle ϕ_T, in increments of $\Delta\phi_T = \phi_T/N$. Therefore, the characteristic transfer matrix of a TN cell **[16]**, **[25]**, with its front c–axis oriented at an angle α_T and total twist ϕ_T, see **Fig. 2.10c**, is given by:

$$W_T(\alpha_T) = R^{-1}(\alpha_T) \times \begin{bmatrix} \cos(\phi_T) & -\sin(\phi_T) \\ \sin(\phi_T) & \cos(\phi_T) \end{bmatrix} \times \begin{bmatrix} \cos(X) - i\frac{\Gamma_T}{2}\frac{\sin(X)}{X} & \phi_T\frac{\sin(X)}{X} \\ -\phi_T\frac{\sin(X)}{X} & \cos(X) + i\frac{\Gamma_T}{2}\frac{\sin(X)}{X} \end{bmatrix} \times R(\alpha_T) \qquad (2.18)$$

where $X = \left(\phi_T^2 + \Gamma_T^2/4\right)^{1/2}$ and Γ_T is the phase delay of a TN cell with thickness d_T, see **Fig. 2.10c**. Therefore, a HN cell is a particular case of TN cells with twist angle $\phi_H = 0°$.

It is important to note that the elements {1,1} and {2,1} of (2.17) and (2.18) refer to the output light polarized at 0º to the x−axis (T_x) and at 90º to the x−axis (T_y), respectively, when the input beam is x–polarized.

2.4. Applications and Advantages of NLC devices

The range of possible applications of LC devices is very broad and its direct application is the manufacture of displays. Currently, active matrix LC displays (AMLCD) are a very competitive technology in this area, compared to other technologies such as plasma display panels (PDP), field emission displays (FED), vacuum fluorescent displays (VFD) organic light emitting diode screens (OLED) and thin−film electroluminescent displays (TFEL). However, the applications of LC devices are not limited to the development of displays, although this is the application that generates more benefits **[5]**.

The unique electro−optic properties of LCs also make them suitable material for many nondisplay applications. nematic liquid crystal devices are nowadays extensively used in multiple photonics applications as: variable attenuators, wavelength tunable filters and switches, focus−tunable lenses, beam−steering devices, spatial light modulators, integrated devices based on optical waveguiding, tunable lasers, optical nonlinear components **[26]** and sensors **[27]**.

In general, the competitiveness of nematic LC devices in the different photonic applications is due to their main advantages:

- They are stable and reliable since no movable parts are used.
- They use small control voltages (few volts) and have low electrical power consumption.
- They have a great potential for optical modulation due to their large optical electro−optic effect.
- They are a mature technology, with ease of manufacturing and low cost.

On the other hand, they have some disadvantages:

- Their response time is in the order of millisecond. However, in the last years, nematic liquid crystal cells with response times lower than 3 ms **[28]** and 2 ms **[29]**, as well as nanosecond response **[30]** and different techniques to reduce the response time below 1 ms **[8]** have been reported.
- Most of the applications require an input polarizer that can suppose 3dB of losses (as minimum) if the input beam is random polarized. This can be easily overcome using designs with polarization diversity schemes (see appendix B).

LC devices are very sensitive to birefringence variations with the wavelength (dispersion) and the temperature. These effects have a greater impact on optical devices with staked structures **[31]**, **[32]** (e.g. filters, interleavers, broadband switches) for broadband applications, where the temperature might not be controlled (e.g. in low cost SI−POF networks with WDM). The characterization method presented in this Chapter (below) and the design included in **Chapter 3** and **Chapter 4** are essential tools to reduce, or even eliminate, the effects of temperature and dispersion in the performance of optical devices based on LCs for SI−POF networks.

2.5. Spectral Method for Fast Characterization Arbitrary TN Cells

The optical characteristics and performance of a TN based device depends significantly on four cell parameters **[16]**, **[12]**, **[33]**: the molecular twist angle (ϕ_T), the rubbing direction angle (α_T) at the input surface, the cell thickness (d_T) and the LC material birefringence Δn, which depends on the wavelength (λ). Therefore, there is a constant need for accurate characterization of the LC cells parameters during the manufacturing processes for quality control or for the posterior modeling of the optical devices.

2.5.1. Characterization Methods of TN Cells: State of the Art

Several characterization methods have been proposed in the past. They are typically classified as single wavelength methods or spectral methods.

Single wavelength methods, as a rule, are more reliable in an experiment. However, they are able to determine the retardation ($d_T \times \Delta n$) for a fixed wavelength only. Therefore, they are inherently unable to determine the wavelength dispersion of Δn, $\Delta n(\lambda)$. The most common single wavelength method for characterizing TN cells is proposed by Soutar and Lu **[20]**. It consists of the non−linear fitting of a theoretical model, based on the Jones Matrix calculus. The transmittances of the TN cell between parallel and crossed polarizers are measured at a fixed λ, and at different output polarizer (analyzer) angles, α_A, between 0° and 360°. This is an effective method, but it is not able to determine unequivocally the twist sense and the rubbing direction angle, due to the mathematical ambiguities of its theoretical model. Many single wavelength methods have been proposed to find a unique answer for ϕ_T and α_T **[21]**, **[22]**, **[23]**, **[24]**, **[34]**, **[35]** and **[36]**. But, they require multiple rotation angles (azimuth angles) for the polarizers or the LC cell, additional measurements using polarimeters, with different wavelengths or voltage levels, or applying analytical conditions.

On the other hand, spectral methods allow to determine $\Delta n(\lambda)$, even considering the transmission ripple of the LC devices caused by the multiple reflections between the indium tin oxide (ITO) layers deposited on the inner cell surfaces **[37]**, overcoming this important limitation of single wavelength methods. However, the spectral methods reported to date are not able to determine ϕ_T, the ϕ_T sense, α_T and $d_T \times \Delta n(\lambda)$ simultaneously **[37]**, **[38]**, **[39]**, **[40]**. This is because, in general, most of the characterization methods proposed to date are oriented to displays applications, where the determination of $|\phi_T|$, α_T and $\Delta n(\lambda)$ is enough. However, the performance of the optical communication devices based on stacked structures of LC cells **[32]**, **[41]**, **[42]**, **[31]**, is very sensitive to the ϕ_T sense as well as the other parameters.

2.5.2. Ambiguities in Methods that use TN Cells between LPs

The most common display applications and characterization schemes use a TN cell between parallel and/or crossed polarizers and Jones Matrix. These methods cannot find a unique solution for all the TN cell parameters simultaneously, due to the ambiguities of the theoretical model. For example, from (2.18) and considering an input beam polarized at 0º to the x–axis, the magnitude of the transmitted beam polarized at 90º to the x–axis, for crossed polarizers, is given by:

$$T_y = \left(\sin(\phi_T)\cos(X) - \frac{\phi_T}{X}\cos(\phi_T)\sin(X) \right)^2 + \left(\frac{\Gamma_T}{2X}\sin(2\alpha_T + \phi_T)\sin(X) \right)^2 \qquad (2.19)$$

And, since Jones matrices are unitary, the transmitted beam polarized at 0º to the x–axis, for parallel polarizers, can be expressed as $T_x = 1 - T_y$.

Equation (2.19) is not able to distinguish the ϕ_T sense or the difference between α_T and $\alpha_T + 90º$. These are called ambiguous situations. For example, using (2.19) in the cases where $[\alpha_T, \phi_T] = [0º, 90º]$, $[0º, -90º]$, $[90º, 0]$ and $[90º, -90º]$, the same magnitude of T_Y is obtained and it is given by:

$$T_y = \cos(X)^2 + \left(\frac{\Gamma_T}{2}\frac{\sin(X)}{X} \right)^2 \qquad (2.20)$$

For this reason, the characterization methods that use a single TN cell between parallel or crossed polarizers, and Jones matrices based models, cannot determine a single solution for ϕ_T and α_T.

2.5.3. Proposed Characterization Method

In this section, a new spectral method for the precise determination of TN cells parameters is presented. The method consists of measuring the transmittance, between parallel and crossed polarizers, of a reference wave plate, H, with well known characteristics, in series with the TN sample, as shown in **Fig. 2.11** scheme. Optical transmittances are measured rotating H for different azimuth angles, α_{Hm} where $m = 1, 2 \ldots M$ ($M = 3$ is enough), in the optical spectrum of interest. Then, the TN cell parameters are determined by fitting the theoretical model to the experimental curves. The model is obtained with the Jones Matrix calculus and the extended Cauchy model (for the LC birefringence dispersion calculations). The curve fitting is done by implementing a genetic algorithm (GA) with wide searching limits and without specific initial conditions. This procedure allows determining the rubbing angle, α_T, the twist angle, ϕ_T, and its sense, as well as the dispersion of the LC retardation, $d_T \times \Delta n(\lambda)$, simultaneously, with few measurements, and using a simple procedure.

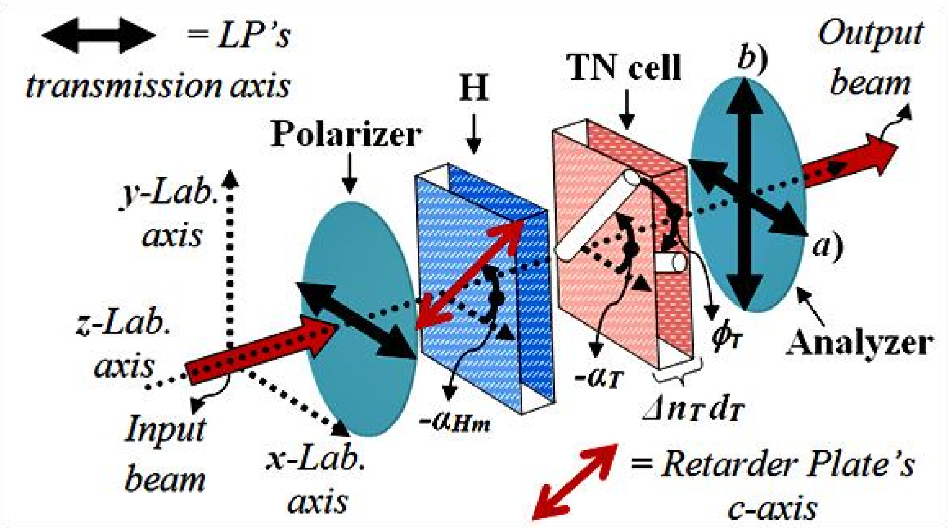

Fig. 2.11: Proposed characterization scheme. The angle variations in the clockwise direction are positive. *a*) Parallel polarizers and *b*) crossed polarizers.

2.5.3.1. *Theoretical model and polarization function*

The transfer function of the scheme shown in **Fig. 2.11** can be simply represented by multiplying the Jones matrices of H and the TN cell, see (2.17) and (2.18). This is expressed as:

$$W = W_T\left(\alpha_T\right) W_H\left(\alpha_{Hm}\right) \tag{2.21}$$

Then, considering an input beam polarized at 0º to the x–axis, the magnitude of the element $W[2,1]$ represents the transmitted beam polarized at 90º to the x–axis:

$$\begin{aligned} T_y = & \left\{ \begin{array}{l} \frac{1}{2}\cos\left(\frac{\Gamma_H}{2}\right)\left[\sin\left(\phi_T + X\right) + \sin\left(\phi_T - X\right)\right] + \\ \frac{\phi_T}{2X}\cos\left(\frac{\Gamma_H}{2}\right)\left[\sin\left(\phi_T - X\right) - \sin\left(\phi_T + X\right)\right] + \\ \frac{\Gamma_T}{4X}\sin\left(\frac{\Gamma_H}{2}\right)\left[\cos\left(-2\alpha_{Hm} + \sigma_3 + X\right) - \cos\left(-2\alpha_{Hm} + \sigma_3 - X\right)\right] \end{array} \right\}^2 \\ & + \left\{ \begin{array}{l} \frac{\phi_T}{2X}\sin\left(\frac{\Gamma_H}{2}\right)\left(\sigma_2 - \sigma_1\right) - \frac{1}{2}\sin\left(\frac{\Gamma_H}{2}\right)\left(\sigma_1 + \sigma_2\right) + \\ \frac{\Gamma_T}{4X}\cos\left(\frac{\Gamma_H}{2}\right)\left[\cos\left(\sigma_3 + X\right) - \cos\left(\sigma_3 - X\right)\right] \end{array} \right\}^2 \end{aligned} \tag{2.22}$$

where $\sigma_1 = \sin(2\alpha_{Hm} + \phi_T - X)$, $\sigma_2 = \sin(2\alpha_{Hm} + \phi_T + X)$ and $\sigma_3 = 2\alpha_T + \phi_T$. It is important to note that α_T, α_{Hm} and ϕ_T are referenced from the x–laboratory axis and are positive in the clockwise direction, as it is shown in **Fig. 2.11**. In this model is considered that the TN cells have zero or negligible pre–tilt angle.

Now, a polarization function is defined in order to relate T_y and T_x, eliminating the influence of the losses and the ripple on the transmission spectrum of the experimental measurements for the curve fitting procedure. Since the transmission spectra are obtained for different α_{Hm}, the theoretical polarization function is defined as:

$$P_{tm}(\alpha_{Hm}) = \frac{T_y(\alpha_{Hm}) - T_x(\alpha_{Hm})}{T_y(\alpha_{Hm}) + T_x(\alpha_{Hm})} = 2T_y(\alpha_{Hm}) - 1 \tag{2.23}$$

where $m = 1, 2, \ldots M$, and the sub−index t indicates that it refers to the theoretical curves, from (2.22). The polarization function $P_{tm}(\alpha_{Hm})$ varies between −1 and 1 and it describes the preponderance of transmitted light polarized at 0° to the x−axis over transmitted light polarized at 90° to the x−axis. $P_{tm}(\alpha_{Hm}) = -1$ means that the transmitted beam is x−polarized and $P_{tm}(\alpha_{Hm}) = 1$ means that the transmitted beam is y−polarized.

2.5.3.2. *Minimum azimuth angles α_{Hm} for solving the ambiguities*

Now, the potential of the proposed method for solving the ambiguities in the determination of TN cells parameters is analyzed by using the polarization function $P_{tm}(\alpha_{Hm})$, defined by (2.23). $P_{tm}(\alpha_{Hm})$ is simulated using a TN cell of 5CB material (with $\Delta n = 0.1785$ at 589 nm and 25°C **[9]**) and $d_T = 5\ \mu$m, considering four ambiguous combinations of $[\alpha_T, \phi_T]$ ([0°, 90°], [0°, −90°], [90°, 0°] and [90°, −90°]) and a commercial wave plate (H) of Quartz (SiO_2), with $d_H = 1$ mm, in the range from 420 to 886 nm. The same wave plate and spectral range are used in the experimental section. Each ambiguous combination is simulated with four values of α_{Hm} ($\alpha_{H1} = 0$ °, $\alpha_{H2} = -15°$, $\alpha_{H3} = -30°$ and $\alpha_{H4} = -45°$) in order to calculate the respective $P_{tm}(\alpha_{Hm})$.

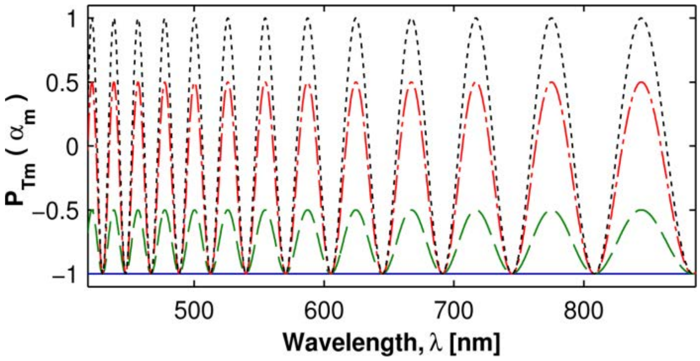

Fig. 2.12: Behavior of the polarization function $P_{tm}(\alpha_{Hm})$ of a wave plate H of Quartz (SiO_2), with $d_H = 1$ mm and $\alpha_{H1} = 0°$ (blue solid line), $\alpha_{H2} = -15°$ (green dashed line), $\alpha_{H3} = -30°$ (red dash−dot line) and $\alpha_{H4} = -45°$ (black dotted line).

First, **Fig. 2.12** shows the behavior of $P_{tm}(\alpha_{Hm})$ without including the TN cell, i.e., considering only H at the different values of α_{Hm}. It is observed that when the c−axis of H is at 0° with respect to the x−axis there is no change in the polarization state of the beam emerging from the H plate, with regard to the beam coming from the polarizer. The maximum change in the polarization state of the beam coming from the polarizer is produced when *c*−axis of H is at −45° with respect to the *x*−axis.

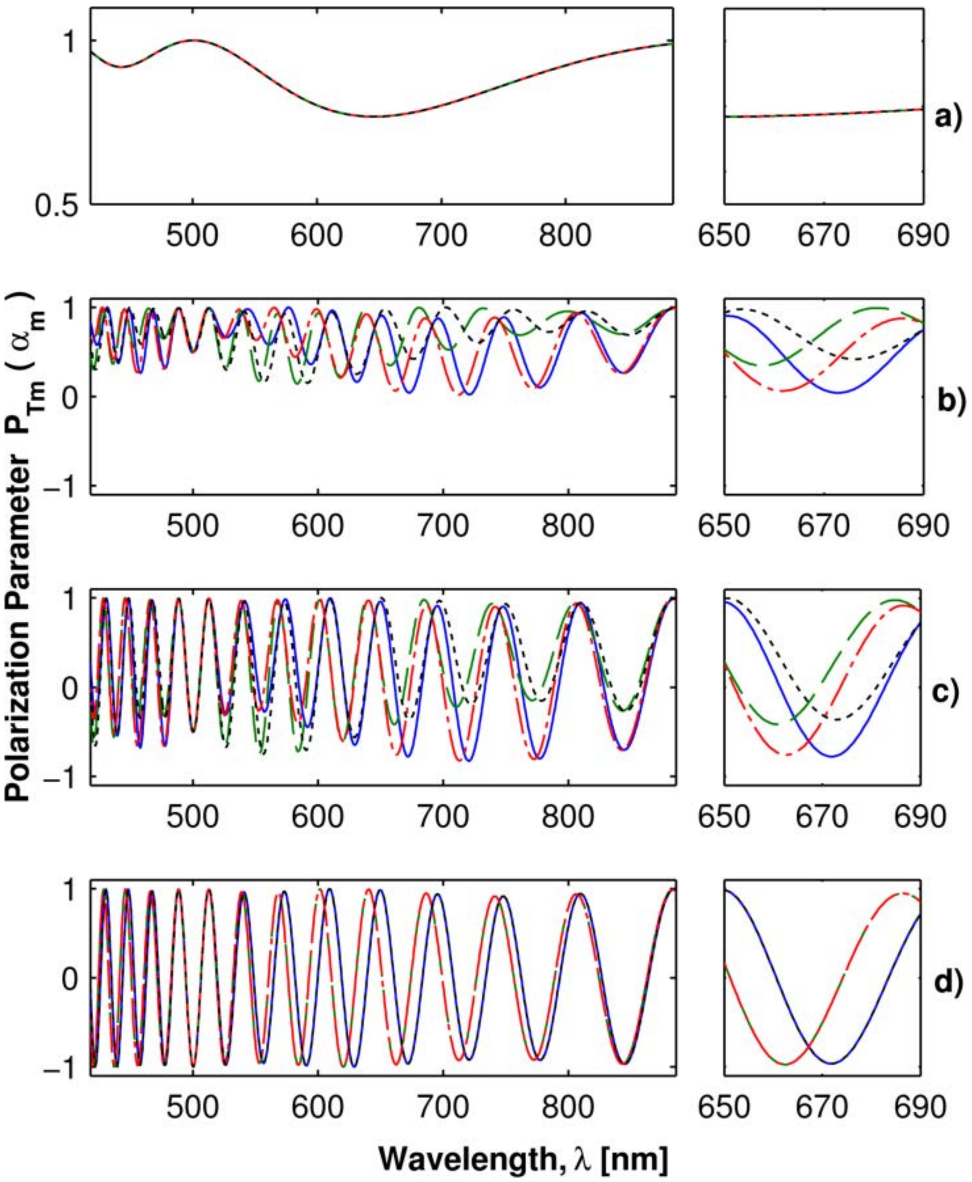

Fig. 2.13: Behavior of the polarization function $P_{tm}(\alpha_{Hm})$ of the proposed characterization method, considering a TN cell of 5CB and 5 μm thickness with four ambiguous values of [α_T, ϕ_T] = [0°, 90°] (blue solid line), [0°, −90°] (green dashed line), [90°, 90°] (red dash−dot line) and [90°, −90°] (black dotted line). H is a wave plate of Quartz with d_H = 1 mm and it is rotated at a) α_{H1} = 0 °, b) α_{H2} = −15°, c) α_{H3} = −30° and d) α_{H4} = −45°.

Then, **Fig. 2.13** shows the behavior of $P_{tm}(\alpha_{Hm})$ for the characterization system, i.e., considering the TN cell and H at the four values of α_{Hm} for each ambiguous combination of [α_T, ϕ_T]. It can be seen that $P_{t1}(\alpha_{H1} = 0°)$ has the same response for the different [α_T, ϕ_T] combinations. This case represents only the contribution of the TN cell since H has no effect, therefore, (2.22) is equivalent to (2.19). On the other hand, $P_{t4}(\alpha_{H4} = -45°)$ has equivalent responses for [0°, 90°] and [90°, −90°] and for [0°, −90°] and [90°, 90°], which represent two ambiguous situations. However, $P_{t2}(\alpha_{H2} = -15°)$ and $P_{t3}(\alpha_{H3} = -30°)$ have different curves for each $[\alpha_T, \phi_T]$ combination. Therefore, it can be seen that there is no ambiguity at $P_{tm}(\alpha_{Hm})$ for $0° < \alpha_{Hm} < -45°$ in the considered spectral range.

Therefore, $P_{t1}(\alpha_{H1} = 0°)$ will be used to determine the parameters of the TN cell, while $P_{t2}(\alpha_{H2} = -15°)$ and $P_{t3}(\alpha_{H3} = -30°)$ will be used to eliminate the uncertainty between the ambiguous situations of α_T and ϕ_T.

The phenomena shown in **Fig. 2.13** can be described as follows. The TN cell rotates 90º the polarization state of the incident beam, from being x−polarized to be y−polarized, at ~500 nm and ~900 nm. That is why in these regions, all the ambiguous situations of **Fig. 2.13** (b, c and d) are overlapped with a value that equals to the values shown in **Fig. 2.12** at these wavelengths but with opposite sign. While in the others regions, e.g. between 550 nm to 800 nm, the TN cell is not able to rotate completely the incident light. Therefore, in this region we see variations in the amplitude and periodicity that are particular for each ambiguous situation, which allows their identification. Therefore, the proposed method depends on the existence of spectral regions where the conversion efficiency of the TN cell is less than 100%, which are related to the Mauguin minima. This is highly dependent on the LC cell retardation and it is analyzed in the discussion section.

2.5.3.3. Nonlinear fitting algorithm: Genetic Algorithm (GA)

The nonlinear fitting algorithm adjusts the theoretical model, given by (2.22), to the experimental transmittances between parallel and crossed polarizers named, $T_{xe}(\alpha_{Hm})$ and $T_{ye}(\alpha_{Hm})$, respectively, which are obtained by using an experimental set−up based on the scheme of **Fig. 2.11**. $T_{xe}(\alpha_{Hm})$ and $T_{ye}(\alpha_{Hm})$ are related by the experimental polarization function, $P_{em}(\alpha_{Hm})$, which is given by:

$$P_{em}(\alpha_{Hm}) = \frac{T_{ye}(\alpha_{Hm}) - T_{xe}(\alpha_{Hm})}{T_{ye}(\alpha_{Hm}) + T_{xe}(\alpha_{Hm})} \tag{2.24}$$

The curve fitting can be done with any fitting algorithm. In this work it is performed by using a Genetic Algorithm (GA). Its random nature increments the possibility of finding a global minimum, moreover it allows implementing black−box function or constrains, which can be discontinuous and non−differentiable, as part of the objective function **[43]**. The curve fitting procedure considers α_T, ϕ_T, d_T and $\Delta n(\lambda)$ as unknown variables. Therefore, the vector of fitting variables (considered as an individual by the GA) is defined as:

$$x = [\alpha_T,\ \ \phi_T,\ \ d_T,\ \ A_{eo},\ \ B_{eo},\ \ C_{eo}] \tag{2.25}$$

where $A_{eo} = A_e - A_o$, $B_{eo} = B_e - B_o$ and $C_{eo} = C_e - C_o$ are the coefficients of the Cauchy model that define $\Delta n(\lambda)$, from (2.1) and (2.2). And the objective function to be minimized is given by:

$$F_{obj}\left(x\right)=\frac{1}{M}\sum_{m=1}^{M}\sqrt{\frac{1}{L}\sum_{i=1}^{L}\left[P_{em}\left(\lambda_i,\alpha_{Hm}\right)-P_{tm}\left(\lambda_i,\alpha_{Hm},x\right)\right]^2} \qquad (2.26)$$

where L is the number of wavelength sampled (λ_1, λ_2, … λ_L). This expression represents the mean value of the root mean square error (RMSE) between the theoretical and experimental values of the M curves. Then, the fitting algorithm finds the optimal values of x that fits the theoretical model to the experimental measurements for each α_{Hm}.

It is important to note that this method determines the LC cell optical path (retardation). Then, in order to determine $\Delta n(\lambda)$, d_T must be known, and vice versa.

2.5.3.4. Experimental verification: Characterization of two different TN cells

In order to demonstrate the effectiveness and simplicity of the proposed method, two experiments are presented. In each case, a different TN cell is characterized and the resulting $\Delta n(\lambda)$ is compared with the respective expected value. The TN cells were manufactured with zero or negligible pre−tilt angle. These characterizations are performed with the following procedure.

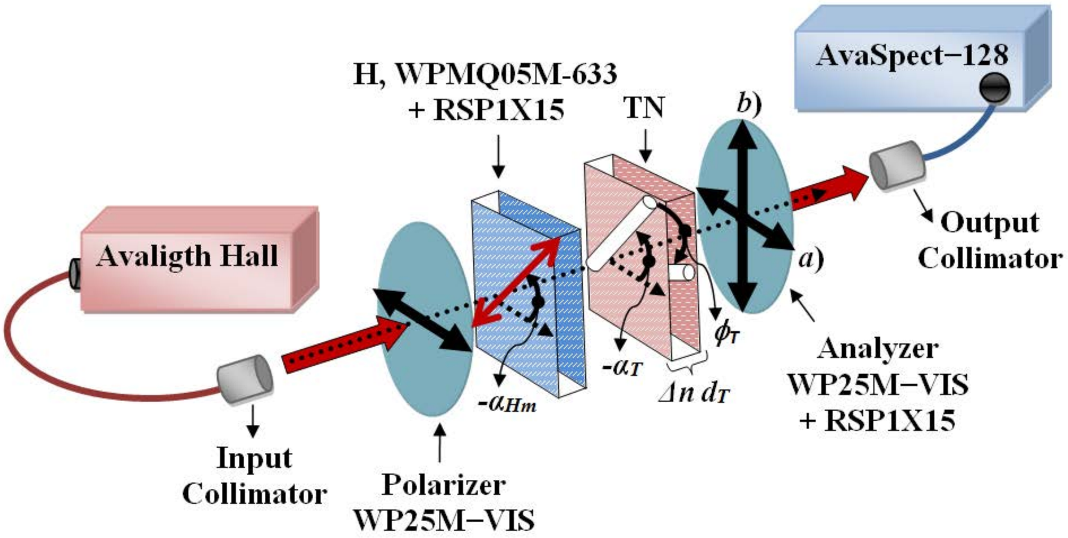

Fig. 2.14: Experimental setup. The angle variations in the clockwise direction are positive. a) Parallel polarizers, for $T_{xe}(\alpha_{Hm})$ and b) crossed polarizers, for $T_{ye}(\alpha_{Hm})$.

The experimental set−up is shown in **Fig. 2.14**. The input beam is obtained from a halogen light source and the transmittance measurements are taken with the spectrometer AvaSpect−128, with a spectral range from 360 nm to 886 nm and 4 nm of spectral resolution. Multimode optical fibers with collimators are used at the input and output ports. The input collimator produces a beam of 5 mm diameter. The polarizers have a diameter of 25 mm and an extinction ration > 250:1 in the range from 420 nm to 886 nm. The wave plate, H, is the WPMQ05M−633 and its α_{Hm} variations are done with a manual rotation mount at 15° rotation steps. The values chosen for α_{Hm} are: α_{H1} =

0º, $\alpha_{H2} = -15$º and $\alpha_{H3} = -30$º. $\alpha_{H1} = 0$º represents the TN cell behavior, while $\alpha_{H2} = -15$º and $\alpha_{H3} = -30$º allows to identify the univocal solution of α_T and ϕ_T. The transmittance curves $T_{xe}(\alpha_{Hm})$, parallel polarizers, and $T_{ye}(\alpha_{Hm})$, crossed polarizers, for $m = 1$, 2 and 3, are measured in the range from 420 nm to 886 nm (limited by the polarizers and spectrometer operation ranges).

Once $T_{xe}(\alpha_{Hm})$ and $T_{ye}(\alpha_{Hm})$ are obtained, the experimental polarization parameters $P_{em}(\alpha_{Hm})$ are calculated, for $m = 1$, 2 and 3, and the curve fitting procedure is performed. The population size is set to 1000 (number of x combinations per iteration) and the maximum number of iterations is set to 100. Wide search limits are set for α_T, ϕ_T and $\Delta n(\lambda)$ ($-110° \leq \alpha_T \leq 110°$, $80° \leq |\phi_T| \leq 100°$, $0 \leq A_{eo} \leq 0.4$, $0 \leq B_{eo} \leq 0.03$ and $0 \leq C_{eo} \leq 0.03$) and all the initial conditions are set to 0, in order to demonstrate the strong convergence capacity of the proposed method. d_T is fixed to its respective theoretical value (for each characterized TN cell), since $\Delta n(\lambda)$ has been set as a variable.

➢ First experiment: 5CB TN Cell

In this experiment, a TN cell made with 5CB LC material, 90º twists and 5.1 μm thickness (named TN1) is characterized.

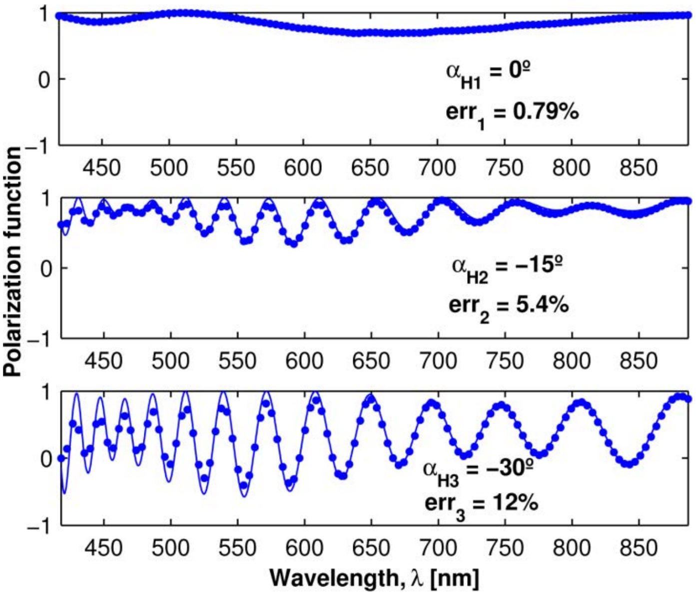

Fig. 2.15: Polarization parameters of the TN cell TN1 in series with H. Solid lines represent the curve fitting, $P_{tm}(\alpha_{Hm})$, and the dots represent experimental measurements, $P_{em}(\alpha_{Hm})$.

Fig. 2.15 shows the curves of the polarization function $P_{em}(\alpha_{Hm})$ for the 3 different values of α_{Hm} (dots). From these data, the nonlinear fitting procedure finds the optimal theoretical model for TN1, which is defined by: $\alpha_{T1} = 82.6°$, $\phi_{T1} = -87.1°$, $d_{T1} = 5.1$ μm, $A_{eoT1} = 0.1605$, $B_{eoT1} = 0.0011$ and $C_{eoT1} = 0.0017$. The curve fitting results are also shown in **Fig. 2.15** (solid lines), where e_{rrm} represents the root mean square error (RMSE) between the experimental and theoretical curves.

In **Fig. 2.16**, the resulting birefringence of TN1, $\Delta n_{T1}(\lambda)$, which is defined by: $A_{eoT1} = 0.1605$, $B_{eoT1} = 0.0011$ and $C_{eoT1} = 0.0017$ (solid line), is compared with the birefringence of the 5CB LC material, taken from **[9]** (see, **Table 2.1**), which is defined by: $A_{eo} = 0.1569$, $B_{eo} = 0.0029$ and $C_{eo} = 0.0016$ (dots). The maximum relative error between both curves is less than 1% in the range from 420 nm to 886 nm.

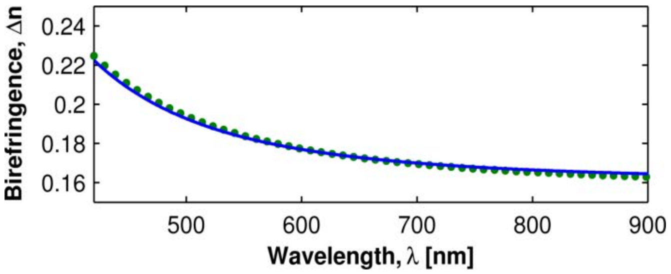

Fig. 2.16: Resulting birefringence of the TN cell TN1, defined by $A_{eoT1} = 0.1605$, $B_{eoT1} = 0.0011$ and $C_{eoT1} = 0.0017$ (solid line), and the theoretical birefringence of the 5CB LC material, defined by $A_{eo} = 0.1569$, $B_{eo} = 0.0029$ and $C_{eo} = 0.0016$ (dots).

➢ Second experiment: High–Birefringence (1658) TN Cell

In this experiment, a TN cell made with 1658 LC, 90º twist and 5.1 μm thickness (named TN2) is characterized. This is an experimental LC material synthesized at the Military University of Technology in Warsaw.

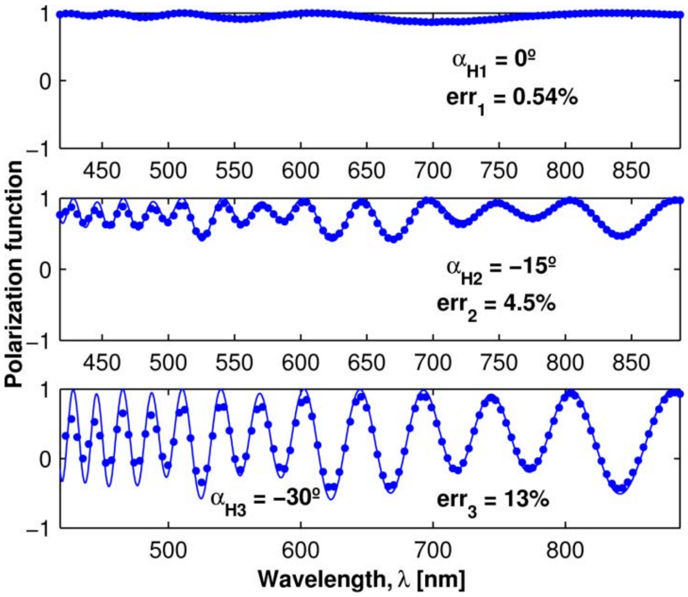

Fig. 2.17: Polarization parameters of the TN cell TN2 in series with H. Solid lines represent the curve fitting, $P_{tm}(\alpha_{Hm})$, and the dots represent experimental measurements, $P_{em}(\alpha_{Hm})$.

Fig. 2.17 shows the experimental polarization parameter $P_{em}(\alpha_{Hm})$ for the 3 different values of α_{Hm} (dots). And in the same figure, the theoretical model responses are plotted (solid lines). This model is obtained with the nonlinear fitting algorithm, and it is defined by α_{T2} = 86.2°, ϕ_{T2} = −91.4°, d_{T2} = 5.1 μm, A_{eoT2} = 0.3103, B_{eoT2} = 0 and C_{eoT2} = 0.0063.

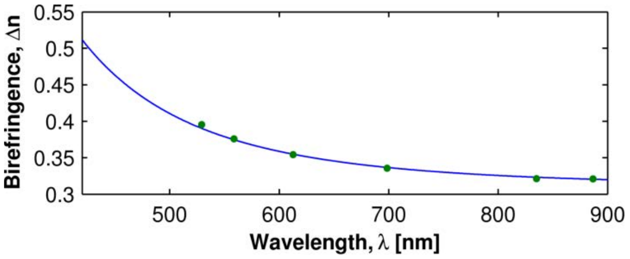

Fig. 2.18: Resulting birefringence of the TN cell TN2, defined by A_{eoT2} = 0.3103, B_{eoT2} = 0 and C_{eoT2} = 0.0063 (solid line), and the expected birefringence values of the LC1658 at some wavelengths, previously obtained from a homogeneous cell by a different characterization method (dots).

In **Fig. 2.18**, the resulting birefringence of TN2, $\Delta n_{T2}(\lambda)$, which is defined by: A_{eoT2} = 0.3103, B_{eoT2} = 0 and C_{eoT2} = 0.0063 (solid line), is compared with the birefringence values of the 1658 LC material measured at 6 different wavelengths (dots). These values were obtained for cells, of the same material (HN cells), using a different characterization method **[44]**. The validity of these data is tested in **Chapter 3 [42]**, and the points are limited between 520 nm and 886 nm due to the LPs and the spectrometer used in their characterization **[42]**. The relative error between $\Delta n_{T2}(\lambda)$ and the previous characterized values **[44]**, **[42]** is less than 1.3%.

2.5.3.5. Discussion and Remarks

The proposed method allows unambiguously determining the most important parameters of TN cells, unlike other spectral methods, with a fast and simple procedure. And unlike single wavelength methods, it can also accurately determine the LC birefringence spectral dispersion, $\Delta n(\lambda)$.

It has been shown that only 6 measurements are required, since a spectrometer can measure simultaneously all the wavelengths, unlike a polarimeter or a single detector. The smaller number of measurements decreases the error sources. Moreover, (2.22) is not mathematically complicated, as it keeps the simplicity of using Jones matrix, and solves the ambiguities of (2.19), without the need to perform additional measurements or analysis.

The system uses manual rotation mounts and a low resolution spectrometer. So the proposed method can be simpler and cheaper than those using high−resolution motorized rotation stages, polarimeters and monochromatic light sources.

The simple approach of using Jones matrix has allowed designing a fast fitting algorithm. The previous section results were obtained using a population of 1000 individuals (number of combinations of x per iteration) and 116 wavelengths (spectral range from 420 nm to 886 nm with a 4 nm resolution). Under these conditions, the average convergence time was 20” (35 iterations on average) using a computer with CPU Intel® Core™2 Duo @ 2.66 GHz and RAM of 3.25 GB. The search time can be reduced to 12” using a spectral resolution of 8 nm (58 wavelengths), with very similar results to those obtained in the previous section.

It is important to note that $e_{rr3} > e_{rr2} > e_{rr1}$ in **Fig. 2.15** and **Fig. 2.17**. This is because the amplitude of the peaks of $P_{em}(\alpha_{Hm})$ increases according as α_{Hm} approaches to ±45° and therefore a better sampling resolution is required. However this does not affect the calculation of the cell parameters. The adjustment of the curve $P_{e1}(\alpha_{H1} = 0°)$, given by e_{rr1}, defines the accuracy in the calculation of the cell parameters, since there is no influence of H, as is demonstrated in the birefringence results (**Fig. 2.16** and **Fig. 2.18**). While the adjustment of the curves $P_{e2}(\alpha_{H2} = -15°)$ and $P_{e3}(\alpha_{H2} = -30°)$, given by e_{rr2} and e_{rr3}, define the uniqueness of α_T and ϕ_T. For example, the solutions of α_T and ϕ_T of cell TN1 are α_{T1} = 82.6° and ϕ_{T1} = −87.1° with e_{rr1} = 0.79%, e_{rr2} = 5.4% and e_{rr3} = 12%; however, if we replace α_{T1} by α_{T1}+90°, the same value of e_{rr1} is obtained but the values of e_{rr2} and e_{rr3} change to 23% and 40%, respectively.

The search limits of α_T and $\Delta n(\lambda)$ are wide. This allows characterizing high birefringence LC cells, such as those made of LC1658 material. This method can obtain the unique solution for the α_T and ϕ_T of TN cells with retardations between 0.91 μm and 1.85 μm; e.g. TN1 has retardation = 5.1 μm × 0.1786 (at 589 nm and ~25 ºC) ≈ 0.91 and TN2 has retardation = 5.1 μm × 0.3625 (at 589 nm and ~25 ºC) ≈ 1.85. This is described in next sub−section. ϕ_T limits were set in $80° \leq |\phi| \leq 100°$, since it was known that cells were 90° twisted. This range is large in comparison with those reported in **[36]**, of 90º±5º. However, different tests have been performed with larger limits on ϕ (even with $-360° \leq \phi \leq 360°$), by using α_H = 0°, −15°, −30° and −45°, with an average convergence time of 24”. These limits include cells with arbitrary twists, even super−twisted cells ($|\phi_T| = 270°$).

The results of $\Delta n_{T1}(\lambda)$ and $\Delta n_{T2}(\lambda)$ have relative errors less than 1.3%, respect to the theoretical values, which demonstrates the effectiveness and accuracy of the method. In general, the possible difference between Δn or d_T and their theoretical value are given by others characteristics of the cell, as the pretilt angle, dopants (for twist purpose) or the temperature effects. It is important to note that the rubbing angle values, α_T, are referenced from the x−axis, which is defined by the orientation of the input polarizer.

The proposed method do not considers the pre−tilt angle of the cells, so it is designed to characterize TN cells with zero or negligible pre−tilt angle. However, the pre−tilt angle can also be included in the model considering its effects on the variation of the effective birefringence **[45]**.

➢ Retardation range that can be characterized unambiguously

In order to demonstrate that the proposed method can distinguish between the possible ambiguous situations of α_T and ϕ_T in TN cells with wide retardation ranges, it is important to know how different are the curves of $P_{t2}(\alpha_{H2} = -15°)$ and $P_{t3}(\alpha_{H3} = -30°)$, produced by the different combinations of $[\alpha_T, \phi_T]$. A new parameter is defined to estimate the degree of differentiation, ΔP_{min}. It is obtained by subtracting the different curves of the **Fig. 2.13b** and **Fig. 2.13c**, two by two, then, the root mean square (RMS) of each subtraction is calculated and the minimum RMS value is selected. The maximum possible value of ΔP_{min} is 2. If $\Delta P_{min} = 2$, the curves produced by the ambiguous combinations are 100% different. On the other hand, if $\Delta P_{min} = 0$, the curves produced by the ambiguous combinations are equivalent. Then, ΔP_{min} defines the capability of the proposed characterization method to identify the unique answer of the parameters of an unknown TN cell at a specific α_{Hm}.

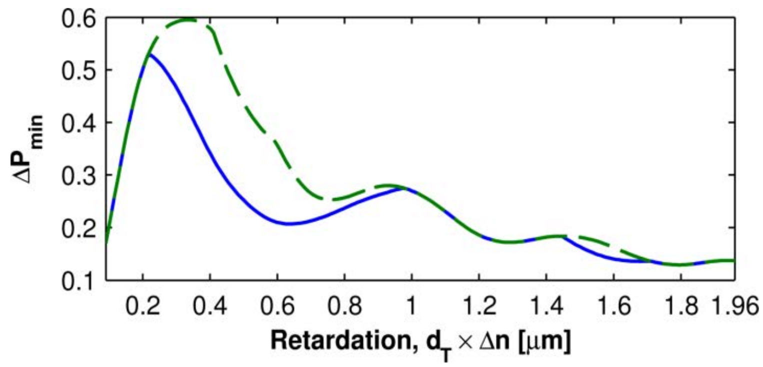

Fig. 2.19. ΔP_{min} of the curves of $P_{t2}(\alpha_{H2} = -15°)$ (solid line) and $P_{t3}(\alpha_{H3} = -30°)$ (dashed line) produced under the different combinations of $[\alpha_T, \phi_T]$ of a TN cell of 5CB material using the proposed characterization method.

The curves of $P_{t2}(\alpha_{H2} = -15°)$ and $P_{t3}(\alpha_{H3} = -30°)$, produced under the different combinations of $[\alpha_T, \phi_T]$ shown in **Fig. 2.13**, are obtained simulating a TN cell of $d_T = 5$ μm and 5CB material, with retardation of 5 μm × 0.1786 (at 589 nm and ~25 ºC) ≈ 0.89 μm. In this case, the resulting ΔP_{min} of $P_{t2}(\alpha_{H2} = -15°)$ and $P_{t3}(\alpha_{H3} = -30°)$ is about 0.28. In order to determine the minimum and maximum retardation of the TN cells that can be characterized with the proposed system, **Fig. 2.19** shows the variation of ΔP_{min} for values of d_T between 0.5 and 11 μm, which represent retardations between ~0.09 and ~1.96 μm for cells of 5CB at 589 nm at 25 ºC, under the same conditions of the simulations presented in **Fig. 2.13**, for $\alpha_{H2} = -15°$ (solid line) and $\alpha_{H3} = -30°$ (dashed line). It can be seen that $\Delta P_{min} > 0.13$ in the whole considered range, which includes very thin cells **[37]**. $\Delta P_{min} > 0.13$ is sufficient to identify the unique solution for the parameters (α_T, ϕ_T) of an unknown TN cell by using the proposed method. This is demonstrated in the experimental section by characterizing a TN cell of 1658 LC (TN2), with retardation of about 1.85 μm ($\Delta P_{min} \approx$

0.13, see **Fig. 2.19**). Cells with more retardation can be characterized using more azimuth angles, α_{Hm}.

➢ Other Experiments

During the development of this method, other tests were performed using wave plates of low order, e.g. a HN cell of 5CB and 5 μm. **Fig. 2.20** shows an example of the azimuth angles used for the characterization of a 5CB TN cell of 5 μm, as well as the experimental polarization functions (solid line) used and the resulting theoretical polarization functions (dots) obtained. These results are presented to shown than using a low order wave plate more azimuth angles are required but the curve fitting is better. In these tests the convergence time was up to 4 times greater, since more iteration were required, and the results were less accurate. So the characterization scheme based on the reference wave plate of Quartz used in **section 2.5.3.**4 is preferred.

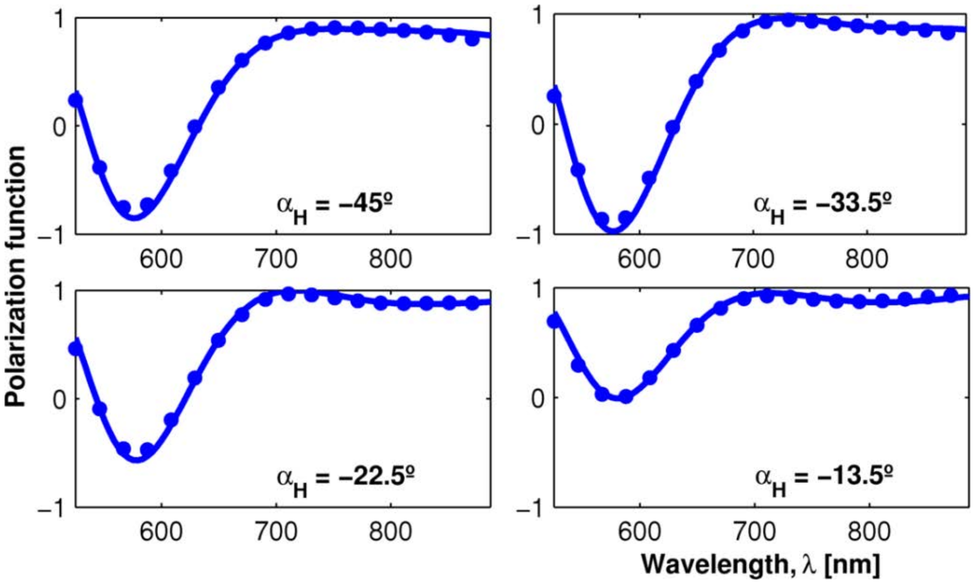

Fig. 2.20: Polarization functions for the characterization of TN cell by using a HN cell as reference retarder plate. Dots represent experimental measurement, $P_{tm}(\alpha_{Hm})$, and solid lines represent the curve fitting $P_{em}(\alpha_{Hm})$.

All the tests done with this method, including the results of the previous section, were performed using experimental LC cells.

2.6. References

[1] P. J. Pinzón, I. Pérez, J. M. Sánchez–Pena and C. Vázquez, "Spectral method for fast measurement of twisted nematic liquid crystal cell parameters," *Applied Optics,* vol. 53, no. 23, pp. 5230–5237, 2014.

[2] I.–C. Khoo, Liquid Crystals: Physical Properties and Nonlinear Optical Phenomena, New York: Wiley Interscience, 1994.

[3] M. Schadt, "The History of Liquid Crystal Display and Liquid Crystal Material," *Liquid Crystals,* vol. 5, pp. 57–71, 1989.

[4] I. P. Garcilópez, "Contribución a la Caracterización y Optimización Electroóptica de," Tesis Doctoral, Universidad Carlos III de Madrid, Madrid, 2003.

[5] J. C. Torres Zafra, I. Pérez Garcilópez and J. M. Sánchez Pena, Caracterización, modelado eléctrico y desarrollo de nuevas aplicaciones de dispositivos basados en cristales líquidos, Leganés: Universidad Carlos III de Madrid, 2009.

[6] J. M. Otón, "Electrooptics of Liquid Crystal Displays," in *II Workshop on LCD*, Lisbon, 1996.

[7] V. G. Chigrinov, Liquid crystal devices: physics and applications, London: Artech House, 1999.

[8] L. P. Amosova, V. N. Vasil'ev, N. L. Ivanova and E. A. Konshina, "Ways of increasing the response rate of electrically controlled optical devices based on nematic liquid crystals," *Journal of Optical Technology,* vol. 77, no. 22, pp. 79–87, 2010.

[9] J. L. Li, C.–H. Wen, S. Gauza, R. Lu and S.–T. Wu, "Refractive indices of liquid crystals for display applications," *Journal of Display Technology,* vol. 1, no. 1, pp. 51–61, 2005.

[10] J. Li, S. Gauza and S. T. Wu, "Temperature effect on liquid crystal refractive indices," *Journal of Applied Physics ,* vol. 96, no. 1, p. 19, 2004.

[11] T. Kohki, M. Hasegawa, K. Mitsuhiro, N. Itoh, R. Hasegawa and M. Sakamoto, Alignment Technology and Applications of Liquid Crystal Devices, United Kingdom: Taylor & Francis, 2005.

[12] P. C. Lallana, "Advanced devices based on fibers, integrated optics and liquid crystals for WDM networks," Leganés, 2011.

[13] S.–T. Wu and D.–K. Yang, Fundamentals of Liquid Crystal Devices, Great Britain: Wiley, 2006.

[14] S. Elston and R. Sambles, The Optics of Thermotropic Liquid Crystals, London: Taylor & Francis Ltd, pag. 291–291., 1998.

[15] S.–T. Wu and D.–K. Yang, Reflective Liquid Crystal Displays, England: Jhon Wiley & Sons Ltd, pag. 38., 2001.

[16] P. Y. Yeh and C. and Gu, Optics of Liquid Cristal Displays, Canada: Wiley & Sons, Inc., pag. 395–399, 1999.

[17] B. Li, &. Chua and S. J., Eds., Optical Switches, Materials and Design, Woodhead Publishing in Materials, 2010.

[18] Y.–L. Lo, Y.–F. Chung, C.–C. Liao and W.–H. Hsieh, "Transmitted Ellipsometry Method for Extracting Physical Parameters of TN/VA/Inverse–TN Liquid Crystal Cells," *IEEE Journal of Quantum Electronics,* vol. 49, no. 3, pp. 259–266, 2013.

[19] D. A. Yakovlev, V. G. Chigrinov and H. S. Kwok, Modeling and Optimization of LCD Optical Performance, Wiley, 2014.

[20] C. Soutar and K. Lu, "Determination of the physical properties of an arbitrary twisted–nematic liquid crystal cell," *Opt. Eng.,* vol. 33, no. 8, pp. 2704–2712, 1994.

[21] H. P. AG, "OptiXplorer Manual," 2007. [Online]. Available: http://www.pa.msu.edu/courses/2011fall/PHY431/Labs/Optixplorer_Manual_v2.8f_sec.pdf. [Accessed 22 04 2014].

[22] J. A. Davis, I. Moreno and D. B. Allis, "Ambiguities in measuring the physical parameters for twisted–nematic liquid crystal spatial light modulators," *Opt. Eng.,* vol. 38, no. 4, pp. 705–709, 1999.

[23] H. Kim and Y. H. lee, "Unique measurement of the parameters of a twisted–nematic liquid–crystal display," *Applied Optics,* vol. 44, no. 9, pp. 1642–1649, 2005.

[24] V. Duran, J. Lancis, E. Tajahuerce and Z. Jaroszewicz, "Cell parameter determination of a twisted–nematic liquid crystal display by single–wavelength polarimetry," *Journal of Applied Physics,* vol. 97, no. 4, pp. 043101,043101–6, 2005.

[25] B. E. Saleh and K. Lu, "Theory and design of the liquid crystal tv as an optical spatial phase modulator," *Opt. Eng.,* vol. 29, no. 3, pp. 240–246, 1990.

[26] J. Beeckman, K. Neyts and P. J. M. Vanbrabant, "Liquid–crystal photonic applications," *Optical Engineering,* vol. 50, no. 8, p. 081202, 2011.

[27] C. Marcos, J. M. Sánchez–Pena, J. C. Torres and J. I. Santos, "Temperature–Frequency Converter Using a Liquid Crystal Cell as a Sensing Element," *sensors,* vol. 12, pp. 3204 – 3214, 2012.

[28] D. H. Song, J. Kim, K. Kim, S. Rho, H. Lee, H. Kim and T. Yoon, "Ultrafast switching of randomly−aligned nematic liquid crystals," *Opt. Express,* vol. 20, p. 11659−11664, 2012.

[29] Y. Ha, H. Kim, H. Park and D. Seo, "Enhancement of electro−optic properties in liquid crystal devices via titanium nanoparticle doping," *Opt. Express,* vol. 20, p. 6448−6455, 2012.

[30] V. Borshch, S. V. Shiyanovskii and O. D. Lavrentovich, "Nanosecond Response in Nematic Liquid Crystals for Ultrafast Electro−Optic Devices," in *CIOMP−OSA Summer Session on Optical Engineering, Design and Manufacturing*, 2013.

[31] P. J. Pinzón, C. Vázquez, I. Pérez and J. M. Sánchez–Pena, "Synthesis of asymmetric flat–top birefringent interleaver based on digital filter design and genetic algorithm," *IEEE Photonics Journal,* vol. 5, no. 1, p. 7100113, 2013.

[32] Q. Wang, G. Farrell, T. Freir and J. She, "Optimal design of broadband linear polarization converters/switches," *J. Opt. A: Pure Appl. Opt. ,* vol. 7, no. 1, pp. 47–50, 2005.

[33] P. C. Lallana, C. Vázquez and B. Vinouze, "Advanced multifunctional optical switch for multimode optical fiber networks," *Opt. Commun.,* vol. 285, p. 2802–2808, 2012.

[34] C.–J. Yu, Y.–T. Tseng, K.–C. Hsu and C. Chou, "Analytical approach for unique determination of cell parameters and equivalent birefringent parameters of a generally twisted nematic liquid crystal device," *Applied Optics,* vol. 51, no. 33, pp. 7910–7919, 2012.

[35] W.–C. Hung, M.–S. Tsai, C.–R. Wang, I.–M. Jiang and W.–H. Cheng, "Simple parameter determination for twisted nematic liquid–crystal display," *Applied Optics,* vol. 46, no. 17, pp. 3493–3497, 2007.

[36] Y.–L. Lo, Y.–F. Chung, C.–C. Liao and W.–H. Hsieh, "Transmitted Ellipsometry Method for Extracting Physical Parameters of TN/VA/Inverse–TN Liquid Crystal Cells," *IEEE Journal of Quantum Electronics,* vol. 49, no. 3, pp. 259–266, 2013.

[37] S. Valyukh, I. Valyukh and K. Skarp, "Spectrophotometric determination of reflective liquid crystal cell parameters," *J. Appl. Phys. ,* vol. 99, p. 053102 , 2006.

[38] R. Giust and J.–P. Goedgebuer, "Determination of the twist angle and the retardation properties of twisted nematic liquid crystal television by spectral measurements," *Opt. Eng. ,* vol. 37, no. 2, pp. 629–634, 1998.

[39] S. T. Tang and H. S. Kwok, "Transmissive liquid crystal cell parameters measurement by spectroscopic ellipsometry," *J. Appl. Phys.,* vol. 89, no. 1, pp. 80–85, 2001.

[40] J. S. Chae and S. G. Moon, "Cell parameter measurement of a twisted–nematic liquid crystal cell by the spectroscopic method," *Journal of Applied Physics,* vol. 95, no. 7, pp. 3250–3254, 2004.

[41] O. Aharon and I. Abdulhalim, "Liquid crystal Lyot tunable filter with extended free spectral range," *Optics Express,* vol. 17, no. 14, pp. 11426–11433, 2009.

[42] P. J. Pinzón, I. Pérez, C. Vázquez and J. M. Sánchez–Pena, "Reconfigurable 1×2 wavelength selective switch using high birefringence nematic liquid crystals," *Applied Optics,* vol. 51, no. 25, pp. 5960–5965, 2012.

[43] M. Natick, "Global Optimization Toolbox," MatWorks, 2012. [Online]. Available: http://www.mathworks.com/products/datasheets/pdf/global−optimization−toolbox.pdf. [Accessed 23 04 2014].

[44] V. Urruchi, I. Pérez, N. Gaona and J. M. Sánchez–Pena, "Phase Modulation and Optical Anisotropy of High Birefringence Liquid Crystals," *Molecular Crystals and Liquid Crystals,* vol. 502, no. 1, pp. 207–219, 2009.

[45] V. Belyaev, A. Solomatin and D. Chausov, "Phase retardation vs. pretilt angle in liquid crystal cells with homogeneous and inhomogeneous LC director configuration," *Opt. Express,* vol. 21, p. 4244–4249, 2013.

Chapter III:

Reconfigurable Wavelength Selective Devices based on Birefringent Structures

In this chapter, novel proposals of wavelength selective devices, optimized to work in the visible range for SI−POF networks with WDM, are presented. These devices take advantage of the large aperture, low chromatic dispersion and high reliability that offer the birefringent structures as well as the reconfiguration capability that can be achieved with liquid crystal technology. First, the design and simulation of a liquid crystal tunable filter (LCTF) using a high birefringence LC is shown. The periodicity and reconfiguration capability of this filter can be used to design versatile wavelength selective devices such as multiplexers, demultiplexers, interleavers and switches. This is demonstrated in this chapter, with the proposal of a novel reconfigurable 1×2 wavelength selective switch (R−WSS). The performance of the proposed devices (LCTF and R−WSS) can be improved by using optimized birefringent structures. Therefore, a new synthesis method for the design of arbitrary birefringent filters and interleavers is introduced. The effectiveness of this method is tested and compared with the current state of the art at 1550 nm (C−band). Finally, a design example (based on the proposed method) of a birefringent interleaver optimized to work in SI−POF WDM networks is presented.

3.1. Introduction

Wavelength selective devices are fundamental elements in advanced SI−POF networks, especially when visible WDM approach is used, but they are not widely spread yet on the market, mainly due to the important constrains imposed by the SI−POF dimensions and *NA*, which difficult the implementation of well established technologies for glass optical fibers. Besides, reconfiguration can be an important feature required by visible WDM based SI−POF networks, since no standard channels have been defined, but most of the optical devices developed in SI−POF technology do not provide such a characteristic.

In this chapter, novel SI−POF devices with reconfigurable characteristics for visible WDM applications addressing compact, scalable and low consumption solutions, with the potential to have low insertion losses, will be described, simulated and experimentally tested. They operate at the wavelengths of interest for SI−POF applications. These devices will take advantage of the properties of liquid crystal materials for tuning and reconfiguration.

Among the different wavelength selective devices, this chapter is focused on the design of optical filters, interleavers, and wavelength selective switches (WSS). Optical filters selectively transmit the incoming spectrum (or channels) to the output port; they are basic components as part of interleavers and wavelength selective devices for optical communications networks. Optical interleavers separate an incoming spectrum into two complementary set of periodic spectra (odd and even channels) or combine them into a composite spectrum. On the other hand, WSS can redirect any channel from the input spectrum to any of the output ports. Filters, interleavers and WSS play nowadays a key role in wavelength division multiplexing (WDM) systems; they are usually used in gain equalization, dispersion compensation, pre−filtering and channels add/drop applications.

3.2. Design of a Liquid Crystal Tunable Filter (LCTF)

Optical Filters (OFs) selectively transmit light in a wavelength range while blocking or attenuating all other wavelengths. In a Tunable Filter (TF) the spectral transmission changes according to a control signal, either, electrical, mechanical, acoustical, etc. Most common narrow band OFs are based on birefringent structures, Fabry−Perot and Michelson interferometers **[1]**, dichroic filters (also called thin−film filters) **[2]**, **[3]** and magneto−optics effects **[4]**. On the other hand, the most important TFs technologies include the acousto−optics, electro−optics (e.g. using LCs) **[5]** and thermo−optics devices **[2]**, and micro electro mechanical systems (MEMS).

3.2.1. LCTFs based on Birefringent Structures

There are two classical birefringent filters: Lyot and Solc. Lyot filter was discovered independently by B. Lyot **[6]** and Y. Öhman **[7]**. This filter consists of a set of delay stages with wave plates of different widths between linear polarizers (LPs) and bases its operation on the interference of multiple light beams with different phases. Afterwards, Ivan Solc **[8]**, **[9]**, **[10]** demonstrated that it is possible to construct a birefringent filter without intermediate LPs, only LPs at the input and output are needed, by using a stack of wave plates of the same width at specific tilt angles, but its construction is further complicated due to the number of accurate wave plates and precise angles that it needs. An excellent discussion of both types of filters can be found in **[11]**, **[12]**, **[13]**. However, in recent years, a general type of birefringent filter is being explored, which is called arbitrary or optimized birefringent filter or just birefringent filter (BF). The structure of an arbitrary birefringent filter is similar to the structure of Solc filters, with the difference that the tilt angles of the arbitrary birefringent filters are determined using synthesis methods with specific design parameters.

Lyot filter is the dominant type in spectral imaging and spectroscopy applications and the leading tuning technology is the electro‒optical by using liquid crystal variable phase retarders, due to its efficiency and low cost of integration. Other advantages of LCTFs include no need of moving parts for tuning, low driving voltage and low power consumption. LCTFs are polarized devices, therefore the maximum transmittance is less than 50% when the incident light is unpolarized, however the use of light sources of high intensity and cooled charge coupled devices (CCD) enables a lot of applications for this technology. Traditionally, LCTFs applications have been focused on astronomy area **[12]**, but now we also find applications in the fields of medicine, chemistry and biology. A detailed list of LCTFs biomedical applications can be found in **[14]**. LCTFs' applications also include laser tuning **[15]** and remote sensing **[16]**.

Recent publications about LCTFs with operation in the visible (VIS) and near infrared (NIR) range include a four‒stage filter **[17]**, filters with free spectral range extension **[18]**, with side‒lobes reduction **[19]** and with polarization control **[20]**. Transmittance in **[20]** is between 10% and 25%, in the range from 450 to 600 nm, but the polarization state of incoming light is not specified, in **[19]** transmittance for unpolarized light is about 10% in the range from 500 to 700 nm, **[17]** and **[18]** do not provide information about transmittance. To date, the new LCTFs appearing in the market offers tuning range between 420 nm to 730 nm with bandwidth between 15 nm and 55 nm and transmittance for polarized light between 10% and 65%, respectively, using 7 delay stages in configurations mixing Lyot ans Solc structures **[21]**.

The design, testing and modeling of a two−stage LCTF by using a high birefringence nematic LC material (experimental LC cells) is presented in the following. Main advantages of using high birefringence LC are: 1) the reduction of the number of delay stages required to operate in the VIS and NIR range with good performance and 2) the thickness reduction of the delay stages required, this reduces the required applied voltage for tuning control and improves the orientation uniformity of the LC molecules (in very thick cells may appear the so called micro−domains, see **section 2.2**). Filter design is optimized to work in the VIS and NIR spectrum. Modelling and simulations include the LC material birefringence obtained experimentally. Finally, the simulated and experimental results are compared, demonstrating an excellent agreement between them. The measured tuning range is between 610 nm and 820 nm (limited by the LPs ttransmittance and the spectrometer operation range), with bandwidth between 40 nm and 80 nm and transmittance for unpolarized light between 9% and 14%. The overall tuning range is covered with control voltages of less than 1.5 V_{RMS}.

3.2.2. Theoretical Basis of Lyot Filters

The structure of a single stage of a Lyot filter consists in a birefringent medium (wave plate) between linear polarizers (LPs), as shown in **Fig. 3.1**. Transmission axes of polarizers are parallel between them and at 45° to the optical axis of the wave plate. When $n_e < n_o$, as in calcite, the extraordinary axis is called the fast axis and the ordinary axis is called the slow axis. For $n_e > n_o$ the situation is reversed. Under these conditions, when a light beam crosses the input polarizer it is divided into two orthogonal components (E_{wave} and O_{wave}) that travel through the birefringent medium with different paths, with refractive indices, n_e and n_o respectively. Finally, the output polarizer (analyzer) recombines the orthogonal components creating the interference effect.

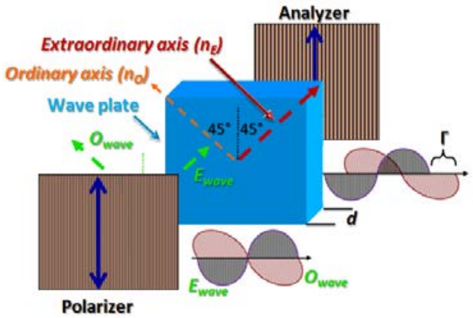

Fig. 3.1: Scheme of a single stage of the Lyot filter.

The Lyot filter consists of a series of *N* single delay stages. Therefore, the transmittance of the *j*th stage, T_j, with j = 1, 2, ..., N, is a function of the phase delay, Γ_j, between the beam's polarization components passing through the birefringent medium. This phase delay is given by:

$$\Gamma_j = 2\pi \frac{\Delta n_j d_j}{\lambda} \tag{3.1}$$

where λ is the wavelength of the input beam, while Δn_j and d_j are the birefringence and thickness of the jth delay stage, respectively (j is often omitted when referring to the first stage, $j = 1$). Generally, each stage is designed so that it had twice the delay of the previous one, then $\Gamma_j = 2^{j-1}\Gamma$ being Γ the lowest delay (first stage, $\Gamma = \Gamma_1$). Using the Jones matrix formalism, it is easy to show that the transfer function of the first stage of the filter is:

$$T_1 = \cos^2\left(\Gamma/2\right) \tag{3.2}$$

In a Lyot filter with N stages and parallel LPs in all of them (see **Fig. 3.2**), the incoming beam can be transmitted in both directions. And in this case the transmission, T_P, is given by:

$$T_P = \prod_{j=1}^{N} \cos^2\left(2^{j-1}\Gamma\!/\!_2\right) = \frac{1}{2^{2N}}\frac{\sin^2\left(2^{N-1}\Gamma\right)}{\sin^2\left(\Gamma\!/\!_2\right)} \tag{3.3}$$

T_P is a periodic function and the set of wavelengths with peak transmittance or central wavelengths, λ_{Pk}, are those having a delay Γ, which is an integer multiple of 2π. Those wavelengths are given by:

$$\lambda_{Pk} = \frac{\Delta n d}{k} \tag{3.4}$$

where k = 1, 2, 3,…, defines the peak wavelength order. On the other hand, the bandwidth of transmission band around λ_{Pk} is mainly defined by the number of stages, N.

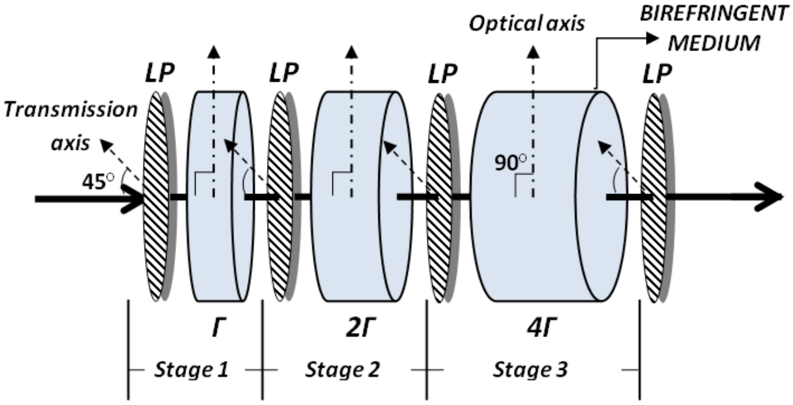

Fig. 3.2: Structure of a 3 Stages Lyot filter with parallel LPs in all the stages and transmission T_P. The incoming beam can be transmitted in both directions.

A Lyot filter with crossed polarizers in the lowest delay stage, and parallel polarizers in the others stages, can be implemented by changing orientation of last polarizer **[22]**, see **Fig. 3.3.** In this configuration, the input beam should enter through the stage with the highest delay. In this case, the filter transmission is given by:

$$T_C = \sin^2\left(\Gamma/2\right)\prod_{j=2}^{N}\cos^2\left(2^{j-1}\Gamma/2\right) = \frac{1}{2^{2N}}\frac{\sin^2\left(2^{N-1}\Gamma\right)}{\cos^2\left(\Gamma/2\right)} \tag{3.5}$$

T_C is a periodic function and the set of wavelengths with peak transmittance, λ_{Cm}, are those having a delay Γ which is an integer multiple of π. Those wavelengths are given by:

$$\lambda_{Cm} = \frac{2\Delta nd}{m} \tag{3.6}$$

where m = 1, 2, 4,…, defines the peak wavelength order.

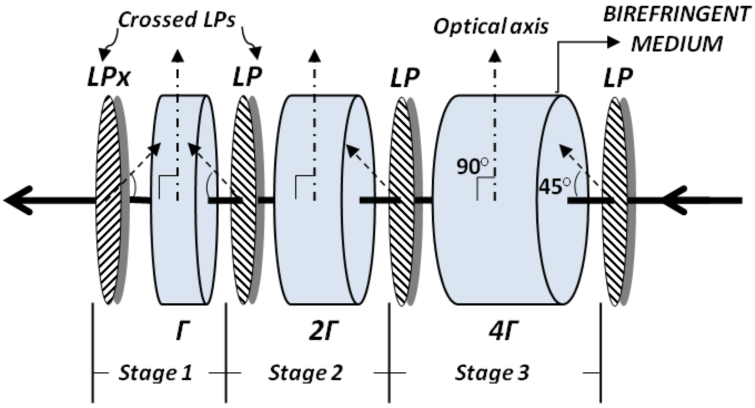

Fig. 3.3: Structure of a 3 Stages Lyot filter with crossed LPs in the stage with lowest delay, Γ, and transmission T_C. The incoming beam can only be transmitted in a single direction.

3.2.2.1. Optical Filters Parameters

In order to determine the optical filters performance, a set of parameters that characterize its operation are defined. Thus we can determine which filter is best suited for a specific application. The following briefly describes some of the most common parameters.

- **Bandwidth or Full Width Half Maximum (*FWHM*)**: measures the spectral separation between two points of the passband of the filter where the transmittance reaches 50% of the peak value. This parameter gives an idea of the filter selectivity.
- **Central wavelength**: is the average wavelength between the endpoints of the *FWHM*. It is not necessarily the peak in transmittance curve, see (3.4) and (3.6).
- **Free spectral range (*FSR*)**: if the filter spectral response is periodic in frequency, this period is precisely the *FSR*. Therefore, at multiples of the *FSR* the filter transfer function is repeated. The *FSR* can also be defined as the wavelength range between two consecutive peaks of maximum transmittance. It is proportional to the filter delay Γ.
- **Passband**: The filter passband or transmission band is the spectral region ranging from [central wavelength – *FWHM*/2] to [central wavelength + *FWHM*/2].

- **The finesse ($\Im$)**: is another parameter that measures the filter spectral selectivity. It is defined as the ratio between *FSR* and *FWHM*. Therefore, if the finesse is higher, the selectivity is greater. To the same order peak, $\Im$ can be increased and *FWHM* decreased by increasing the number of interfering beams in the filter (number of stages, *N*), however this does not affects the *FSR*.

Table 3.1 shows a resume of the previously described parameters defined for a Lyot filter with parallel polarizers in all the stages and with crossed polarizers in the lowest delay stage, assuming that the input beam enters through the highest delay stage.

TABLE 3.1. RESUME OF THE MOST IMPORTANT PARAMETERS OF THE LYOT FILTERS WITH PARALLEL POLARIZERS IN ALL THE STAGES AND WITH CROSSED POLARIZERS IN THE LOWER DELAY STAGE. SEE ANNEXES FOR THE DETAILED CALCULATIONS.

Parallel polarizers		Crossed polarizers	
$\lambda_{Pk} = \frac{\Delta nd}{k}$	(3.4)	$\lambda_{Cm} = \frac{2\Delta nd}{m}$	(3.6)
$FSR_k = \lambda_k - \lambda_{k+1} = \frac{\lambda_k}{k+1}$	(3.7)	$FSR_m = \lambda_m - \lambda_{m+1} = \frac{\lambda_m}{m+1}$	(3.8)
$FWHM_k = \frac{8\left(2^{N-1}\Delta nd\right)}{16\left(2^{N-1}k\right)^2 - 1} \approx \frac{\lambda_k}{2^N k}$	(3.9)	$FWHM_k = \frac{8\left(2^{N}\Delta nd\right)}{4\left(2^{N}m\right)^2 - 1} \approx \frac{\lambda_m}{2^{N-1} m}$	(3.10)
$\Im_k = \frac{FSR_k}{FWHM_k} \approx 2^N \frac{k}{k+1}$	(3.11)	$\Im_k = \frac{FSR_k}{FWHM_k} \approx 2^{N-1} \frac{m}{m+1}$	(3.12)

3.2.2.2. Lyot Filter Tuning

In a tunable Lyot filter, each stage is designed with a fixed delay plus a variable delay. In the particular case of a LCTF, the variable delay is obtained by using homogeneous nematic liquid crystal cells. Nematic LC devices with homogeneous alignment (HN cells) work as variable wave plates. The operation of a LC variable wave plate is shown in the **Fig. 3.4**. If the voltage applied to LC device, V, is less than threshold, V_{th}, the birefringence is given by $\Delta n = n_e - n_o$, where n_o and n_e are the ordinary and extraordinary refractive indices of the LC material, respectively. When V is above V_{th}, the LC director axis tilts in direction of resulting electrical field with an angle, $\theta(V)$, measured from the LC device surface, changing the effective birefringence $\Delta n_{eff} = n_e(\theta) - n_o$, from a maximum value, $\Delta n_{eff} = \Delta n$ ($V \leq V_{th}$ then $\theta = 0°$) to a minimum value $\Delta n_{eff} \cong 0$ ($V \gg V_{th}$ then $\theta \cong 90°$). In practical cases, the effective birefringence does not become zero due to anchoring of LC molecules on the cell surfaces.

In a LCTF, the Lyot stages are designed such that Γ is composed by a fixed delay, Γ_{fix}, plus a variable delay, Γ_{LC}, fulfilling the condition $\Gamma_j = 2^{(j-1)}\Gamma$. However, if the birefringence of the LC material is high enough to fulfil the required parameters, the stages can be designed by only using

HN cells. This eliminates the mismatches in the delay between the fixed and variable wave plates due to the differences in their dispersion profiles.

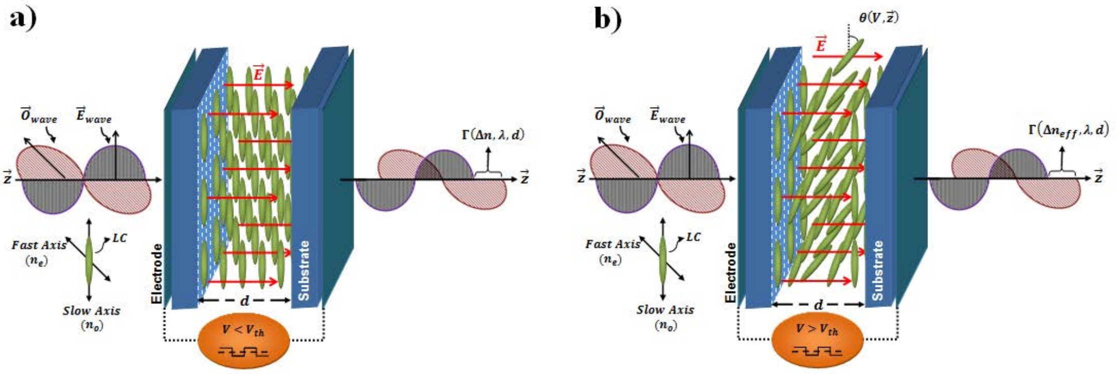

Fig. 3.4: Structure and operation of a LC variable wave plate: a) with V under threshold and b) with V above threshold.

3.2.3. Design of the Proposed LCTF using High−Birefringence LCs

The schematic of the two−stages LCTF presented in this work is shown in **Fig. 3.5**. In this scheme the light source is the AvaLigth lamp with a spectral range from 360 to 2500 nm, transmittance measurements are done by using an AvaSpect spectrometer that operates from 360 to 886 nm with 4 nm resolution. Both the spectrometer and light source are from Avantes and use FC−UV100−2 optical fiber tails with core diameter of 200 nm, *NA* of 0.22, optimized from 200 to 750 nm and COL−UV/VIS collimators. Linear polarizers (LPs) are of the LPVIS050 series from Thorlabs.

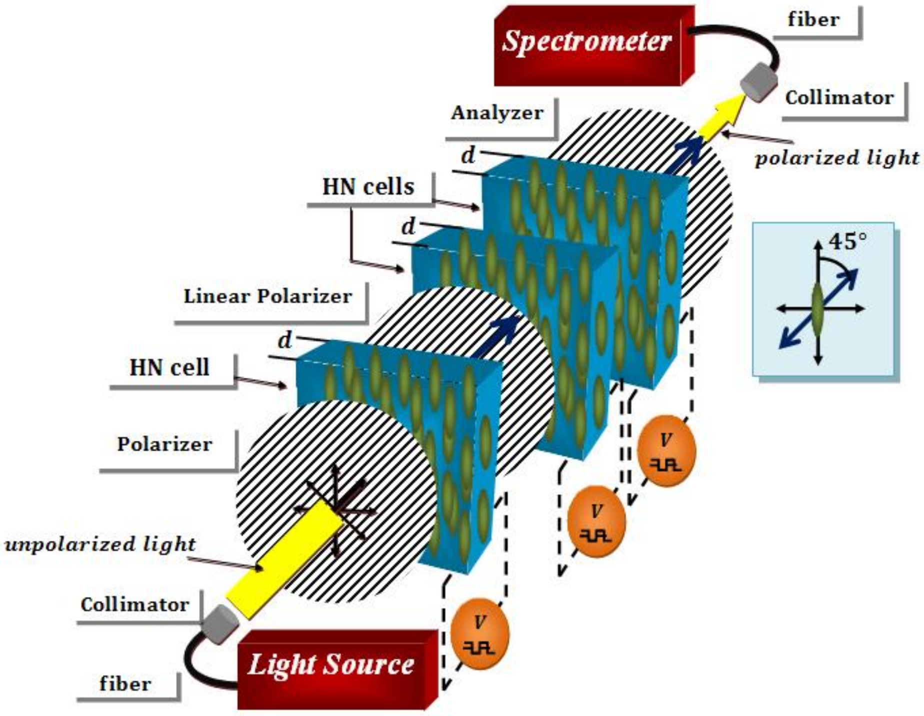

Fig. 3.5: Scheme of a two−stage liquid crystal tunable optical filter.

High birefringence of the LC material allows a simple design in which is not necessary to use a fixed delay in the filter stages to obtain good results of *FSR* and *FWHM* in VIS−NIR range, avoiding birefringence differences between fixed wave plates and LC devices due birefringence dispersion of LC material. High birefringence also allows to use low control voltages and to obtain simple and versatile devices.

3.2.3.1. Liquid Crystal Birefringence Measurements

Three different HN cells have been used in the proposed design, as shown in **Fig. 3.5**. They have been manufactured with 1658−LC material and 5.1 μm thicknesses (d), and they are called 1658−HN1, 1658−HN2 and 1658−HN3. This is a high−birefringence LC material synthesized in the Military University of Technology in Warsaw. The dispersion profile, $\Delta n(\lambda,V)$, of those cells has been experimentally determined in the range from 525 to 886 nm for V between 0 and 7 V_{RMS} (at 1 kHz) with resolution of 5 mV_{RMS}. The results are shown in **Fig. 3.6** and **Fig. 3.7** and the detailed characterization process used is shown in Appendix A.

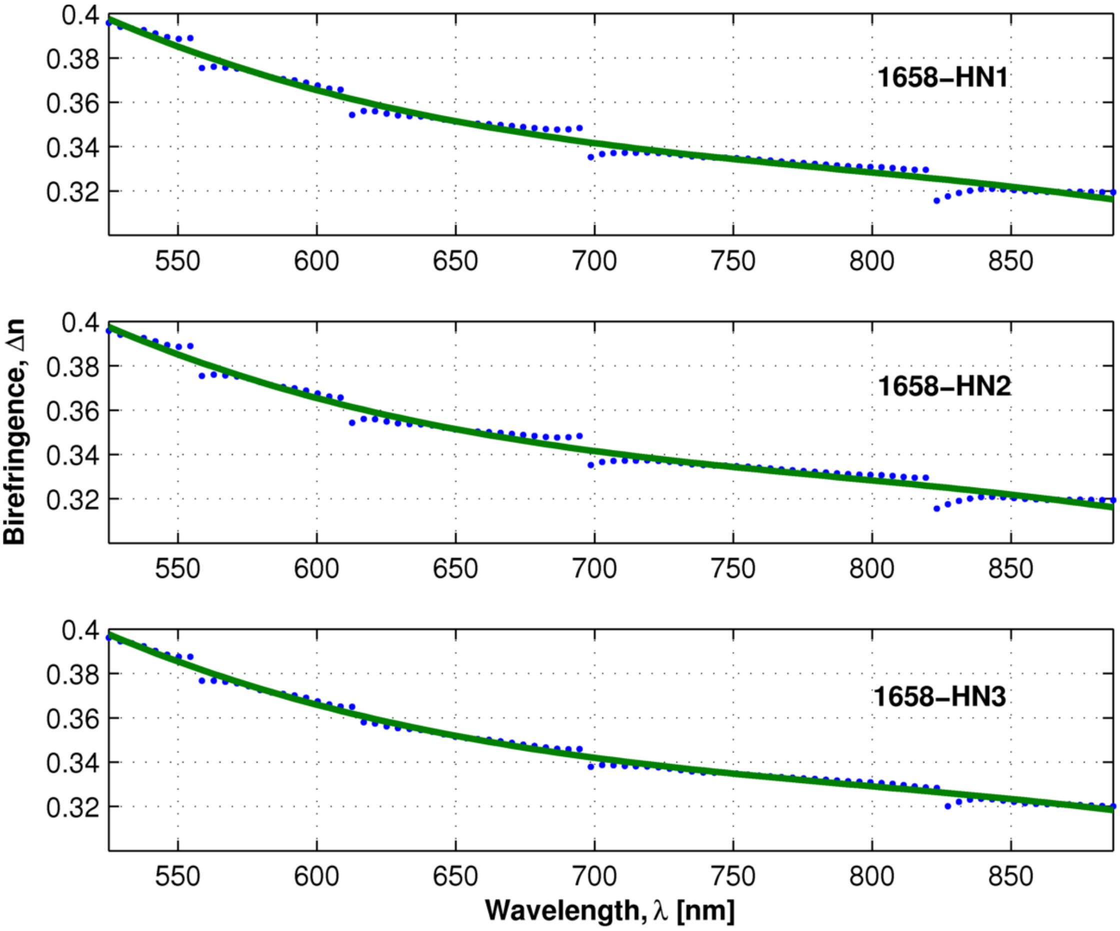

Fig. 3.6: Birefringence results of the three HN cells of 1658 LC material and 5.1 thicknesses that have been characterized at $V = 0\,V_{RMS}$. Experimental calculations are represented by dots and the polynomial regressions (dispersion profiles) are represented by solid lines.

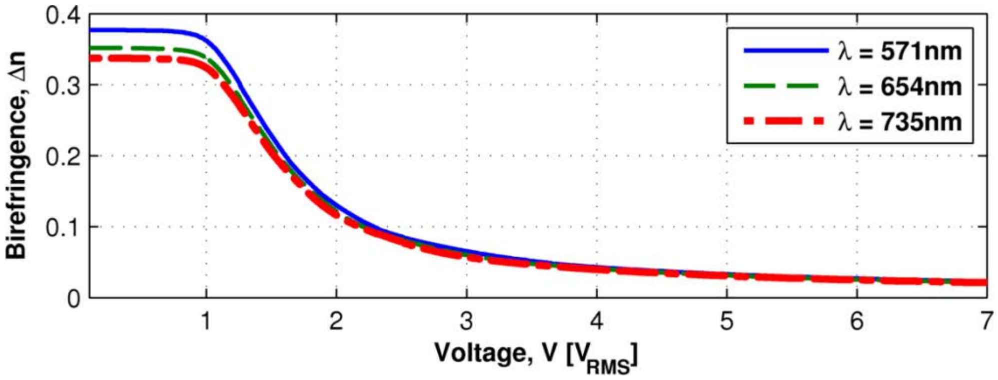

Fig. 3.7: Results of the effective birefringence as a function of the applied voltage of the cell 1658−HN1 at three different wavelengths. The characterization done includes wavelengths between 520 and 886 nm.

➢ Transmittance of the LCTF Components

In order to estimate the total losses of the filter, transmittances of individual components (LC devices and polarizers) have been experimentally determined. LC devices transmittance is about 81% between 500 and 900 nm. **Fig. 3.8a** shows the transmittance of a single HN cell and the transmittance of the three cells in series. LPs (LPVIS050) transmittance is about 70% at 600 nm and 82% at 900 nm for polarized light, for unpolarized light this transmittance is the half, as shown in **Fig. 3.8b.**

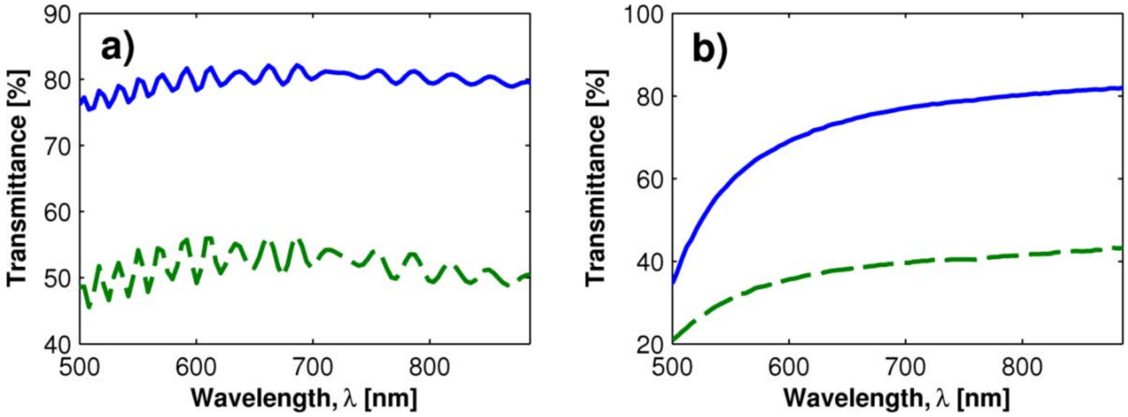

Fig. 3.8: a) Transmittance of the HN LC cells of 1658 LC material: one LC cell (solid line) and three LC cells in series (dashed line). b) Transmittance of the LPs for parallel polarized light (solid line) and unpolarized light (dashed line).

3.2.3.2. LCTF Modeling and Measurements

For LCTF simulation, a Matlab program, based on the Jones Matrix formalism, has been developed. The simulation program allows to simulate the behavior of each stage independently, taking into account all the filter elements such as: number of stages, number of birefringent plates at each stage, tilt angles (e.g. possibility of considering variations from the fixed tilt angle of 45º used in Lyot structure), transmittance of the components and the birefringence of the LC material as well as its dispersion profile. Experimental effective LC birefringence and transmittance of the filter elements are used in the simulation. The real filter transmittance is measured by using the AvaSpect spectrometer with different applied voltages (*V*). In **Fig. 3.9** is shown the filter response results for four applied voltages to LC devices in first and second stage (see **Fig. 3.5**). The simulations results for the same applied voltages are also shown in the figure for comparison.

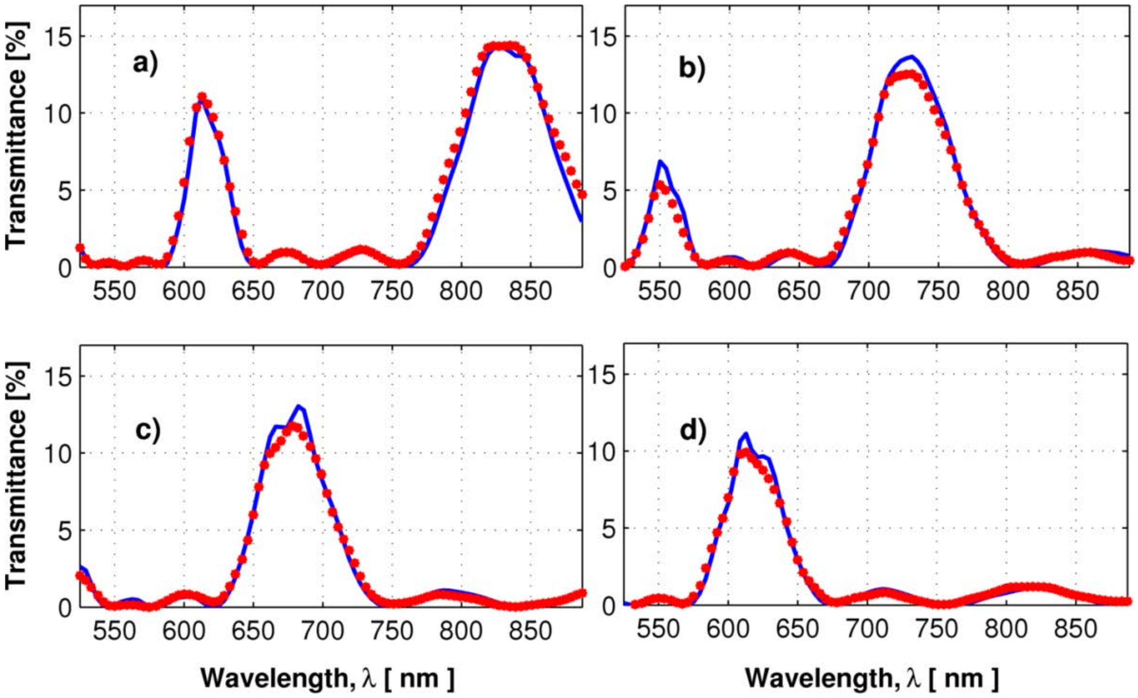

Fig. 3.9: Transmittance results of the two−stage LCTF at different applied voltages: dot line represents experimental values, solid line represents simulated values, where *V*(V_{RMS}) = a) 0.8, b) 1.2, c) 1.3 and d) 1.420.

3.2.3.3. LCTF Performance

Fig. 3.10 shows the experimental tuning of the second order peak ($\lambda_{P(k=2)}$), for control voltages between 0.8 and 1.36 V_{RMS}. It can be seen that the LCTF performance depends on the transmission peak order. **Fig. 3.11** shows the performance of the filter working with second order peak, $\lambda_{P(k=2)}$ (see **Table 3.1**). In **Fig. 3.10** and **Fig. 3.11**, it can be seen that for a wavelength range from 600 to 825 nm the transmittance of the second order peak goes from about 9 to 14%, the shape of the transmittance is because of the spectral response of LPs; in the same range, the *FWHM* goes from 40 to 80 nm and the *FSR* from 140 to 220 nm. The *FSR* is defined as the spectral band between the second and third order peaks. The *FWHM* can be reduced by a factor of two adding one filtering stage, but this not affects the *FSR*. To increase the *FSR*, an extra filter stage that satisfies a specific condition for order elimination can be used **[18]**, but this will not affect the *FWHM*. Finally, the same figure shows the second order peak tuning as a function of *V* leaving constant the position of the third order peak when applied voltage is under threshold, this demonstrates that with an applied voltage of 1.42 V_{RMS}, the filter's bandpass can be tuned over the whole *FSR* (220 nm).

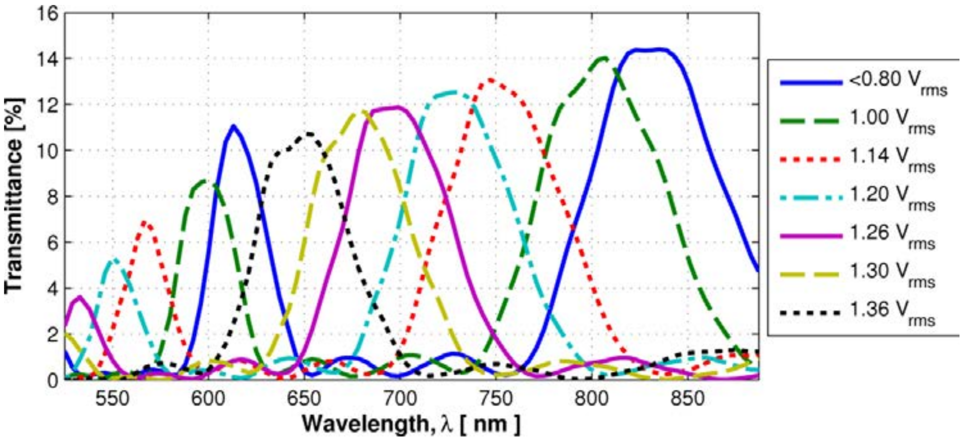

Fig. 3.10: LCTF experimental tuning of the second order peak, $\lambda_{P(k=2)}$.

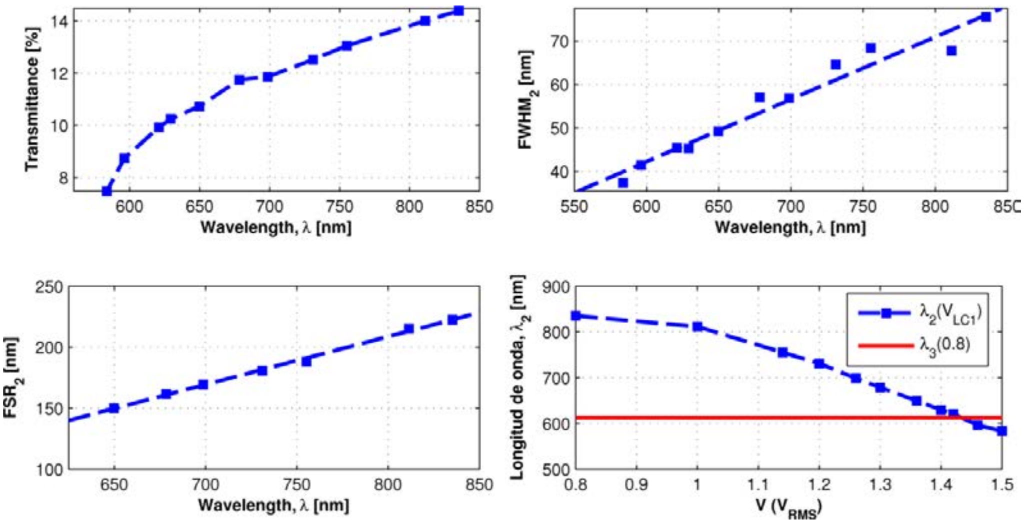

Fig. 3.11: Performance of the second order peak of the two−stage LCTF: a) Transmittance, b) Full width half maximum, c) Free spectral range as function of the peak wavelength tuning and in d) the dash−dotted line is the position of the transmission peak as function of the applied voltage, *V* and the solid line represent the position of the third order peak at $V = 0.8\ V_{RMS}$.

TABLE 3.2: LIQUID CRYSTAL TUNABLE FILTER PERFORMANCE

Operation Range	610 to 820 nm
FSR	220 nm
FWHM	80 nm (max *FWHM* in the operation range)
Control Voltage	$< 1.5\ V_{RMS}$

3.2.3.4. Loss budget and insertion losses improvement

As a consequence of the use of an input polarizer, half of the incoming optical power is filtered. The solution for reducing the insertion losses of LCTFs is by using the polarization diversity method, as the polarization converter presented in Appendix B. In this technique, the input beam is decomposed into its TE (*s*–polarized light) and TM (*p*–polarized light) components. Both components are treated separately and finally recombined. In this way, the device becomes polarization insensitive, and less insertion losses are expected.

The experimental results show that the filter transmittance is lower than 14%, which represents insertion losses of more than 8 dB. These values are the result of the transmittance at the polarizers and LC cells. At 850 nm, the transmittance of the polarizers is about 82% (41% for non–polarized light) and the transmittance of each LC cells is about 79%, therefore, the expected transmittance is lower than 13.6% (0.41×0.79×0.82×0.79^2×0.82), see **Fig. 3.8**.

Therefore, the insertion losses of the proposed LCTF can be improved in about 3 dB using a polarization diversity method and polarizing devices with higher transmittance (e.g. wire grid polarizers have transmittance of about 90% for polarized light).

3.2.4. Applications of the proposed LCTF in SI−POF networks with WDM

In general, there is a whole range of applications for optical filters in the field of optical communications. They are basic to add or remove channels (wavelengths) in communication systems based on WDM. In addition, in new communications networks the signals routing is a function of the wavelength, so it is necessary to dynamically select specific channels and transmit them throughout different paths.

There are also multiple applications related to the compensation of chromatic dispersion in optical communications systems using different filter configurations. Another important aspect is the gain equalization of optical amplifiers, which requires a dependent attenuation of the wavelengths that can be achieved with optical filters. Similarly, optical filters are used to balance the response spectrum of photo−detectors or non−uniform light sources.

In the following, two of the possible applications that may have the LCTF in SI−POF systems based on visible WDM are presented.

3.2.4.1. Interleavers

Many optical filtering and interleaving devices based on birefringent structures such as Lyot and Solc filters **[23]** with low dispersion, high reliability, easy manufacturability and low cost have been proposed. Those devices usually work in dense wavelength division multiplexing (DWDM) systems, require polarization diversity techniques to avoid polarization dependent loss **[24]**, and do not have reconfigurable features. They usually have the input and one of the outputs in a single port **[25]**, so circulators or other devices are needed to separate both signals.

The structure of a 1×2 reconfigurable optical interleaver is shown in **Fig. 3.12**. It is based on the different behaviour of a LCTF using parallel or crossed polarizers in the lowest delay stage. The polarization converter (PolConv) is a device that allows transmitting an unpolarized beam into two parallel beams with the same polarization state reducing the insertion losses (see Appendix B).

This structure combines two inverted LCTFs (the input stage corresponds to the highest delay stage) by using a polarizing beam splitter (PBS): one in transmission, with all polarizers in parallel and the other in reflection, with the lowest stage delay (first stage) between crossed polarizers. Thereby, by the S_1 output only are transmitted wavelengths with a delay of $2\pi k$ in the first stage, represented by (3.4), while by the output S_2 are reflected, only, the wavelengths with a delay of πk in the first stage, represented by (3.6).

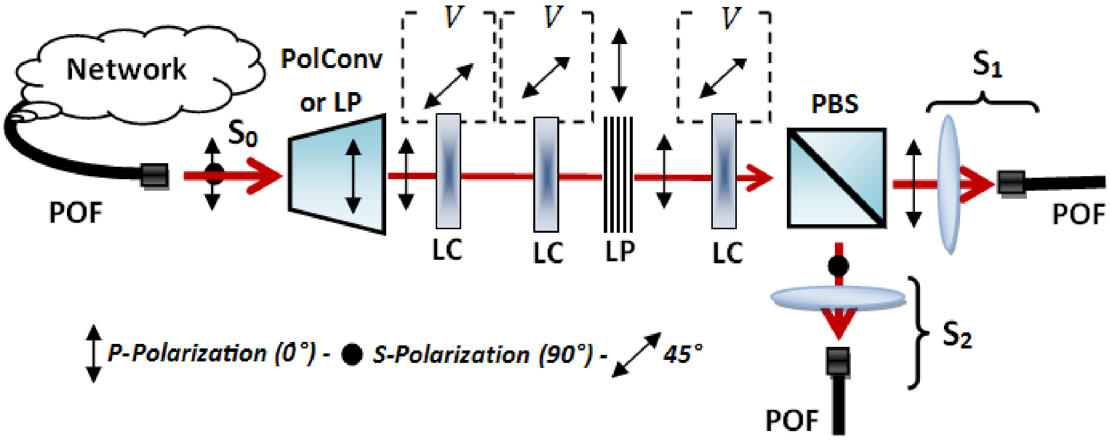

Fig. 3.12: Structure of a reconfigurable 1:2 optical interleaver based on a LCTF

This scheme can be used as multiplexer, demultiplexer o wavelength selective switch depending on the number of channels considered, as the WSS presented in the following sections.

3.2.4.2. Wavelength Selective Switches (WSS)

A 1×*M* wavelength selective switch is an optical device that allows switching any incoming wavelength from its input port to any of the *M* output ports, without the need of optical to electrical conversions. These devices play a key role in protection and reconfiguration tasks of the next generation optical networks. A number of approaches to implement WSS have been demonstrated. Some are based on gratings that spatially disperse the input channels, on micro–electro–mechanical systems (MEMS) or on liquid crystal spatial light modulators **[26]**, **[27]**, **[28]**, **[29]**. Other approaches use silica–based planar lightwave circuits (PLCs) **[30]** or ring resonator **[31]**, **[32]**.

Some LC reconfigurable devices for the VIS range have been reported such as tunable filters **[18]** or multifunctional devices operating as switches, combiners and variable optical attenuators **[33]** but not a wavelength selective switch. In the next section, a reconfigurable 1×2 WSS based on a Lyot filter and high birefringence nematic LCs (as the previous reported LCTF) is proposed. This device is designed to work in VIS range and uses a simple polarization diversity scheme. Simulations and experimental results, in a two channel system compatible with low cost SI–POF networks, are reported.

3.3. Design of a Reconfigurable 1x2 WSS using High Birefringence LCs

This reconfigurable R–WSS is based on tunable Lyot filters designed using high birefringence nematic liquid crystals. Two different configurations are used for allowing spatial switching of different wavelength channels in a compact design. The proposed scheme is shown in **Fig. 3.13**. Although multiple separation wavelengths drops are obtained at the output due to the LCTF periodicity, there is no influence if only two wavelengths (channels) are considered.

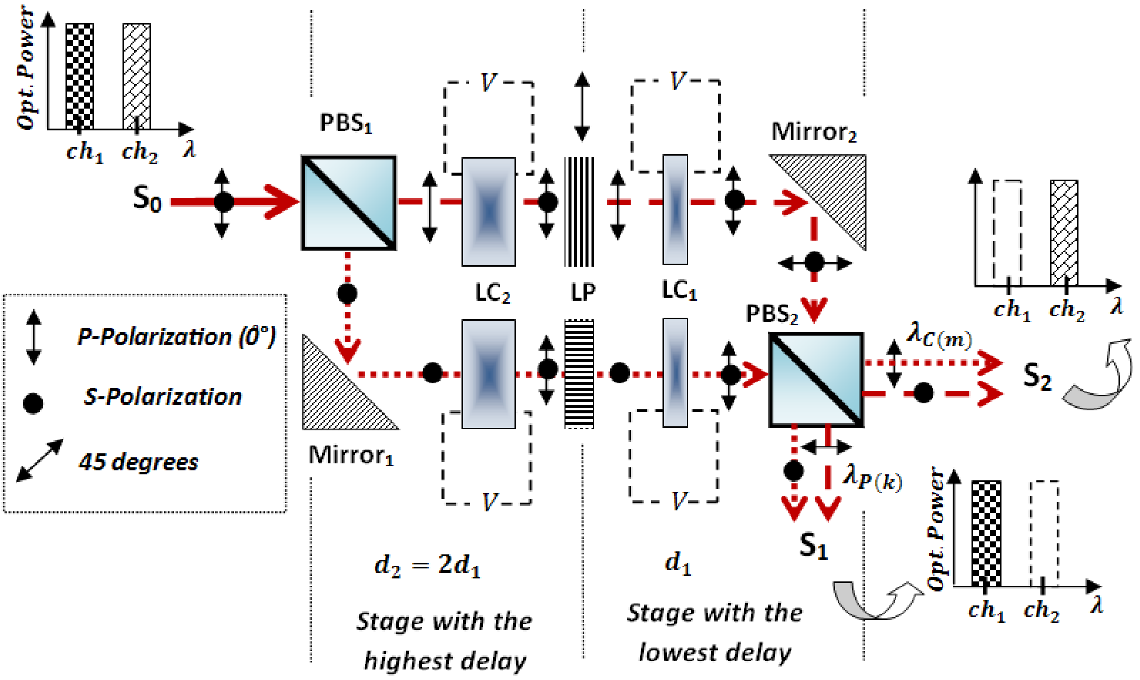

Fig. 3.13: Schematic of a reconfigurable 1×2 WSS with polarization diversity, where d_1 and d_2 are the HN1 and HN2 thickness, and V is the applied voltage.

In this configuration, each arm is based on the LCTF structure presented in the previous section, but using a polarization beam splitter, PBS, at the lowest delay stage. The PBS acts as both, parallel and crossed LPs, for each input light polarization state. The input channels are centred at the transmission band of the equivalent LCTF with parallel and crossed LPs, respectively, see (3.4) and (3.6). Channel centred at transmission band of the LCTF with parallel LPs is transmitted at port S_1

and channel centred at transmission band of the LCTF with crossed polarizers is transmitted at port S_2.

Using a scheme with a single arm, input polarizer limits the maximum theoretical transmittance to 50%. This can be overcome by using a polarization diversity scheme, two arms, as in the reconfigurable WSS shown in **Fig. 3.13**.

3.3.1. Experimental Set–up and Modeling

A reconfigurable 1×2 R−WSS is simulated and experimentally tested. The experimental setup is shown in **Fig. 3.14** (just for a single arm of **Fig. 3.13**). A halogen light source “Avaligth Hall” and a spectrometer “AvaSpect−128” are used. The fiber optic spectrometer has a 360 to 890 nm spectral range, and about 4 nm spectral resolution. Multimode optical fibers and collimators are used at input and output ports.

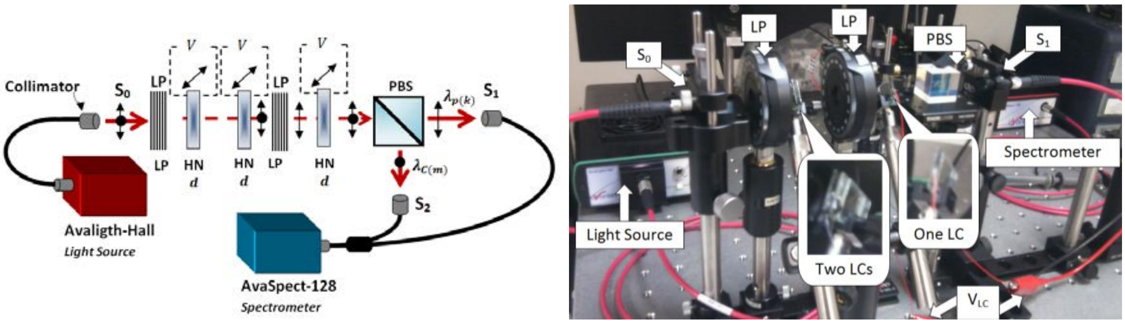

Fig. 3.14: Scheme and photograph of the experimental setup of the reconfigurable 1×2 WSS.

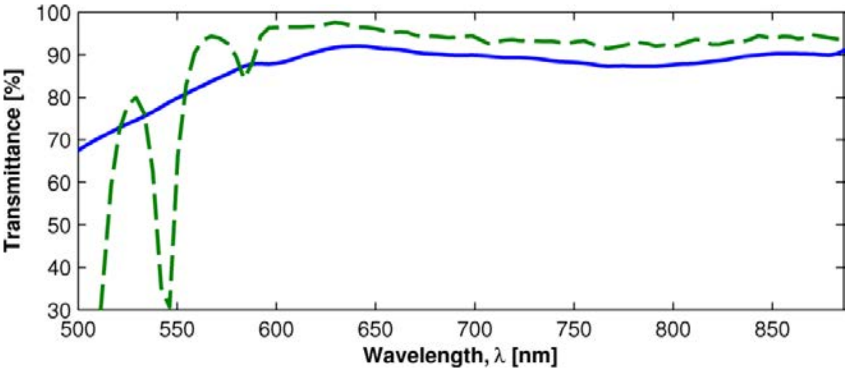

Fig. 3.15: Experimental characterization of the polarization beam splitter (PBS) transmitted output (*p*−pol) and reflected output (*s*−pol), by using polarized light in the transmission axis direction.

The LPs (LPVIS050) have a diameter of 12.5 mm, 550 to 1500 nm operation range and 70% polarized light transmission at 600 nm, as shown in **Fig. 3.8b**. The PBS is a cube of 20 mm × 20 mm × 20 mm, it has transmission higher than 90% in the range from 600 to 700 nm at both polarization states with a split ratio of unpolarized light of 50/50 ± 5%. The characterization of the PBS is shown in **Fig. 3.15**.

The HN LC devices have been specifically designed and manufactured with the LC mixture 1658, which has been synthesized at the Military University of Technology in Warsaw. The dispersion profile, $\Delta n(\lambda,V)$, of those cells has been determined in the range from 525 to 886 nm for V between 0 and 7 V_{RMS} (at 1 kHz) with resolution of 5 mV_{RMS}, see **Fig. 3.6** and **Fig. 3.7** (Appendix A shows the details of the characterization done).

HN cells used have a thickness $d = 5.1$ μm and birefringence $\Delta n \sim 0.38$ at 633 nm (at $V < V_{th}$, $V_{th} = 0.75$ V_{RMS}). From (3.1) a delay $\Gamma = 19.23$ rad is obtained with those values. In comparison, a commercially available low−birefringence LC mixture MLC−9200−100 ($\Delta n \approx 0.11$ at 633 nm) produces the same delay with a thickness $d = 17.6$ μm **[34]**, **[35]**. Thicker LC cells have higher transmission loss and response time which deteriorate the overall device performance. The 1658 mixture has Δn higher enough to have a good performance in the VIS range, allowing a design only based on HN devices. Then, to fulfil the design condition, $\Gamma_j = 2^{j-1}\Gamma$, one LC device is used in the first stage and two LC devices are used in the second stage, see **Fig. 3.14**. The same control voltage, V [V_{RMS}], is applied to all LC cells. **Fig. 3.16** shows the experimental tuning of the S_1 and S_2 output for 2 different control voltages.

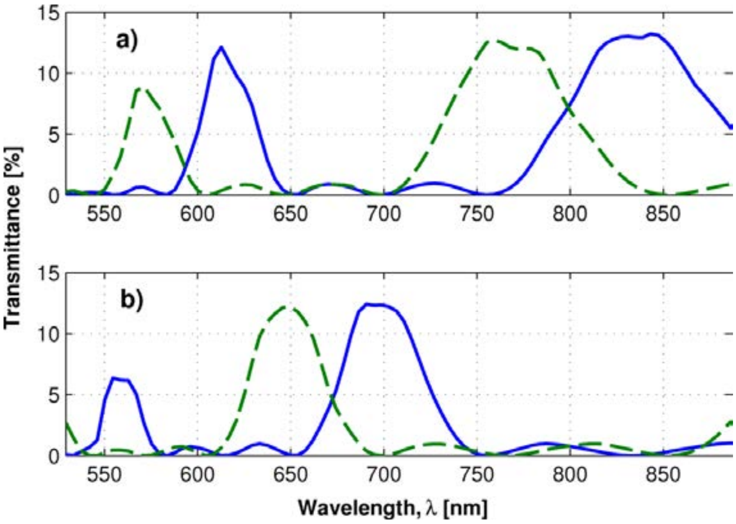

Fig. 3.16: Experimental tuning of the 1×2 R−WSS (a) output S_1 and (b) output S_2. $V = 0.8$ V_{RMS} (solid line), $V \approx 0.8$ V_{RMS} (dashed line), $V \approx 1.1$ V_{RMS} (dash−dot line).

The comparison between the 1×2 WSS measurements and simulations are shown on **Fig. 3.17**, for a particular V of 0.8 V_{RMS} applied to all LC cells. The simulations are based on the simulation program described in **section 3.2.3.2**, reported elsewhere **[36]**. For getting accurate simulation results, experimental LC cells, LPs and the PBS characteristics previously reported, were used. It can be seen that there is a good agreement between simulations and experimental results. So, using the individual experimental characterization of WSS elements and the developed simulation program, transmission results for different 1×2 WSS configurations can be derived.

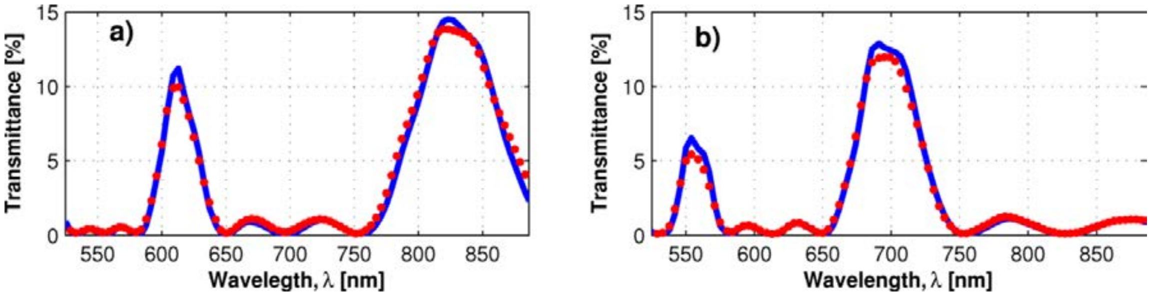

Fig. 3.17: 1×2 WSS transmission versus wavelength, simulations (solid lines) and experimental results (dotted lines) $V = 0.8$ V$_{RMS}$: (a) output S_1 and (b) output S_2.

3.3.2. Reconfiguration Capability and Performance

In the following, a reconfigurable 1×2 WSS with polarization diversity in a POF network application is tested by using the simulation program of the previous section. This device (see **Fig. 3.13**) can demultiplex, switch or block two wavelengths channels (ch_1 and ch_2) between one input port and two output ports. The transmission states are controlled by applying the appropriate voltage to all LC cells. **Table 3.3** summarizes the eight possible transmission states of this 1×2 reconfigurable WSS.

TABLE 3.3. RECONFIGURABLE 1×2 WSS TRANSMISSION STATES.

State	V (V_{RMS})	Channel at each output port:		Description
		S_1	S_2	
1	V_1	ch_1	ch_2	$ch_1 \rightarrow S_1$ and $ch_2 \rightarrow S_2$
2	V_2	ch_2	ch_1	$ch_2 \rightarrow S_1$ and $ch_1 \rightarrow S_2$
3	V_3	ch_1	none	$ch_1 \rightarrow S_1$ and none $\rightarrow S_2$
4	V_4	none	ch_1	none $\rightarrow S_1$ and $ch_1 \rightarrow S_2$
5	V_5	ch_2	none	$ch_2 \rightarrow S_1$ and none $\rightarrow S_2$
6	V_6	none	ch_2	none$\rightarrow S_1$ and $ch_2 \rightarrow S_2$
7	V_7	ch_1 and ch_2	none	(ch_1 and ch_2) $\rightarrow S_1$ and none $\rightarrow S_2$
8	V_8	none	ch_1 and ch_2	none $\rightarrow S_1$ and (ch_1 and ch_2) $\rightarrow S_2$

LED−based channels at 560 (ch_1) and 621 nm (ch_2) with full width half maximum, *FWHM*, of 20 nm are considered as the two channels that come from a WDM−SI−POF network **[37]**. The 1×2 R−WSS is designed using all elements previously described in this section along with 98% reflectivity mirrors. An optimization algorithm, based on the characterization information of the LC devices, is used for determining the LC control voltages for reaching the different WSS transmission states presented in **Table 3.3**. The following control voltages are obtained from this optimization process: [V_1, V_2, ..., V_8] = [1.175, 0.210, 1.530, 1.790, 1.955, 1.640, 2.100, 3.225] V_{RMS}. The voltage of 0.21 V_{RMS} can be replaced by any voltage below 0.75 V_{RMS} (V_{th}). Simulations are shown on **Fig. 3.18** for transmission states reported on **Table 3.3**. Impairments such as insertion loss, pass−band effects, and crosstalk attenuation, are also calculated. They are given by:

- **Insertion losses (*IL*):** For the transmission state in which the channel ch_t is transmitted through the output S_x (desired output), with x = 1 or 2, the $IL(ch_t)_{Sx}$ is defined as is defined as:

$$IL(ch_t)_{Sx} = -10\log\left[\frac{P(ch_t)_{Sx}}{P(ch_t)_{So}}\right] \quad with \quad \begin{cases} t=\{1,2\} \\ x=\{1,2\} \end{cases}, \tag{3.13}$$

where $P(ch_t)_{Sx}$ and $P(ch_t)_{So}$ are optical power at the output S_x and at the input S_o, respectively, for the wavelength channel, ch_t. In these calculations whole spectrum of each channel is considered.

- **Crosstalk Attenuation (*CTA*)**: For the transmission state in which the channel ch_t is blocked at the output S_y (undesired output), with y = 1 or 2, the $CTA(ch_t)_{Sy}$ is defined as:

$$CTA(ch_t)_{Sy} = -10\log\left[\frac{P(ch_t)_{Sy}}{P(ch_t)_{So}}\right] \quad with \quad \begin{cases} t=\{1,2\} \\ y=\{1,2\} \end{cases}, \tag{3.14}$$

where $P(ch_t)_{Sy}$ and $P(ch_t)_{So}$ are optical power at the output S_y and at the input S_o, respectively, for the wavelength channel, ch_t. Output channel optical power is calculated at the maximum transmission.

Fig. 3.18 shows that, insertion losses of 3.4 to 6 dB and crosstalk attenuation ratios from 16 to 21 dB, in the different configurations, are obtained. The *CTA* can be improved by adding more filtering stages to the 1×2 R−WSS design but at the expense of increasing *IL*, or using optimized birefringent filters, with low−side lobes. In a future work and after an optimization process, different voltage levels at each LC cell will be applied to improve *CTA* ratio among others.

In this section, a 1×2 R−WSS, based on a Lyot filter structure, using specific high birefringence nematic LCs, has been designed and tested. The system working principle has been demonstrated in the visible spectrum region for SI−POF networks.

A versatile behaviour for the 1×2 reconfigurable WSS is obtained by applying the same voltage to each LC cell. Performance of a two channel system, at 560 and 621 nm, is shown after optimizing LC voltages.

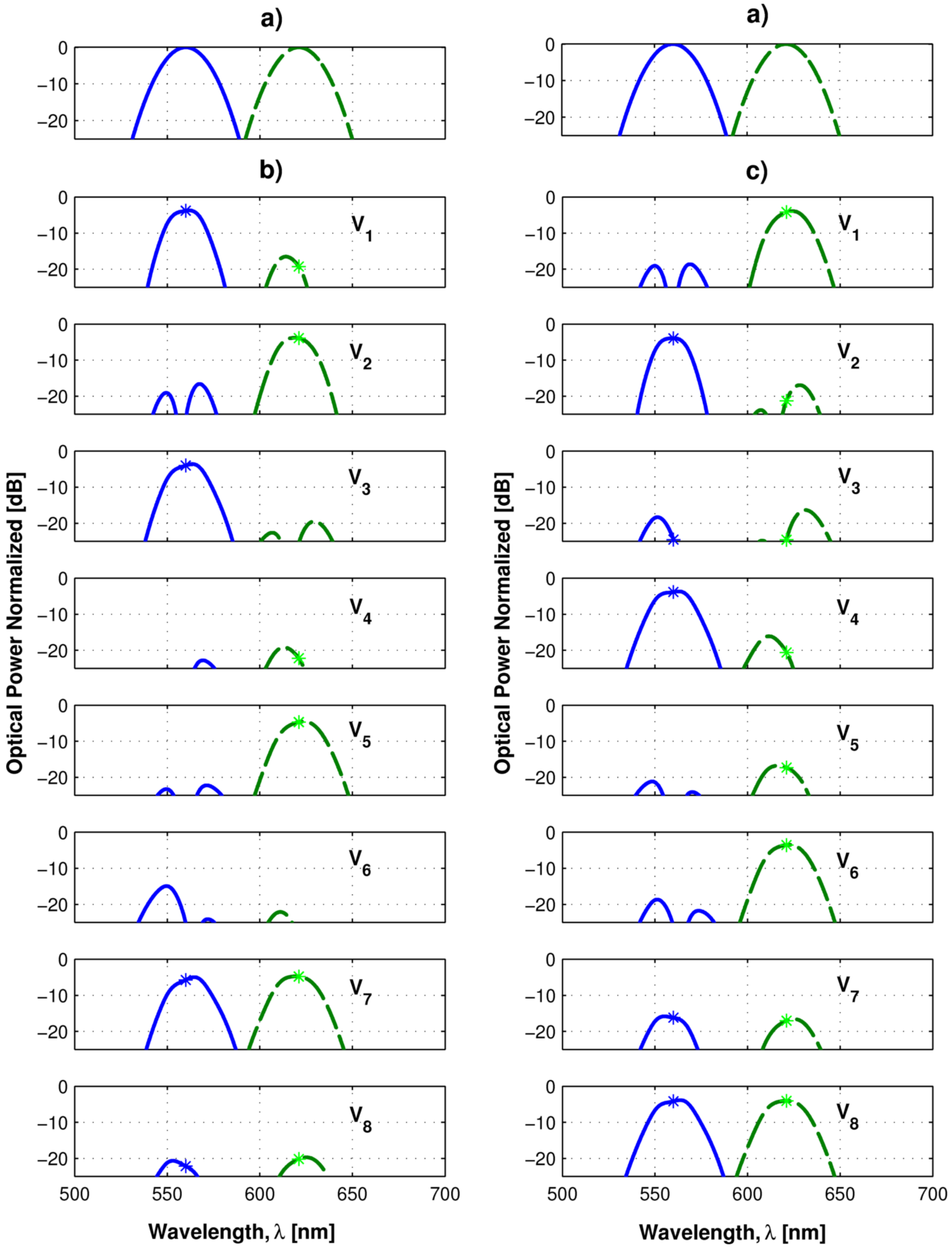

Fig. 3.18: Normalized optical power of 1×2 WSS with polarization diversity versus wavelength in ch_1 (solid line) and ch_2 (dashed line) with [V_1, V_2, ..., V_8] = [1.175, 0.210, 1.530, 1.790, 1.955, 1.640, 2.100, 3.225] V_{RMS}. (a) S_0 input spectrum, (b) S_1 output spectrum, (c) S_2 output spectrum. Asterisks mark the central channel wavelengths.

This system allows demultiplexing, switching or blocking any channel through any output port using voltages from 0 to 3 V_{RMS}. Maximum *ILs* of 6 dB, and *CTAs* better than 16 dB, are obtained. The *IL* can be easily reduced by using polarizers with a better transmittance, for example, wire grid polarizers have transmittance >83% in the range from 400 to 700 nm with extinction ratio >800:1 **[38]**. On the other hand, the *CTA* can be highly improved by applying individual voltages to each LC cell or using tunable birefringent filters with optimized structures.

3.4. Synthesis Method of Asymmetric Flattop Birefringent Interleavers Based on Digital Filter Design and Genetic Algorithm

As mentioned in the introduction section (**section 3.1**), interleavers are filters that separate an incoming spectrum into two complementary set of periodic spectra (odd and even channels), or combine them into a composite spectrum. Therefore, the Reconfigurable 1×2 WSS presented in the previous section, which is based on the LCTF designed in **section 3.2**, can be considered as an interleaver filter. This interleaver is based on a Lyot filter structure; therefore, it can be classified as a birefringent interleaver. However, Lyot filters have large side−lobes (low crosstalk attenuation) and symmetric pass−bands (odd and even channels) with conical shape, as can be shown in **Fig. 3.9**, **Fig. 3.17** and **Fig. 3.18**. Performance of the proposed LCTF, and therefore the performance of the Reconfigurable 1×2 WSS, can be significantly improved by using designs with low side−lobes (high crosstalk attenuation) and/or asymmetric passbands with flattop. This has motivated the development of a new method of synthesis of asymmetric flattop birefringent interleavers, which is presented in this section. Usually, flattop interleavers are designed to work in high−speeds DWDM networks at about 1550 nm (C−Band). Therefore, the performance of the proposed method will be tested and analyzed in this wavelength range. Further on, the **section 3.5** shows the application of this synthesis method in the synthesis of flattop LCTFs in the VIS range (e.g. for SI−POF applications) as well as a comparison with other LCTF designs based on Lyot and Solc structures.

3.4.1. Asymmetric interleavers

Asymmetric interleavers separate the odd and even channels with different pass−bandwidths. In fact, symmetric interleavers are a particular case in which both channel groups have the same pass−bandwidths. As an example, asymmetric interleavers allow accommodating the next generation systems with 40 Gbit/s signals in the larger bandwidth and maintaining legacy systems with 10 Gbit/s signals in the smaller bandwidth **[39]**, **[40]**. This is an effective and low cost solution to extend the existing legacy network capacity, for systems upgrade and bi–directional network implementations.

Many approaches have been demonstrated to implement interleavers, based on interference effects due to their intrinsic periodic response. Most interleavers are based on Michelson interferometers, Mach–Zehnder interferometer (MZI) or birefringent filter principles, and they are implemented in bulk optics, all fiber or integrated optics technologies **[23]**, **[41]**. In these configurations, different phase–dispersion elements such as ring resonators (RR), Gires–Tournois etalons and resonant cavities, may be used to improve their box–like characteristic **[42]**, **[43]**. But those solutions increase considerably the interleaver's chromatic dispersion (CD) and its sensitivity to manufacturing tolerances. Interleavers can also be implemented by using Fabry–Perot filters **[44]**, Bragg diffraction gratings and Arrayed Waveguide Gratings (AWG) **[41]**.

Birefringent interleavers are implemented in bulk optics and use lattice structures to get flattop designs. These interleavers are highly reliable and easy to manufacture, use passive temperature compensation schemes and require polarization diversity to avoid polarization dependent loss (PDL) **[45]**. Since they operate in transmission, their transfer functions in the *Z*–domain have only zeros so they can be designed to have zero dispersion without any type of compensation. Chromatic dispersion is a critical factor in 40 Gbit/s systems and beyond. Interleavers with large CD use compensation schemes, based on double–pass designs with opposite CD slopes, to cancel the overall CD or use novel configurations mixing MZI and Gires–Tournoise etalons **[46]**. These additional elements increase the insertion loss and device complexity, but even manufacturing tolerances still cause a small amount of CD **[45]**. This is the reason for being flattop birefringent interleavers an attractive choice in high data rate applications **[47]**.

3.4.2. Synthesis Methods of Asymmetric Flattop Birefringent Filters: State–of–the–Art

In general, lattice interleaver designs include methods based on Fourier series, digital filter design and computational optimization, but most of them do not take into account a simultaneous analysis of both outputs, which is an essential aspect in interleavers design. Fourier series based method uses a lattice structure with delay lines multiples of a unit value **[41]**. This method uses *M*–simultaneous equations to determine an *M*–order filter structure to fit an ideal transfer function shape. It requires high–order filters to obtain low side–lobes.

Digital filter design method is based on the mathematical equivalence of the finite impulse response filters (FIRs) and the lattice interleavers with delay lines of a constant value **[39]**, **[47]**,

[48]. This method uses a FIR filter with transfer function $H(z)$, to find the structural parameters of the equivalent lattice interleaver in an iterative way. Any FIR filter synthesis method can be used to get $H(z)$, this allows good control over the design parameters. But previous developments of this design method applied to interleaver designs, as those reported in **[47]**, do not consider the reciprocal output (e.g. even channels), neither chromatic dispersion is considered, limiting the control over fundamental parameters at both interleaver's outputs.

Computational optimization based methods use a global optimization algorithm, such as genetic algorithm, to fit a specific transfer function to an ideal response, by finding the best variable values. In the synthesis of interleavers, by only using this method, the parameters at both outputs can be controlled, but with low precision and for a fixed interleaver order **[49]**.

In this work, a synthesis method of asymmetric flattop birefringent interleavers is proposed. It conjugates the advantages of digital filter design methods, in the Z−transform domain, and computational optimization. It allows accurate designs at both outputs (odd and even channels) in terms of key parameters such as bandwidths, isolation, ripple, chromatic dispersion and asymmetry. Genetic algorithms allow parameters optimization at both outputs with the required behaviour in a simple and effective way. The proposed method allows also designing interleavers with minimum dispersion and order.

3.4.3. Structure of a Birefringent Interleaver Filter

A flattop birefringent filter (BF) has a lattice structure consisting on a stack of M birefringent plates, with different azimuth angles, α_n, being $n = 1,2,\ldots,M$, relative to xy−plane, bounded between linear polarizers, LPs. LP at the output is called analyzer and has an azimuth angle α_{M+1}. Filter operation is based on the interference of an input light beam with multiple delayed versions of itself **[6]**, **[7]**. **Fig. 3.19** shows the schematic of a flattop BF. In this scheme, phase shifters can be used to alter the polarization of the light beams between consecutive birefringent plates.

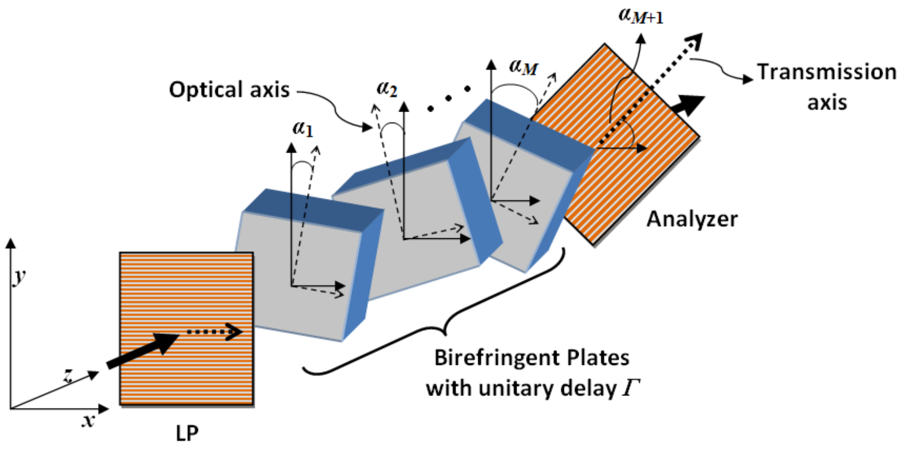

Fig. 3.19: Lattice structure of a birefringent filter.

Each birefringent plate produces a unitary delay, Γ, that is a function of the input beam with frequency, *f*, and speed, *c*, and the birefringent medium of thickness, *d*, and birefringence, Δ*n*. This delay is expressed as:

$$\Gamma = \frac{2\pi}{c} f \Delta n d \tag{3.15}$$

The contribution of multiplying *M* birefringent plates is represented by the characteristic matrix Q^M, which is expressed as:

$$Q^M = \prod_{n=1}^{M} \left[R(\alpha_n) \right] \times \left[W(\Gamma) \right] \times \left[R^{-1}(\alpha_n) \right] \tag{3.16}$$

where *n* is the stage number, *R* is a rotation matrix respect to the *xy*–plane and *W* is the Jones matrix of the birefringent plate. These matrices are given by:

$$R(\alpha_n) = \begin{pmatrix} \cos(\alpha_n) & \sin(\alpha_n) \\ -\sin(\alpha_n) & \cos(\alpha_n) \end{pmatrix}, W(\Gamma) = \begin{pmatrix} e^{\frac{-i\Gamma}{2}} & 0 \\ 0 & e^{\frac{i\Gamma}{2}} \end{pmatrix} \tag{3.17}$$

Considering that the analyzer has an azimuth angle, α_{M+1}, the output relative to the *xy*–plane is given by:

$$\left[Q^{M+1} \right] = \left[Q^M \right] \times \left[R(\alpha_{M+1}) \right] \times \left[P_X \right] \times \left[R^{-1}(\alpha_{M+1}) \right] \tag{3.18}$$

where P_X is the Jones matrix of a LP parallel to the *x*–axis, and it is given by:

$$P_X = \begin{pmatrix} 1 & 0 \\ 0 & 0 \end{pmatrix} \tag{3.19}$$

$[Q^{M+1}]_{11}$ and $[Q^{M+1}]_{21}$ represent the output polarization components parallel to the *x*–axis (*x*–polarized), T_x, and parallel to the *y*–axis (*y*–polarized), T_y, called also bar and cross outputs, respectively, when the input beam is *x*–polarized.

For interleaving applications, the bar and cross outputs are separated by using a polarization beam splitter element.

3.4.4. Synthesis Method in the Z–Transform Domain

By analogy with an ordinary MZI interferometer the two optical axes of the birefringent medium can be regarded as *M* pairs of delay lines, as part of the interfering arms. And the azimuth angles, in the form of relative azimuth angles, θ_{n-1}, ($\theta_0 = \alpha_1$, $\theta_1 = \alpha_2 - \alpha_1$,…, $\theta_{M-1} = \alpha_M - \alpha_{M-1}$, $\theta_M = \alpha_{M+1} - \alpha_M$, see **Fig. 3.19**), are analogous to *M*+1 coupling constants. Then, Jinguji and Kawachi synthesis method **[50]** can be used for synthesizing flattop BFs, as already reported **[39]** and **[47]**. In this work, the relation between BFs and the *Z*–transform domain is analyzed following a similar procedure to that presented in **[51]**. It is considered that there are no phase shifters and there is no loss in any of the elements; so that their transfer functions are unitary. The dispersion of the elements is neither considered.

The unitary delay Γ can be related to the *Z*–Transform domain, being $z = exp(i\Gamma)$. Then, from (3.17), $W(z)$ can be expressed as:

$$W(z) = \begin{pmatrix} z^{-\frac{1}{2}} & 0 \\ 0 & z^{\frac{1}{2}} \end{pmatrix} \tag{3.20}$$

From (3.16), the characteristic matrix $Q^M(z)$ is a 2×2 unitary matrix, which can be expressed as follows:

$$Q^M(z) = \begin{bmatrix} H^M(z) & -F^M(z)^* \\ F^M(z) & H^M(z)^* \end{bmatrix} \tag{3.21}$$

where the superscript * denotes the Hermitian conjugation (reverse polynomial).

The terms $H^M(z)$ and $F^M(z)$ are polynomials of degree M, where $H^M(z)$ is the bar transfer function and $F^M(z)$ is the cross transfer function. If the input beam is *x*–polarized, they can be expressed as:

$$H^M(z) = \left(\sum_{k=0}^{M} a_k z^{-k}\right) z^{M/2} \tag{3.22}$$

$$F^M(z) = \left(\sum_{k=0}^{M} b_k z^{-k}\right) z^{M/2} \tag{3.23}$$

where coefficients, a_k and b_k, are the impulse response of the FIR filters of order M, $H^M(z)$ and $F^M(z)$, respectively.

From (3.21) it is shown that Q^M is a unimodular matrix, so their components are related by:

$$H^M(z)H^M(z)^* + F^M(z)F^M(z)^* = 1 \tag{3.24}$$

therefore, knowing one of the two transfer functions in Z, the other is immediately defined.

3.4.4.1. Recursive process to relate FIR filters with birefringent interleavers

The following recursive identity is used to relate $H^M(z)$ and $F^M(z)$ with the structural parameters of the equivalent birefringent interleaver **[51]**:

$$[Q_M]\left[Q^{M-1}\right]=\left[Q^M\right] \tag{3.25}$$

where the superscript $M-1$ indicates that the matrix is the result of multiplying the $M-1$ first delay stages, resulting in M−1 order filters, and the subscript M indicates that it is the transfer matrix of the M−th stage. Multiplying both sides of (3.25) by the inverse of Q_M, the following matrix relationship is obtained:

$$\begin{bmatrix} H^{M-1}(z) \\ F^{M-1}(z) \end{bmatrix} = \begin{bmatrix} \cos(\theta_M)z^{1/2} & -\sin(\theta_M)z^{1/2} \\ \sin(\theta_M)z^{-1/2} & \cos(\theta_M)z^{-1/2} \end{bmatrix} \begin{bmatrix} H^M(z) \\ F^M(z) \end{bmatrix} \tag{3.26}$$

Then, from (3.26), $H^{M-1}(z)$ and $F^{M-1}(z)$ can be written as:

$$H^{M-1}(z)=\left\{\sum_{k=1}^{M}\left[a_k\cos(\theta_M)-b_k\sin(\theta_M)\right]z^{-k}\right\}z^{(M+1)/2}+\left[a_0\cos(\theta_M)-b_0\sin(\theta_M)\right]z^{(M+1)/2} \tag{3.27}$$

$$F^{M-1}(z)=\left\{\sum_{k=0}^{M-1}\left[a_k\sin(\theta_M)+b_k\cos(\theta_M)\right]z^{-k}\right\}z^{(M-1)/2}+\left[a_M\sin(\theta_M)+b_M\cos(\theta_M)\right]z^{-(M+1)/2} \tag{3.28}$$

Both polynomials are obtained by multiplying $M-1$ matrices. Comparison of previous equations to (3.22) and (3.23) reveals that the terms outside the summation in (3.27) and (3.28) should be zero. So that the value of the Mth relative azimuth angle, θ_M, is given by:

$$\tan(\theta_M)=\frac{\sin(\theta_M)}{\cos(\theta_M)}=\frac{a_0}{b_0}=-\frac{b_M}{a_M} \tag{3.29}$$

Knowing θ_M, the previous coefficient groups, a_k^{M-1} and b_k^{M-1}, with $k = 0, 1, \ldots, M-1$, can be obtained, which represent the coefficients of the M−1 order filters obtained by multiplying the M−1 previous stages. The whole recursive process is done using the next three equations:

$$a_k^{n-1}=a_{k+1}^{n}\cos(\theta_n)-b_{k+1}^{n}\sin(\theta_n) \tag{3.30}$$

$$b_k^{n-1}=a_k^{n}\sin(\theta_n)+b_k^{n}\cos(\theta_n) \tag{3.31}$$

$$\tan(\theta_{n-1})=\frac{a_0^{n-1}}{b_0^{n-1}}=-\frac{b_{n-1}^{n-1}}{a_{n-1}^{n-1}} \tag{3.32}$$

where n is replaced in inverse order, $n = M, M-1, \ldots, 1$. For each n value, using (3.30) and (3.31), the coefficient groups a_k^{n-1} and b_k^{n-1}, with $k = 0, 1, \ldots, n-1$, are obtained. Then, (3.32) is used to get θ_{n-1}, and starting again the recursive process.

Finally, the azimuth angle of the nth birefringent plate is $\alpha_n=\sum_{m=0}^{n-1}\theta_m$, and the azimuth angle of the analyzer is $\alpha_{M+1}=\sum_{m=0}^{M}\theta_m$.

For simplicity, from now on H^M(z) and $F^M(z)$ will be referred as $H(z)$ and $F(z)$, respectively.

3.4.4.2. Birefringent Interleaver: Design Example

In this section, a simple process to design two reciprocal FIR filters is described as well as the method to find their equivalent birefringent interleaver.

There are many algorithms, and functions, to design FIR filters. In this work, Parks–McClellan optimal equiripple FIR filter design algorithm is implemented by using Matlab functions **[52]**. Main parameters considered in the low–pass filter design (see **Fig. 3.20**) are: the normalized lower (ω_{pass}) and higher (ω_{stop}) cut frequencies, the ripple in the pass–band ($Ripple_H$) and the isolation in the stop–band (Iso_H). Other related parameters are the normalized pass–bandwidth, BW_{passH}, and stop–bandwidth, BW_{stopH}.

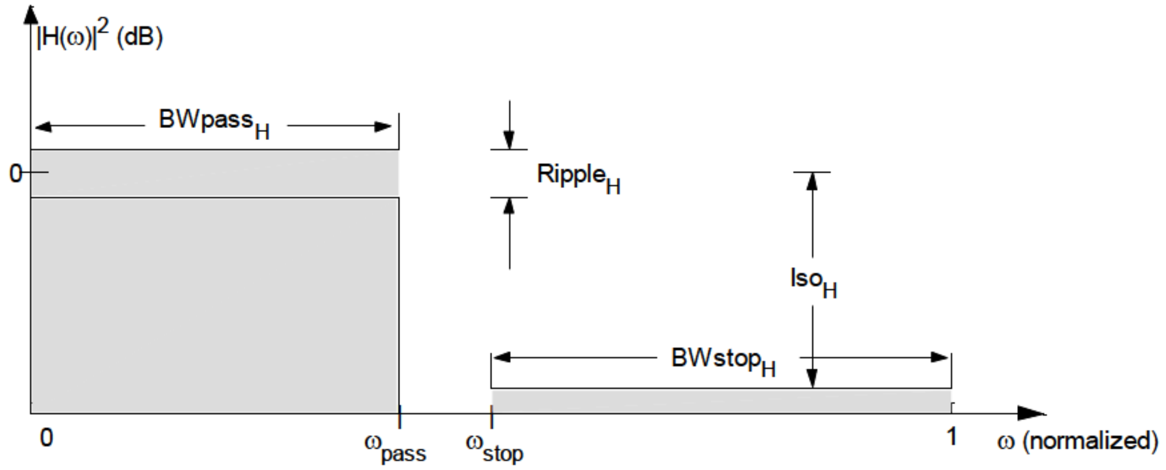

Fig. 3.20: FIR filters specifications and parameters.

All previous parameters are defined for $H(z)$. In the same way, the ripple in the pass–band of $F(z)$, the isolation in its stop–band, its pass–bandwidth and its stop–bandwidth are defined by $Ripple_F$, Iso_F, BW_{passF} and BW_{stopF}, respectively.

The order, stop–bandwidth, ripple and isolation of only one interleaver output can be well designed using previous reported methods **[39]**, **[47]**. Specifications of both outputs can be controlled by relating the ripple of one output with the isolation of the other output. From (3.24), $|F(\omega)|^2 = 1 - |H(\omega)|^2$, then $Ripple_H$ can be related to Iso_F by the following expression:

$$Ripple_H(dB) = 10\log_{10}\left[10^{\frac{Iso_F(dB)}{10}} + 1\right] \qquad (3.33)$$

A design example of an asymmetric birefringent filter is described below to show the potential of the proposed method. Interleaver specifications are shown in **Table 3.4**, where *FSR* is the free spectral range; these values were extracted from those reported in **[53]**.

TABLE 3.4: SPECIFICATIONS OF THE INTERLEAVER DESIGN EXAMPLE.

Parameter	$H(z)$ Symbol	$H(z)$ Value	$F(z)$ Symbol	$F(z)$ Value
25dB Stop−Bandwidth	B_{WstopH}	±0.15	B_{WstopF}	±0.30
Pass−Band Ripple (dB)	$Ripple_H$	$\leq 1.37\times10^{-3}$ over 30% *FSR*	$Ripple_F$	$\leq 1.37\times10^{-3}$ over 15% *FSR*
Stop−Band Isolation (dB)	Iso_H	≤−25 over 15% *FSR*	*Iso*F	≤−25 over 30% *FSR*
Filter Order	M	≤10	M	≤10

ω_{pass}, ω_{stop} and Iso_F are set to 0.15, 0.30 and −30 dB, respectively, and then from (3.33) $Ripple_H$ is set to 4.34×10^{-3}dB, to satisfy the interleaver's requirements of **Table 3.4**. The resulting filter, $H(z)$, is a seventh order filter and its coefficients a_k are shown in **Table 3.5**.

TABLE 3.5: COEFFICIENTS OF THE FILTER $H(Z)$, a_k, AND $F(Z)$, b_k. RELATIVE ANGLES, θ_{n-1}, AND AZIMUTH ANGLES, α_n, OF THE EQUIVALENT BIREFRINGENT INTERLEAVER.

FIR filters Coefficients			Equivalent Birefringent Filter Angles		
k	a_k	b_k	n	θ_{n-1}	αn
0	0.0197	0.2378	1	−1.4884	−1.4884
1	−0.0587	−0.4784	2	−0.0798	−1.5682
2	0.0043	0.3545	3	−0.2583	−1.8265
3	0.5347	−0.0169	4	1.0378	−0.7887
4	0.5347	−0.0956	5	1.0380	0.2494
5	0.0043	0.0001	6	−0.2582	−0.0088
6	−0.0587	0.0064	7	−0.0801	−0.0890
7	0.0197	−0.0016	8	0.0824	−0.0066

Now, reciprocal filter, $F(z)$, is inferred using (3.24). This equation allows to get the $2M$ zeros of $F(z)F(z)^*$ which appear in a pair of the form (b_k, $1/b_k^*$), with $k = 0,\ldots, M$. Using spectral factorization, one of each pair (b_k, $1/b_k^*$) must be selected for $F(z)$ or $F(z)^*$. We chose the M zeros inside the unit circle to infer $F(z)$. The resulting normalized coefficients b_k are shown in **Table 3.5**.

Knowing $H(z)$ and $F(z)$, equations (3.30) to (3.32) are used to find the relative azimuth angles, θ_{n-1}, which define the azimuth angles, α_n, of the 7 birefringent plates ($M = 7$) plus the analyzer. These angles are also shown in **Table 3.5**.

Interleaver dispersion is a very important parameter for determining its performance, especially in high speed systems (40 Gbit/s). Normalized dispersion is defined as the derivate of the group delay **[54]** with respect to the normalized frequency, ω_n, and it is calculated using the following expression:

$$D_n = 2\pi \frac{d}{d\omega_n}\left(-\frac{d}{d\omega_n}\Theta(\omega_n)\right) \tag{3.34}$$

where Θ is the phase, or argument, of the filter response. Then, the filter dispersion in absolute units (s/m) is given by:

$$D = -c\left(\frac{T}{\lambda}\right)^2 D_n \tag{3.35}$$

where T is the filter period (T=1/FSR) and c is the speed of the light.

Fig. 3.21 shows the magnitude response and normalized dispersion of $H(z)$ and $F(z)$, and the resulting interleaver with outputs T_x and T_y. In this figure, the equivalence between the magnitude response and the dispersion of the digital filters and the optical interleaver are observed.

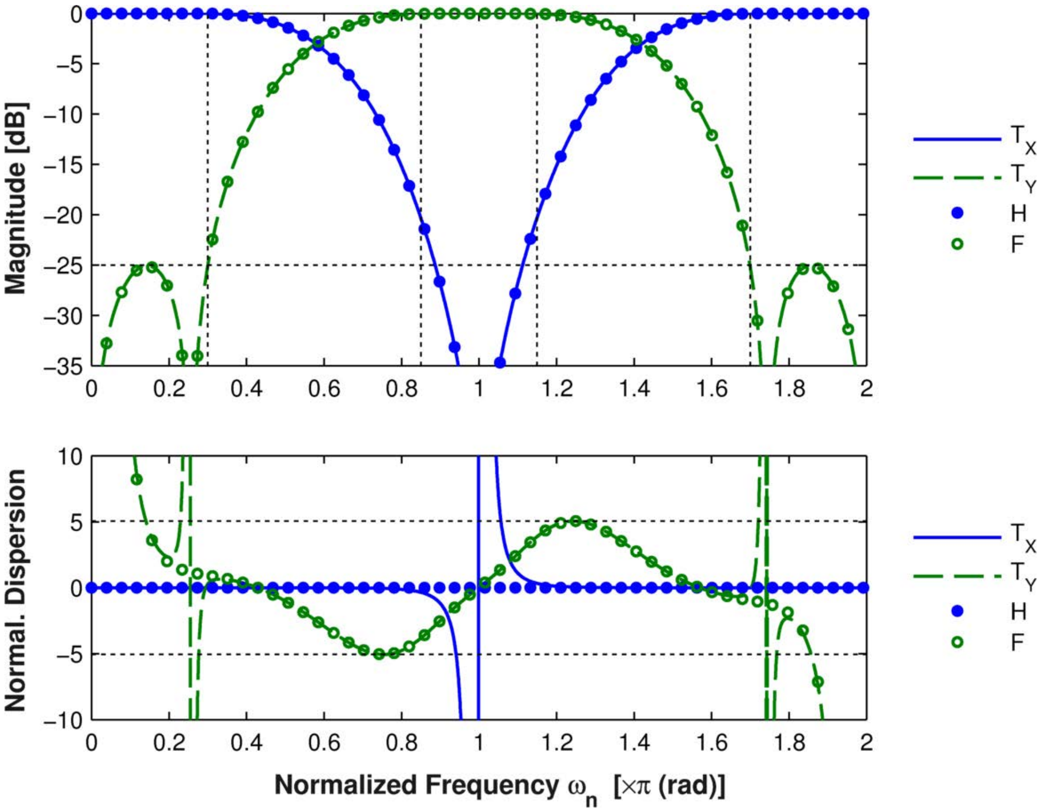

Fig. 3.21: Birefringent interleaver design results.

Table 3.6 shows the performance of the interleaver shown in **Fig. 3.21**. The resulting 0.5 dB normalized pass−bandwidth of T_x and T_y are ±0.4316 and ±0.2715, respectively. In an interleaver with FSR of 100 GHz, those normalized values represent bandwidths of 43.16 GHz and 27.15 GHz. Since $H(z)$ is designed to be a linear−phase filter, T_x has zero dispersion (CD) in the pass−band. This characteristic of T_x is ideal for applications in 40 Gbit/s systems. On the other hand, the normalized dispersion of T_y is ±5.05, this equals to a dispersion, in absolute units, of ±63 ps/nm in an interleaver with FSR = 100 GHz operating at a wavelength of 1550 nm. This value is comparable with the dispersion reported on **[53]** but can be further improved as it is described in the discussion section. In **Table 3.6** it is shown that the 25 dB normalized stop−bandwidth of T_x

and T_y have relative errors of 24.47% and 2.67% from the expected values of ±0.15 and ±0.30, respectively (see also **Table 3.4**).

TABLE 3.6: ANALYSIS RESULTS OF THE ASYMMETRIC BIREFRINGENT INTERLEAVER DESIGN. *M*=7.

Parameter	T_x		T_y	
	Normalized *FSR* = 2	**with *FSR* = 100 GHz at 1550 nm**	**Normalized *FSR* = 2**	**with *FSR* = 100 GHz at 1550 nm**
0.5dB Pass−Bandwidth	±0.4316	43.16 GHz	±0.2715	27.15 GHz
3.0dB Pass−Bandwidth	±0.5781	57.81 GHz	±0.4219	42.19 GHz
25dB Stop−Bandwidth	±0.1133	11.33 GHz	±0.3080	30.80 GHz
Pass− Band Ripple (dB)	13.53×10^{-3} over 30% *FSR*		40.02×10^{-3} over 15% *FSR*	
Stop−Band Isolation (dB)	≤−20 over 15% *FSR* ≤−25 over 11% *FSR*		−25 over 31% *FSR*	
Max CD at 3.0dB Pass−Band	0	0 ps/nm	±5.05	±63 ps/nm

In the next section, an optimization process is proposed to reduce the error between the designed interleaver parameters and the expected design parameters, including the dispersion of the output T_y.

3.4.5. Genetic Algorithm for Interleavers Design Optimization

The synthesis method that is proposed uses digital filter design algorithms for interleavers' optimization, which can be regarded as black−box functions. Therefore, the optimization problems must be solved using a global optimization algorithm **[55]**.

The genetic algorithm, GA, is a global optimization algorithm that, due to its random nature, improves the possibilities of finding a global solution. GA solves optimization problems by mimicking the principles of biological evolution **[55]**. GA minimizes an objective function, $F_{obj}(x)$, where x is a vector of variables, considering these variables as chromosomes, x as an individual, and the group of individuals as a population. This approach has been previously used in designing photonic−crystal waveguide interleavers **[56]** and birefringent interleavers **[39]**, **[49]**, but not in combination with a digital signal processing approach.

GA can be used to optimize $H(z)$, adjusting T_x and T_y to the expected response, see **Table 3.4** and **Table 3.6**. Using GA in combination with FIR filters design algorithms gives simplicity, since the only required variables to define the vector x are the normalized lower (ω_{pass}) and higher (ω_{stop}) cut frequencies, and the interleaver's isolation, *Iso*. Then, the vector of variables x is given by:

$$x = \left[\omega_{pass}, \quad \omega_{stop}, \quad Iso \right] \tag{3.36}$$

It is efficient, because the procedure is fast (few seconds) and slightly independent of the interleaver's order. And it is flexible, since allows adjusting specific parameters.

Next, two optimization examples are shown to illustrate the proposed procedure.

3.4.5.1. *Optimizing Bandwidth and Isolation*

It is defined the next objective function for adjusting the bandwidth and isolation of $|H(\omega)|^2$ and $|F(\omega)|^2$ to the desired values:

$$F_{obj1}(x) = \left(\left| \frac{0.15 - Bw_{stop}H}{0.15} \right| + \left| \frac{0.30 - Bw_{stop}F}{0.30} \right| + \left| \frac{Iso_H - Iso_F}{Iso_H} \right| \right) \times 100 \tag{3.37}$$

The vector x includes the variables used in the Parks−McClellan FIR filter design algorithm that has been implemented by using Matlab functions **[52]**. All terms of (3.37) depend on the frequency response of filters that are obtained from a specific x vector, see **section 3.4.4.2**. The first two terms adjust the bandwidths to the specific values of ±0.15 and ±0.3, and the third term ensures that the isolation of both outputs is equal. Stop−bandwidths are measured at −25 dB, then, the minimum isolation at the stop−band will be always less that −25 dB.

Optimization is performed by setting the searching bounds from x = [0.05 0.55 25] to x = [0.45 0.95 60]. In this optimization, the error of $F_{obj1}(x)$ is 0.1144%, with the following combination of variables x_1 = [0.2242 0.0998 43.3646]. The minimum value that can be achieved by the objective function depends on the considered parameters; in the case of $F_{obj1}(x)$ its minimum possible value is zero.

Fig. 3.22 shows the comparison between the interleaver designed in the previous section with output T_x and T_y and the optimized interleaver of this example with outputs T_{x1} and T_{y1}. This optimization adjusts the isolation of T_{x1} and T_{y1} to −43.28 dB and their stop−bandwidths to the expected values of ±0.15 and ±0.30, respectively. This optimization also increases the normalized dispersion of Ty_1 from ±5.05 to ±6.8 which corresponds to ±85 ps/nm in an interleaver with *FSR* = 100 GHz operating at 1550 nm. The dispersion increment is the cost of improving the filter response and it is mainly due to the fact that the optimized filter has an order, M = 9, that it is higher than the order of the previous filter, M = 7. Anyhow, in previous designs **[47]**, it is reported an isolation of −40 dB for only one output and using an order M =14, so it has a higher dispersion.

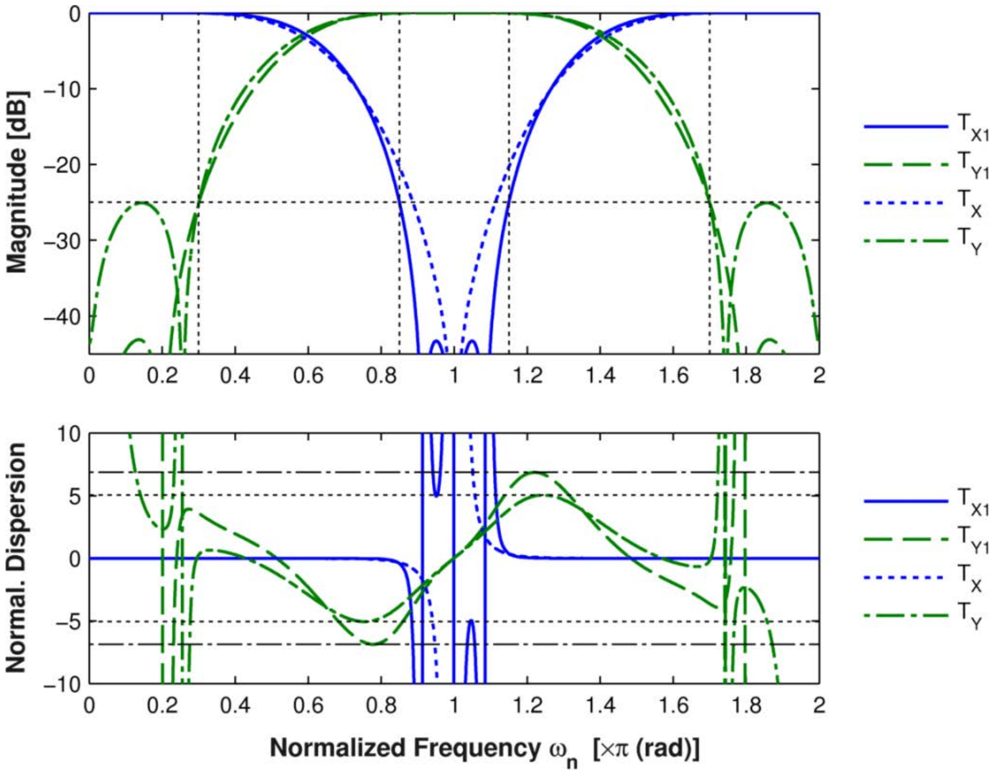

Fig. 3.22: Magnitude response and normalized dispersion of the Birefringent Interleaver with outputs T_x and T_y and the interleaver optimized using GA with outputs T_{x1} and T_{y1}.

Table 3.7 shows the normalized parameters of the optimized interleaver shown in **Fig. 3.22**, and the respective absolute values for an interleaver with unitary delay, Γ, designed to have a *FSR* = 100 GHz (50 GHz channel spacing) operating at 1550 nm. In **[23]** it can be found the design of Γ to fulfil these conditions with an athermal configuration, showing the manufacturing feasibility of the proposed design.

TABLE 3.7: ANALYSIS RESULTS OF BANDWIDTH AND ISOLATION OPTIMIZATION (FIRST OPTIMIZATION). RESULTING INTERLEAVER'S ORDER *M*=9.

Parameter	**T_{x1}**		**T_{y1}**	
	Normalized *FSR* = 2	**with *FSR* = 100 GHz at 1550 nm**	**Normalized *FSR* = 2**	**with *FSR* = 100 GHz at 1550 nm**
0.5dB Pass−Bandwidth	±0.4568	45.68 GHz	±0.2703	27.03 GHz
3.0dB Pass−Bandwidth	±0.5986	59.86 GHz	±0.4013	40.13 GHz
25dB Stop−Bandwidth	±0.1501	15.01 GHz	±0.3000	30.00 GHz
Pass− Band Ripple (dB)	13.68×10^{-3} over 30% *FSR*		13.80×10^{-3}	
Stop−Band Isolation (dB)	≤−25 over 15% *FSR* −43.28 over 10% *FSR*		≤−25 over 30% *FSR* −43.28 dB at 22% *FSR*	
Max CD at 3.0dB Pass−Band	0	0 ps/nm	±6.86	±85.66 ps/nm

3.4.5.2. *Optimizing Bandwidth Considering Dispersion*

The pass−bandwidths can be further optimized, without significantly increasing the dispersion, by using the following objective function:

$$F_{obj2}(x)=\left|\frac{0.15-Bw_{stop}H}{0.15}\right|\times 100+\left|\frac{0.30-Bw_{stop}F}{0.30}\right|\times 100+D_{n\_\max F}+c_1 M \tag{3.38}$$

First and second terms of $F_{obj2}(x)$ adjust the bandwidths to the specific values of ±0.15 and ±0.3, the third term minimizes the maximum normalized dispersion of $F(z)$, D_{n_maxF}, and the last term minimizes the interleaver's order, which also reduces D_{n_maxF}. In this objective function, it is not included the isolation because it is not possible to optimize simultaneously all variables in an effective way. Anyway, as stated in previous example, stop−bandwidth is measured at −25 dB then isolation value will always be less that −25 dB. In this function, the weighting coefficient, c_1=2, is used to give relative importance rank to the interleaver's order, M.

Optimization is performed by setting the same searching bounds than in previous example. The resulting error of $F_{obj2}(x)$ = 21.52%, with a combination of variables x_2 = [0.2921 0.1689 28.9235]. The order of $H(z)$ will be $M \geq 3$, due to the implemented function **[52]**, therefore, the theoretical minimum value of $F_{obj2}(x)$ is 6 and it increases with M.

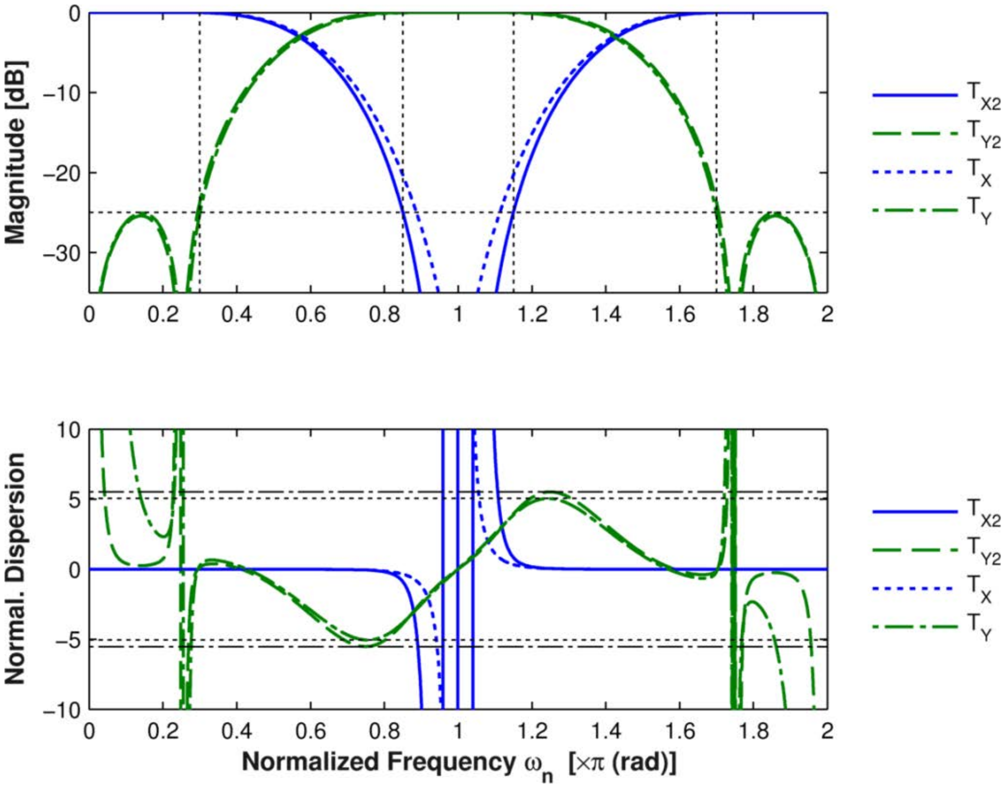

Fig. 3.23: Magnitude response and normalized dispersion of the Birefringent Interleaver with outputs T_x and T_y and the Interleaver optimized using GA with outputs T_{x2} and T_{y2}.

Fig. 3.23 shows a comparison between the interleaver designed in **section 3.4.4.2**, with outputs T_x and T_y, and the optimized interleaver of this section with outputs T_{x2} and T_{y2}. This optimization example adjusts the stop−bandwidths of $H(z)$ and $F(z)$ to the expected values of ±0.15 and ±0.30, respectively, and improves the isolation of T_x below −25 dB over 15% *FSR*, with a minimum increment of D_{n_maxF}, from ±5.05 to ±5.52, maintaining the interleaver's order in M=7. The isolation of T_y is also improved below −25 dB over 30% *FSR*. The minimum isolations at the stop−bands of $H(z)$ and $F(z)$ are not exactly equal, since this parameter is not included in $F_{obj2}(x)$.

TABLE 3.8: ANALYSIS RESULTS OF BANDWIDTHS OPTIMIZATION CONSIDERING DISPERSION (SECOND OPTIMIZATION). RESULTING INTERLEAVER'S ORDER M=7.

Parameter	T_{x2}		T_{y2}	
	Normalized *FSR* = 2	**with *FSR* = 100 GHz at 1550 nm**	**Normalized *FSR* = 2**	**with *FSR* = 100 GHz at 1550 nm**
0.5dB Pass−Bandwidth	±0.4235	42.35 GHz	±0.2900	29.00 GHz
3.0dB Pass−Bandwidth	±0.5671	56.71 GHz	±0.4329	43.29 GHz
25dB Stop−Bandwidth	±0.1499	14.99 GHz	±0.2942	29.42 GHz
Pass− Band Ripple (dB)	18.17×10^{-3} over 30% *FSR*		14.00×10^{-3} over 15% *FSR*	
Stop−Band Isolation (dB)	≤−25 over 15% *FSR*		−25dB over 30% *FSR*	
Max CD at 3.0dB Pass−Band	0	0 ps/nm	±5.52	±68.93 ps/nm

Table 3.8 shows the normalized parameters of the optimized interleaver shown in **Fig. 3.23**. These results show that this optimization example adjusts the pass−bandwidths to the desired values and improves the isolation of T_{y2} with slight variations in dispersion, in comparison with the non−optimized interleaver (**Table 3.6**).

3.4.6. Discussion and Remarks

Although, synthesis of flattop birefringent filters based on digital filter design methods have been previously reported, they have just considered only the design of one of the outputs **[47]**. But interleavers' performance is based on odd and even channels spatial separation, so both outputs must be considered. As an illustrative example, the direct, T_{x10}, and crossed, T_{y10}, outputs, of the birefringent filter designed in **[47]**, are shown in **Fig. 3.24**.

It is shown that T_{x10} output isolation is −43 dB, being a good value for a single output filter. However, T_{y10} output isolation is only −15.5 dB. This isolation value is low for being used as an interleaver. A new optimized design is shown at **Fig. 3.24**, with outputs T_{xOPT} and T_{yOPT}, with −42 dB isolation at both outputs, maintaining the pass−band and stop−band characteristics of T_{x10}.

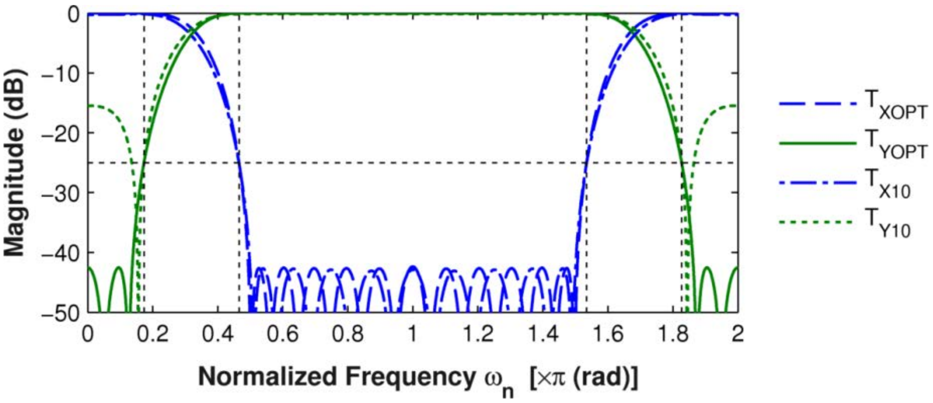

Fig. 3.24: Direct, T_{x10}, and crossed, T_{y10}, outputs of the birefringent filter designed in [47], M=14. Direct, T_{xOPT}, and crossed, T_{yOPT}, outputs of an optimized interleaver, M=20.

Add−drop filter designs based on infinite impulse response filters **[57]** are neither applicable to asymmetric interleaver applications, as they are symmetric and have intrinsically higher dispersion. The design method proposed in **section 3.4.4.2** is simple, fast and effective. This method, relaying on digital filter design algorithms, allows designing the stop−bandwidth and isolation of each interleaver output independently. This is a fundamental property in birefringent asymmetric interleaver synthesis. Further adjustments of specific parameters can be carried out in a second step by using genetic algorithms (GA) as described in **section 3.4.5**.

The results of **Fig. 3.21** to **Fig. 3.23** show that it is possible designing birefringent interleavers with an output with zero dispersion. For getting this, the equivalent FIR filter must have linear phase response. From (3.21), $H^M(z)$ and $H^M(z)^*$ are equal, therefore, in order to obtain a direct output with linear phase, $H^M(z)$ can be an odd or even order filter with symmetric coefficients (type I or II). On the other hand, $F^M(z)$ and $-F^M(z)^*$ are equal, therefore, in order to obtain a crossed output with linear phase, $F^M(z)$ must be an odd order filter with anti−symmetric coefficients (type IV). It is a difficult task designing both, $H^M(z)$ and its reciprocal $F^M(z)$, to be exactly linear phase filters; but the effects of dispersion can be reduced by using low order filters or by using an optimization process as the one proposed in **section 3.4.5**. Even previous designs with dispersion of ±50 ps/nm were claimed as linear phase filters **[58]**. Anyway, in those cases where asymmetric interleaver is used to increase network traffic adding high bit rate channels at 40 Gbit/s while keeping legacy 10 Gbit/s systems, higher bit rate channels can be located in the null CD penalty output. This solution avoids using complex configurations as those reported in **[46]**.

The proposed optimization process, based on GA, allows adjusting the interleaver response to desired values, as it is shown in **Fig. 3.22** and **Fig. 3.23** (first and second optimization examples, respectively). In the first optimization example, the pass−bandwidths and isolation are highly improved but the interleaver order and dispersion are increased to values below those reported in

[47], for the same isolation. In the second optimization example, the pass−bandwidth and isolation are also improved maintaining the interleaver order and slightly increasing its dispersion. The optimizations can be oriented to adjust specific parameters by using the appropriate objective function, as it is shown in **section 3.4.5.1** and **section 3.4.5.2**.

With the proposed optimization process, it is also possible reducing the interleaver's order to $M = 4$ by removing the constraint that $H^M(z)$ has to be a filter with exactly linear phase response. In this case, the resulting maximum dispersion is ±50 ps/nm (±4 normalized), at both outputs, and the other parameters are maintained with good performance (isolation of −25 dB over 30% *FSR* and 13% *FSR* at T_x and T_y, respectively).

The dispersion of the interleaver outputs is defined by the linearity of the FIR filter that represents each output. It increases when increasing the output's box−like **[41]** characteristics.

Resulting dispersion of all examples are better than those obtained with MZRRI configuration in the order of ±200 ps/nm at 1550nm without compensation **[46]**, or equivalent to previous linear phase designs in specific configurations **[58]**.

Genetic algorithm can also be used for tolerance analysis and design optimization based on fabrication tolerances.

3.5. Design of an Optimized Birefringent Interleaver for SI−POF WDM Networks

Optimized birefringent structures are a versatile solution for designing wavelength selective devices for SI−POF WDM networks due to their reconfiguration capacity, since they can be easily manufactured with LC technology, and flexibility, since any FIR filters synthesis method can be used [75]. Designs presented in the previous section were done for the 1550 nm transmission window, in order to directly compare the potential of the proposed synthesis method with similar ones. In this section we present the comparison between a Lyot, a Solc and an arbitrary birefringent filter (designed with the previous reported synthesis method) operating in the visible spectrum range. It is demonstrated that the utilization of arbitrary birefringent structures can highly improve the performance of the wavelength selective devices for SI−POF networks presented in this chapter.

3.5.1. Lyot, Solc and arbitrary birefringent filters performance

As mentioned at the beginning of this chapter, a Lyot filter consists of a set of delay stages composed by retarder plates of different widths between polarizers, as the 3−stage Lyot filter shown in **Fig. 3.25a**. The optical axes of the wave plates are placed at 45º with respect to the polarizers axes (azimuth angle) and each stage has twice the delay (Γ) of the previous one. Solc filters eliminate the need of Lyot filters for using multiple polarizers. Solc filters consist of a stack of M retarder plates between only two linear polarizers. In this case, all the retarder plates have the same delay and each one is at a specific azimuth angle α_1, ... α_M, e.g. a fan Solc filter has parallel polarizers ($\alpha_A = 0º$) and $\alpha_1 = \alpha$, $\alpha_2 = 3\alpha$, $\alpha_3 = 5\alpha$, ..., $\alpha_M = (2M-1)\alpha$, being $\alpha = 45º/M$, see **Fig. 3.25b**.

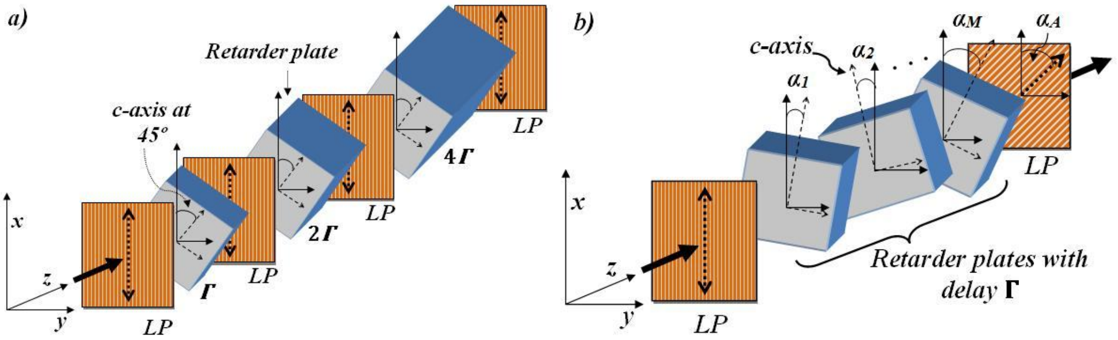

Fig. 3.25: General structures of: a) Lyot filter of 3 stages and b) Solc Filters.

Now, let us compare Lyot and Solc filters. For example, 3−stage Lyot filters require 4 polarizers and the equivalent of 7 retarder plates with delays Γ, as shown in **Fig. 3.25a**. In contrast, a Solc filter with the same number of retarder plates requires only 2 polarizers. From this point of view, Solc filters are a more interesting choice than Lyot filters. However, as shown in **Fig. 3.26**, the adjacent side lobes suppression is better for the case of Lyot filters.

However, the potential of the Solc filters structure can be exploited by placing the retarder plates illustrated in **Fig. 3.25b** at arbitrary azimuth angles, in a type of filters called lattice or birefringent filters. Birefringent filters can be designed by using optimization methods or in the Z−transform domain, by using their relation with FIR filters, as was discussed in the previous section (**section 3.4.4**). For example, an arbitrary birefringent filter of seven retarder plates, obtained from a seventh order FIR filter, is presented in **Fig. 3.26**. The azimuth angles of the retarder plates are: $\alpha_1 = 6.07º$, $\alpha_2 = 15.18º$, $\alpha_3 = 28.65º$, $\alpha_4 = 45.00º$, $\alpha_5 = 61.35º$, $\alpha_6 = 74.81º$, $\alpha_7 = 83.92º$ and $\alpha_A = 0º$. This filter performs a uniform suppression of the adjacent side lobes with a maximum value better than both the Lyot and Solc filters. It could even be designed to have a narrow bandpass.

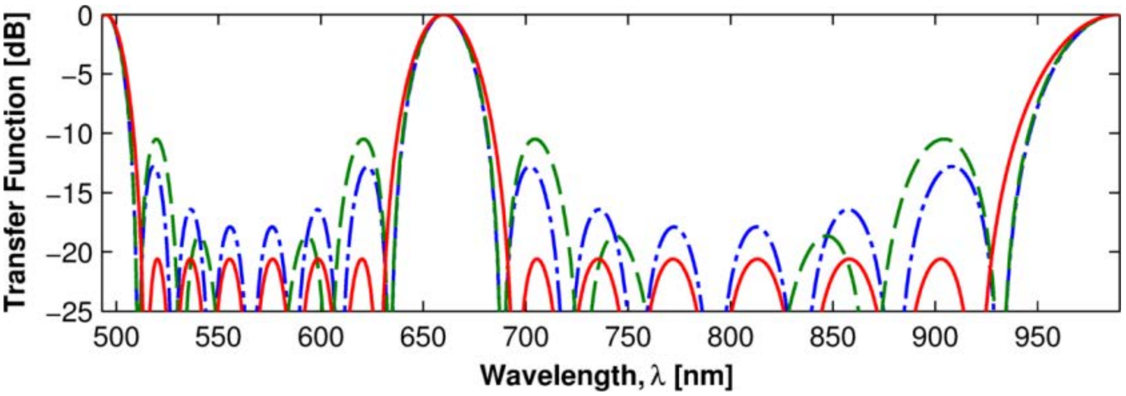

Fig. 3.26: Transfer functions of different birefringent filters: 3 stages Lyot Filter (dash−dot line), Solc filter with 7 retarder plates (dashed line) and arbitrary birefringent filter of 7 retarder plates designed in the Z−transform domain (solid line). Retarder plates with $\Gamma = 2\pi\times1.98\mu\mathrm{m}/\lambda$ are considered in all the filters.

3.5.2. Optimized VIS−interleaver performance

Comparison shown in **Fig. 3.26** demonstrates that arbitrary birefringent filters are a better design alternative than Lyot and Solc structures. Therefore, they are a good option to improve the performance of the proposed LCTF, presented in **section 3.2.3**. In the same way, arbitrary birefringent interleavers are an excellent option to improve the performance of the reconfigurable 1×2 R−WSS presented in **section 3.3**. This is shown with the following design example.

An optimized interleaver is designed by using the synthesis method proposed in **section 3.4.4**. An interleaver with symmetrical outputs, flattop pass−bands and isolation in the stop−bands lower than −15 dB is specified in the optimization process described in **section 3.4.5**. Then, the seventh order FIR filters $H_{VIS}(z) = 0.02408 - 0.10281\ z^{-1} + 0.089292\ z^{-2} + 0.48521\ z^{-3} + 0.48521\ z^{-4} + 0.089292\ z^{-5} - 0.10281\ z^{-6} + 0.02408\ z^{-7}$ and $F_{VIS}(z) = 0.35089 - 0.53005\ z^{-1} + 0.26081\ z^{-2} + 0.12052\ z^{-3} - 0.058093\ z^{-4} - 0.023598\ z^{-5} + 0.011622\ z^{-6} - 0.0016544\ z^{-7}$ are obtained. Those FIR filters are used to find the azimuth angles of the equivalent birefringent interleaver, with the recursive process shown in **section 3.4.4.1**, resulting in: $\alpha_1 = -86.07^\circ$, $\alpha_2 = -96.74^\circ$, $\alpha_3 = -101.40^\circ$, $\alpha_4 = -48.68^\circ$, $\alpha_5 = 4.02^\circ$, $\alpha_6 = 0.67^\circ$, $\alpha_7 = -11.34^\circ$ and $\alpha_A = -7.41^\circ$ (7 wave plates). The normalized response of $H_{VIS}(z)$ and $F_{VIS}(z)$ and the normalized response of the direct (T_{xVIS}) and cross (T_{yVIS}) outputs of the equivalent birefringent interleaver are shown in **Fig. 3.27**.

Now, in order to simulate the interleaver performance in the VIS range, HN cells of 1658 LC material and 3.05 μm thickness are considered. We must remember that small variations in thickness in practical cases can be corrected with the applied voltage. The LC birefringence in this simulation is modeled with the Cauchy model with $A_{eo} = 0.3103$, $B_{eo} = 0$ and $C_{eo} = 0.0063$. Those coefficients where obtained in the range from ~400 to 900 nm (see **section 2.5.3.4**).

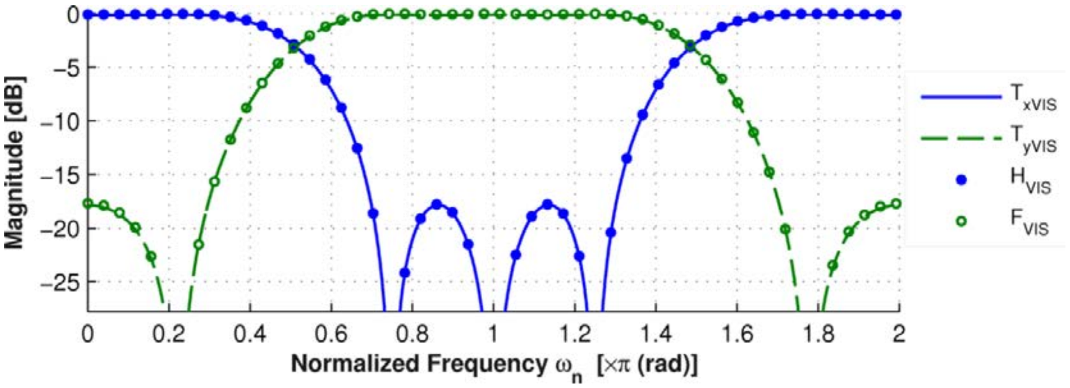

Fig. 3.27: Normalized response of the FIR filters $H_{VIS}(z)$ and $F_{VIS}(z)$ and normalized response of the direct (T_{xVIS}) and cross (T_{yVIS}) outputs of the equivalent birefringent interleaver.

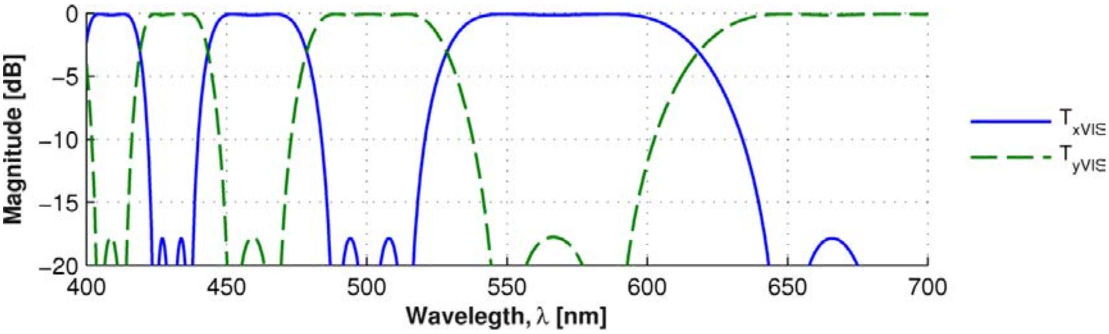

Fig. 3.28: Spectral response of the optimized birefringent interleaver in the VIS range, where T_{xVIS} and cross T_{yVIS} are the direct and cross outputs, respectively.

Fig. 3.28 shows the spectral response of the optimized birefringent interleaver in the VIS range. The response is flattop and the isolation is <−15 dB and uniform in both outputs. This interleaver was designed to split or combine common channels used in SI−POF WDM networks **[59]** (e.g. 410, 430, 470, 510, 590 and 650 nm). The tuning capacity that offer the LC variable wave plates (HN cells) allows an interesting reconfiguration capacity, as shown in the LCTF and the 1×2 R−WSS previously proposed in this chapter.

3.6. References

[1] A. Bhatnagar and W. Livingston, Fundamentals of Solar Astronomy, Singapore: World Scientific Publishing Company, 2005.

[2] L. Domash, E. Ma, N. Nemchuk and A. Payne, "Tunable thin film filters," *Optical Fiber Communications Conference,* vol. 2, pp. 23–28, 2003.

[3] J. Reichman, Handbook of optical filters for fluorescence microscopy, Brattleboro: Chroma Technology Corp., 1998.

[4] G. Agnelli, A. Cacciani and M. Fofi, "The Magneto–Optical Filter," *J. Solar Physics,* vol. 44, no. 2, pp. 509–518, 1975.

[5] N. Gat, "Imaging spectroscopy using tunable filters: a review," *Proc. SPIE* 4056*, Wavelet Applications VII,* p. 50, 2000.

[6] B. Lyot, "Optical Apparatus With Wide Field Using Interference of Polarized Light," *Compt. Rend. Acad. Sci. Paris.,* vol. 197, p. 1593, 1933.

[7] Y. Öhman, "A New Monochromator," *Nature,* vol. 141, pp. 157–158, 1938.

[8] I. Solc, "Birefringent Chain Filters," *Opt. Soc. America,* vol. 55, pp. 621–625, 1965.

[9] J. W. Evans, "Solc Birefringent Filter," *Opt. Soc. America,* vol. 48, pp. 142–143, 1958.

[10] K. Fredga and J. .. A. Högbam, "A Versatile Birefringent Filter," *Solar Physics,* vol. 20, pp. 204–227, 1971.

[11] J. W. Evans, "The Birefringent Filter," *J. Opt. Soc. America,* vol. 39, pp. 229–242, 1949.

[12] S. Micael, The sun: an introduction, Springer: Berlin, 2004.

[13] E. Wolf, Progress in Optics, Elsevier, 1971.

[14] S. J. Woltman, G. P. Crawford and G. D. Jay, Liquid Crystals: Frontiers in Biomedical Applications, Singapore: World Scientific Publishing, 2007.

[15] B. Wacogne, J. P. Goedgebuer, A. P. Onokhov and M. Tomilin, "Wavelength tuning of a semiconductor laser using nematic liquid crystals," *IEEE J. Quant. Electron.,* vol. 29, no. 4, pp. 1015–1017, 1993.

[16] R. Gree, C. Sarture, C. Chovit, J. Faust, P. Hajek and H. Novak, "AVIRIS: a New Approach to Earth Remote," *Opt. Photon. News,* vol. 6, pp. 30–33, 1995.

[17] Y. Konga, G. Yang and X. Huang, "Multiple–Stage Liquid Crystal Tuned Filter," *International Journal for Light and Electron Optics,* vol. 122, pp. 1723–1729, 2011.

[18] O. Aharon and I. Abdulhalim, "Liquid crystal Lyot tunable filter with extended free spectral range,," *Opt. Express ,* vol. 17, pp. 11426–11433, 2009.

[19] G. Yang, Z. Zheng, H. Li and X. Liu, "Method to Reduce Sidelobes of Multistage Lyot Filter," *Applied Optics,* vol. 49, no. 8, pp. 1280–1287, 2010.

[20] J. Beeckman, T. Hui and P. J. M. Vanbrabant, "Polarization Selective Wavelength Tunable Filter," *Molecular Crystals and Liquid Crystals,* vol. 502, no. 1, pp. 19–28, 2009.

[21] I. Thorlabs, January 2015. [Online]. Available: http://www.thorlabs.de/newgrouppage9.cfm?objectgroup_id=3488.

[22] O. Aharon and I. Abdulhalim, "Liquid crystal Lyot tunable filter with extended free spectral range," *Optics Express,* vol. 17, no. 14, pp. 11426–11433, 2009.

[23] S. Cao, J. Chen, J. N. Damask, C. Doerr, L. Guiziou, G. Harvey, Y. Hibino, H. Li, S. Suzuki, K.–Y. Wu and P. Xie, "Interleaver technology: comparisons and applications requirements," *J. Lightwave Technol.,* vol. 22, pp. 281–289, 2004.

[24] M. F. Huang, J. Chen, J. Yu, S. Chi and G. K. Chang, "A Novel Dispersion–Free Interleaver for Bidirectional DWDM Transmission Systems," *J. Lightwave Technol.,* vol. 25, pp. 3543–3554, 2007.

[25] C. Lee, R. Wang, P. Yeh and W. Cheng, "A New Scheme of Birefringent Optical Interleaver Employing Ring Cavity as Phase–Dispersion Element," *Conference and Photonic Applications Systems Technologies, OSA Technical Digest Series (CD) (Optical Society of America,* 2007*),* p. JTuA, 2007.

[26] D. M. Marom, D. T. Neilson, D. S. Greywall, C. S. Pai, N. R. Basavanhally, V. A. Aksyuk, D. O. López and F. Pardo, "Wavelength–selective 1 x K switches using free–space optics and MEMS micromirrors: theory, design, and implementation," *J. Lightwave Technol,* vol. 23, p. 1620–1630, 2005.

[27] J. S. Patel and Y. Silberberg, "Liquid Crystal and Grating–Based Multiple–Wavelength Cross–Connect Switch," *IEEE Photonic Tech. L.,* vol. 7, p. 514–516, 1995.

[28] B. Fracasso, J. L. de Bougrenet de la Tocnaye, M. Razzak and C. Uche, "Design and performance of a versatile holographic liquid crystal wavelength selective optical switch," *J. Lightwave Technol.,* vol. 21, p. 2405–2411, 2003.

[29] C. Vázquez, I. Pérez, P. Contreras, B. Vinouze and B. Fracasso, "Liquid Crystal Optical Switches," in *Optical Switches – Materials and Design, B. Li, S. J. Chua, eds.*, Cambridge, Woodhead Publishing, 2010, Chap. 9.

[30] K. K. Suzuki, T. Mizuno, M. Oguma, T. Shibata, H. Takahashi, Y. Hibino and A. Himeno, "Low loss fully reconfigurable wavelength–selective optical 1xN switch based on transversal filter configuration using silica–based planar lightwave circuit," *IEEE Photonic Tech. L.,* vol.

16, pp. 1480–1482, 2004.

[31] C. V z quez, P. C. P. C. Lallana, J. Montalvo, J. M. Sanchez Pena, A. d'Alessandro and D. Donisi, "Switches and tunable filters based on ring resonators and liquid crystals," *Proc. SPIE* 6593*,* p. 34, 2005.

[32] K. K. Vlachos, C. Raffaelli, S. Aleksic, N. Andriolli, D. Apostolopoulos, H. Avramopoulos, D. Erasme, D. Klonidis, M. N. Petersen, M. Scaffardi, K. Schulze, M. Spiropoulou, S. Sygletos, I. Tomkos, C. Vázquez, O. Zouraraki and F. Neri, "Photonics in switching: enabling technologies and subsystem design," *J. Opt. Netw.,* vol. 8, pp. 404–428, 2009.

[33] P. C. Lallana, C. Vázquez and B. Vinouze, "Advanced multifunctional optical switch for multimode optical fiber networks," *Optics Communications,* vol. 285, pp. 2802–2808, 2012.

[34] J. Li, C.–H. Wen, S. Gauza, R. Lu and S.–T. Wu, "Refractive indices of liquid crystals for display applications," *Journal of Display Technology,* vol. 1, no. 1, pp. 51–56, 2005.

[35] M. Polyanskiy, "Refractive Index Database," [Online]. Available: http://refractiveindex.info/?group=LC&material=MLC–9200–100. [Accessed 16 February 2015].

[36] P. J. Pinzón, I. Pérez, V. Urruchi, C. Vázquez and J. M. Sanchez–Pena, "Tunable Optical Filter using High Birefringence Nematic Liquid Crystals," in *OPTOEL*, Santander, 2011.

[37] O. Ziemann, J. Krauser, P. E. Zamzow and D. W. , POF Handbook: Optical Short Range Transmission Systems, 2nd ed, Singapore: Springe, 2008.

[38] Throlabs, December 2014. [Online]. Available: http://www.thorlabs.de/newgrouppage9.cfm?objectgroup_id=5510.

[39] X. Yang and J. Zhang, "Optimum Design of Asymmetric Birefringent Interleaver Based on FIR Digital Filter Design Technique," *Microwave Conference,* pp. 595–598, 10–12 Sept 2008.

[40] H. Lu, K. Wu, Y. Wei, B. Zhang and G. Luo, "Study of all–asymmetric interleaver based on two–stage cascaded Mach–Zehnder interferometer," *Optics Communications,* vol. 285, pp. 1118–1122, 2011.

[41] T. Chiba, "Waveguide interleaving filters," *Proc. SPIE*5246*,* p. 532–538, 2003.

[42] B. B. Dingel, "Recent development of novel optical interleaver: performance and potential," *Proc. SPIE*5246*,* pp. 570–581, 2003.

[43] C. Lee, R. R. Wang, P. Yeh and W. Cheng, "A New Scheme of Birefringent Optical Interleaver Employing Ring Cavity as Phase–Dispersion Element," *in Conference on Lasers and Electro–Optics/Quantum Electronics and Laser Science Conference and Photonic Applications Systems Technologies, OSA Technical Digest Series (CD) (Optical Society of America,* 2007*),* paper JTuA30.

[44] S. A. Alboon and R. G. Lindquist, "Flat–top / distortionless tunable filters based on liquid crystal multi cavities for DWDM applications," *Southeastcon,* 2008. *IEEE,* pp. 117–122, 2008.

[45] W. Li, Q. Guo and S. Gu, "Interleaver technology review," *Proc. SPIE*4906*,* p. 73–80, 2002.

[46] Y. Zhang, W. Huang, X. Wang, H. Xu and Z. Cai, "High–Extinction–Ratio Multipassband Filter With Flat–Top and Low–Dispersion," *IEEE Journal of Quantum Electronics,* vol. 46, pp. 860–870, 2010.

[47] R. H. Chu and G. Town, "Birefringent filter synthesis by use of a digital filter design algorithm," *Appl. Opt.,* vol. 41, p. 2002, 3412–3418.

[48] R. M. de Ridder and C. G. H. Roeloffzen, "Interleavers," in *Wavelength Filters for Fibre Optics*, vol. 123, H. Venghaus, Ed., Singapore, Springer, 2006, pp. 381–432.

[49] Q. Wang and S. He, "Optimal design of a flat–top interleaver based on cascaded M–Z interferometers by using a genetic algorithm," *Opt. Commun.,* vol. 224, pp. 229–236, 2003.

[50] K. Jinguji and M. Kawachi, "Synthesis of coherent two–port lattice–form optical delay–line circuit," *J. Lightw. Technol.,* vol. 13, pp. 73–82, 1995.

[51] S. E. Vargas, Contribución al Diseño de Filtros Ópticos para Redes con Multiplexación en Longitud de Onda, Leganés: Universidad Carlos III de Madrid, Escuela Politécnica Superior, 2003.

[52] MatWorks, "Parks–McClellan optimal FIR filter design," 2012. [Online]. Available: http://www.mathworks.es/help/toolbox/signal/ref/firpm.html. [Accessed 1 Junio 2014].

[53] Optoplex, "Asymmetric Optical Interleaver," 2011. [Online]. Available: http://www.optoplex.com/Asymmetric_Interleaver.htm. [Accessed 1 Junio 2014].

[54] C. K. Madsen and J. H. Zhao, Optical Filter Design and Analysis: A Signal Processing Approach, Wiley, 1999.

[55] MatWorks, "Global Optimization Toolbox," 2012. [Online]. Available: http://www.mathworks.com/products/datasheets/pdf/global–optimization–toolbox.pdf. [Accessed 1 Junio 2014].

[56] L. Rosa, K. Saitoh, K. Kakihara and M. Koshiba, "Genetic–Algorithm Assisted Design of C–Band CROW–Miniaturized PCW Interleaver," *J. Lightwave Technol.,* vol. 27, pp. 2678–2687, 2009.

[57] O. S. Ahmed, M. A. Swillam, M. H. Bakr and X. Li, "Efficient design optimization of ring resonator–based optical filters," *J. Lightwave Technol.,* vol. 29, pp. 2812–2817, 2011.

[58] Q. J. Wang, Y. Zhang and C. Y. Soh, "Design of linear–phase two–port optical interleavers using lattice architectures," *Opt. Lett.,* vol. 31, pp. 2411–2413, 2006.

[59] M. Joncic, M. Haupt and U. H. P. Fischer, "Spectral Grids for VIS WDM Applications over SI–POF," *POF Conference,* pp. STD–130, 2011.

Chapter IV:

Reconfigurable LC Optical Routers

In this chapter the design and experimental characterization of two new proposals for 1×2 reconfigurable LC optical routers (LC–ORs) are presented. Both LC−ORs are based on LC polarization rotators (PRs) and have been designed to work in SI–POF WDM networks. The first LC–OR proposal allows blocking or redirecting the input light beam through only one or through the two output ports simultaneously, with the possibility of controlling the optical power level at each output. In order to maintain constant the output power level, output power is monitored and a feedback control loop adjusts the LC cells attenuation. Power stabilization can be required, among others, to prevent damages to the optical receivers caused by irregular optical power variations and to maintain the optical power between the eye–safety limits, specially, in In−Home and Office networks. The second LC–OR is a novel proposal based on an achromatic LC PR. This router can work in the spectral range used in SI–POF networks (400 to 700 nm) with low wavelength and temperature dependences. The achromatic PR design is done with a new synthesis method, which is effective, fast and simple and has good agreement with experimental results. Performance improvement with respect to previously reported devices with similar structure have also been analyzed. To our knowledge, this is the first reported LC–OR that can redirects uniformly a wide spectrum input beam (300nm).

4.1. Introduction

Nowadays, optical routers are key components in optical communications and sensor networks. They allow optical routing without converting the transmitted information into the electrical domain. The elimination of the two required conversions (optical to electrical and electrical to optical) improves the system performance, reducing the network equipment and increasing its bandwidth. These devices work by selectively routing optical signals delivered through one or more input ports to one or more output ports, in response to supervisory control signals. Different technologies could be applied to route optical signals, applications of which depend on the topology of the optical network and the switching speed required **[1]**. Cutting–edge optical routing technologies include micro–electromechanical systems (MEMS) as well as acousto–optical, thermo–optical, opto–optical and electro–optical (EO) devices.

Opto–mechanical switches are based on the movement of some mechanical devices such as prisms, mirrors or directional couplers. As a subsection of the opto–mechanical technology, MEMS have a great interest in telecommunications applications. MEMS consist of small mobile refractive surface mirrors that route the incident light beams to their destination **[2]**, **[3]**.

Acousto–optic switches are based on the acousto–optic effect of some materials, such as the paratellurite (TeO2) **[4]** and the lithium niobate LiNbO3 **[5]**. An acoustic wave travelling along the material induces a periodical strain that alters its refractive index. The refractive index modulation induced in the material causes a dynamic phase grating than can diffract light. If the material is isotropic, the diffraction induced by the acousto–optic effect causes beam deflection, and if the material is anisotropic the deflection caused comes along with variation in light polarization.

Other solutions include the thermo–optic switches whose operation is based on the variation of the refractive index of the material by modifying its temperature. This type of switches has a great variety of implementations, but they are mainly based on using an interferometric mechanism in which the refractive index variation induces a change in the interference condition. This effect facilitates the light switching **[6]**, **[7]**.

Opto–optical switches are based on the intensity–dependent nonlinear effects in optical waveguides, such as the two–photon absorption phenomenon (TPA) **[8]**, the lightwave self action that induces the self phase modulation (SPM) phenomenon and the Kerr effect that causes the four wave mixing (FWM) and the cross phase modulation (XPM) **[9]**.

Finally, electro–optic switches perform switching by using electro–optics effects. The main technologies are based on Lithium Niobate (LiNbO3) **[10]**, semiconductor optical amplifiers (SOA)

[11], electro–holographic (EH) **[12]**, Bragg gratings electronically switched **[13]** and liquid crystals.

SI–POF technology presents special constrains in the design of any optical communication device (filters, interleavers, multiplexers, demultiplexers and routers). Especially due to its large physical dimensions and *NA*, and the large spectral bandwidth used in WDM applications (400 to 700 nm). For this reason, not all the previous mentioned switching technologies could be applied in the VIS range for SI–POF applications.

LC technology is an excellent option for implementing optical devices for SI–POF applications, as is discussed in previous chapters. This routing technology has been widely applied in the IR range for silica optical fiber based networks and some applications have been demonstrated in the VIS range for SI–POF. In the following, a brief introduction to the LC optical routers is presented.

4.2. Liquid Crystal Optical Routers

Liquid Crystal Optical Routers use different physical mechanisms to steer the light such as polarization management, reflection, wave–guiding and beam–steering (2D or 3D). However, most LC–ORs are based on polarization modulation using nematic LC cells in combination with polarization selective calcite crystals (PBS) to steer the light **[14]**, **[15]**, **[16]**, **[17]**, **[18]**. Main advantages of LC technology include no need of moving parts for routing reconfiguration, low driving voltage and low power consumption. But, the response time of nematic LC devices is usually in the order of several milliseconds, so they are ideal for protection and recovery applications and optical add/drop multiplexing, which demand fewer restrictions on routing time. However, in the last years, nematic LC cells with response times lower than 3 ms **[19]** and 2 ms **[20]**, as well as nanosecond response **[21]** and different techniques to reduce the response time below 1 ms **[22]** have been reported. On the other hand, ferro−electric (FE) LC offers response times in the order of micro−seconds but their operation is limited to the on/off states (bistable) **[23]**, **[24]**.

Usually, and especially in applications where channel equalization is needed, LC–ORs use twisted nematic LC cells, acting as polarization rotators with a continuous operation mode (intermediate transmission levels) **[16]**, **[25]**. Then, these routers can also operate as variable optical attenuators (VOAs) by splitting the input signals at the outputs with a variable ratio depending on the applied voltage **[17]**, **[18]**, **[19]**, **[20]**, **[21]**.

The basic structure of a 1×2 router based on TN cells is presented in **Fig. 4.1** **[26]**. In this device, the light from the input port (Port 1) passes through the input polarizer (LP) and then is guided to one of its output ports (Port 2 or Port 3) depending on the voltage applied to the TN cell.

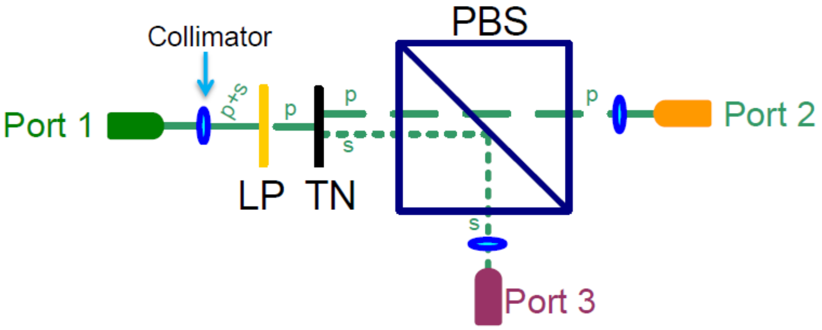

Fig. 4.1: Basic structure of a 1×2 LC optical router.

As a consequence of the use of an input polarizer, half of the incoming optical power is filtered. The solution for reducing the insertion losses of the optical switch based on TN cells is by using the polarization diversity method. In this technique, the input beam is decomposed into its TE (*s*–polarized light) and TM (*p*–polarized light) components. Both components are treated separately and finally recombined. In this way, the device becomes polarization insensitive, and less insertion losses are expected, as in the polarization insensitive 2×2 optical switch based on TN cells presented in **[27]**. The same principle, as well as the polarization converter device shown in appendix B, can be applied to the designs reported in this chapter.

Then, typical low response time and high insertion losses issues of LC–ORs can be easily overcome. Moreover, their advantages and functionality has been wide demonstrated, especially in silica optical fiber based networks.

In the following two new 1×2 LC–OR are presented. Those devices are especially designed to work in SI–POF based networks and include novel features.

4.3. Reconfigurable LC–OR with Output Power Level Control

In this section, the structure of a new reconfigurable 1×2 LC–OR based on two TN devices and a PBS is presented and experimentally tested. This router allows blocking or redirecting the input light beam either to only one of the output ports or to both output ports simultaneously, with the possibility to stabilize the power levels of the outputs independently. Those features can be required, among others, to prevent damages to the optical receivers caused by irregular optical power variations and to maintain the optical power between the eye safe limits, specially, in In−Home and Office networks. As the optical input power fluctuates, the output power is monitored and a feedback control loop adjusts the TN cells transmittance and maintains the output power level at a relatively constant level. This configuration and its performance have been reported in **[25]**.

The schematic design of the router is shown in **Fig. 4.2**. A light emitting diode (LED) is used as input light source. The input and output ports are made of SI–POF, including lenses to collimate the input light and to focus the output light beams. A PBS is placed at the input port to divide the non–polarized input beam into two orthogonal components: one component is transmitted with *p*–polarization and the other is reflected 90º with *s*–polarization. In each output of the PBS a TN cell, sandwiched between crossed polarizers, is located to provide the routing function and power control of the output light beam. The system also includes an electronic block to control the router's operation through two independent voltages: V_{LC1}, control voltage of LC cell 1 (LC_1) and V_{LC2}, control voltage of LC cell 2 (LC_2).

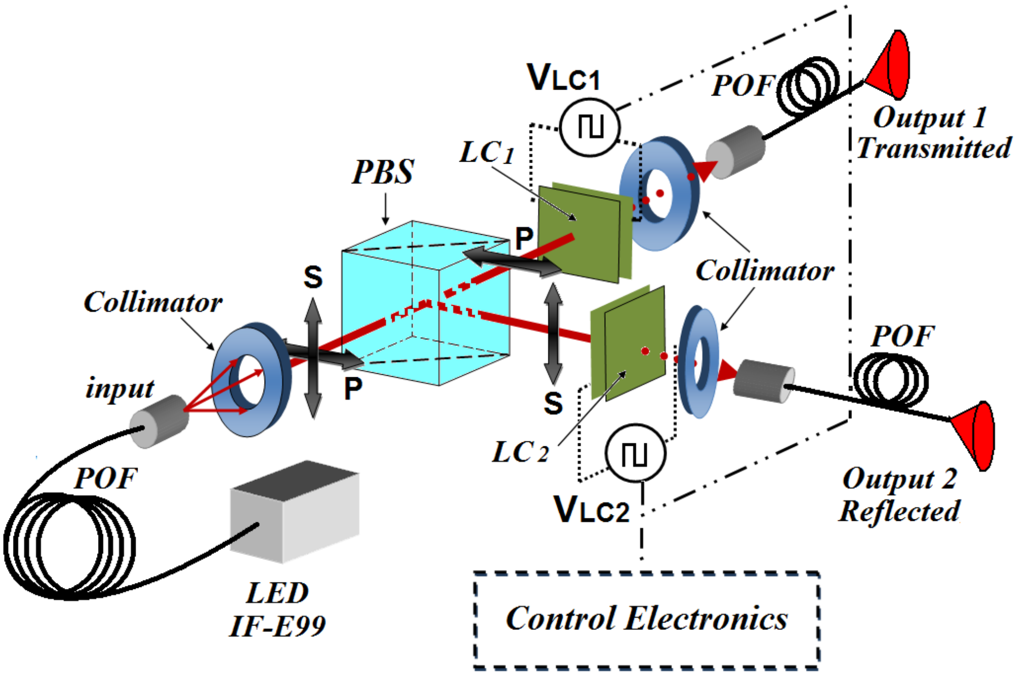

Fig. 4.2: Structure of the proposed reconfigurable 1×2 LC–OR with output power level control.

Next, a brief description of the router components is presented:

- The LED used is the IF–E99. This high speed red LED, housed in a connector less style plastic fiber optic package, has its output spectrum peak at a wavelength of 650 nm with a full width half maximum, FWHM, of 10 nm. The device package is optimized with internal micro lens to couple into standard 1 mm core SI–POF.
- The SI–POF at the input and output ports is the POF HFBR–E889 328–C, this fiber has a 1 mm core, its numerical aperture is ~0.47 and its losses are about 0.22 dB/m at 650 nm. The

input lens is biconvex with a diameter of 25.5 mm and focal length of 25 mm, while the lenses at the output ports are plano–convex with diameter of 25.5 mm and focal length of 20 mm. Both outputs are positioned at the same distance from the light source (each router arm has the same length).

- The PBS used in the assembly is from the BPS0402 series, with dimensions of 20×20×20 mm, it has a wavelength range of operation from 650 to 850 nm and presents a transmittance of the *p*–polarized component, T_P, higher than 95%, and a reflectance of the *s*–polarized component, R_S, higher than 95%. The split ratio, T_P/R_S, is 50/50 ±5% for random polarized light.
- TN cells are placed between crossed polarizers. When the voltage applied to the TN cells is less than threshold voltage, V_{th}, the device rotates the linear polarized light, which passes through the input polarizer, 90º so it is transmitted through the analyzer (maximum optical transmission). On the other hand, if the voltage applied is much higher than threshold, the input light polarization is not rotated; therefore it is blocked by the analyzer (minimum optical transmission). The TN devices are oriented so that incident polarized light component has the maximum optical transmission through the input polarizer. It is important to note that the light coming from the PBS is linear polarized, so the input polarizer of each cell in not necessary in a final application.
- The control electronics provides the V_{LC1} and V_{LC2} signals which define the router operation mode. These signals are 1 kHz square waveforms with root mean square (V_{RMS}) values between 0 and 4. The control signals are generated by a digital–analog converter DAC0800 working in a basic bipolar output configuration. The voltage values and the 1 kHz frequency generated by the DAC are achieved by controlling the input binary data using a FPGA (Field Programmable Gate Array).

4.3.1. Router Operation and Performance

The input beam has a random polarization which is split into two orthogonal components by the PBS, which are referred as the transmitted and the reflected components with *p* and *s* polarization states, respectively. Each component goes to a TN cell with the input polarizer oriented in the same direction that the incoming light. System operation is based on controlling the optical power in output 1 and output 2 through the independent variation of the control signals, V_{LC1} and V_{LC2}, applied to each LC cell. Control electronics, which provides the control signals, allows four basic routing modes, as shown in **Fig. 4.3**, with the possibility of intermediate transmission values (between maximum and minimum transmission).

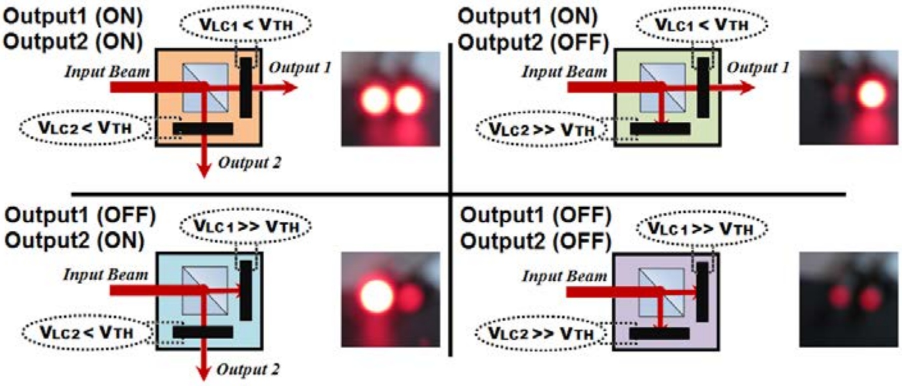

Fig. 4.3: 1×2 optical router working modes.

Optical power has been measured by using an optical power meter. In order to get a LED characterization, the optical power is measured at the LED's output (router input). The optical power is also measured on the output 1, without the light passing through the router (only by collimators and air) to know the free–space and fiber–to–fiber coupling losses (coupling *IL*). These results are presented on **Fig. 4.4** and show that the coupling *IL* are about 9.3 dB. It is important to note that these losses can be reduced to values lower than 1 dB using optimized coupling optics, as can be shown in **Chapter 5**.

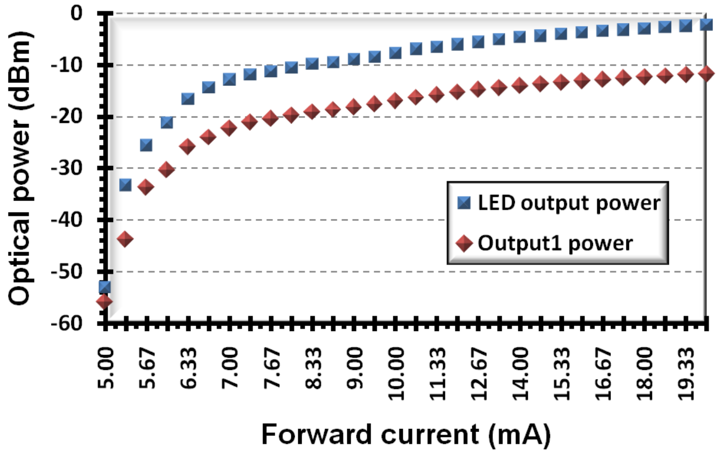

Fig. 4.4: LED optical power as a function of forward current measurements at the LED output and at the output 1, without passing the light through the router.

On the other hand, to analyze the LC–OR performance, next nomenclature is used:

- P_{OUT}(ON): output power of an output port in the ON state (maximum optical transmission), $V_{LC} < 1.5V_{RMS}$.
- P_{OUT}(OFF): output power of an output port in the OFF state (minimum optical transmission), $V_{LC} > 4V_{RMS}$.
- P_{IN}: incident input power (LED IF–E99 beam), without passing through the optical router (only by collimators and air).

A brief resume of the system performance is show in **Table 4.1**, where *IL* are the optical losses in decibels that include the losses of the PBS (L_{PBS}) and the losses of the LC (L_{LC}), $IL = L_{PBS} + L_{LC}$. The measured L_{PBS} is 3.65 dB and 3.27 dB for the transmitted and reflected component, respectively. For non polarized light L_{LC} is about 5.91 dB. On the other hand, for polarized light L_{LC} depends essentially of the quality of LC polarizers, and the orientation of the entrance polarizer with respect to the incident beam. In the measurements reported on **Table 4.1**, the L_{LC} is about 2.9 dB for the polarized light coming from the PBS. Therefore, the router *IL* can be reduced by improving the alignment of the input polarizer of the LC cells and the polarization direction of the beam transmitted or reflected by PBS, using polarizers with antireflection coatings at the operating wavelength or by eliminating the input polarizer of the LC cells.

TABLE 4.1. MAIN PARAMETERS OF THE PROPOSED 1×2 OPTICAL ROUTER WITH OUTPUT POWER CONTROL LEVEL.

Parameter	**Definition**	**Measured Value**	
		***Output* 1**	***Output* 2**
Insertion Loss (*IL*)	$IL = -10\log\left(\frac{P_{OUT(ON)}}{P_{IN}}\right)$	6.39 dB	6.40 dB
Rejection Ratio (*RR*)	$RR = 10\log\left(\frac{P_{OUT(ON)}}{P_{OUT(OFF)}}\right)$	26.41 dB	25.13 dB
Crosstalk Attenuation (*CTA*)	$CTA = 10\log\left(\frac{P_{OUT(OFF)}}{P_{IN}}\right)$	−32.80 dB	−31.53 dB

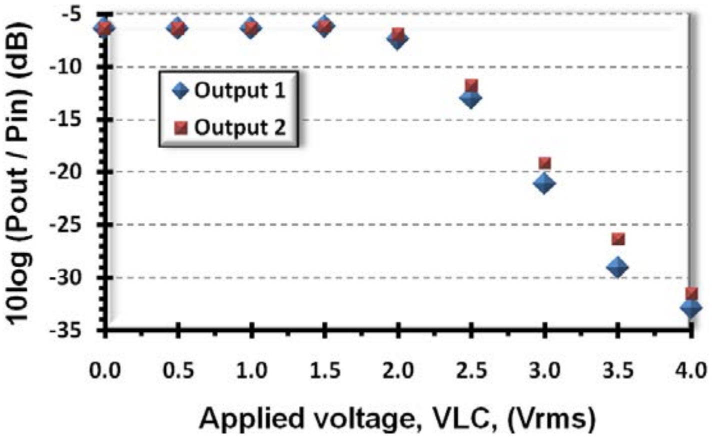

Fig. 4.5: Insertion losses for the outputs 1 and 2 as a function the applied voltage to LC cell.

Fig. 4.5 shows the insertion losses of output 1 and output 2 as a function of voltage applied to the LC devices. These experimental results show the symmetry of the two output ports. Finally, switching time has also been measured, as the time elapsed from activating the switching command to the moment the *IL* of the switch path achieves the 90% of its final value. The average value has been 15 ms.

4.3.2. Output Power Level Control

This configuration allows stabilizing the optical output power by using a scheme like the implemented in this work, see **Fig. 4.6**.

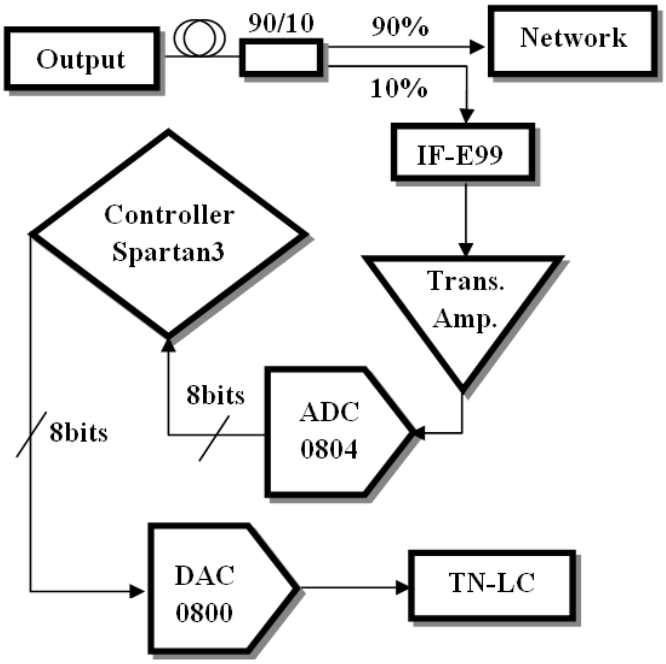

Fig. 4.6: Schematic diagram of the powerr stabilization system.

At each router output, a 90/10 splitter is used to transmit and to analyze the output power. A 10% of the optical signal is directed to an IF–D93 photodarlington detector connected to a trans–impedance amplifier to perform optical to electrical conversion. The resulting voltage level is converted to binary information by an analog–digital converter (ADC) and it is sent to a FPGA, which controls the system. The FPGA generates an output signal, S_{LC}, of 8 bits and switches its value between S_{LC} and not(S_{LC}) at a frequency of 1 kHz with an encoding that allows to the digital–analog converter (DAC), operating at bipolar mode, generating the appropriate control signal to stabilize the output power switch.

Fig. 4.7 shows the optical power stabilization on the output 1, in the face of variations on the optical input power. Additionally, it also shows the direct variation of the optical power on the output 2, without stabilization, as result of the same input variations. The output power can be stabilized to a value, P_{ES}, in a range that depends on the following parameters: minimum input power, P_{MIN}, and maximum power, P_{MAX}, of the system, rejection ratio, *RR*, and insertion loss, *IL*, so that $P_{MAX} - IL - RR < P_{ES} < P_{MIN} - IL$.

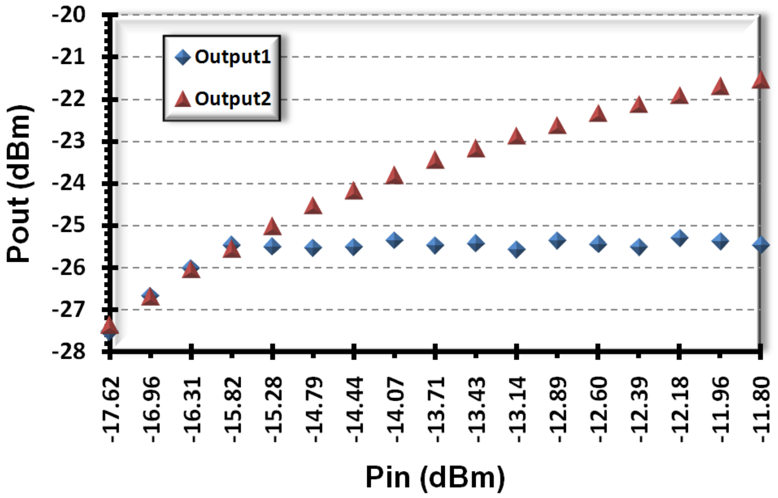

Fig. 4.7: Output power as a function of the input power for the outputs 1 and 2, with the output1 stabilized to –25.7dBm and without stabilization at the output 2.

4.3.3. Discussion and Remarks

In this section, a reconfigurable 1×2 optical router has been designed and experimentally tested. The router allows blocking or redirecting the input light beam either to only one of the output ports or to both output ports simultaneously. The router has about 6.4 dB insertion loss, 26 dB rejection ratio, –32 dB crosstalk attenuation and 15 ms switching time. Insertion losses can be improved to levels of less than 5 dB eliminating the input polarizer of the TN cells (since the light coming from the PBS is polarized).

Additionally, a control of the optical power level at each output has also been carried out to prevent damages to the optical receivers caused by irregular input power variations or to keep the optical power inside eye–safety limits. As the optical input power fluctuates, the output power is monitored and a feedback control loop adjusts the attenuation and maintains the output power level at a relatively constant level.

The independent operation of both outputs and the output power level control, are novel features of this type of optical routes. This router may be used in applications like SI–POF local area networks for allowing redundant paths or reconfigurable multicasting in access networks.

4.4. Design of a Novel Broadband LC–OR with Low Thermal Dependence

It is a matter of fact that the performance of a TN based LC–OR is optimum only for specific wavelengths (those given by Mauguin Minima) **[28]**. Besides, the LC birefringence, which defines Mauguin Minima, is very temperature dependent **[26]**, requiring temperature compensated designs or controllers. These are important limitations even in the most recent published LC devices **[29]**. These two drawbacks can be overcome by replacing the TN cells (see **Fig. 4.1** and **Fig. 4.2**) with optimized polarization rotators (PRs) based on structures of stacked LC cells, as we have reported in **[30]**.

The second LC–OR design presented in this chapter is a novel and very useful configuration specially designed to work in SI–POF networks with WDM. It is a broadband LC–OR with low thermal dependence based on an achromatic PR. The PR design is done using three nematic LC cells with a synthesis method based on a new optimization approach, in order to have optimum response across the 400 to 700 nm spectrum. The router performance, measured in terms of insertion loss and crosstalk uniformity, is experimentally tested in the range from 400 to 700 nm and it is compared against the performance of a router based on a single TN cell. It is also demonstrated, by simulation results, that the proposed broadband router allows splitting the input signal between the outputs ports with adjustable split ratio and low wavelength dependence, and that it offers a very low dependence with the temperature in a broadband range thanks to its spectral uniformity.

4.4.1. Polarization Rotators

PRs modify the orientation of a linear polarized beam in a specific angle, e.g. from being *x*–polarized to be *y*–polarized. The most common PR scheme consists of a single TN cell as the used in the previous section, while achromatic or broadband designs include TN cells, retardation plates and/or homogenous nematic LC (HN) cells **[31]**, **[32]**, **[33]**, **[34]**, **[35]**. The synthesis of PR presented in this section is done using the Jones formalism presented in **Chapter 2**. In the following, the most relevant information used for modelling TN and HN cells is presented.

4.4.1.1. HN and TN cells Modelling

The operation of a nematic LC cell is based on the optical birefringence, Δn, between the fast and slow axes of its molecules (slow axis is called *c*–axis). A HN cell, with thickness d_H and birefringence Δn_H, produces a phase delay between the polarization components of a light beam, with wavelength λ, that is given by:

$$\Gamma_H = 2\pi \frac{\Delta n_H d_H}{\lambda} \tag{4.1}$$

hereinafter, the sub index H can be replaced by T, in order to refer to a TN cell.

The birefringence wavelength dependence, $\Delta n(\lambda)$, is a very important parameter for designing broadband devices with stacked structures **[32]**, **[36]**. In this work, $\Delta n(\lambda)$ is represented with the extended Cauchy model **[37]**, which is expressed as:

$$\Delta n(\lambda) = A_{eo} + \frac{B_{eo}}{\lambda^2} + \frac{C_{eo}}{\lambda^4} \qquad (4.2)$$

where A_{eo}, B_{eo} and C_{eo} are the differences between the extraordinary and ordinary Cauchy coefficients $A_e - A_o$, $B_e - B_o$ and $C_e - C_o$, respectively.

The LC *c*–axis angle with respect to the cell surface is defined as the tilt angle, θ. Without applied voltage, HN and TN cells have $\theta \cong 0^{\circ}$ (usually a pre–tilt angle is added). In a HN cell the front and rear molecules have the same orientation angle, while in a TN cell (there is a twist angle, ϕ_T, between them. Therefore, HN cells are a particular case of TN cells without twist angle, and their Jones representation **[28]** is given by the transfer matrix:

$$W_H(\alpha_H) = R^{-1}(\alpha_H) \times \begin{bmatrix} e^{-i\frac{\Gamma_H}{2}} & 0 \\ 0 & e^{i\frac{\Gamma_H}{2}} \end{bmatrix} \times R(\alpha_H) \qquad (4.3)$$

where $R(\alpha_H)$ is the rotation matrix of the *c*–axis orientation angle (α_H) respect to the *x*–axis given by:

$$R(\alpha) = \begin{pmatrix} \cos\alpha & \sin\alpha \\ -\sin\alpha & \cos\alpha \end{pmatrix} \qquad (4.4)$$

On the other hand, the Jones of a TN cell **[28]**, with its front *c*–axis oriented at an azimuth angle α_T and with a total twist ϕ_T, is given by the transfer matrix:

$$W_T(\alpha_T) = R^{-1}(\alpha_T) \times \begin{bmatrix} \cos(\phi_T) & -\sin(\phi_T) \\ \sin(\phi_T) & \cos(\phi_T) \end{bmatrix} \times \begin{bmatrix} \cos(X) - i\frac{\Gamma_T}{2}\frac{\sin(X)}{X} & \phi_T \frac{\sin(X)}{X} \\ -\phi_T \frac{\sin(X)}{X} & \cos(X) + i\frac{\Gamma_T}{2}\frac{\sin(X)}{X} \end{bmatrix} \times R(\alpha_T) \qquad (4.5)$$

where $X = \left(\phi_T^{\,2} + \Gamma_T^{\,2}/4\right)^{1/2}$ and Γ_T is the phase delay of a TN cell with thickness d_T. It is important to note that the elements {1,1} and {2,1} of (4.3) and (4.5) refer to the output light polarized at 0° to the *x*–axis (T_x) and at 90° to the *x*–axis (T_y), respectively, when the input beam is *x*–polarized.

Section 2.3 shows more information about the optical modeling of HN and TN cells using Jones Matrices.

4.4.1.2. Single TN cell based PR

A TN based PR consists of a TN cell bounded between linear polarizers, LPs, parallels to the LC front and rear *c*–axes. Most common design uses a TN cell with 90° twist, e.g., assuming $\alpha_T = 0^{\circ}$, input and output LPs are parallel to the *x*–axis and *y*–axis, respectively (crossed LPs). In this configuration with no applied voltage (*V*), an input *x*–polarized beam is transmitted with *y*–polarization direction, according to:

$$T_y = \cos(\mathrm{B})^2 + \left(\frac{\Gamma_T}{2}\frac{\sin(\mathrm{B})}{\mathrm{B}}\right)^2 \tag{4.6}$$

with $\mathrm{B} = [(\pi/2)^2 + (\Gamma_T/2)^2]^{1/2}$. T_y from (4.6) presents periodic peaks at the Mauguin minima, given by:

$$\frac{\Delta n_T d_T}{\lambda} = \frac{1}{2}\sqrt{4N^2 - 1} \quad with \quad N = 1, 2, ... \tag{4.7}$$

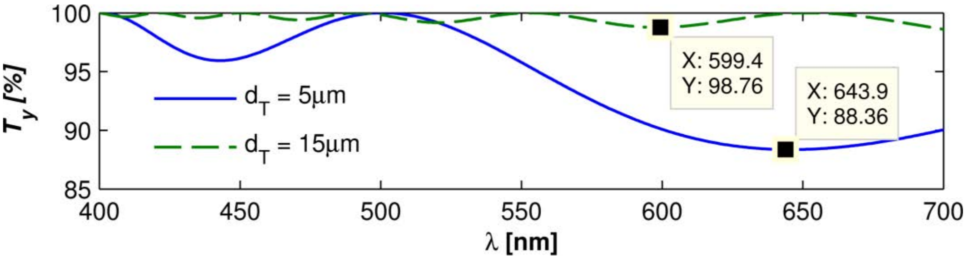

Fig. 4.8: Transmittance of a PR based on a TN cell of 5CB material with d_T = 5μm and 15μm.

Fig. 4.8 shows the transmittance or rotation efficiency, T_y, in the range from 400 to 700 nm of two PRs, based on 5 μm and 15 μm thickness TN cells filled with commercial 5CB material. The 5 μm TN cell based PR has $T_y \geq 88\%$. The efficiency is improved to $T_y \geq 98\%$ using a 15 μm TN cell, which can be considered as an achromatic design, but the response time, τ, in this case is 9 times the τ of the 5 μm cell, since $\tau \propto d^2$ **[33]**. Typically, a 5 μm TN cell has $\tau \sim 20 - 30$ ms **[31]**. Therefore, others achromatic PR designs are needed in order to improve the LC–ORs' spectral response, without increasing the response time.

4.4.2. Achromatic Polarization Rotators

Many approaches have been proposed for designing achromatic PRs, with structures equivalent to that shown in **Fig. 4.9**. Some designs are based on multiple TN cells, as the one reported in **[33]** with experimental $T_y \geq 92\%$ in the VIS using two TN cells of 20 μm thickness. Other designs are based on a TN between HN cells **[32]**, **[35]** or fixed retardation plates **[31]**, **[34]**. There have also been reported PRs based on ferro−electric LCs with a bistable operation and an almost achromatic response **[24]**.

To our knowledge, the achromatic designs, based on the **Fig. 4.9** scheme, exposed in **[31]** and **[32]** present the best performance reported to date. They are based on optimization algorithms and have been done in the range from 400 to 700 nm. In **[31]**, it is reported a design composed of a front retarder plate with $d_1 = 45.29$ μm and $\alpha_1 = 89.96$º, a TN cell with $d_T = 6.20$ μm, $\phi_T = 90.12$º and $\alpha_T = 0^\circ$ of E7 LC mixture, and a rear retarder plate with $d_2 = 4.83$ μm and $\alpha_2 = -89.91^\circ$. The input LP is oriented at an azimuth angle $\beta = 1.64^\circ$. This PR presents $T_y \geq 97.8\%$ and it is designed after optimizing 7 variables (β, ϕ_T, α_1, α_2, d_T, d_1 and d_2). On the other hand, two designs using E7 LC material are reported in **[32]**. The first design is based on three TN cells between crossed LPs. The corresponding optimization includes thickness, azimuth and twist angles of each LC cell (9 variables). The optimal values are: $d_1 = 1.36$ μm, $\alpha_1 = -31.4^\circ$, $\phi_1 = 57^\circ$, $d_2 = 2.26$ μm, $\alpha_2 = -58.3^\circ$, $\phi_2 = 31.1^\circ$, $d_3 = 1.54$ μm, $\alpha_3 = 59.9^\circ$, $\phi_3 = 62.9^\circ$, for cells 1, 2 and 3, respectively. The device has $T_y \geq 99.95\%$, which represents the best rotation efficiency reported to date. In the second design of **[32]**, the cells 1 and 3 are HN (ϕ_1 and $\phi_3 = 0^\circ$) and the cell 2, which is placed between cells 1 and 3, is a TN cell. Then, 7 variables are used in this optimization and the optimal values are: $d_1 = 2.49$ μm, $\alpha_1 = -79^\circ$, $d_2 = 3.94$ μm, $\alpha_2 = 10.9^\circ$, $\phi_2 = 66.5^\circ$, $d_3 = 2.47$ μm, $\alpha_3 = -11^\circ$. This second device has $T_y \geq 98.87\%$. These designs are obtained with optimization algorithms that use between 7 and 9 variables. Optimization processes with fewer variables are often more effective and faster. They also consider LC cells with very specific parameters, complicating the manufacture of the PR and increasing its tolerances. These publications do not include experimental results. In the next section, the implementation of a broadband LC–OR based on an achromatic PR is described. The achromatic PR design is done with a new synthesis method, which is effective, fast and simple and has good agreement with experimental results.

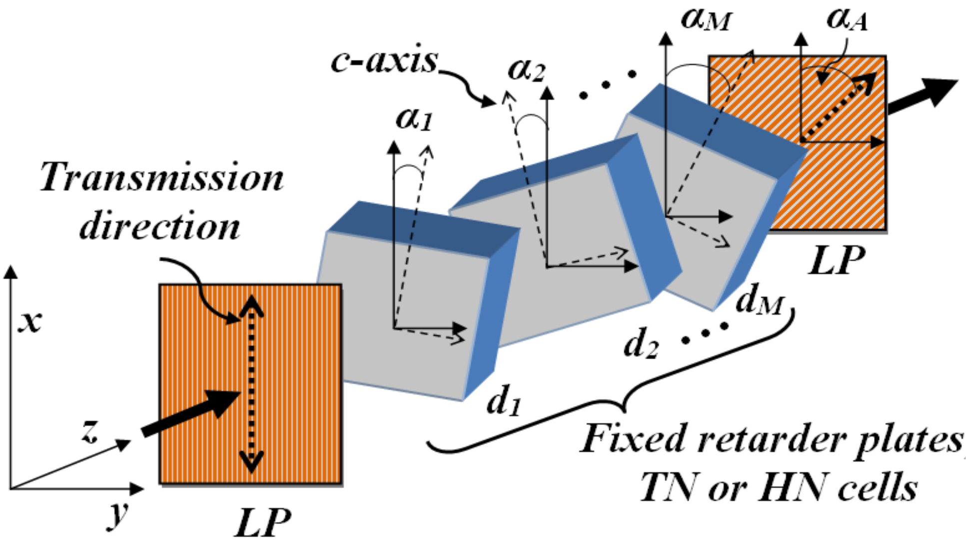

Fig. 4.9: Achromatic polarization rotator scheme, with M elements, where d_1… d_M are thickness and α_1… α_M and α_A are azimuth angles.

4.4.3. Proposed Broadband 1×2 LC–OR

The proposed LC–OR scheme is shown in **Fig. 4.10**. It is composed by an input LP, parallel to the x–axis, an achromatic PR as polarization modulator, and an output polarization beam splitter (PBS) as polarization selective element.

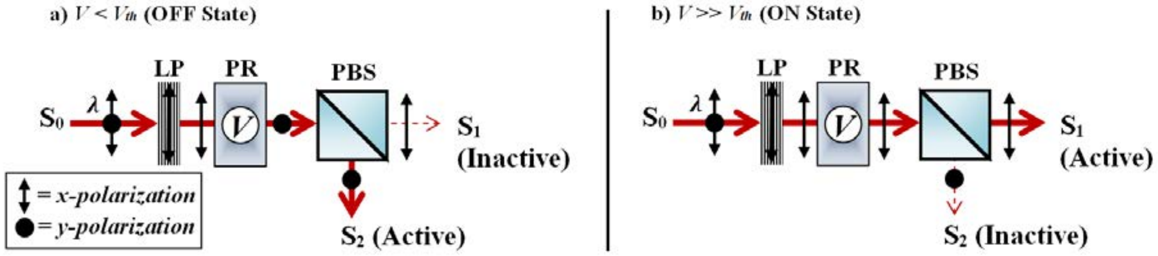

Fig. 4.10: Scheme of the proposed 1×2 LC optical router: a) OFF state, b) ON state). S_0: input port, S_1 and S_2: output ports, V: control voltage and V_{th}: threshold voltage.

4.4.3.1. *Synthesis of the Achromatic PR*

From the state–of–the art presented in **section 4.4.2**, it can be seen that there are multiple configurations for designing achromatic PRs, which include: TN cells, fixed retarder plates and variable retarder plates of HN cells and even of ferroelectric LC cells. However, the configuration based on a TN cell between HN cells offers one of the best polarization rotation efficiencies (T_y) and is less complex that the one based on 3 TN cells **[32]**, so it is used in our design. Moreover, the design method is aimed to be simple and fast. So LC cells of the same material with fixed thickness are considered. It is also considered a TN cell with 90º twist in order to reduce the manufacturing complexity, since 90º–TN cells are very common and commercially available.

The achromatic PR is based on the scheme of **Fig. 4.9**. It is composed by three LC cells of 5CB material and 5.1 μm thickness. The front and rear cells are HN and they are referred as H_1 and H_2, while the middle cell is TN with 90º twist angle and it is referred as T. An x–polarized input beam is considered and the losses are neglected. Then, from (4.3) to (4.5), the transfer function of T_y is given by the element {1,2} of the transfer matrix:

$$W = P_x(\alpha_A) \times W_{H2}(\alpha_{H2}) \times W_T(\alpha_T) \times W_{H1}(\alpha_{H1}) \tag{4.8}$$

where P_x is the transfer matrix of the output LP (analyzer), which is given by:

$$P_x = R(-\alpha_A)\begin{pmatrix} 1 & 0 \\ 0 & 0 \end{pmatrix} R(\alpha_A) \tag{4.9}$$

And α_A, α_{H2}, α_T , α_{H1} are the azimuth angles of each element (LP, H_1, T and H_2, respectively) measured from the x–axis **[28]**, as it is shown in **Fig. 4.9**.

The design process objective is to find the best azimuth angle of each LC cell and the analyzer (α_{H1}, α_T, α_{H2} and α_A) to obtain the desired response, or rotation efficiency T_y, in the range from 400 to 700 nm. Note that $T_y = W_{\{1,2\}}$ from (4.8) when the input beam is x–polarized, see (4.5). The optimization is performed by using a Genetic Algorithm (GA). The proposed optimization problem considers only azimuth angle of each LC cell and the analyzer, $x = [\alpha_{H1}, \alpha_T, \alpha_{H2}, \alpha_A]$ and minimizes the next objective function:

$$F_{obj}(x) = RMS\left[T_r - T_y(\lambda, x)\right] \quad with \quad 400nm \leq \lambda \leq 700nm \tag{4.10}$$

where *RMS* represents the root mean square and T_r is the required transmission of T_y that is 1 in this case.

The searching time was 5 sec and the optimal values are $\alpha_{H1} = 74.76°$, $\alpha_T = -1.56°$, $\alpha_{H2} = 12.12°$ and $\alpha_A = 86.88°$, obtaining $T_y \geq 99.28\%$ in the range from 400 to 700 nm, as shown in **Fig. 4.11a**). The attenuation of the T_x polarization component, represented as T_x[dB] = 10×log10(1 − T_y), is shown in the same figure (b). The result is T_x[dB] < −21 dB in the range from 400 to 700 nm. T_x[dB] must be as low as possible. It is important to note that for practical purposes, α_A represents the azimuth angle of the PBS's reflection axis, which is orthogonal to its transmission axis.

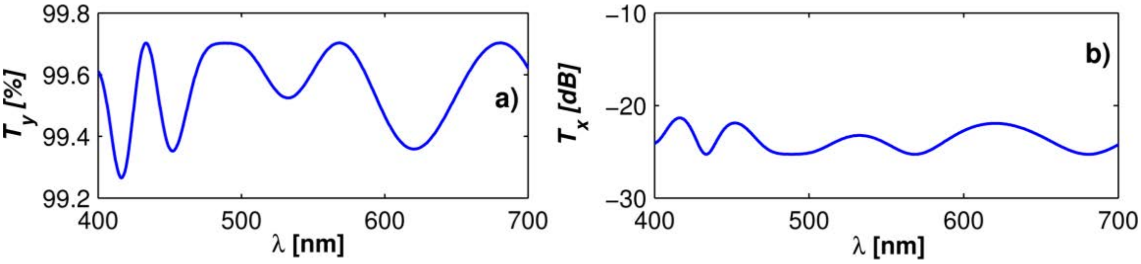

Fig. 4.11: Theoretical response of the proposed design ($\alpha_{H1} = 74.76°$, $\alpha_T = -1.56°$, $\alpha_{H2} = 12.12°$ and $\alpha_A = 86.88°$): a) Transmittance of the T_y polarization component and b) Attenuation of the T_x polarization component, T_x[dB] = 10×log10(1 – T_y).

This design is as good as previous state of the art with more complex designs. The considered LC cells are commercial; this reduces manufacturing tolerances and facilitates the final device construction.

4.4.3.2. Broadband 1×2 LC–OR performance

In this section, the performance of the proposed router is experimentally tested and it is compared against the performance of a router based on a single TN cell of 5CB material, 5.1 μm thickness and 90º twist angle, as the described in section 4.4.1.2, named simple router.

According to the operating principle of the router, in the OFF state, when $V < V_{th}$, S_1 is the inactive output and S_2 is the active output. While in the ON state, when $V \gg V_{th}$, S_1 is the active output and S_2 is the inactive output, as shown in **Fig. 4.10**. The optical power of S_1 and S_2 is represented as P_{S1} and P_{S2}, respectively. The router performance is evaluated in terms of the insertion loss, *IL*, and the crosstalk attenuation, *CTA*. The *IL* is defined as the ratio of the power transmitted by the active output from the input power, P_{in}, and it is expressed as:

$$IL_{OFF} = -10\log\left(\frac{P_{S2}}{P_{in}}\right)_{when \quad V<Vth} \quad or \quad IL_{ON} = -10\log\left(\frac{P_{S1}}{P_{in}}\right)_{when \quad V>>Vth} \tag{4.11}$$

On the other hand, *CTA* is defined as the ratio of the power transmitted by the inactive output from the input power, P_{in}, and it is expressed as:

$$CTA_{OFF} = -10\log\left(\frac{P_{S1}}{P_{in}}\right)_{when \quad V<Vth} \quad or \quad CTA_{ON} = -10\log\left(\frac{P_{S2}}{P_{in}}\right)_{when \quad V>>Vth} \tag{4.12}$$

It is important to note that *IL* is a value higher than 0 dB, and it must be as small as possible; and that *CTA* is also a value higher than 0 dB, but it must be as large as possible.

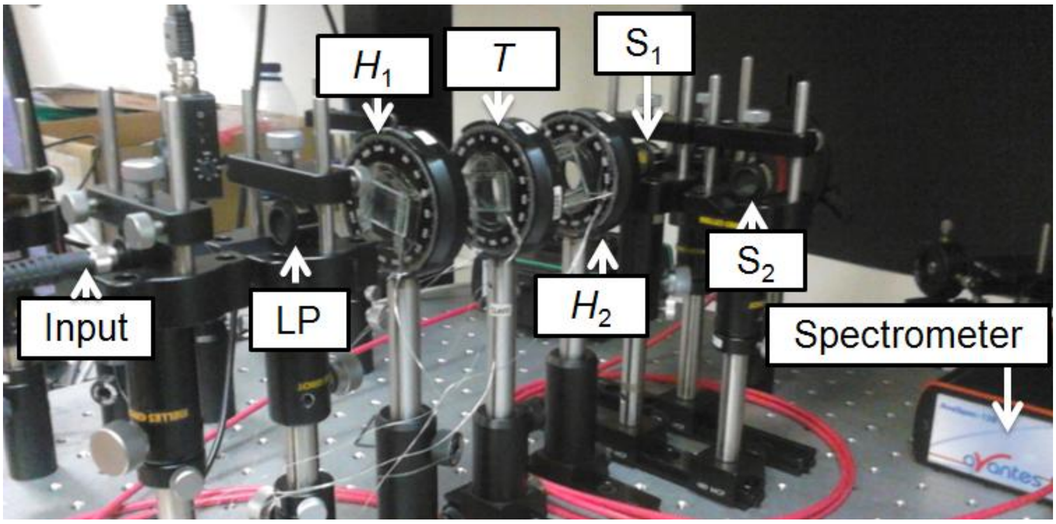

Fig. 4.12: Experimental set–up. H_1 and H_2 are HN cells and T is a TN cell.

The experimental set−up used to test the router performance is shown in **Fig. 4.12**. The LC cells are experimental devices and are mounted on manual rotation mounts. A halogen light source and a spectrometer are used. The fiber optic spectrometer has a 360 nm to 890 nm spectral range, and about 4 nm of spectral resolution. Multimode optical fibers and collimators are used at input and output ports. In this characterization, the PBS is replaced by two LPs, which represent the PBS's transmission and reflection axes. This is done in order to avoid moving the spectrometer's fiber, keeping the constant the power reference for the 0% and 100% transmission, which are named dark and white references, respectively. The LPs are from the series WP25M−VIS with operation range from 420 to 700 nm. For the transmittance calculation, the white reference is taken with parallel LPs and the dark reference is taken with crossed LPs, in order to eliminate the influence of the LPs.

The *IL* and *CTA* values of the proposed LC−OR are shown in **Fig. 4.13** and **Fig. 4.14**, respectively. The results are compared with results of the simple LC–OR obtained under the same characterization conditions.

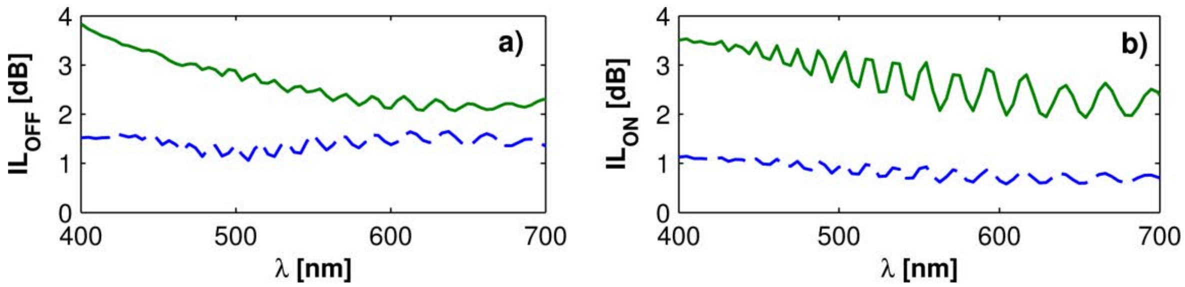

Fig. 4.13: *IL* measurements of the proposed router (solid line) and the simple router (dashed line), where: a) is the *IL* of the S_2 output ($V < V_{th}$, IL_{OFF}) and b) is the *IL* of the S_1 output ($V \gg V_{th}$, IL_{ON}).

The *IL* of the S_1 output (IL_{ON}) is first analyzed, since it does not depend on the PR efficiency; it only depends on the transmittance of the LC cells. As shown in **Fig. 4.13b**, the average IL_{ON} of the simple router is 0.84 dB and the average IL_{ON} of the proposed router is 2.74 dB, which is 3.3 times the IL_{ON} of the simple router since it is made by 3 LC cells. On the other hand, the *IL* of the S_2 output (IL_{OFF}) includes also the effect of the rotation efficiency. Theoretically, if the rotation efficiency is 100%, $IL_{OFF} = IL_{ON}$. As shown in **Fig. 4.13a**, the simple router has average IL_{OFF} of 1.42 dB, which represents a variation of 69% from its average IL_{ON}, while the proposed router has average IL_{OFF} of 2.64 dB, which represents a variation of only 3.6% from its average IL_{ON}.

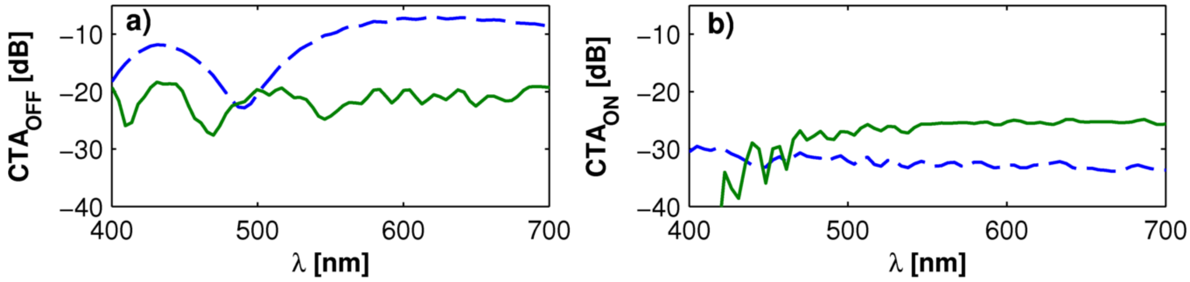

Fig. 4.14: Crosstalk attenuation measurements of the proposed router (solid line) and the simple router (dashed line a) OFF state ($V < V_{th}$) and b) ON state ($V >> V_{th}$).

The *CTA* of the S_2 output (CTA_{ON}) does not depend on the PR efficiency, it mainly depends on the capacity of the LC cells to reach $\theta \cong 90^o$ when $V \gg V_{th}$. As shown in **Fig. 4.14b**, the CTA_{ON} of the simple router is lower than –30 dB, while the CTA_{ON} of the proposed router is lower than –25 dB. Those values can be regulated applying a lower voltage. On the other hand, the *CTA* of the S_1 output (CTA_{OFF}) is mainly defined by the rotation efficiency. As shown in **Fig. 4.14a**, the CTA_{OFF} of the simple router has a maximum value of –7 dB. This represents a poor performance and a variation of 23 dB from its maximum CTA_{ON}. While in the case of the proposed router the CTA_{OFF} has maximum value of –18.68 dB.

4.4.4. Discussion and Remarks

The proposed PR design allows a significant improvement of the spectral response of LC optical routers, as in those previously reported **[14]**, **[16]**, **[17]**, **[25]**, in a broadband range, and may even improve the response of LC devices reported recently **[29]**. **Fig. 4.15** shows the resume of the proposed broadband 1×2 LC–OR performance. Those results show that the router has quite similar values of *IL* in both outputs (OFF and ON states) in the range from 400 to 700 nm, as well as *CTA* values lower than –18.68 dB, as is analyzed previously (**section 4.4.3.2**). This performance is required for routing channels in SI–POF–WDM networks uniformly **[38]**, **[39]**, since in these networks the channels have wide bandwidths (LED sources are often used, and the proposed grid is very wide **[40]**, **[41]**, **[42]**, **[43]**. The router improvement has been done without complicating its construction and using commercially available LC cells (fixed thicknesses).

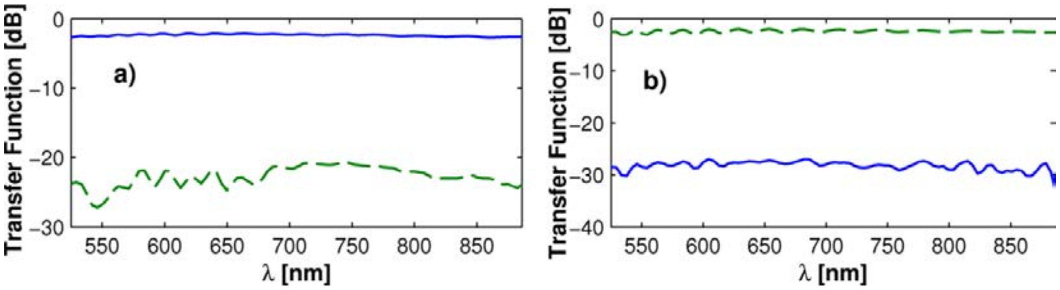

Fig. 4.15: Transfer function of the outputs S_2 (dashed lines) and S_1 (solid lines) of a broadband 1×2 LC–OR for SI–POF WDM networks in the a) OFF state ($V << V_{th}$) and b) ON state ($V >> V_{th}$). Attenuation of S1 output for $V >> V_{th}$ (solid line of b) depends of the applied voltage and can be regulated to be about –20dB.

Fig. 4.16a shows a comparison between the crosstalk attenuation in the off state, CTA_{OFF}, from the experimental results (see **Fig. 4.14a**) and the theoretical design (see **Fig. 4.11b**). The shapes of both curves are very similar. However, there are some discrepancies; the experimental curve (solid line) shows a kind of vertical and horizontal offsets, as well as slightly greater amplitude, from the theoretical curve (dashed line).

This is because, the theoretical model of **Fig. 4.16a** is obtained considering that $d_{H1} = d_{H2} = d_T = 5.1\ \mu$m, $\phi_T = 90°$, $\alpha_{H1} = 74.76°$, $\alpha_T = -1.56°$, $\alpha_{H2} = 12.12°$ and $\alpha_A = 86.88°$ (original design data, see **section 3.1**). However, the LC cells used in the set–up are experimental devices and they are mounted on manual rotation stages (see **Fig. 4.12**), so it is normal to have some variations from the theoretical values in the experimental set–up. In **Fig. 4.16b** is presented an example of how the variations of the theoretical values of the azimuth angles and thicknesses of all the LC cells, as well as the twist angles of the TN cell, can produce a result from the theoretical model more close to the experimental results. The simulation plotted in **Fig. 4.16b** (called fitted model) is obtained considering that $d_{H1} = 5.042\ \mu$m, $d_{H2} = 5.025\ \mu$m, $d_T = 5.080\ \mu$m, $\phi_T = 86.1°$, $\alpha_{H1} = 74°$, $\alpha_T = -3°$, α_{H2}

= 11º and α_A = 87º. The fitted model shows how the tolerance of some parameters can affect the experimental results. Those values (angles and thicknesses) are obtained using an optimization routine considering reasonable tolerances given by the experimental set–up (rotation mounts and LC cells).

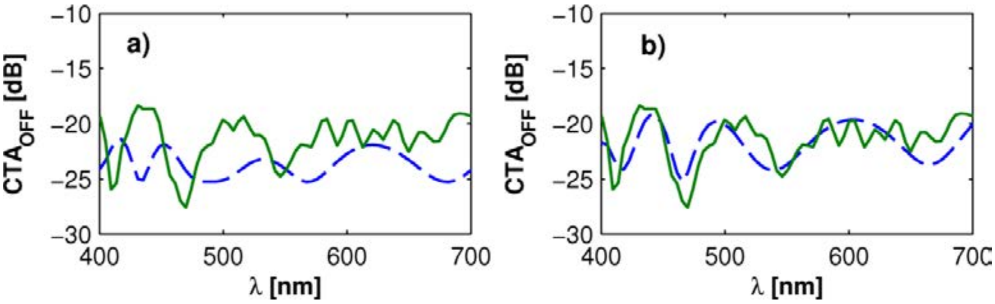

Fig. 4.16: Theoretical model (dashed line) and experimental results (solid line) comparison a) original design data: d_{H1} = d_{H2} = d_T = 5.1 μm, ϕ_T = 90º, α_{H1}= 74.76º, α_T = −1.56º, α_{H2} = 12.12º and α_A = 86.88º b) fitted model considering reasonable tolerances in design parameters: d_{H1} = 5.042 μm, d_{H2} = 5.025 μm, d_T = 5.080 μm, ϕ_T = 86.1º, α_{H1}= 74º, α_T = −3º, α_{H2} = 11º and α_A = 87º.

It is important to note that the LC cells used do not include any anti–reflection coating. This is one of the factors that cause the ripple of *IL* (see **Fig. 4.13**). The *IL* and its ripple are mainly caused by the electrodes of Indium Tin Oxide (ITO) of the LC cells. For example, the transmission of a 400 Å thick ITO film is 81% and 95% at 400 and 700 nm, respectively **[44]**. Each LC cell of the proposed router has its own electrodes (6 electrodes in total). Therefore, it would be necessary to use electrodes optimized over the range from 400 to 700 nm or compact structures in order to reduce the losses **[34]**.

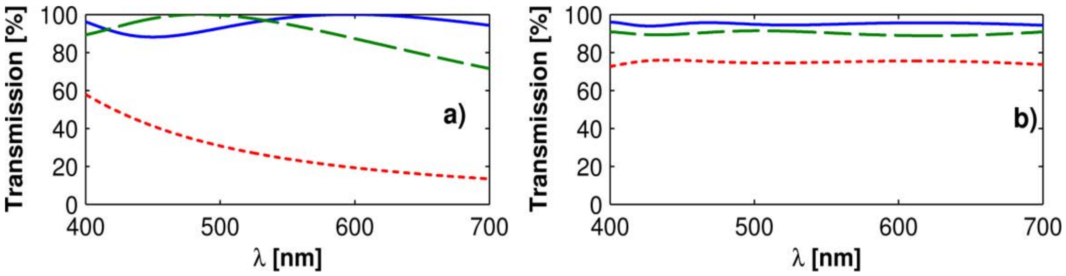

Fig. 4.17: Intermediate transmission levels of the S_2 output of the: a) simple router with θ_T = 38.69º (solid line), 47.33º (dashed line) and 65.36º (dotted line) and b) proposed broadband router with [θ_{H1}, θ_T, θ_{H2}] = [41.65º, 38.69º, 38.38º] (solid line), [47.33º, 47.33º, 51.18º] (dashed line) and [62.36º, 65.36º, 52.06º] (dotted line) for *Tr* = 0.95, 0.90 and 0.75, respectively. The transmittance effects of the LC cells electrodes are not considered.

A very important feature of this type of optical router is the ability to control split ratio of the output power, P_{out}, since $P_{S1} + P_{S2} = P_{out}$. The split ratio is controlled by the applied voltage to the

LC cells, which modifies the tilt angle, θ, of the LC molecules between 0º and 90º. **Fig. 4.17a** shows that the transmittance of the S_2 output of the simple router is very wavelength dependent for intermediate transmission levels (intermediate θ values). However, the proposed router allows intermediate transmission levels, or variable split ratios, with good spectral uniformity in the VIS range, by applying different control voltages to each LC cell, as it is shown in **Fig. 4.17b**. In this figure, three intermediate transmission levels of the S_2 output of the proposed router are shown. For simplicity, the control voltages of each cell are represented as the tilt angles θ_{H1}, θ_T and θ_{H2}, for the cells H_1, T and H_2, respectively. The value of each tilt angle is found with an optimization process similar to the one presented in **section 2.3**, maintaining fixed the azimuth angles ($\alpha_{H1} = 74.76°$, $\alpha_T = -1.56°$, $\alpha_{H2} = 12.12°$ and $\alpha_A = 86.88°$) optimizing the vector $x = [\theta_{H1}, \theta_T, \theta_{H2}]$ in order to obtain the desired transmission levels T_r.

On the other hand, an important drawback of the LC based devices is the strong dependence of the birefringence with the temperature (T). The birefringence of the 5CB material versus the temperature, $\Delta n(T)$, is presented in **[45]** at 546 nm, 589 nm and 633 nm, see **section 2.1.2.2**. Therefore, the birefringence versus temperature of others wavelengths, $\Delta n(T, \lambda)$, can be extrapolated by using the extended Cauchy model **[37]**, see **section 2.1.2.1**. The **Fig. 4.18** shows the variation of CTA_{OFF} with the temperature of both routers using this approximation of $\Delta n(T, \lambda)$. As shown in **Fig. 4.18a**, the simple router has optimum CTA_{OFF} at 535 nm when the temperature is 20 ºC and it shift to 509 nm and 470 nm when the temperature is 25 ºC and 30 ºC, respectively. As result, for a fixed wavelength, e.g. at 509 nm, the *CTA* changes between < −20 dB to −10 dB with a variation of only 10 ºC. On the other hand, the proposed router has a very low dependence of its CTA_{OFF} with the temperature, thanks to its spectral uniformity, as shown in **Fig. 4.18b**. The proposed router has a maximum variation of 4 dB in its CTA_{OFF} in the range from 400 to 650 nm for a temperature variation between 20 ºC and 30 ºC. In the case of the experimental results, the reported values are valid up to 900 nm (see **Fig. 4.15**). Then, if the spectral response is shifted due to a temperature increment, the maximum *CTA* will continue to be less than –18.68 dB.

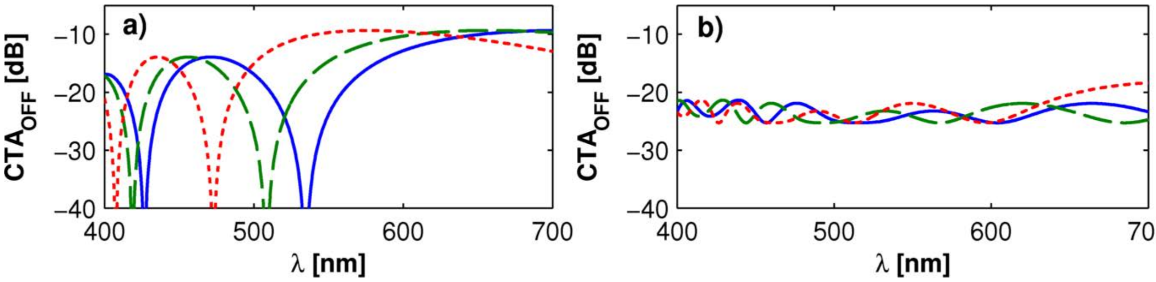

Fig. 4.18: CTA_{OFF} of the a) simple router and b) proposed router at 20 ºC (solid line), 25 ºC (dashed line) and 30ºC (dotted line).

4.5. References

[1] S. J. Chua (Editor) and B. Li (Editor), Optical Switches: Materials and Design, Woodhead Publishing in Materials, 2010.

[2] P. De Dobbelaere, K. Falta, S. Gloeckner and S. Patra, "Digital MEMS for Optical Switching," *IEEE Communications Magazine,* vol. 40, no. 3, pp. 88–95, 2002.

[3] R. Ramaswami, K. N. Sivarajan and G. H. Sasaki, Optical Networks: a practical perspective, Morgan Kaufmann Publishers Inc, 2002.

[4] J. Sapriel, D. Charissoux, V. Voloshinov and V. Molchanov, "Tunable Acoustooptic Filters and Equalizers for WDM Applications," *Journal of Lightwave Technology,* vol. 20, no. 5, pp. 892–899, 2002.

[5] A. D'Alessandro, D. A. Smith and J. E. Baran, "Polarisation–Independent Low–Power Integrated acousto–optic tunable filter/switch using APE/Ti polarisation splitters on lithium niobate," *Electronics Letters,* vol. 29, no. 20, pp. 1767–1769, 1993.

[6] K. Sakuma, H. Ogawa, D. Fujita and H. Hosoya, "Polymer Y–branching thermo–optic switch for optical fiber communication system," in 8*th Microoptics Conference, MOF'*01, Osaka, Japan, 2001.

[7] J. Leuthold and C. H. Joyner, "Multimode Interference Couplers with Tunable Power Splitting Ratios," *Journal of Lightwave Technology,* vol. 19, no. 5, p. 700, 2001.

[8] V. R. Almeida, C. A. Barrios, R. R. Panepucci and M. Lipson, "All–Optical Control of Light on a Silicon Chip," *Nature,* vol. 431, pp. 1081–1084, 2004.

[9] M. Xiaohua and G. S. Kuo, "Optical Switching Technology Comparison: Optical MEMS vs. Other Technologies.," *IEEE Communications Magazine,* vol. 41, no. 11, pp. s16–s23, 2003.

[10] R. Krahenbuhl, M. M. Howerton, J. Dubinger and A. S. Greenblatt, "Performance and Modeling of Advanced Ti:LiNbO3 Digital Optical Switches," *Journal of Lightwave Technology,* vol. 20, no. 1, pp. 92–99, 2002.

[11] K. Nashimoto, H. Moriyama, S. Nakamura, M. Watanabe, T. Morikawa, E. Osakabe and K. Haga, "PLZT electro–optic waveguides and switches," in *Optical Fiber Communication Conference and Exhibit*, 2001.

[12] A. J. Agranat, "Electroholographic wavelength selective crossconnect," in *Nanostructures and Quantum Dots/WDM Components/VCSELs and Microcavaties/RF Photonics for CATV and HFC Systems,* 1999 *Digest of the LEOS Summer Topical Meetings*, 1999.

[13] L. H. Domash, C. Yong–Ming, P. Haugsjaa and M. Oren, " Electronically switchable waveguide Bragg gratings for WDM routing," in *Vertical–Cavity Lasers, Technologies for a*

Global Information Infrastructure, WDM Components Technology, Advanced Semiconductor Lasers and Applications, Gallium Nitride Materials, Processing, and Devi, 1997.

[14] C. Vázquez, I. Pérez, P. Contreras, B. Fracasso and B. Vinouze, Optical Switches: Materials and Design, S. J. Chua and B. Li, Eds., Woodhead Publishing in Materials, 2010, Chapter 8.

[15] Y. Fujii, "Low–Crosstalk 2 x 2 Optical Switch Composed of Twisted Nematic Liquid Crystal Cells," *IEEE Photonics Technology Letters,* vol. 5, no. 6, pp. 715–717, 1993.

[16] C. Vázquez, J. M. Sánchez–Pena, S. E. Vargas, L. A. Aranda and I. Pérez, "Optical Router for Optical Fiber Sensor Networks Based on a Liquid Crystal Cell," *IEEE Sensors Journal,* vol. 3, no. 4, pp. 513–518, 2003.

[17] P. Lallana, C. Vázquez and B. Vinouze, "Advanced multifunctional optical switch for multimode optical fiber networks," *Optics Communications,* vol. 285, no. 12, pp. 2802–2808, 2012.

[18] M. W. Geis, R. J. Molnar, G. W. Turner, T. M. Lyszczarz, R. M. Osgood and B. R. Kimball, "30 to 50 ns liquid–crystal optical switches," in *Proc. SPIE* 7618, 2010.

[19] D. H. Song, J.–W. Kim, K.–H. Kim, S. J. Rho, H. Lee, H. Kim and T.–H. Yoon, "Ultrafast switching of randomly aligned nematic liquid crystals," *Optics Express,* vol. 20, pp. 11659–11664, 2012.

[20] Y. S. Ha, H. J. Kim, H. G. Park and D. S. Seo, "Enhancement of electro–optic properties in liquid crystal devices via titanium nanoparticle doping," *Optics Express,* vol. 20, no. 6, pp. 6448–6455, 2012.

[21] V. Borshch, S. V. Shiyanovskii and O. D. Lavrentovich, "Nanosecond Response in Nematic Liquid Crystals for Ultrafast Electro–Optic Devices," in *CIOMP–OSA Summer Session on Optical Engineering, Design and Manufacturing*, Changchun, China, 2013.

[22] L. P. Amosova, V. N. Vasil'ev, N. L. Ivanova and E. A. Konshina, "Ways of increasing the response rate of electrically controlled optical devices based on nematic liquid crystals," *Journal of Optical Technology,* vol. 77, no. 2, pp. 79–87, 2010.

[23] V. G. Chigrinov, "Photoaligning and Photopatterning—A New Challenge in Liquid Crystal Photonics," *Crystals,* vol. 3, no. 1, pp. 149–162, 2013.

[24] P. Xu, X. Li and V. G. Chigrinov, "Double Cell Achromatic Ferroelectric Liquid Crystal Displays Using Photoalignment Technology," *Japanese Journal of Applied Physics,* vol. 45, no. 1, p. 200, 2006.

[25] P. J. Pinzón, I. Pérez, C. Vázquez and J. M. Sanchez–Pena, "1 × 2 Optical RouterWith Control of Output Power Level Using Twisted Nematic Liquid Crystal Cells," *Molecular Crystals and Liquid Crystals,* vol. 533, no. 1, pp. 36–43, 2012.

[26] C. Vázquez, J. M. Sanchez–Pena and A. L. Aranda, "Broadband 1x2 Polymer Optical Fiber

Switches Using Nematic Liquid Crystals," *Optics Communications,* vol. 224, no. 1–3, 2003.

[27] C. Vázquez, J. M. Sanchez–Pena, P. C. Lallana and M. A. J. Pontes, "Development of a 2x2 optical switch for plastic optical fiber using liquid crystal cells," in *Proceedings of SPIE* 5840*: Photonics Materials, Devices and Applications*, 325–335, 2005.

[28] P. Yeh and C. Gu, Optics of Liquid Crystal Displays, second ed. ed., New York: John Wiley & Sons, 2010.

[29] M. Decker, C. Kremers, A. S. I. Minovich, A. E. Miroshnichenko, D. Chigrin, D. N. Neshev, C. Jagadish and Y. S. Kivshar, "Electro–optical switching by liquid–crystal controlled metasurfaces," *Optics Express,* vol. 21, no. 7, pp. 8879–8885, 2013.

[30] P. J. Pinzón, I. Pérez, C. Vázquez and J. M. Sánchez–Pena, "Broadband 1×2 Liquid Crystal Router with Low Thermal Dependence for Polymer Optical Fiber Networks," *Optics Communications,* vol. 333, pp. 281–287, 20014.

[31] Q.–H. Wang, T. X. Wu, X. Zhu and S.–T. Wu, "Achromatic polarization switch using a film–compensated twisted nematic liquid crystal cell," *Liquid Crystals,* vol. 31, no. 4, pp. 535–539, 2004.

[32] Q. Wang, G. Farrell, T. Freir and J. She, "Optimal design of broadband linear polarization converters/switches," *Journal of Optics A: Pure and Applied Optics,* vol. 7, no. 1, p. 47, 2005.

[33] A. B. Golovin, O. P. Pishnyak, S. V. Shiyanovskii and O. D. Lavrentovich, "Achromatic linear polarization switch for visible and near infrared radiation based on dual–frequency twisted nematic cell," in *Proc. SPIE* 6135*, Liquid Crystal Materials, Devices, and Applications XI*, 2006.

[34] R. K. Komanduri, K. F. Lawler and M. J. Escuti, "Multi–twist retarders: broadband retardation control using self–aligning reactive liquid crystal layers," *Optics Express,* vol. 21, no. 1, pp. 404–20, 2013.

[35] Z. Zhuang, Y. J. Kim and J. S. Patel, "Achromatic linear polarization rotator using twisted nematic liquid crystals," *Applied Physics Letters,* vol. 76, no. 26, p. 3995, 2000.

[36] P. Pinzón, C. Vázquez, I. Pérez and J. Sanchez Pena, "Synthesis of Asymmetric Flat–Top Birefringent Interleaver Based on Digital Filter Design and Genetic Algorithm," *IEEE Photonics Journal,* vol. 5, no. 1, 7100113, 2013.

[37] J. Li, C.–H. Wen, S. Gauza, R. Lu and S.–T. Wu, "Refractive indices of liquid crystals for display applications," *Journal of Display Technology,* vol. 1, no. 1, pp. 51–56, 2005.

[38] U. H. P. Fischer and M. J. M. Haupt, "Optical Transmission Systems Using Polymeric Fibers," in *Optoelectronics – Devices and Applications*, P. Predeep, Ed., InTech Europe, 2011.

[39] L. Bilro, N. Alberto, J. Pinto and R. Nogueira, "Optical Sensors Based on Plastic Fibers," *Sensors,* vol. 12, no. 9, pp. 12184–12207, 2012.

[40] O. Ziemann, J. Krauser, P. E. Zamzow and W. Daum, POF Handbook :Optica lShort Range Transmission Systems, Second ed., New York: Springer, 2008.

[41] O. Ziemman and L. V. Bartkiv, "POF–WDM, theTruth," in 20*th International Conference on Plastic Optical Fibers*, Bilbao, Spain, 2011.

[42] M. Jončić, M. Haupt and U. H. P. Fischer, "Four–channel CWDM system design for multi–Gbit/s data communication via SI–POF," in *roc. SPIE* 9007*, Broadband Access Communication Technologies VIII*, 2013.

[43] M. Jončić, M. Haupt and U. H. P. Fischer, "Investigation on spectral grids for VIS WDM applicationsover SIPOF," in *ITG Symposium: Photonic Networks*, Leipzing, Germany, 2013.

[44] I.–C. Khoo and S.–T. Wu, Optics and Nonlinear Optics of Liquid Crystals, New Jersey: World Scientific, 1993.

[45] J. Li, S. Gauza and S. T. Wu, "Temperature effect on liquid crystal refractive indices," *Journal of Applied Physics ,* vol. 96, no. 1, p. 19, 2004.

Chapter V:

Efficient Multiplexers/Demultiplexers for Visible WDM Transmission over SI−POF Technology

This chapter reports the design and experimental characterization of low−loss diffraction grating based multiplexer/demultiplexer (Mux/DeMux) devices for step−index polymer optical fiber (SI−POF) networks. First, it is studied the possibility of implementing low−loss Muxes/DeMuxes based on diffractive elements for SI−POF networks and a 3 channel Mux/DeMux proposal, based on a transmissive diffraction grating, with experimental insertion loss (*IL*) from 3.6 to 5.8 dB and adjacent channel crosstalk attenuation (*CTA*) from 16.4 to 28.6 dB **[1]** is presented. Then, a 5 channel SI−POF Mux/DeMux having *IL* of 2.9 to 4 dB, pass bandwidths at –3 dB > 30 nm, *CTA* > 30 dB and size of ~65 mm×55 mm, is demonstrated **[2]**. It is based on a reflective diffraction grating and an aspheric lens. The theoretical analysis presented is used to further reduce the system size to ~37 mm×30 mm and to increase the number of channels to 8 keeping *ILs* < 4.5 dB. These experimental results have good agreement with theoretical expectations. The 5 and 8 channel Muxes/DeMuxes presented in this work have the best characteristics, in terms of performance, number of channels and size, reported in experimental systems.

5.1. Introduction

Wavelength Division Multiplexing (WDM) is being proposed as the most important solution to expand the transmission capacity of step−index polymer optical fiber (SI–POF) based networks. Current proposals of WDM transmission over SI–POF are based on spectral grids with channels in the visible range (VIS), between 400 and 700 nm **[3]**, using laser diodes (LDs) based transmitters. Visible WDM systems using offline−processed DMT modulation, and data rates up to 14.77 **[4]** and 21 Gbit/s **[5]** over 50 m, with 4 and 6 channels, respectively, have been recently reported. In both systems, the average data rate per channel is about 3.5 Gbit/s with bit error rate of 1×10^{-3}.

In the WDM technique, the different wavelengths which are jointly transmitted over the fiber (multiplexing) must be separated at the receiver (demultiplexing) to regain all the information. Therefore, for a typical WDM link two key–elements are, at the very least, indispensable and have to be introduced: a multiplexer and (Mux) and a demultiplexer (DeMux).

On the other hand, most important limitation of visible WDM links over SI–POF is the power budget reduction due to the current Muxes/DeMuxes high insertion losses (*ILs*), limiting the transmission capacity of each channel in comparison with single channel systems, for the same transmitted power **[6]**. This can be overcome by reducing the Muxes/DeMuxes' *ILs*, and/or increasing the transmission power. But the latter solution increases the system power consumption and is only suitable for scenarios where working outside the eye–safety–limit is allowed **[4]**, **[5]**. Mux/DeMux devices with *ILs* ≈ 3.5 dB per channel allow to establish SI−POF visible WDM systems with transmission power per channel near to the eye safety limit (<1 mW), that can be used in network topologies **[7]** where the fiber containing all the WDM channelss is kept away from the end user. Therefore, the development of Mux/DeMux devices with lower *ILs* and higher channel counts than the current proposals is essential in order to implement efficient visible WDM based SI–POF links, working near the eye–safety–limit and using low−power technology **[6]**, especially for In–Home and Office networks **[7]**. On the other hand, the design of Mux/DeMux devices with a reduced size is another important requirement for the effective implementation of visible WDM based SI–POF networks.

In this chapter, diffraction grating based Muxes/DeMuxes for visible WDM transmission over SI–POF technology, with low *IL*, large rejection bandwidth, high crosstalk attenuation and a compact size, in comparison with the current state–of–the–art, are presented. Thus, it is first reviewed the Mux/DeMux devices state−of−the−art for visible WDM based SI–POF networks. There are also presented some basics concepts about diffraction gratings. Then, the possibility of implementing low−loss Muxes/DeMuxes based on diffractive elements for SI−POF networks, by using three simple transmissive diffraction setups is studied. As result, it is presented a 3 channel Mux/DeMux proposal, based on a transmissive diffraction grating. Next, a 5 channel SI–POF Mux/DeMux is demonstrated. It is based on a reflective diffraction grating and an aspheric lens. The theoretical analysis presented is used to further reduce the system size and to increase the number of channels to 8 keeping low *ILs*. The 5 and 8 channel Muxes/DeMuxes presented in this work have the best characteristics, in terms of performance, number of channels and size, reported in experimental systems and are an excellent choice for the implementation of visible WDM links over SI–POF with a low power budget reduction compared to single channel systems.

5.2. Muxes/DeMuxes for Visible WDM Transmission over SI–POFs

Muxes/DeMuxes are basic elements in the WDM approach. However, most Muxes/DeMuxes for glass optical fibers (GOF) **[8]**, **[9]**, **[10]**, or for graded index POF with low *NA* and diameter **[11]** are not suitable for SI–POFs. This is due to the spectral range and spectral bandwidths used for visible WDM over SI–POFs **[3]**, and the SI–POF physical characteristics, which produces beams with a large diameter and divergence.

5.2.1. Evaluation parameters

The Muxes/DeMuxes performance is evaluated in terms of number of channels, insertion loss (*IL*), adjacent channels crosstalk attenuation (*CTA*) and adjacent channels isolation. These parameters are defined for a demultiplexer with a single input port and n output ports ($P_{\lambda n}$, n = 1, 2, 3, N) bellow, following the recommendation ITU–T G.671 and the **Fig. 5.1** scheme, where λ_n is the nominal wavelength range of the output port $P_{\lambda n}$, λ_x is a wavelength (or wavelength range) different from λ_n, while P_{in} and P_{out} are the input and output optical power of the different wavelengths, respectively.

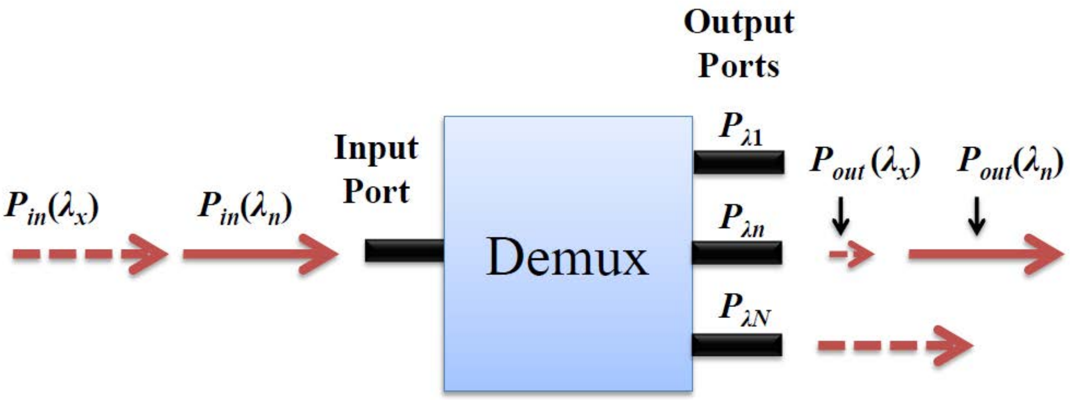

Fig. 5.1: Optical Demultiplexer Schematic for Parameter´s Definition.

- ***IL*** is defined as the ratio of the input, $P_{in}(\lambda_n)$, power of the nominal wavelength (λ_n), or wavelength range, respect to its power, $P_{out}(\lambda_n)$, in its respective output port ($P_{\lambda n}$). It is given by the following formula:

$$IL_{P\lambda n} = -10\log 10\left[\frac{P_{out}(\lambda_n)}{P_{in}(\lambda_n)}\right] \Rightarrow IL_{P\lambda n} > 0dB \quad (5.1)$$

- ***CTA*****:** is a measure of the part of the optical power, $P_{out}(\lambda_x)$, at each wavelength exiting from the output port ($P_{\lambda n}$) at wavelengths (λ_x) different from the nominal wavelength, or wavelength range, relative to the power of λ_x at the input port (P_{in}). It is given by the following formula:

$$CTA_{P\lambda n} = -10\log 10\left[\frac{P_{out}(\lambda_x)}{P_{in}(\lambda_x)}\right] \Rightarrow CTA_{P\lambda n} > 0dB \quad (5.2)$$

- ***Isolation:*** is a measure of the part of the optical power, $P_{out}(\lambda_x)$, at each wavelength exiting from the output port ($P_{\lambda n}$) at wavelengths (λ_x) different from the nominal wavelength, or wavelength range, relative to the power of the nominal wavelength (λ_n) range at the output port ($P_{\lambda n}$). It is given by the following formula:

$$Isolation_{P\lambda n} = -10\log 10\left[\frac{P_{out}(\lambda_x)}{P_{out}(\lambda_n)}\right] \Rightarrow Isolation_{P\lambda n} > 0dB \quad (5.3)$$

It is important to note that if the nominal wavelength (or wavelength range) is not defined, the spectral bandwidth at −3 dB (or 3 dB bandwidth for short) will be considered for the calculations of the *CTA* and the *Isolation*.

5.2.2. State–of–the–art

A summary of different Muxes/DeMuxes for visible WDM applications over SI–POF is shown on **Table 5.1**. They are mainly based on thin–film filters (TFF) **[4]**, **[12]** prisms **[13]** and diffraction gratings **[5]**, **[14]**, **[15]**, **[16]**. Each technology presents important advantages and limitations.

Thin–film based systems are easy to implement and are a good choice to design Muxes/DeMuxes with low *ILs* and few channels. However, they are too large, especially when multiple channels are used, they require many elements (at least twice the number of channels) and their adjacent crosstalk attenuation (*CTA*) is limited by the rejection ratio of the thin–film beam splitters , so additional pass−band filters on each output are often used, adding complexity to the system. A thin–film filter based 4 channel Mux/DeMux made of three splitter filters, an input lens, 4 output lenses and the respective pass–band filter in each output is reported in **[17]**. The *IL* of this system is between 4 and 10 dB and the *CTA* is between 8 and 15 dB. The *CTA* of this system is improved by using band–pass filters in each output **[4]**. On the other hand, the TTF based 3 channel Mux/DeMux of **[12]** reports *IL* < 5 dB.

TABLE 5.1: CHARACTERISTICS OF SOME MULTIPLEXER/DEMULTIPLEXER DEVICES FOR SI–POF WDM SYSTEMS.

Technology	#Elements	Size [mm×mm]	Channels [nm]	*IL* [dB]	*CTA* [dB]	[Ref.], Year	Remarks
Planar blazed diffraction grating (600 lines/mm)	2	(1)	520, 650	6.2 to 7.5	25	**[12]**, 2002	(2)
Thin film filters	>4(1)	(1)	520, 655	3 to 5	20	**[12]**, 2002	(2)
Holographic concave grating reflector (1200 lines/mm)	1	~20×35(1)	520, 570, 655	2	20	**[14]**, 2005	(3), (4), (5)
Ellipsoid and Spherical grating mirrors (1200 lines/mm)	1	~30×26(1)	480, 520 630	(1)	30	**[16]**, 2008	(3) (4)
Prism	2	79×94	470, 520, 655	12 to 19	4.6 to 26.8	**[13]**, 2008	(2)
Blazed grating on an aspheric mirror (500 lines/mm)	1	13×20	450, 520 650(7)	(1)	(1)	**[15]**, 2013	(3) (5) (6)
Thin film filters	12	Large(1)	405, 450, 528, 646	3.3 to 5.7	>30	**[4]**, 2014	(2) (8)
Planar Holographic Diffraction Grating (1800 lines/mm)	2	diam.≥75(1)	405, 442, 459, 490, 515, 655	<10	20 to >30	**[5]**, 2014	(2)
Planar blazed diffraction grating (600 lines/mm)	2	65×55	504, 515, 650	3.5 to 4.5	>30	**[18]**, 2014	(2)
			405, 470, 530, 588, 650	2.8 to 3.9	>30	In this work**[2]**	(2)
Planar blazed diffraction grating (1200 lines/mm)	2	57×50	435, 465, 497, 530, 562, 595, 625, 655	3.2 to 4.5	>30	In this work**[2]**	(2)

Notes: (1) Unspecified or not analyzed; (2) Experimental results with ports made of SI–POF; (3) Simulations without experimental results; (4) The diameter of the SI–POF is not considered in the simulations; (5) A detection layer is considered at the output; (6) SI–POF input with 0.38 *NA* and 0.98 mm diameter; (7) An extra channel at 405nm is included, but only channels with high *CTA* are considered; (8) There is a thin–film filter in each output to improve the crosstalk.

In contrast, prism–based Muxes/DeMuxes require few elements (input and output lenses and the prism) and are cheaper, but usually show a low performance in terms of both *IL* and *CTA*. For example, the prism based Mux/DeMux reported in **[13]** can separate 3 channels, at 470 nm, 520 nm and 655 nm, a distance of 1.2 mm, but with *ILs* of 19.3 dB, 12.1 dB and 14 dB, respectively, and with *CTA* between 4.6 dB and 26.8 dB.

Proposals based on concave gratings have very good expectations due to their potential small size, since the light spatial separation and focusing are performed with a single element. However, they require diffractive elements that to date are not easy to manufacture **[15]**, so their experimental performance has not yet been reported. Simulations show that concave gratings based Mux/DeMuxes can separate 3 channels with, gap of 2 mm, using concave gratings with 1200 lines/mm (or grooves/mm) **[16]**.

Muxes/DeMuxes based on planar blazed diffractions grating are to date a promising option for implementing compact devices (only 2 elements are required) with low *ILs* and multiple channels. In this work, diffraction grating based Muxes/DeMuxes of up to 8 channels with *ILs* < 4.5 dB and *CTA* > 30 dB are reported. The Muxes/DeMuxes demonstrated in this work **[2]** have the best characteristics, in terms of performance, number of channels and size, reported in experimental systems so far. These devices allow the implementation of visible WDM links over SI–POF with a low power budget reduction compared to single channel systems.

5.3. Diffraction Gratings Basic Concepts

Fig. 5.2 shows a basic dispersion scheme. It consists of a transmissive diffraction grating and a focusing lens, with effective focal length (EFL) *f*. It is assumed that the incident beam is collimated, therefore, the system has focusing distance *q*, where *q* = *f*.

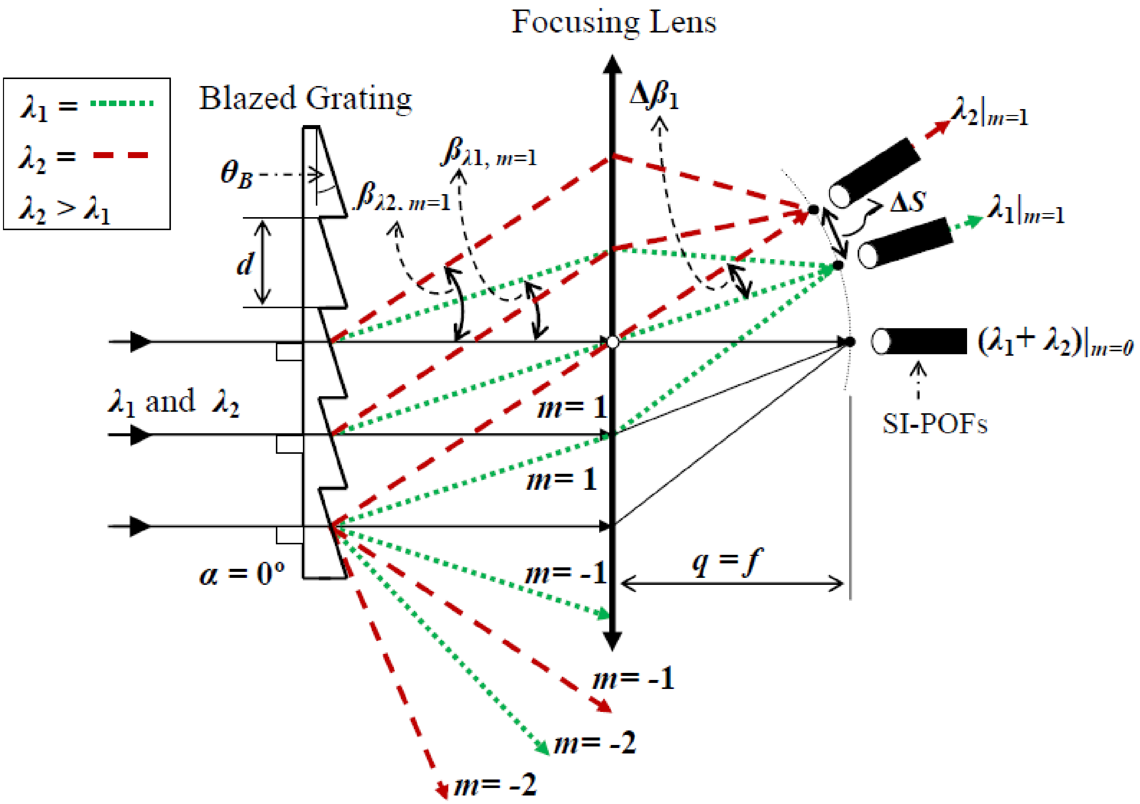

Fig. 5.2: Basic dispersion scheme based on a transmissive diffraction grating and a focusing lens.

5.3.1. Grating Equation

As shown in **Fig. 5.2**, when a monochromatic beam, with wavelength λ, is incident on a grating surface with angle α, respect to the surface normal, it is diffracted into a discrete direction with diffraction angle β_λ, which is given by:

$$m\lambda = d\left[\sin(\alpha) + \sin(\beta_\lambda)\right] \tag{5.4}$$

where d is the grating pitch, generally represented as groove density $G = 1/d$, in lines/mm or grooves/mm, and m is an integer of propagating diffraction orders, being $-2d<m\lambda<2d$ **[19]**.

The difference between diffraction angles of order m of two given wavelengths, λ_1 and $\lambda_2 = \lambda_1 + \Delta\lambda$, is defined as angular dispersion, $\Delta\beta_m$, Differentiating (5.4), the angular dispersion is given by:

$$\Delta\beta_m = \frac{m}{d\sqrt{1-\left(\sin(\alpha) - m\lambda/d\right)^2}}\Delta\lambda \tag{5.5}$$

The scheme of **Fig. 5.2** produces a linear dispersion, ΔS, between different focused spots (e.g. λ_1 and λ_2), by using the cosine theorem this chord length is given by:

$$\Delta S = 2q\sin(\Delta\beta_1/2) \tag{5.6}$$

In demultiplexing applications, ΔS defines the spatial separation between consecutive channels.

5.3.2. Diffraction Gratings Classification and Diffraction Efficiency

Diffraction gratings are usually divided according to several criteria: their geometry, their material, their efficiency behaviour, their manufacturing method, their working spectral interval, or their usage **[20]**. The gratings used in this work are planar and can be classified in transmission and reflection gratings, and in symmetrical (also called binary) and blazed gratings. It is easy to distinguish between reflective and transmissive gratings, the former working in reflection regime and the latter in transmission. On the other hand, when the grating groove is symmetrical, **Fig. 5.3**, normally incident light delivers equal efficiencies into the symmetrical orders (+1 and −1, +2 and −2, etc.). On the other hand, blazed grating are usually characterized by a triangular groove shape, see **Fig. 5.2**. They are optimized to achieve maximum grating efficiency at a specific diffraction order. This is done for a specific λ (blaze wavelength), which is defined by the grooves shape, especially by θ_B (blaze angle). The power distribution, of a given diffracted wavelength, into the different propagating orders is defined as the diffraction efficiency, or grating efficiency. It is highly dependent on the groove profile and the design wavelength **[19]**. This parameter defines mainly insertion losses of the diffraction grating based demultiplexers.

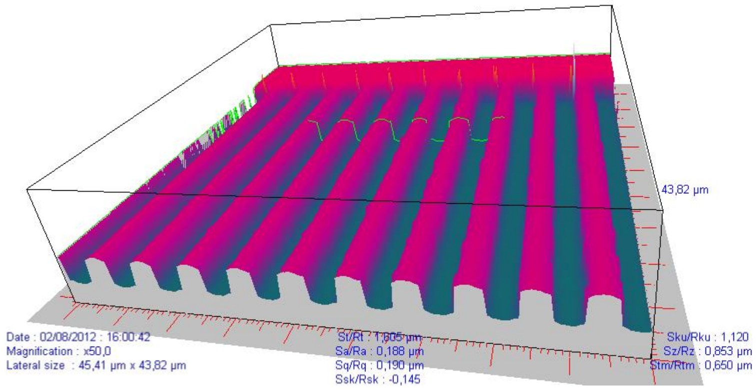

Fig. 5.3: Symmetrical transmissive diffraction grating manufactured at Telecom Bretagne (France).

Fig. 5.3 shows an example of the structure of a symmetrical transmissive diffraction grating. This sample was manufactured during a researching stay at the Optics Department of Telecom Bretagne under the supervision of Prof. K. Heggarty.

5.4. Analysis of Transmissive Diffraction Gratings for SI−POF Muxes/DeMuxes

In this section, three simple multiplexing/demultiplexing schemes for SI−POF networks, named systems 1, 2 and 3, are analyzed. System 1 and 2 are based on the coupling optic schemes shown in **Fig. 5.4** and **Fig. 5.5**, respectively, using a transmissive grating with blazed profile placed at points DG, as the one shown in **Fig. 5.2**. This type of grating is very easy to align and allows testing the effectiveness of both systems in a simple way. In system 3, a solution for implementing compact reflective systems is analyzed. It is based on the **Fig. 5.6** scheme, which implements a grating−prism (grism) **[21]** as the dispersive element at point GP.

In the three systems, the beam that passes through lenses L$_1$, L$_2$ and L$_3$ has a diameter B_D, the divergence of the beam that passes the input collimator is θ_{DIV}, O_D and S_D are the spot diameter at the input and output collimators, respectively, while IL_1, IL_2 and IL_3 are the insertion losses of each section.

These schemes of (**Fig. 5.4**, **Fig. 5.5** and **Fig. 5.6**) are designed to be simple, cheap and with low *IL*. SI−POF fiber collimators (M011−TU2) are used, since they are easy to adapt to straight tip (ST) connectors. These collimators have effective focal length $f_C \approx 4.6$ mm, clear aperture (*CA*) ≈ 4.7 mm and external diameter of 5.1 mm. The collimator *CA* limits the O_D and S_D to about 4.7 mm and the collimator f_C produces a theoretical divergence $\theta_{DIV}/2$ = 106.5 mrad. In systems 1 and 3 (**Fig. 5.4** and **Fig. 5.6**), lenses L1 and L2 have focal length f_L of 155 mm and *CA* of 50 mm; then, the theoretical beam diameter B_D is 33.14 mm, while the experimental B_D is about 32 mm. In the case of the system 2 (**Fig. 5.5**), lens L3 has focal length f_L of 100 mm and CA of 50 mm; then, the theoretical beam diameter B_D is 40.62 mm, while the experimental B_D is about 40 mm.

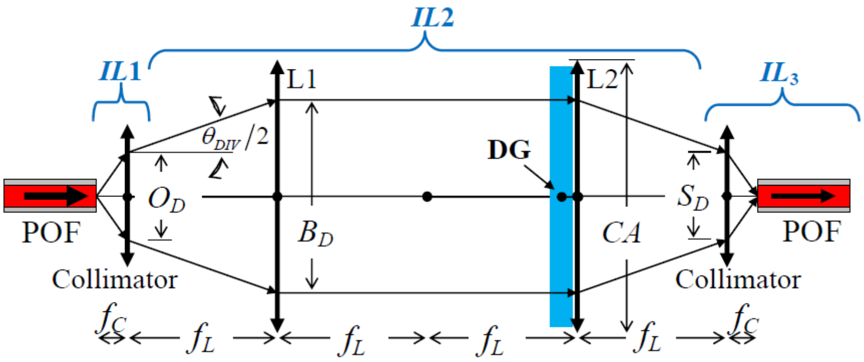

Fig. 5.4: Coupling optics of the System 1.

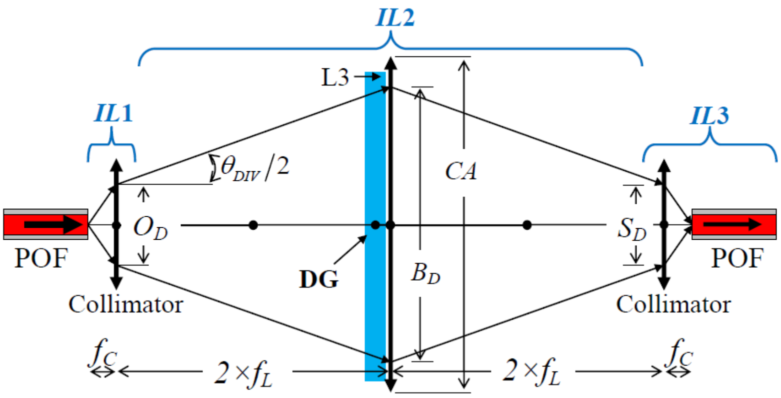

Fig. 5.5: Coupling optics of the System 2.

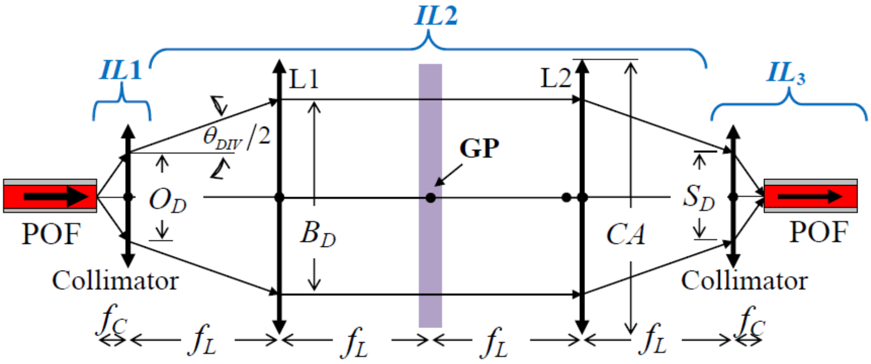

Fig. 5.6: Coupling optics of the System 3.

The diffraction grating implemented in systems 1 and 2 is specifically manufactured by using a prototyping process in Telecom Bretagne. It has a pitch $d \approx 4.0$ μm, $CA = 45$ mm and it is optimized to work at 597 nm. Its diffraction efficiency is 51.05% (2.92 dB of IL) and 50.12% (3 dB of IL) at 532 nm and 655 nm, respectively, for the first diffraction order ($m = +1$). The grism implemented in system 3 has a $d \approx 3.33$ μm and it is designed with a binary grating profile (symmetrical grating). Therefore, its diffraction efficiency is very low **[19]** (power is distributed across many diffraction orders).

5.4.1. Insertion Loss of Coupling Optics

In the experimental setup, insertion losses of coupling optics are mainly defined by the losses of the mismatch between the beam diameter and the clear aperture of the optical elements, the back−reflection loss of each surface and misalignments in the optical system.

The input collimator clear aperture loss can be calculated from a uniform beam, for highly multimodal SI−POF, as:

$$CAL = -10\log_{10}\left(CA/D_F\right)^2 \tag{5.7}$$

where D_F is the diameter of the beam in the free space from the SI−POF that is given by:

$$D_F = 2f\tan\left(\sin^{-1} NA\right) \tag{5.8}$$

Therefore, with $f = f_C \approx 4.6$ mm and $CA = \approx 4.7$ mm, the collimators CAL is about 1.06 dB. The lenses CA are larger than the beam diameters BD; therefore, no CAL are produced.

TABLE 5.2: RESULTS OF THE CHARACTERIZATION OF THE FIRST AND SECOND COUPLING OPTICS SCHEMES.

IL	Mean measured values at system:		Theoretical values & Comments
	1 and 3	2	
IL_1	1.47dB		**Input Collimator:** *BRL* of 2 surfaces (0.36 dB) + *CAL* (1.06 dB) ≈ 1.42 dB. It can be reduced using collimators with larger *CA* (larger numerical aperture) and antireflection coatings.
IL_2	1.50dB	0.96dB	**Lenses System:** 25 mm of BK7 material have 90% transmission or 0.46 dB. Then, in system 1 and 3, $IL_2 \geq BRL$ of 2 surfaces (0.36 dB) + 0.46 dB = 0.82 dB. And in system 2, $IL_2 \geq BRL$ of 2 surfaces (0.36 dB) + 0.46 dB + *BRL* of 2 surfaces (0.36 dB) = 1.18dB.
IL_3	2.24dB	2.34dB	***IL*₃** is defined by the *BRL* of two SI−POF surfaces (0.36 dB), the attenuation of 1 m of SI−POF (~0.22 dB) and the coupling efficiency to the output fiber. Therefore, the coupling efficiency is about 1.7 dB in both cases. The coupling efficiency is highly dependent of the misalignments of the optical system, variations in the focalization distance of the output collimator and the SI−POF surfaces polishing. The M011−TU2 SI−POF collimator is easy to handle but difficult to align with precision.
IL_T	5.21dB	4.77dB	Theoretically, system 1 and 2 have total ***IL* > 4.52 dB** (1.42dB + 0.82dB + 0.36dB + 0.22dB + 1.7dB) and system 2 has total ***IL* > 4.88 dB** (1.42dB + 1.18dB + 0.36dB + 0.22dB + 1.7dB).

The back−reflection loss, *BRL*, or Fresnel Loss, produced when light passes from a medium with refractive index n_1 to another with refractive index n_2 is given by:

$$BRL = -10\log_{10}\left[1-\left(\frac{n_1-n_2}{n_1+n_2}\right)^2\right] \tag{5.9}$$

BRLs are typically ~0.18 dB (per surface), since the refraction index of the SI–POF core and the lenses are ~1.5. **Table 5.2** summarizes the losses measured in the implementation of the coupling optic schemes shown in **Fig. 5.4** to **Fig. 5.6**. This table compares the experimental values with the theoretical ones.

5.4.2. Experimental Characteristics of the Diffraction Systems 1, 2 and 3

Systems 1, 2 and 3 are characterized with an input beam composed by two channels, ch_1 and ch_2, with central wavelengths λ_1 = 532 nm and λ_2 = 655 nm. Both channels are multiplexed using a 1:2 SI–POF coupler. **Fig. 5.7** shows the spatial separation, ΔS, between the focused spots of each channel in the different systems.

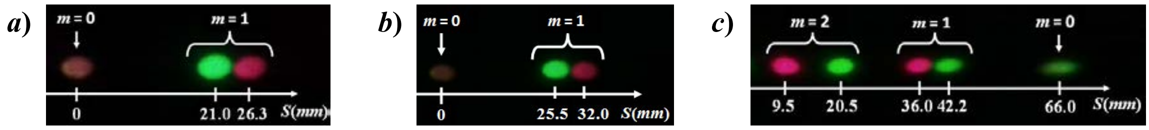

Fig. 5.7: Spatial separation, ΔS, of the focused spot, at the output collimators, of systems a) 1, b) 2 and c) 3.

The system 1 was originally designed to place the diffraction grating at the midpoint between L1 and L2 (see **Fig. 5.4**). However, when the diffraction grating is placed at that point, the light path is partially blocked by the L_2 mount, due to the large distance. Therefore, the diffraction grating is placed just in front of L_2, point DG, obtaining ΔS = 5.3 mm meanwhile the theoretical value from (5.5) and (5.6) is 4.9 mm. This difference is mainly due to adjustments in the focusing distance (from L_2 to the output collimator). This distance was adjusted to get the best coupling efficiency to the output fiber, for both channels. It was observed that ΔS does not change when the grating is moving backwards, since the light beam is collimated. The input and output collimator used in this system can be eliminated if lenses L_1 and L_2 are replaced by lenses with $NA \geq 0.5$ (e.g. aspherical lenses). This reduces the required spatial separation between adjacent channels and the system size.

In system 2, see **Fig. 5.5**, the lenses L_1 and L_2 are replaced by L_3, reducing the number of elements and *IL*. It is observed that the diffraction grating must be placed as closest as possible to L_3, at point DG, since the beam is very divergent, so that ΔS = 6.5 mm; meanwhile the theoretical value is 6.4 mm. In this case, ΔS is reduced when diffraction grating is moved away from L_3, as a tuning capacity (e.g. the central wavelength of the output ports change by moving the grating). In this system, the diffraction grating can be printed on the plane surface of L_3, further reducing the number of optical elements and *IL*, without complicating the manufacturing process.

In system 3, see **Fig. 5.6**, the grisim is placed at the midpoint between L_1 and L_2, point GP, since, unlike diffraction gratings, grisims produce on−axis dispersion. For this reason the zero order diffraction (m=0) has the largest angular dispersion (β_λ), being partially blocked by L_2 mount. Meanwhile, the β_λ of first and second diffraction orders (m = 1 and 2) are small enough not to be blocked, and to produce the necessary $\Delta\beta$ to properly separate λ_1 from λ_2 a distance ΔS = 6.2mm (for m = 1). The tested grism has a binary grating profile; therefore, its efficiency is not comparable to the efficiency of the diffraction grating with blazed profile used in systems 1 and 2. These results show the feasibility of using grisims as a long term solution for implementing systems in reflection configurations in POF−WDM networks, similar to those used in IR for silica optical fibers **[9]**, **[22]**.

TABLE 5.3: EXPERIMENTAL INSERTION LOSSES (*ILS*) OF THE DIFFRACTION SYSTEMS 1 AND 2.

Description	System 1 at:		System 2 at:	
	533nm	655nm	533nm	655nm
Total system losses	8.27dB	8.50dB	8.22dB	8.28dB
Focusing at a detection layer(1)	5.98dB	6.16dB	5.65dB	5.63dB

Notes: (1) A detection layer is considered, therefore, the output SI–POF attenuation and coupling losses are not included.

Table 5.3 presents a summary of the losses of the systems 1 and 2. These results show that, the first and second proposed diffractive setups are close to fulfill the requirements for being implemented as SI−POF visible WDM Mux/DeMux devices **[6]**. The crosstalk attenuation (*CTA*) in both systems is higher than 20 dB, since both channels are well separated and the focusing distances for both channels are quite similar. Design requirements, such as ΔS and system size, can be relaxed by using GRIN lenses as collimators. Similar to the solutions reported by **[9]**, but using one GRIN lens per POF port, due to SI−POF large diameter (a = 1mm). A similar solution can be achieved by using POF tapers.

5.4.3. Transmissive Mux/DeMux Proposal

In this section, a transmissive diffraction grating based Mux/DeMux proposal for SI−POF WDM is presented. It is based on the system 1 scheme. This scheme is chosen because the input and output collimators used in **Fig. 5.4** can be eliminated by using lenses with $NA \geq 0.5$, this reduced the required spatial separation between adjacent channels; and because, as demonstrated in the previous section, in this scheme the diffraction grating can be placed just in front of the focusing lens, therefore, it can be easily adapted into a compact reflective scheme (as will be shown later in this chapter).

Three channels are considered for the design, with central wavelengths at 405nm, 532nm and 655nm, that represent channels number 1, 7 and 13 of a previous SI−POF WDM grid proposal **[17]**. Laser light sources with 30nm FWHM, and a transmissive diffraction grating with $d = 3.3\mu$m (600 grooves/mm), efficiency of 50% to 75% in the channels spectrum range and CA = 50 mm is chosen. From (5.5) and (5.6), the grating CA limits q to be less than 45.7mm, in order to get $B_D <=$ 50mm. It is considered q = 40mm, in order to separate all channels a distance $\Delta S \geq$ 1.45 mm. With q = 40 mm a source with 30nm FWHM will be distorted less than 0.37mm, in the full spectrum range. This value represents the increment in the spot width due to the spectral bandwidth of the channels and it is calculated from (5.5) and (5.6). Focused spots are designed to have S_D = 1 mm (considering monochromatic channels). Then, the minimum required separation is 1.37mm. Therefore $\Delta S \geq$ 1.45mm guarantees the separations of the different channels with high CTA.

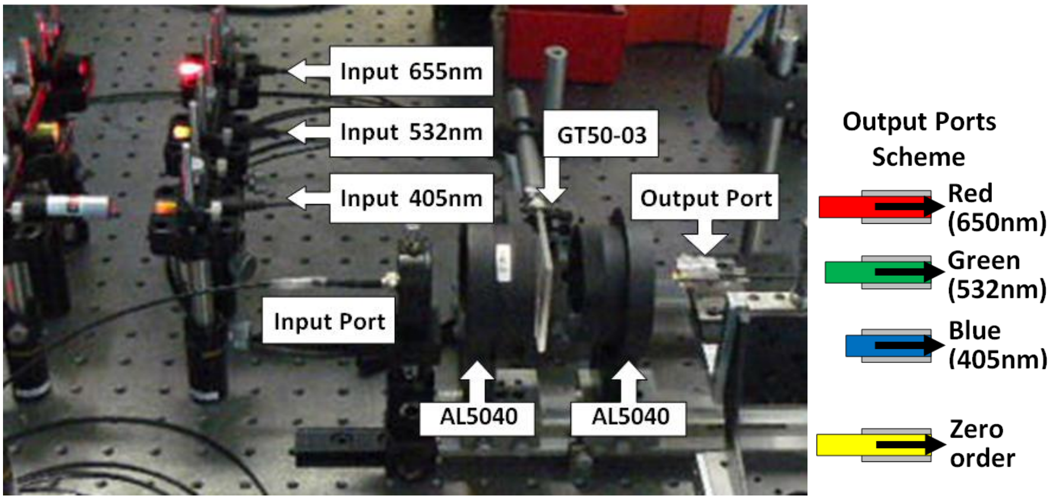

Fig. 5.8: Photograph of the transmissive diffraction grating based Mux/DeMux for SI−POF WDM networks. Ports are made of SI−POF. Lenses AL5040 have EFL = 40mm and *CA* = 50mm. The diffraction grating GT50−03 has 600 grooves/mm ($d = 3.33\mu$m) and *CA* = 50mm.

The experimental setup is shown in **Fig. 5.8**. It has ~60mm diameter and ~120mm length. It is tested using 3 laser sources at 405nm, 532nm and 655nm, and an optical power meter. The output ports have different focal lengths due to the large dispersion of the lenses in the considered spectrum. This is represented in the output port scheme of **Fig. 5.8**. Therefore, in order to perform the power measurements, a single SI−POF is moved across the position of the different ports by using a 3−axes stage.

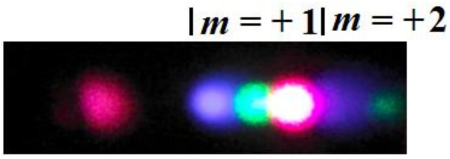

Fig. 5.9: Focused spots of each channel in the proposed transmissive diffraction grating based Mux/DeMux for SI−POF WDM networks.

The experimental setup separates the consecutive channels a distance $\Delta S \geq 1.5$mm. The focused spots of each channel are shown in **Fig. 5.9** (only first diffraction orders are measured). The output SI−POF is placed at the position of each port (Blue, Green and Red) in order to measure the power coupled from each channel in each port. The results are shown in **Fig. 5.10**. In accordance with the definitions of *IL*, *CTA* and Isolation reported in the ITU recommendation ITU−T G.671, see **section 5.2.1,** the total *IL* of the channels at 405 nm, 532 nm and 655 nm are 5.8 dB, 3.6 dB and 4.2 dB, respectively. The *CTA* of the channel at 655 nm is higher than 40 dB at the green and blue ports, and the *CTA* of the channel at 532 nm is higher than 28 dB at the red and blue ports, which represents very good values. The *CTA* of the channel at 405 nm is higher than 20 dB at the red and green ports. Finally the isolation values of the blue, green and red ports are higher than 28.6 dB, 20.4 dB and 16.4 dB, respectively.

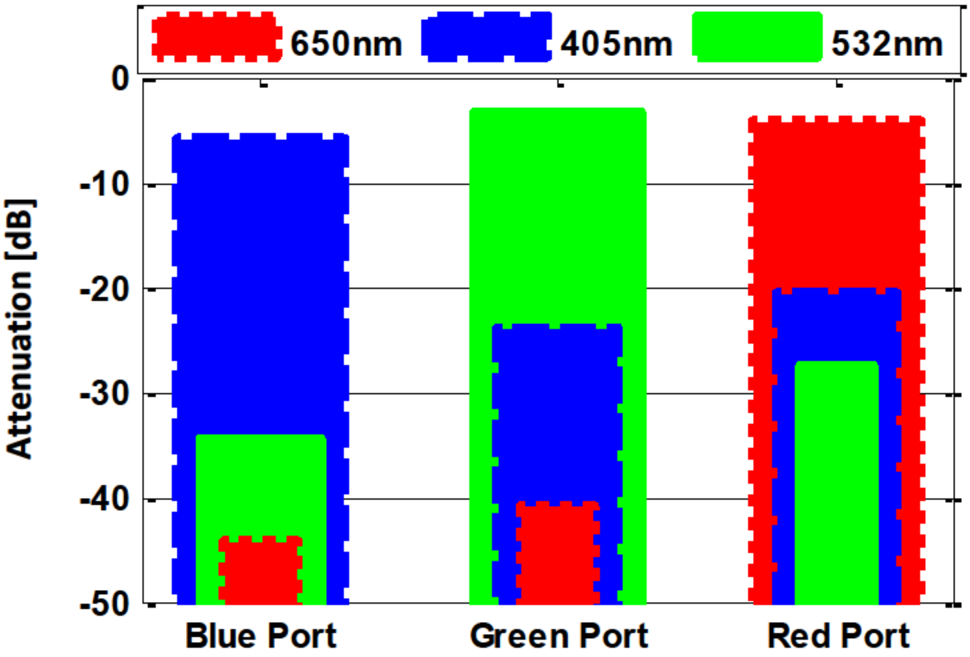

Fig. 5.10: Attenuation of each output port for the different wavelengths.

Fig. 5.10 shows that the performance of each port gets worse as their position moves away from the central axis of the system. Therefore, all the ports must be as close as possible to the central axis of the system.

It is important to note that the size of the proposed system can be reduced by half using a reflective diffraction grating as only 2 elements will be necessary; that a diffraction grating with a higher number of lines/mm must be used in order to increase the number of channels without increasing the system size; and that the position of each port must be optimized by using an optical ray tracing software, due to the important variations in the focal length of each channel in the system since a large spectral range is used.

5.5. Reflective Diffraction Gratings based Mux/DeMux for SI–POF

This section presents the scheme and the theoretical basics used to design low–loss Muxes/DeMuxes based on reflective diffraction gratings, considering the conclusions shown in the previous section. The designs specifications include the number of channels and the shorter and longer wavelengths of the considered spectral grid.

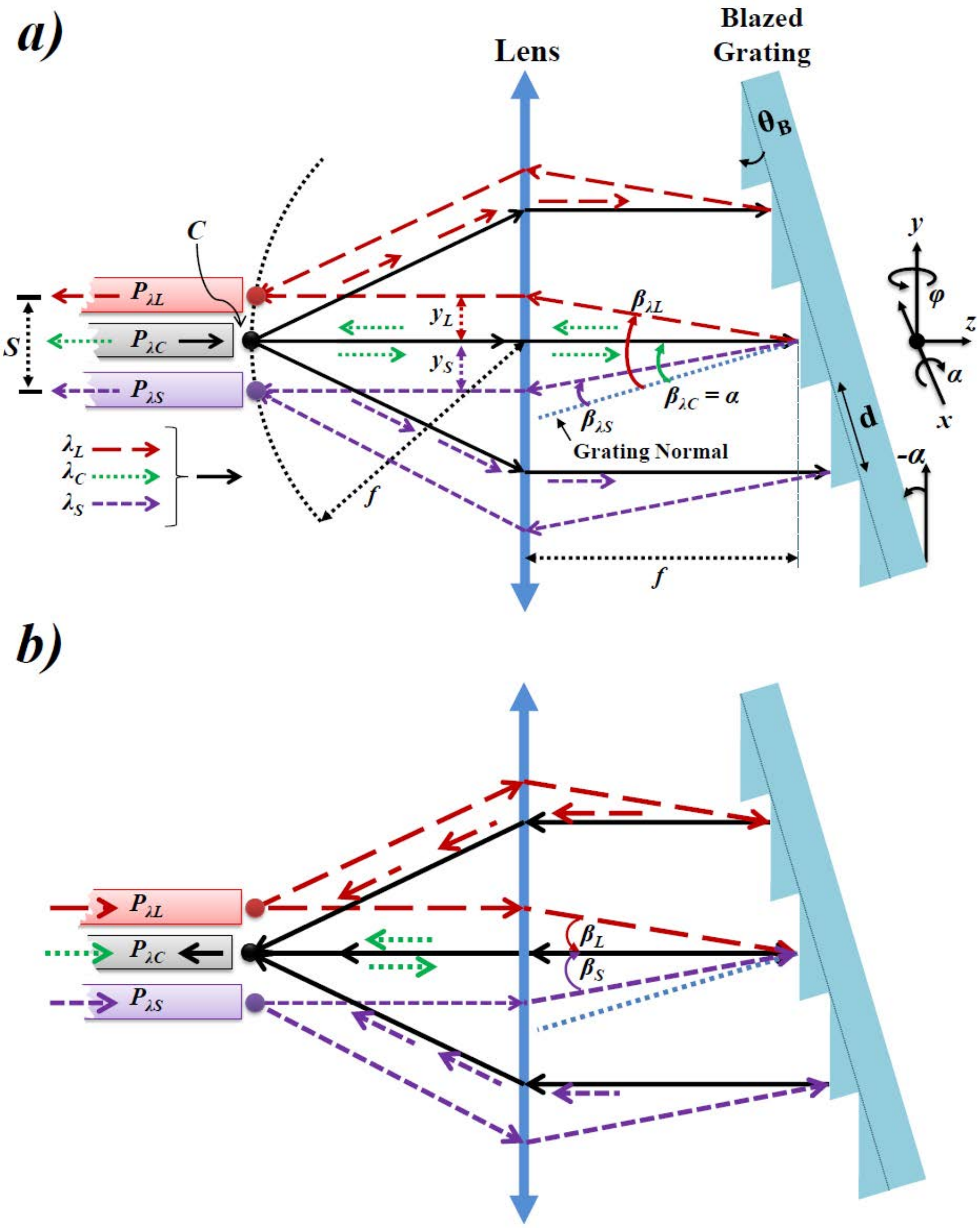

Fig. 5.11: Layout of SI–POF Mux/DeMux: a) ray tracing in demultiplexing and b) ray tracing in multiplexing.

Fig. 5.11 shows the layout of the proposed low–loss SI–POF Mux/DeMux. It consist of a reflective blazed diffraction grating with blazing angle θ_B, grating pitch d and tilt angle about the x–

axis α; and a collimating/focusing lens with effective focal length f and pupil diameter D_L. The light, which emerges (see **Fig. 5.11a**) from the common port, $P_{\lambda C}$, located at C point, contains the central wavelength λ_C, and the wavelengths of the extreme channels to be demultiplexed, which are referred as λ_S, for the shorter wavelength (at ~400 nm) and as λ_L, for the longer wavelength (at ~700 nm). The ports $P_{\lambda S}$ and $P_{\lambda L}$ are named on those channels wavelengths. The system is bidirectional. So the rays that emerge from $P_{\lambda S}$ and $P_{\lambda L}$ are multiplexed in $P_{\lambda C}$, as shown in **Fig. 5.11b.**

In this layout, a light beam is directed at the diffraction grating. The grating reflects back a plurality of collimated beams of light, each within a different wavelength (λ) range and at a specific direction defined by a diffraction angle β_λ given by (5.4).

5.5.1. Central Wavelength in Littrow Configuration

The Mux/DeMux is designed for λ_S and λ_L, and their required spatial separation, represented by $S = y_L + y_S$, see **Fig. 5.11a**. This design can be done optimizing the *ILs* of specific channels, as ports closest to $P_{\lambda C}$ have a better coupling efficiency. This can be used in order to fulfill the power requirements of a specific WDM system. In our general case, there are two main objectives: 1) minima *ILs* and 2) channels uniform *ILs* or all channels *ILs* near to the minimum value. The system shown in **Fig. 5.11** is bidirectional. Therefore, for simplicity, the design process is done only in the demultiplexing direction, see **Fig. 5.11a**.

The diffraction scheme is done using a Littrow configuration for λ_C, in order to obtain a symmetrical system, so that the fiber to fiber coupling efficiency between $P_{\lambda C}$ and the extremes ports will be approximately equal. In a Littrow configuration the diffracted beam (λ_C) is back–reflected in the incident beam direction. This means that $\beta_{\lambda C} = \alpha$, and from (5.4) this is achieved when:

$$\sin(\alpha) = m\lambda_C/(2d) \qquad (5.10)$$

In order to get the maximum diffraction efficiency at λ_C (for optimum *IL*), $\alpha = \beta_{\lambda C} = \theta_B$ needs to be met. In a bidirectional system, it is possible to prevent that some of the reflected light returns to the central port including a tilt angle in the diffraction grating about the $y-$axis (φ).

On the other hand, λ_S and λ_L have diffraction angles $\beta_{\lambda S}$ and $\beta_{\lambda L}$, respectively, see **Fig. 5.11a**. These angles are measured from $\beta_{\lambda C}$ as β_S and β_L, see **Fig. 5.11b**, and are given by:

$$\beta_{\{S,L\}} = \alpha - \sin^{-1}\left[m\lambda_{\{S,L\}}/d - \sin(\alpha)\right], \qquad (5.11)$$

The channels centered at λ_S and λ_L are spatially separated, in the y–axis direction, from the central point C, a distance given by:

$$y_{\{S,L\}} = f \tan\left(\beta_{\{S,L\}}\right), \tag{5.12}$$

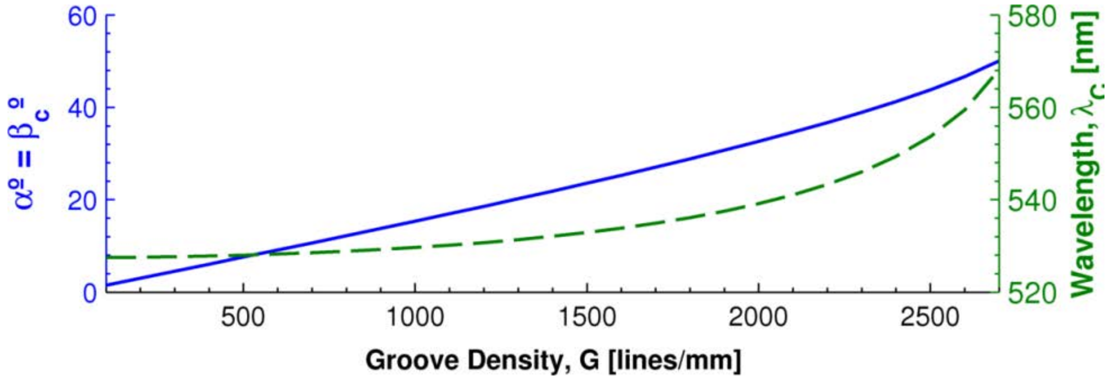

Fig. 5.12: Dependence of λ_C (dashed line, right axis) and the $\alpha = \beta_{\lambda C}$ (solid line, left axis) with the groove density for $\lambda_S = 405$nm and $\lambda_L = 650$nm.

λ_C is a wavelength that, considering a specific diffraction grating (fixed d and m), generates the same angular dispersion between λ_S and λ_L ($\beta_S = \beta_L$). Therefore, from (5.10) and(5.11), λ_C must satisfy the following condition:

$$\sin^{-1}\left[m(2\lambda_S - \lambda_C)/(2d)\right] + \sin^{-1}\left[m(2\lambda_L - \lambda_C)/(2d)\right] = 2\sin^{-1}\left[m\lambda_C/(2d)\right]. \tag{5.13}$$

The grating pitch (d) is usually expressed as the groove density in lines/mm or grooves/mm as $G = 1\times10^{-3}/d$. **Fig. 5.12** shows λ_C satisfying (5.13) and $\alpha = \beta_{\lambda C}$ from (5.10) versus the diffraction grating groove density, considering $\lambda_S = 405$ nm and $\lambda_L = 650$ nm. λ_C can be approximated to $\lambda_C = (\lambda_S + \lambda_L)/2 = 527.5$ nm for $G < 1200$ lines/mm (see **Fig. 5.12**).

5.5.2. Lens' f–number and Diameter

SI–POF Muxes/DeMuxes require a higher spatial separation between the different channels than the Muxes/DeMuxes for GOFs, due to the larger SI–POF cladding diameter (~1 mm). A 5 channel SI–POF Mux/DeMux requires $S = (\Delta y_S + \Delta y_L) > 5$ mm. This value is 8 times greater than the required GOFs spatial separation in 125 μm cladding diameter multimode fibers. As shown in (5.4) and (5.12), S can be increased by increasing G or f. However, the variations in G and f have an important impact in the system performance and cost. The design criteria for selecting the optimum optics (collimating/focusing lens), depending on S, G and f, for the efficient transmission of all the channels in multiplexing and demultiplexing is given below.

Beams in free space from SI–POFs have a diameter given by (5.8). The optics must be able to efficiently collimate and focus those beams. The NA range where the lens efficiently transmits the beam is represented as the *f*–number, defined as the ratio of *f* to the diameter of the lens' entrance pupil, D_L, expressed as:

$$f/\# = \frac{f}{D_L} \tag{5.14}$$

Therefore, in order to collimate the beam that emerges from a SI–POF with $NA = 0.48$ and diameter D_F, from (5.8), it is required an $f/\# < 0.91$, considering that $D_L = D_F$ in (5.14).

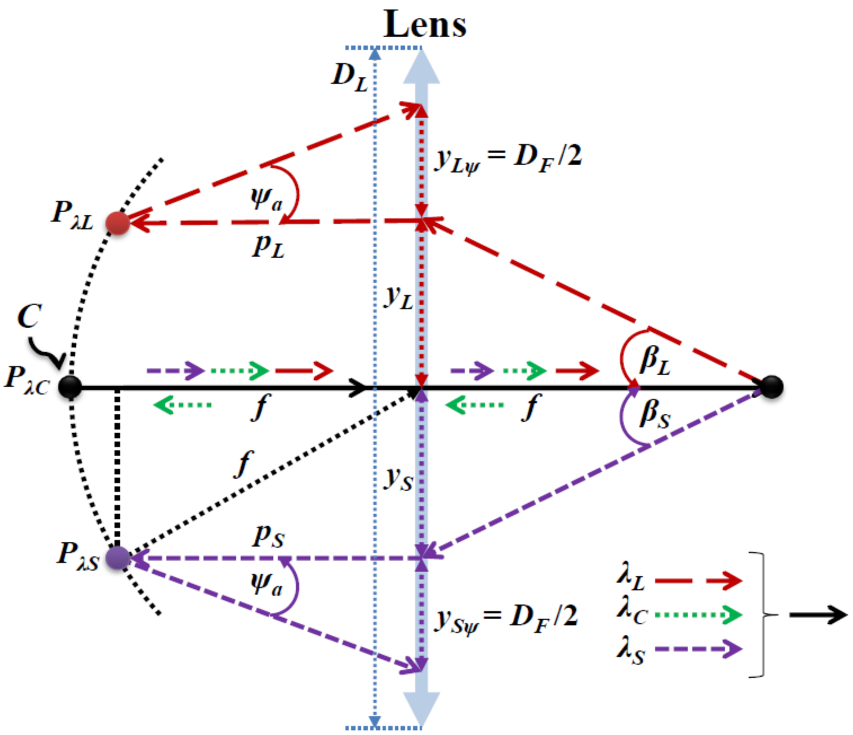

Fig. 5.13: Diameter of the lens required for the transmission of the extreme. *f*: focal length, β_S and β_L: diffraction angles for λ_S and λ_L.

The proposed diffraction scheme is symmetrical, if condition (5.13) is fulfilled. However, in practical cases it is normal that $y_S + y_{S\psi} \neq y_L + y_{L\psi}$, especially due to the variation of *f* with the wavelength, or due to choosing a λ_C that does not satisfy the symmetrical condition (5.13) to overcome the extreme channels (λ_S and λ_L) differences on their diffraction efficiencies. The optics must be able to transmit the multiple beams (from the different input/output ports) over its entrance pupil, with total diameter D_L. From **Fig. 5.13** the diameter must be greater than:

$$D_L \geq \max\left\{y_S + y_{S\psi}, y_L + y_{L\psi}\right\}, \tag{5.15}$$

where $y_{S\psi} = p_S \times \tan(\psi_a)$, with $p_S = (f^2 - y_S^2)^{1/2}$ and $\psi_a = \sin^{-1} NA$, and $y_{L\psi} = p_L \times \tan(\psi_a)$, with $p_L = (f^2 - y_L^2)^{1/2}$. p_S and p_L can be approximated to *f*, if $f >> y_S$ and $f >> y_L$ (e.g. with y_S and y_L <4 mm and $f >$ 20 mm, the relative error of this approximation is less than 2%). Considering this approximation, the required optics must have a:

$$f/\# \leq \min\left\{\frac{1}{\tan(\beta_S)+\tan(\psi_a)}, \frac{1}{\tan(\beta_L)+\tan(\psi_a)}\right\}, \tag{5.16}$$

Then, *f/#* is almost independent of *f* if $f >> y_S$ and $f >> y_L$. **Fig. 5.14** shows the *f/#* versus *G* from (5.16) with $\lambda_S = 405$ nm, $\lambda_L = 650$ nm and SI–POFs with *NA* = 0.48, for *m* = 1. It can be shown how the required *f/#* decreases as the grating *G* increases. Small *f/#* (lenses with small *f* and a large D_L) make the optical system more expensive. The *f/#* required both can be satisfied using aspheric lenses.

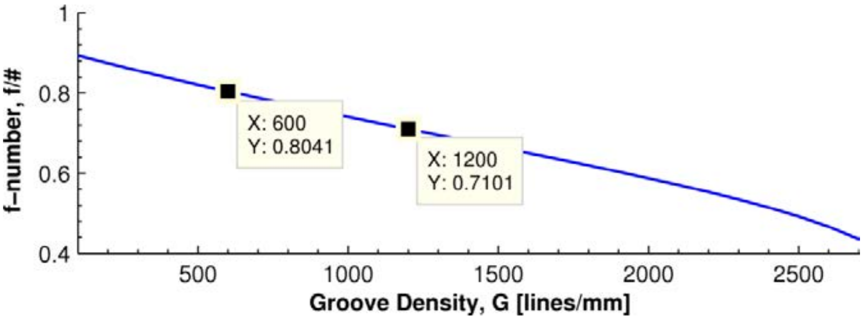

Fig. 5.14: *f*–number to transmit the resulting beams versus the groove density

5.5.3. Spatial Separation between Channels

Channels' spatial separation depends on *G* and *f*. Higher *G* values require more complex optics and can reduce the grating efficiency, due to the manufacturing tolerances **[19]**. But, the use of large *f* values results in bulky systems. Therefore, for a fixed *G*, the optimum *f* must be chosen in order to obtain the desired spatial separation between the different SI–POF channels in the smallest possible system. The tradeoff between *G* and *f* will be analyzed in the following examples. The objective is to separate more than 5 SI–POF channels (input/output ports), distributed in a spectrum with extreme wavelengths λ_S = 405 nm and λ_L = 650 nm, a distance greater than 1 mm between consecutive channels, therefore $S = y_S + y_L => 5$ mm.

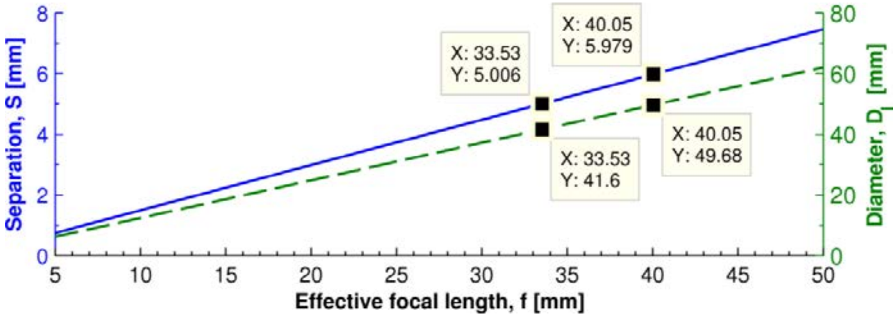

Fig. 5.15: Spatial separation (solid line, left vertical axis) and beam diameter (dashed line, right vertical axis) versus *f*. *G* = 600 lines/mm.

In the first example we consider a blazed diffraction grating with *G* = 600 lines/mm. **Fig. 5.15** shows the resulting spatial separation, *S*, and the entrance pupil diameter, D_L, of the lens required as a function of f, from (5.11) (5.12) and (5.15). In this figure, it can be shown that $S > 5$ mm can be obtained using a lens with $f > 33.5$ mm and $D_L > 41.6$ mm ($f/\# < 0.8$, see **Fig. 5.14** for G = 600 lines/mm).

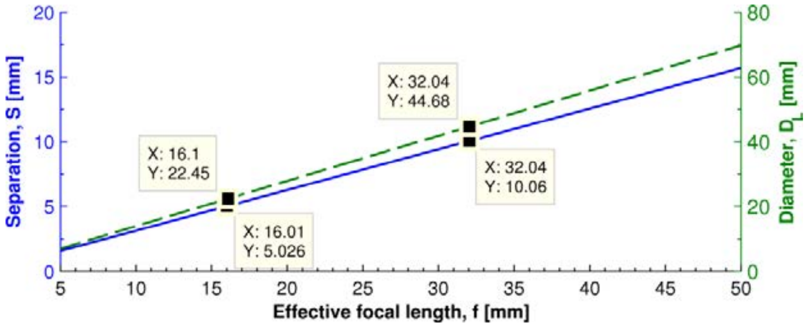

Fig. 5.16: Spatial separation (solid line, left vertical axis) and beam diameter (dashed line, right vertical axis) versus *f*. *G* = 1200 lines/mm.

In the second example it is analysed the effect of increasing G to 1200 lines/mm, the result is shown in **Fig. 5.16**. In this case, the required 5 mm total spatial separation can be achieved with $f >$ 16.1 mm and $D_L > 22.45$ mm ($f/\# < 0.71$, see **Fig. 5.14** for G = 1200 lines/mm). Economical aspherical lenses that fulfill these characteristics are available, making possible the implementation of this design. This configuration gives the option to design an efficient and compact SI–POF Mux/DeMux. This will be analyzed in **section 5.7.3**.

5.6. Five Channels SI–POF Mux/DeMux

Theoretical basics presented in the previous section (**section 5.5**) provide a guide to know the required optics to design efficient diffraction grating based Muxes/DeMuxes for SI–POFs, from the number of channels and the shorter and longer wavelength extremes of the considered spectral grid. Equations previously analyzed are based on ideal elements. An optimized design, based on the characteristics of real optical elements, is now reported.

In this section, the optimized design of a 5 channel Mux/DeMux for SI–POF WDM networks is presented. It is based on the first design example analyzed in **section 5.5.3** using the scheme shown in **Fig. 5.17**. The five input/output ports are named $P_{\lambda n}$, with $n = 1, 2\ldots, 5$, and their channels cover the spectral range of 405 nm to 650 nm: $\lambda_1 = \lambda_S = 405$ nm, $\lambda_2 = 466.25$ nm, $\lambda_3 = 527.5$ nm, $\lambda_4 =$ 588.75 nm and $\lambda_5 = \lambda_L = 650$ nm; which correspond to channels: 1, 4, 7, 10 and 13 of a previous SI–POF WDM grid proposal **[3]**. A distance greater than 1 mm between consecutive ports is required. This requirement can be fulfilled using an aspheric lens with $f = 40$ mm and $D_L = 50$ mm, as shown in **section 5.3.3**. In this case, the spatial separation between the extreme channels is about 6 mm; see **Fig. 5.15** (more than 1.2 mm between adjacent channels). The considered diffraction grating has an area of 50 mm × 50 mm, G = 600 lines/mm, $\theta_B = 8.62°$ (providing maximum efficiency at 500 nm) and diffraction efficiency between 56% and 68% (for non polarized light) in the range of 400 nm to 650 nm **[23]**.

Fig. 5.17: Layout of the five channel SI−POF Mux/DeMux.

Fig. 5.17 shows important aspects of the Mux/DeMux layout. The common port, $P_{\lambda C}$, is placed at the system center, *C* point (at $y = 0$ and $x = 0$). All the ports are separated 1 mm (SI−POF cladding diameter) from *C* in the *x*−axis direction; this separation is controlled by the diffraction grating tilt angle about the *y*−axis (φ), for a fixed *f* value. The distance of each port from *C* in the *y*−axis direction is defined by Δy_n. The distance of each port from *C* in the *z*−axis is defined by Δz_n. Finally, *p* and p_G are the distances from *C* to the Lens surface 1, and from the Lens surface 2 to the Grating surface, respectively, in the *z*−axis direction ($x = 0$ and $y = 0$). The design is done using a ray tracing optical design software. The main target is to optimize the fiber to fiber coupling efficiency (η_{Cn}) from the port $P_{\lambda C}$ to the different channels ($P_{\lambda n}$) ports. It is also targeted uniform *ILs* of the extreme channels ($P_{\lambda 1}$ and $P_{\lambda 5}$), by a proper selection of λ_C. **Table 5.4** summarizes the main characteristics of the proposed design, based on the schematic shown on **Fig. 5.17**.

TABLE 5.4: SPECIFICATIONS OF THE PROPOSED 5 CHANNELS MUX/DEMUX, $G = 600$ LINES/MM.

General characteristics						
Central wavelength, $\lambda_C = 540$ nm (for *IL* of $P_{\lambda 1}$ = *IL* of $P_{\lambda 5}$) $p = 30.479$ mm, $p_G = 15$ mm, $\alpha = \beta_{\lambda C} = -9.327^\circ$, $\varphi = -0.727^\circ$						
Input/Output Ports Configuration						
Channel/ Port $P_{\lambda n}$	λ_n [nm]	Δz_n [mm]	Δy_n [mm]	η_{Cn} [%]	η_{Gn} [%]	*IL* [dB] (Expected)
$P_{\lambda 1}$	405.00	2.325	−3.1	79	62	3.1
$P_{\lambda 2}$	466.25	0.984	−1.75	88	67	2.3
$P_{\lambda 3}$	527.50	0.130	−0.3	94	67	2.0
$P_{\lambda 4}$	588.75	–0.434	1.18	93	63	2.3
$P_{\lambda 5}$	650.00	–0.813	2.7	88	56	3.1
Spatial Separation						
$\lvert\Delta y_1 - \Delta y_2\rvert = 1.35$, $\lvert\Delta y_2 - \Delta y_3\rvert = 1.45$, $\lvert\Delta y_3 - \Delta y_4\rvert = 1.48$, $\lvert\Delta y_4 - \Delta y_5\rvert = 1.52$, $S = \lvert\Delta y_5 - \Delta y_1\rvert = 5.8$						

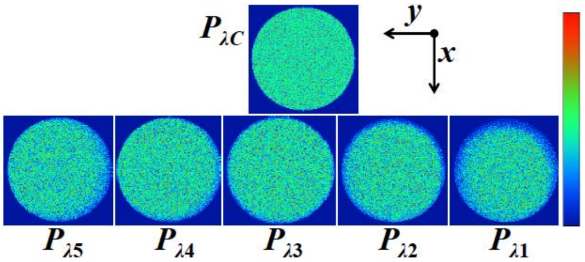

Fig. 5.18: Beam profiles of multimode fiber−to−fiber coupling efficiency calculations between $P_{\lambda C}$ and each input/output port.

The coupling efficiency (η_{Cn}) is calculated considering a circular object with 1 mm of diameter (central port, $P_{\lambda C}$), with *NA* of 0.5 (worst case) and a uniform radiation profile (worst case), see **Fig. 5.18**. This means that each point in the SI−POF surface is radiating with the same intensity and with a *NA* of 0.5. η_{Cn} is calculated from the rays that reach an image of 1 mm of diameter with $NA < 0.5$ using a geometric image analysis **[24]**. **Fig. 5.18** shows the resulting beam profile at the end face of each SI−POF input/ouput port and **Table 5.4** shows the respective values of η_{Cn}. Each *ch* expected *IL* is calculated with η_{Cn} and the approximated grating efficiency (η_{Gn}) taken from **[23]**. The spatial separation between adjacent *chs* is greater than 1.35 mm, with S = 5.8 mm (see **Table 5.4**). This value is in good agreement with values predicted on **Fig. 5.15**.

5.6.1. Experimental Characterization

The experimental setup is shown in **Fig. 5.19**. The distance from the fiber holders (H_0 and H_1) to the rear surface of the grating is about 65 mm and the setup diameter is about 55 mm. It has a common port, $P_{\lambda C}$ (H_0) and 5 input/output ports, $P_{\lambda n}$ (H_1), with $n = 1, 2\ldots, 5$. Each input/output port has its own focusing distance ($p + \Delta z_n$), see **Table 5.4**. The transfer function characterization is done by moving the H_1 holder to the different channel positions with a micrometric *xyz* translation stage.

Spectral measurements are done using a Halogen Light Source and a high speed Spectrometer with spectral resolution of about 4 nm in the spectral range from 360 nm to 886 nm (128 pixels), using the following procedure: 1) the light source is connected to the spectrometer using 3 m of SI−POF, with mode scramblers next to the source and to the spectrometer, this measurement represents the reference spectra (0 dB reference), 2) the 3 m of SI−POF is cut in half and each end is polished, 3) the SI−POF section attached to the light source is connected to the common port holder (H_0) and the SI−POF section that is attached to the spectrometer is connected to the input/output port holder (H_1), 4) The holder H_1 is positioned at the different port locations, from **Table 5.4**. It is important to note that the mode scramblers are used to improve measurements realiability and repeatability, by reducing the dependence of the wavelength pass–bands and *ILs* of the Mux/DeMux with the type of light source or the launch conditions, as shown in the discussion section (**section 5.7**).

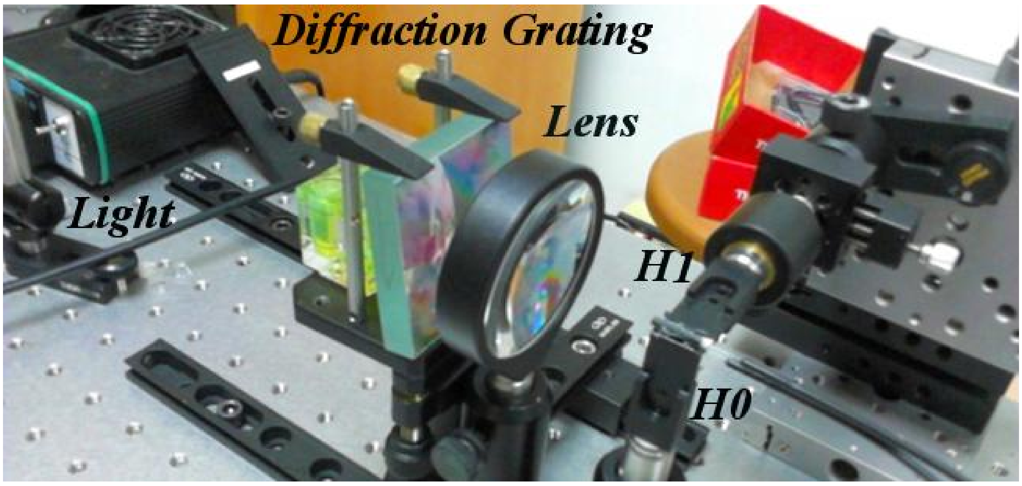

Fig. 5.19: Experimental setup of the 5 channel Mux/DeMux: H_0: holder of the common fiber, H_1: input/output fiber holder.

The transfer function of each input/output port in the spectral range from 390 to 700 nm is shown in **Fig. 5.20**. It can be seen that the *IL* per channel is less than 4 dB. This value includes the *IL* produced by two polished surfaces. Fresnel losses per PMMA–air interface is typically ~4% (Lens is AR Coated: 350 – 700 nm). It is also shown that the spectral bandwidth at –25 dB is higher than 41 nm. More specifically, those bandwidths at −25 dB are: 43 nm at $P_{\lambda 1}$, 43 nm at $P_{\lambda 2}$, 42 nm at $P_{\lambda 3}$, 41 nm at $P_{\lambda 4}$, 42 nm at $P_{\lambda 5}$. The spectral bandwidths at −3 dB are represented by shaded areas on **Fig. 5.20**. The −3 dB spectral bandwidth of each *ch* is greater than 30 nm. And the crosstalk attenuation (*CTA*) is greater than 30 dB. The *CTA* is a measure of the part of the optical power at each λ exiting from the port $P_{\lambda n}$ at wavelengths outside its 3 dB bandwidth.

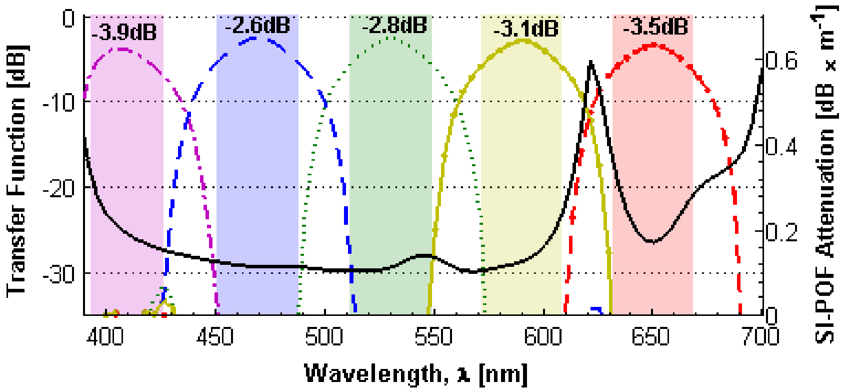

Fig. 5.20: Transfer function of the 5 channel Mux/DeMux: (dash–dot line) $P_{\lambda 1}$, (dashed line) $P_{\lambda 2}$, (dotted line) $P_{\lambda 3}$, (solid line) $P_{\lambda 4}$ (solid line with point markers) $P_{\lambda 5}$.

It is important to note that the measurements 40 dB below the reference signal are limited by the spectrometer sensitivity. It is also shown the SI–POF attenuation characterized with the same light source and spectrometer. The measured attenuation at 405, 470, 530, 588 and 650 nm is 0.21, 0.11, 0.11, 0.12 and 0.17 dB/ m, respectively. **Table 5.5** shows the summary of the proposed 5 channel Mux/DeMux parameters. This table also presents an experimental and expected *ILs* comparison. It can be seen that there is a good agreement between them.

TABLE 5.5: PERFORMANCE SUMMARY OF THE 5 CHANNEL MUX/DEMUX.

Channel/ Port $P_{\lambda n}$	λ [nm]	Band–pass at:		Insertion Losses	
		–3dB	–25dB	Experimental	Experimental –Expected$^{(1)}$
$P_{\lambda 1}$	405	30 nm	43 nm	3.9 dB	0.8 dB
$P_{\lambda 2}$	470	35 nm	43 nm	2.6 dB	0.3 dB
$P_{\lambda 3}$	530	38 nm	42 nm	2.8 dB	0.8 dB
$P_{\lambda 4}$	588	37 nm	41 nm	3.1 dB	0.8 dB
$P_{\lambda 5}$	650	37 nm	42 nm	3.5 dB	0.4 dB

Notes: (1) Expected *ILs* are given in **Table 5.4**.

5.7. Discussion and Remarks

The proposed diffraction scheme is used for designing an efficient and compact diffraction grating based 5 channel Mux/DeMux for visible WDM transmission over SI−POF technology. This Mux/DeMux is able to separate adjacent SI−POF channels a distance greater than 1.35 mm, with a total separation (between the extreme channels) of 5.8 mm. The spectral bandwidths at −3 dB and −25 dB are greater than 30 nm and 38 nm, respectively, in all the channels. The −25 dB spectral bandwidth indicates that if the transmitters used have a spectra bandwidth < 38 nm, there will be no channel crosstalk between any of them. The most important characteristics of the proposed Mux/DeMux are its low and uniform *ILs*. These characteristics allow the implementation of efficient transmission links based on visible WDM over SI−POF, since the power budget reduction, produced by the low *ILs*, does not impose a limit to the real improvement of the link capacity. Some authors **[6]**, **[14]**, set the *ILs* per channel to 5 dB as a reasonable value, for a real increase in the link transmission capacity using SI−POF WDM. The *ILs* of the 5 channel Mux/DeMux are less than 4 dB and loss uniformity is 1.1 dB. This Mux/DeMux is compact if compared to the current state−of−the−art and presents one of the best performances reported to date.

Another aspect that it must be highlighted is that none of the recently proposed SI−POF transmission links based on visible WDM are bidirectional **[5]**, **[4]**. This is due to the high *ILs* of the current Mux/DeMux proposals or due to their complexity and size. The proposed 5 channels Mux/DeMux allows the implementation of bidirectional links, made entirely with SI−POFs, including losses of less than 8 dBs (<4 dB in multiplexing and <4 dB in demultiplexing). It is important to note that a simple 4:1 SI−POF coupler have *ILs* up to 8 dB **[25]**.

From **Table 5.4** and **Table 5.5** is shown that there is a good agreement between the theoretical design and the experimental results. The small differences between the expected and experimental *ILs* are mainly due to the effects of Fresnel losses in each PMMA−air interface, to the imperfections in the POF surfaces and to the tolerances in the experimental setup.

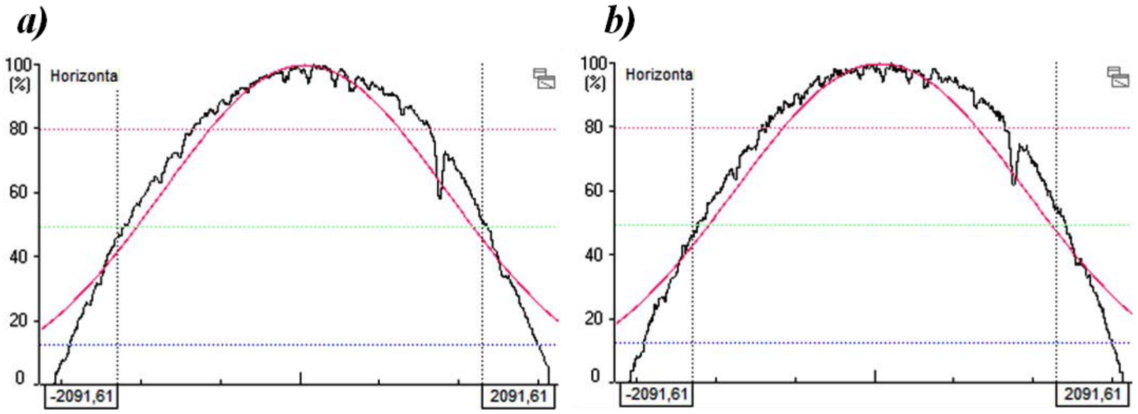

Fig. 5.21: Output beam profile measures: a) without mode scramblers (FWHM=4166.67μm); b) with mode scramblers (FWHM=4234.99μm).

The use of the mode scrambler at the POF input results in the same angular emission pattern independently of the chosen light source, which greatly improves the measurements realiability and repeatability **[25]**. **Fig. 5.21** shows the measurements of the horizontal beam profile at ~5 mm of $P_{\lambda C}$ when a blue LED source (IF E92) is launched on the input fiber, with and without mode scramblers. It can be shown that there is not a reduction in the beam profile. On the other hand, **Fig. 5.22** shows the characterization of the shortest and longest wavelength channels with and without mode scramblers. It can be seen that lower insertion losses, about −0.5 dB (at the central wavelength), are obtained when mode scramblers are not used. Therefore, the *IL* measured using mode scramblers can be considered as a limit of the worst expected value.

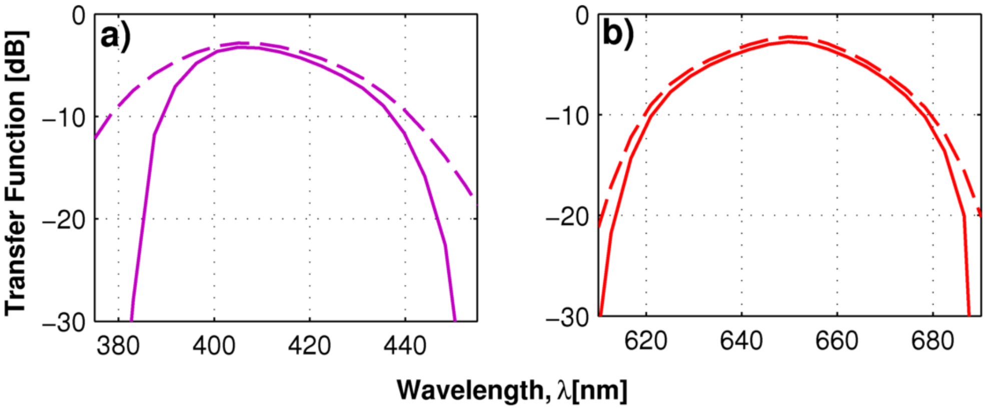

Fig. 5.22: Mux/DeMux characterization with (solid lines) and without (dashed lines) mode scramblers: a) port $P\lambda 1$ = 405 nm, b) port $P\lambda 5$ = 650 nm. *ILs* of the polished surfaces at the input/output ports are not included.

5.7.1. Tolerances and ports' central wavelength tuning

The tolerances of the proposed Mux/DeMux are mainly related to the position tolerance of the output ports, since it is the most sensitive parameter. The position of the output ports (holder H_1 in **Fig. 5.19**) is controlled with a micrometric *xyz* translation stage. The other distances in the system are adjusted with much less precision tools. The *ILs* of the extremes ports are the most sensitive to the variations in their optimized positions.

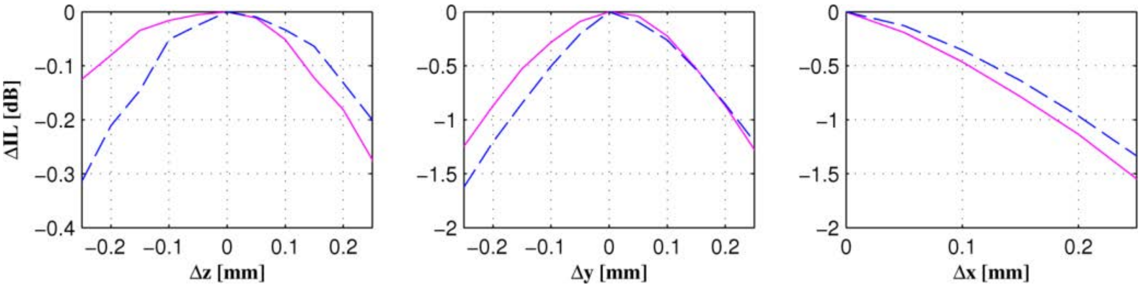

Fig. 5.23: Insertion losses variation (Δ*IL*) versus *z*, *y* and *x* positions: (solid line) 405 nm, (dashed line) 650 nm.

Fig. 5.23 shows the experimental characterization of the *ILs* variation (Δ*IL*) of the ports centered at 405 nm ($P_{\lambda 1}$) and 650 nm ($P_{\lambda 5}$) against the variations in the *z*, *y* and *x* direction from their optimized positions ($\Delta z_n + \Delta z$, $\Delta y_n + \Delta y$, $\Delta x_n + \Delta x$), see **Table 5.4**. It can be seen that the variations in the *z* direction of up to ±0.25 mm increase the *ILs* of both ports in less than 0.3 dB. On the other hand, the variations in the *y* and *x* direction have similar effects and a higher impact in the Δ*IL*. In order to maintain the Δ*IL* of both channels below 0.5 dB, the variations in the *y* and *x* directions must be less than ±0.1 mm and 0.1 mm, respectively.

Ports position shifts in the *y* direction have an almost linear effect in their central wavelength shifts, $\Delta\lambda$. **Fig. 5.24** shows the central wavelength of the input/output ports (H_1 from the experimental setup) as they are moved away from the central position. In can be seen that the experimental central wavelength variation is almost linear and is given by:

$$\Delta\lambda[nm] \approx -43.48 \times \Delta y[mm] \tag{5.17}$$

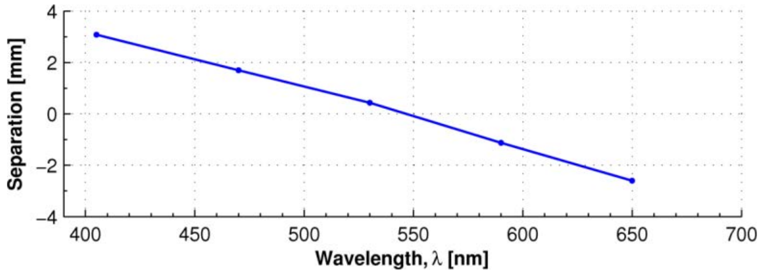

Fig. 5.24: Separation in the *y*−axis direction from the central point C versus the central wavelength at the output port versus it in 5 channel Mux/DeMux.

The separation between adjacent channels is greater than 1.35 mm. Therefore, in a final application, the central wavelength of each port shown in **Fig. 5.20** can be tuned up to $\Delta\lambda$ = 15.22 nm (Δy = 0.3 mm), in order to accommodate specific channels. Obviously, this fact reduces the band–pass bandwidths. However, even if the pass bandwidths values reported in **Table 5.4** are reduced by 15 nm, they still allow the use of laser sources, with little or no interference **[5]**.

5.7.2. Scalability: 8 channels Mux/DeMux

It is possible to increase the spatial separation between the extreme channels (λ_S = 405 nm and λ_L = 650 nm) to $S \approx 9$ mm using a diffraction grating with G = 1200 lines/mm and a lens with f = 35 mm and $D_L \geq 45$ mm ($f/\# < 0.71$, from **Fig. 5.14**), as shown in **Fig. 5.16**. This configuration is also experimentally tested. However, due to the low performance of the available diffraction grating at 405 nm, the design is optimized to accommodate 8 channels in the range from 430 nm to 655 nm. The experimental transfer function of each channel is shown in **Fig. 5.25**. In this case, λ_1 = 430 nm, λ_2 = 465 nm, λ_3 = 497 nm, λ_4 = 530 nm, λ_5 = 562 nm, λ_6 = 595 nm, λ_7 = 625 nm, λ_8 = 655 nm. The separation between consecutive channels is greater than 1.23 mm ($|\Delta y_1 - \Delta y_2|$ = 1.24, $|\Delta y_2 - \Delta y_3|$ = 1.23, $|\Delta y_3 - \Delta y_4|$ = 1.28, $|\Delta y_4 - \Delta y_5|$ = 1.29, $|\Delta y_5 - \Delta y_6|$ = 1.32, $|\Delta y_6 - \Delta y_7|$ = 1.25, $|\Delta y_7 - \Delta y_8|$ = 1.23), with total separation of S = 8.84 mm. The variation of the central wavelength, $\Delta\lambda$[nm], in all the channels is $\approx -25.6\times\Delta y$[mm] and the *ILs* are lower than 4.5 dB with uniformity of 1.3 dB. The size is reduced to about 57 mm of length by 50 mm of height. The spectral band–pass bandwidth at −3 dB of all the channels is greater than 20 nm, and their spectral band–pass bandwidths at −25 dB are between 12 nm and 21 nm (16 nm at $P_{\lambda1}$, 17 nm at $P_{\lambda2}$, 17 nm at $P_{\lambda3}$, 21 nm at $P_{\lambda4}$, 21 nm at $P_{\lambda5}$, 17 nm at $P_{\lambda6}$, 12 nm at $P_{\lambda7}$, 18 nm at $P_{\lambda8}$). In comparison with the 6 channel Mux/DeMux reported on **[5]**, this proposal is more compact and has half its *ILs* (having an improvement of up to 5 dB).

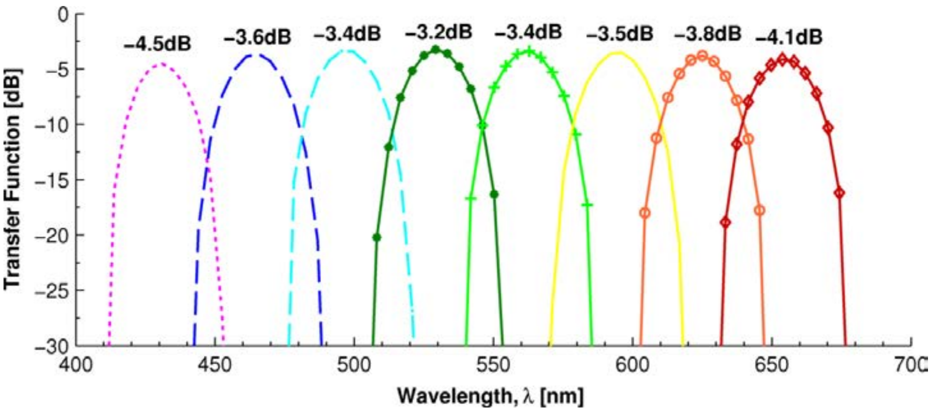

Fig. 5.25: Transfer function of a 8 channel Mux/DeMux. The channels' central wavelength are: λ_1 (dotted line), λ_2 (dashed line), λ_3 (dashed line with dot markers), λ_4 (solid line with dot markers), λ_5 (solid line with × markers), λ_6 (solid line), λ_7 (solid line with circle markers) and λ_8 (solid line with diamond markers).

5.7.3. Size Reduction

The good agreement between theoretical and experimental results allows projecting how much the system size can be reduced, keeping low *ILs*. It is possible to spatially separate 5 channels a total distance of about 6 mm using a diffraction grating with G = 1200 lines/mm, and a lens with f = 20 mm and diameter of D_L = 25 mm, as shown in the second example analyzed in **section 5.5.3** (**Fig. 5.16**). The lens requirement can be easily fulfilled using an aspheric lens ($f/\#$ < 0.71, from **Fig. 5.14**). In this case the Mux/DeMux size can be reduced to less than 37 mm in length and 30 mm in height, which represents a reduction factor of 1.75 in length and 2.2 in height.

5.7.4. Application in Self–Referencing Fiber–Optic Intensity Sensors

The advantages of optical metrology with plastic optical fiber have attracted the attention of the scientific community, as they allow the development of low–cost or cost competitive systems compared with conventional technologies **[26]**. Most plastic optical fiber sensors are based on detection of intensity variations. However, they need to use a self−referencing technique **[27], [28], [29]** to avoid false reading caused by light source fluctuations or other undesired losses.

The Mux/DeMux devices proposed in this work have a potential application for the implementation of intensity SI−POF sensors based on self–reference techniques using visible WDM schemes. As in the case of the SI–POF temperature sensor with dual–wavelength compensation of power fluctuations reported in **[30]**. This sensing system is based on the ratio of the output transmittances at two different wavelengths in a single macro–bend temperature sensor to avoid possible errors related to undesired optical power fluctuations. Reported transmittance measurements are done using a high–speed spectrometer. However, in a final application, the spectrometer can be replaced by low cost diffraction grating based Mux/DeMux in order to reduce the system power consumption, cost, complexity and to increase its portability.

5.8. References

[1] P. J. Pinzón, K. Heggarty, C. Vázquez and I. Pérez, "Diffraction grating–based Multiplexers for SI–POF networks," in *ICPOF*, Buzios, Brazil, 2013.

[2] P. J. Pinzón, I. Pérez and C. Vázquez, "Efficient Multiplexer/Demultiplexer for Visible WDM Transmission over SI–POF Technology," *IEEE/OSA Journal of Lightwave Technology,* vol. 33, no. 17, pp. 3711–3718, 2015.

[3] M. Jončić, M. Haupt and U. Fischer, "Standardization Proposal for Spectral Grid for VIS WDM Applications over SI–POF," in *Proceedings of POF Congress*, Atlanta, 2012.

[4] M. Jončić, R. Kruglov, M. Haupt, R. Caspary, J. Vinogradov and U. H. P. Fischer, "Four–Channel WDM Transmission Over 50 m SI–POF at 14.77 Gb/s Using DMT Modulation," *IEEE Photonics Technology Letter,* vol. 26, pp. 1328–1331, 2014.

[5] R. Kruglov, J. Vinogradov, S. Loquai, O. Ziemann, C.–A. Bunge, T. Hager and U. Strauss, "21.4 Gb/s Discrete Multitone Transmission over 50–m SI–POF employing 6–channel WDM," in *OFC*, San Francisco, CA, 2014.

[6] O. Ziemman and L. V. Bartkiv, "POF–WDM, theTruth," in 20*th International Conference on Plastic Optical Fibers*, Bilbao, Spain, 2011.

[7] Y. Shi, C. Okonkwo, D. Visani, E. Tangdiongga and T. Koonen, "Distribution of Broadband Services Over 1–mm Core Diameter Plastic Optical Fiber for Point–to–Multipoint In–Home Networks," *Journal of Lightwave Technology,* vol. 31, no. 6, pp. 874 – 881, March 2013.

[8] T. Fukushima and T. Sakamoto, "A 7×6 optical fiber grating demultiplexer–multiposition switch for 0.64–0.88 μm band," *J. Lightw. Technol.,* vol. 14, no. 5, p. 867–872, May 1996.

[9] W. J. Tomlinson III, "Wavelength division multiplexer". U.S. Patent 4.111.524, September 1978.

[10] A. A. M. Kok, A. M. S. Musa, A. Borreman, M. B. J. Diemeer and A. Driessen, "Completely multimode arrayed waveguide grating–based wavelength demultiplexer," in *IEEE Region* 8 *EUROCON* 2003*, Computer as a Tool*, Ljubljana, Slovenia , 2003.

[11] H. P. A. van den Boom, W. Li, P. K. van Bennekom, I. T. Monroy and G. –D. Khoe, "High–capacity transmission over polymer optical fiber," *IEEE Journal of Selected Topics in Quantum Electronics,* vol. 7, no. 3, pp. 461 – 470, May/Jun 2001.

[12] S. Junger, W. Tschekalinskij and N. Weber, "POF WDM Transmission System for Multimedia Data," in *ICPOF*, Tokyo, Japan, 2002.

[13] D. Lutz, M. Haupt and U. H. P. Fischer, "Demultiplexer for WDM over POF in prism–spectrometer configuration," in *Photonics and Microsystems,* 2008 *International Students* *and Young Scientists Workshop*, 2008.

[14] L. V. Bartkiv, Y. V. Bobitski and H. Poisel, "Optical demultiplexer using a holographic concave grating for POF–WDM systems," *Optica Applicata,* vol. XXXV, no. 1, p. 59–66, 2005.

[15] S. Höll, M. Haupt and U. H. P. Fischer, "Design and development of an injection–molded demultiplexer for optical communication systems in the visible range," *Applied Optics,* vol. 52, no. 18, p. 4103–4110, 2013.

[16] M. Haupt and U. H. P. Fischer, "Multi–colored WDM over POF system for Triple–Play," in *SPIE* 6992, 2008.

[17] M. Jončić, M. Haupt and U. H. P. Fischer, "Investigation on spectral grids for VIS WDM applicationsover SIPOF," in *ITG Symposium: Photonic Networks*, Leipzing, Germany, 2013.

[18] P. J. Pinzón, C. Vázquez, I. Pérez and P. Lallana, "Design and Analysis of a WDM System for Multi–Gbit/s Transmission over 50 m of SI–POF," in *ICPOF*, Hiyoshi, Yokohama, 2014.

[19] C. Palmer, Diffraction Grating Handbook, 6th ed ed., Newport Corporation, 2005.

[20] E. G. Loewen and E. Popov, Diffraction Gratings and Applications, Ilustrated ed., CRC Press, 1997.

[21] R. Gratings, "Grisms (Grating Prisms)," [Online]. Available: http://www.gratinglab.com/Information/Technical_Notes/TechNote5.aspx. [Accessed 31 March 2015].

[22] R. K. Wade, "Wavelength division multiplexing/demultiplexing device using dual polymer lenses". US Patent US 6.181.853 B1, 2001.

[23] Thorlabs, March 2015. [Online]. Available: https://www.thorlabs.de/images/tabImages/500_600_Ruled_Grating_Efficiency_Graph_780.gif .

[24] Zemax, "How to Model Coupling Into a Multi–Mode Fiber," 2015. [Online]. Available: 2015. [Accessed 1 June 2015].

[25] O. Ziemann, J. Krauser, P. E. Zamzow and W. Daum, POF Handbook: Optical Short Range Transmission Systems, 2nd ed., Springer, 2008.

[26] L. Bilro, N. Alberto, J. L. Pinto and R. Nogueira, "Optical sensors based on plastic fibers," *Sensors,* vol. 12, p. 12184 – 12207, 2012.

[27] D. S. Montero, C. Vázquez, J. Baptista, J. Santos and J. Montalvo, "Coarse WDM networking of self–referenced fiber–optic intensity sensors with reconfigurable characteristics," *Optics Express,* vol. 18, no. 5, pp. 4396–4410, March 2010.

[28] D. S. Montero, C. Vázquez, I. Möllers, J. Arrúe and D. Jäger, "A Self–Referencing Intensity Based Polymer Optical Fiber Sensor for Liquid Detection," *Sensors,* vol. 9, pp. 6446–6455, 2009.

[29] G. Murtaza and J. M. Senior, "Referencing Schemes for Intensity Modulated Optical Fiber Sensor Systems," in *Optical Fiber Sensor Technology*, Springer US, 2000, pp. 303–336.

[30] A. Tapetado, P. J. Pinzón, J. Zubia and C. Vázquez, "Polymer Optical Fiber Temperature Sensor With Dual–Wavelength Compensation of Power Fluctuations," *Journal of Lightwave Technology,* vol. 33, no. 13, pp. 2716–2723, 2015.

Chapter VI:

Visible WDM System for Real–Time Multi–Gbit/s Bidirectional Transmission in SI–POF

In this chapter, the design, analysis and test of a real–time data communication system based on a step−index plastic optical fiber link (SI−POF) of up to 50 m and a 5–channel visible wavelength division multiplexing (WDM) scheme is presented. Special care in implementing low insertion loss multiplexers/demultiplexers is carried out to allow for greener solutions in terms of power consumption. The system performance and its capacity for bidirectional transmission have been experimentally tested using the extreme channels of the 5–channels grid. The results show that the system can establish a real–time bidirectional link with connection speed of up to 2 Gbit/s (1 Gbit/s per channel) with bit error rate $<1\times10^{-10}$ over 50 m of SI−POF, and it has the potential for expanding its data transmission speed up to 5 Gbit/s. It is also demonstrated that each channel in the proposed system can be configured independently as uplink or downlink, and that its energy consumption is lower than in previous SI−POF WDM proposals, due to the low losses multiplexer/demultiplexer devices and the errorless transmission.

6.1. Introduction

Primarily due to the ‘do–it–yourself’ installation, easy maintenance and high bending tolerance, large core step–index (SI) plastic optical fibers (POFs) are considered more suitable than 50 μm core diameter multimode glass optical fibers (GOFs), perflourinated POFs or graded index POFs in many short–range applications **[1]**. Specifically, in scenarios such as Local Area Networks (LANs), In–Home and Office networks **[2]**, as well as in Automotive **[3]** and Avionic multimedia buses, or in Data Center interconnections **[4]**. Today, the volume of data transmitted by short–range networks, especially by In–Home networks, both to the Internet Service Provider and between different terminals, is increasing beyond the Gbit/s, exceeding the capabilities of current networking technologies (twisted pair, coax cable, Ethernet Cat–5 cable, powerline and wireless) **[5]**. On the other hand, SI–POF technology has also an important application niche in providing a solution to the exponential growth of infotainment devices within the car, along with the proliferation of ADAS (Advanced Driver Assistance Systems) that have created a demand for a more efficient way to interconnect devices within the automobile. ADAS global market is substantially growing in recent years and requires increasing the available bandwidth, nowadays up to 1 Gbit/s **[6]** and potentially in the near future to be increased up to 5 Gbit/s **[7]**.

Initially, transmission with SI–POF has been realized with a single channel, typically at 650 nm, reaching data rates of 100 Mb/s over links of up to 275 m **[8]** and even 531 Mb/s over links of 100 m **[9]**. However, Gbit/s transmission capacity of SI–POF links has been widely demonstrated in recent years, using single channel based systems with different advanced modulation formats and/or adaptive electrical equalization techniques. Reported simulations shows that data rates of 1.25, 2.1 **[10]** and even 6.2 Gbit/s **[11]**, via up to 50 m, can be reached using single channel links, with NRZ, CAP–64 and QAM512 modulations, respectively, with transmitters (*Txs*) based on light emitting diodes (LEDs) **[10]** or laser diodes (LDs) **[11]**. More recent experimental systems demonstrate data rates of Multi–Gbit/s up to 50 m with LD *Txs* **[12]** and up to 3 Gbit/s over 25 m using 8–PAM with LED *Txs* **[13]**. Moreover, fully integrated systems that offer real−time SI−POF links at 1 Gbit/s via up to 50 m using 16−PAM modulation with a LED *Tx* have also been reported **[14]**.

But SI–POF’s data transmission capacity needs a greater exploitation to meet user requirements for higher–data rates with a low power consumption and low cost. This generates an interest in the development of new systems for Multi–Gbit/s transmission over SI–POF, including new transmitters and receivers, and new standards based on SI–POF **[3]**, **[5]**.

After exploiting the capabilities of a single channel transmission, visible wavelength division multiplexing (WDM) is proposed as a solution to expand the transmission capacity of SI–POF based systems. To date, there are several proposals of modulation methods **[10]**, spectral grids **[15]** and multiplexer/demultiplexer devices (Muxes/DeMuxes) **[16]** that allow to implement transmission systems based on visible WDM at data rates of Multi−Gbit/s over SI–POF links **[17]**. Visible WDM transmission over SI–POF is based on a wide spectral grid with channels between 400 and 700 nm, using LD or LED based transmitters **[18]**. Visible WDM systems using offline–processed DMT modulation, and data rates up to 14.77 **[19]** and 21 Gbit/s **[20]** over 50 m of SI−POF, and 8.26 Gbit/s over 75 m **[21]**, with 4 or 6 channels in a single direction, LD based transmitters and bit error rate (BER) of 1×10^{-3}, have been recently reported.

Apart from the physical transmission characteristics of SI–POF, it is equally important to consider the optical components introduced to deploy advanced WDM–based architectures. A typical WDM optical communication link requires, at the very least, both a Mux and a DeMux which provide additional insertion losses into the system. This results in a decrease of the available optical power budget of the system leading to a bit–rate penalty. Most of the SI–POF based Mux/DeMux prototypes reported in literature have been developed on the basis of interference filters and diffraction gratings. However, the use of gratings for WDM–SI–POF applications probably leads to the best results in terms of insertion loss and channels number, as have been shown in **Chapter 5**, where configurations for Muxes/DeMuxes of up to 8 channels with insertion losses of less than 4.5 dB have been reported **[22]**.

In this chapter, the design of a real−time visible WDM system over SI−POF for an efficient performance in terms of Ethernet Data Throughput × length ($D_T\times L$) and energy consumption is presented. The system is bidirectional and each channel can be individually configured as uplink or downlink, unlike other single wavelength bidirectional SI−POF links **[23]**. A 5 channel visible WDM scheme is implemented. The channels multiplexing and demultiplexing is performed using Mux/DeMux devices with low insertion losses and high crosstalk, based on reflective diffraction gratings. The system performance is tested using the extremes channels of the considered spectral grid (405 nm and 650 nm). The experimental results and the analysis done over the SI−POF WDM system shows that the total insertion losses are between 14.5 and 21.5 dB per channel on a 50 m SI−POF link. The performed transmission tests show that the system can establish a real–time bidirectional or unidirectional link at data rates of 2 Gbit/s using 2 channels (1 Gbit/s per channel) over 50 m of SI−POF with BER lower than 1×10^{-10}. The system has the potential of expanding the transmission data rate up to 5 Gbit/s in longer distances, with better energy efficiency than recent proposals. This represents a real improvement in the performance of commercial **[14]** and experimental transmission systems **[10]**, **[11]**.

The chapter is organized as follows. First, the more common multi−level modulation formats for Gbit/s transmission over SI−POF are briefly described. Then, the data transmission system is described in detail. Next, the experimental characterization of the proposed visible WDM SI−POF transmission system, using the channels ch_1 = 405 nm and ch_5 = 650 nm, is presented, including the characterization of a reference single channel link. The performance of the proposed system is compared with the reference link in terms of: impulse response and frequency response, data transmission speed, bit error rate, signal to noise ratio and optical power link budget. An energy efficiency comparison with recently proposed visible WDM systems of 50 m is presented. Finally, the more relevant results are discussed.

6.2. Multi−Level Modulation Formats for Gbit/s Transmission over SI−POF

SI−POF experiences huge bandwidth limitations since its bandwidth distance product is about 50 MHz × 100 m. Therefore, Gbit/s communications over distances from 50 to 100 m with SI−POF require the adoption of mechanisms for increasing the bandwidth efficiency, which are widely adopted for example in copper or radio communications and that are increasingly used in optical communications, such as multi−level modulation schemes or equalizations **[24]**.

Conventional optical communications adopt On−Off Keying (OOK), that is a binary amplitude modulation, thus transmitting one bit per symbol and that in optics can be simplified switching the source ON when transmitting symbol 1 and OFF when transmitting symbol 0 **[24]**. With this simple modulation if we try to transmit 1 Gbit/s we will need to switch on and off the LED at least 10^9 times per second, which translates into a device bandwidth requirement of around 500 MHz.

In recent years, spectrally efficient modulation formats such as PAM (Pulse Amplitude Modulation), CAP (Carrierless Amplitude Phase) or DMT (Discrete MultiTone) have been successfully applied to SI−POF systems in order to transmit data with rates exceeding 1 Gbit/s over distances from 50 to 100 m **[25]**.

PAM is a competitive alternative baseband, which provides a one−dimensional multi−level signal encoding. The relatively low power consumption and complexity of the PAM−based transceiver offers a good potential for a cost−effective solution **[26]**. 10 Gbit/s data transmission over 25−m SI−POF link is reported in **[27]**.

DMT modulation technique used as a basic modulation algorithm for digital subscriber lines (DSL) provides high spectral efficiency, flexibility and tolerance to inter−symbol interference (ISI). But while this DMT modulation format makes good use of the available bandwidth, it requires considerable signal processing at the transmitter and receiver, due to the requirements of discrete Fourier transform (DFT) and inverse discrete Fourier transform (IDFT), which is translated in high power consumption **[26]**. It also adds latency to the transmission due to the block−wise nature of the DMT modulation format **[27]**. Data rates of about 3.5 Gbit/s (per channel) have been recently demonstrated using DMT over 50 m SI−POF links **[19]**, **[20]**.

CAP modulation, which is also used for DSL, employs two orthogonal signature waveforms to transmit two−dimensional symbols. CAP allows simpler implementation than DMT without the requirement of DFT and IDFT. Promising theoretical and experimental results in POF−based links were published in recent years **[10]**, **[28]**. A successful 2.1 Gbit/s transmission with 64−CAP over 100−m POF with a double step−index profile was reported in **[29]**.

Recent studies have positioned PAM as a promising candidate for next−generation, low−latency Multi−Gbit/s transmission over large core 1 mm polymethylmetacrylate (PMMA) POF **[25]**, **[26]**, **[30]**. However, the modulation performance is also dependent of the error correction and equalization techniques. The POF−PLUS European Project **[2]** shows that the complex modulation formats do not give significant advantage with respect to OOK when equalization is already adopted **[24]**.

6.3. Data Transmission System

A real−time bidirectional link between two points (e.g. two personal computers, PC1 and PC2) at data rates of multiple Gbit/s using *N* visible WDM SI–POF channels is designed from a fully integrated single channel system at 1 Gbit/s over 50 m and novel Mux/DeMux designs with low insertion losses and high crosstalk.

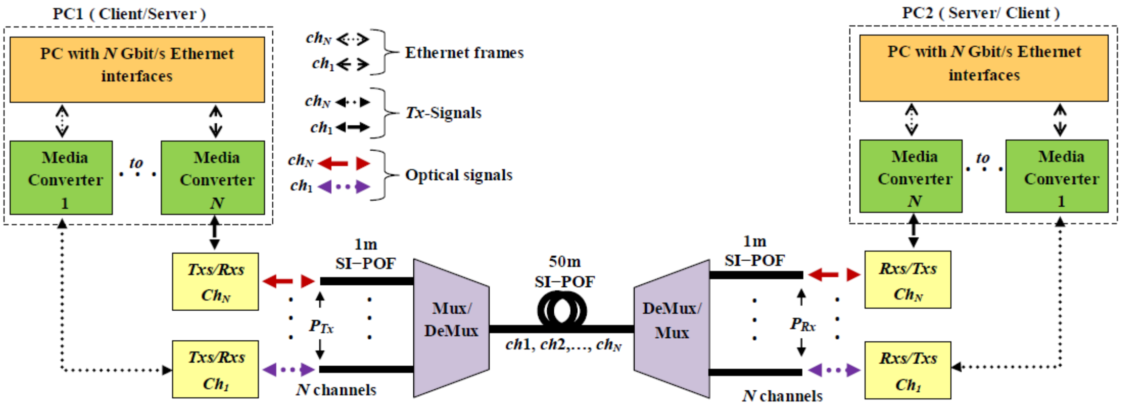

Fig. 6.1: Transmission scheme of the proposed SI–POF visible WDM system with *N* channels between 400 and 700 nm.

Fig. 6.1 shows the general description of the proposed WDM SI−POF transmission system. The objective is to obtain a real−time bidirectional link between two points (client and server) at data rates of Multi−Gbit/s using *N* channels. The PCs are equipped with *N* Gbit/s Ethernet interfaces in combination with *N* Media Converters (MCs) used to generate and to read the transmitted data bits, respectively. The MCs transform the standard Gbit/s Ethernet frames into 16−PAM signals (called *Tx*−signals), and vice versa. In the transmitters (*Txs*), the different *Tx*−signals modulate the Laser Diode (LD) or the Light Emitting Diode (LED) of the respective channels (ch_1, ch_2,... ch_N). Two diffraction grating based Muxes/DeMuxes are used, one to transmit the *N* channels over the SI–POF link of up to 50 m, and other to split the different channels to their respective receivers (*Rxs*) at the end of the link. The optical signals are converted back to electrical signals (*Tx*−signals) at the receivers by using a pin–photodiode based receiver, and finally, the Ethernet frames are recovered by the MCs.

6.3.1. Media Converters and Modulation Format

MCs are part of a fully integrated system **[14]** that is able to establish a 1 Gbit/s link over up to 50 m of SI−POF using a LED based transmitter at 650 nm with average power of –3.15 dBm (power coupled to the fiber), total insertion losses up to 15 dB (at 25ºC) and a pin–photodiode receiver with sensitivity of –20 dBm (at 650 nm and 1 Gbit/s operation). In the proposed system, the LED transmitter of each MC is replaced by different LD or LED based transmitters. Therefore, the MCs are only used to encode the Ethernet frames in to 16–PAM signal, and vice versa. The Ethernet frames are encoded in to 16−PAM symbols using a technique called Multi−Level Coset Coding (MLCC). Details about the signal encoding can be found in **[31]**. **Fig. 6.2** shows an example of the 16–PAM signal generated by the MCs (*Tx*–signal). This is a differential signal composed by the single–ended signal Tx^+ and Tx^-. The channels detection is done using the SI–POF receiver available in the MC boards.

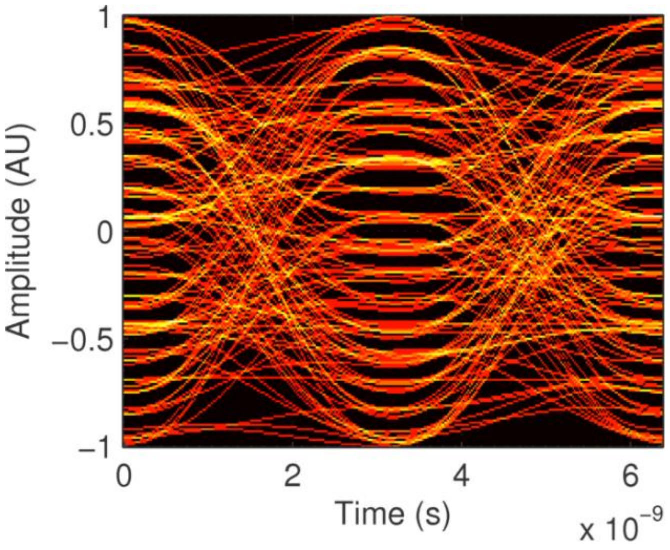

Fig. 6.2 (a) Eye diagram of the 16–PAM signal generated by the MCs (*Tx*–signal). This example is obtained using a digital filter over the measured single–ended *Tx*–signal.

6.3.2. Receiver

The receiver is a complete monolithically–integrated linear optoelectronic receiver that comprises an integrated pin–photodiode with a diameter of 390 μm and the required amplifiers and logic. The receiver features a highly linear trans–impedance amplifier for signals with a wide average optical input power range of up to 0 dBm at a wavelength of 670 nm. At the highest trans–impedance a bandwidth of 30 MHz is attained **[14]**. The MCs evaluation boards require a minimum power of about –20 dBm (at 650nm) at the receiver (including 2 dB losses of receiver coupling loss) to establish a 1 Gbit/s link.

6.3.3. Transmitters

A five channels spectral grid and the characteristic of commercially available LDs or LEDs are considered for the transmitters design. The central wavelengths of the channels ch_1, ch_2, ch_3, ch_4 and ch_5 are 405 nm, 473 nm, 520 nm, 590 nm, and 650 nm, which are close to channels number 1, 4, 7, 10 and 13 of the visible WDM SI–POF grid proposal of **[15]**, respectively. The main characteristics of the light sources considered are shown on **Table 6.1**.

TABLE 6.1: CHARACTERISTICS OF THE LIGHT SOURCES CONSIDERED FOR THE TRANSMITTERS DESIGN.

Model	Central λ [nm]	Current [mA] Threshold	 Operation	Optical power	Notes
DL5146–101S	405	35	70	40 mW (16.0 dBm)	(1)
L473P020MLD	473	50	100	20 mW (13.0 dBm)	(1)
PLT5 520_B4_5_6	520	50	120	30 mW (14.8 dBm)	(1)
LED591E	590	––	20	2 mW (3.0 dBm)	(2)
L650P0007	650	20	28	7 mW (8.5 dBm)	(1)

Notes: (1) there are LED sources available on similar wavelengths; (2) there are no LD sources available on similar wavelengths.

6.3.4. Five Channel Multiplexers/Demultiplexers

The multiplexing and demultiplexing is performed using low *ILs* 5–channel Mux/DeMux devices based on reflective diffraction gratings. Each Mux/DeMux is based on a collimator/focusing lens and a reflective diffraction grating. The experimental setup used is shown in **Fig. 6.3a**. Muxes/DeMuxes have a total size of about 55 mm in length and 65 mm in diameter. The design and characterization of the 5–channel Muxes/DeMuxes implemented in the proposed WDM system are presented in detail on **Chapter 5**.

The experimental transfer function of each channel is shown in **Fig. 6.3b**. The central wavelengths of the channels ch_1, ch_2, ch_3, ch_4 and ch_5 are λ_1 = 405 nm, λ_2 = 470 nm, λ_3 = 530 nm, λ_4 = 588 nm and λ_5 = 650 nm, respectively. The separation between consecutive channels is greater than 1.35 mm, with total separation of S = 5.8 mm between the extremes channels (ch_1 and ch_5). The variation of the central wavelength, $\Delta\lambda$[nm] with respect to the vertical position of the each port (y axis direction) is $\approx -43.48\times\Delta y$[mm]. Therefore, the transfer function of each port can be tuned more than 15.22 nm (Δy = 0.3 mm), in order to accommodate specific channels, as is discussed in **section 5.7.1**. The *ILs* are lower than 4 dB with uniformity of 1.1 dB. The spectral band–pass bandwidth at −3 dB of all the channels is greater than 30 nm, and their spectral band–pass bandwidths at −25 dB are greater than 38 nm. In **Fig. 6.3b**, it is also shown the attenuation of the SI–POF fiber used in the link. The fiber attenuation at 405, 470, 530, 588 and 650 nm is 0.21, 0.11, 0.11, 0.12 and 0.17 dB/m, respectively (measurements are described in **section 5.6.1**). **Table 6.2** shows the characteristics summary of the 5 channel Mux/DeMux design used.

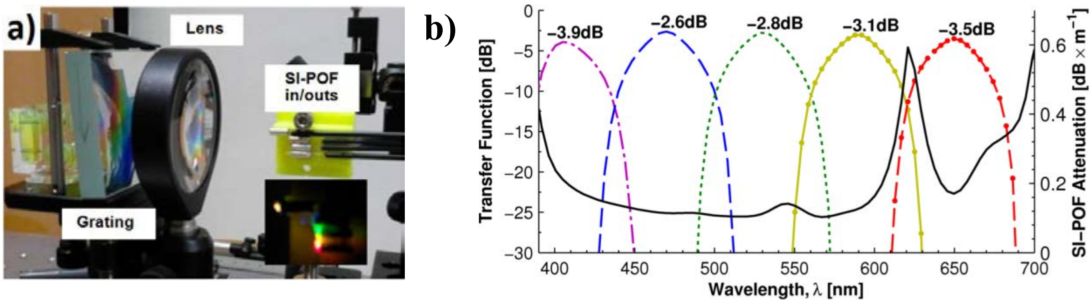

Fig. 6.3 (a) Mux/DeMux experimental setup. (b) Transfer function of a Mux/DeMux configuration with 5 ports and 1 common fiber (left axis) and measured SI−POF attenuation (right axis, solid line).

TABLE 6.2: PERFORMANCE SUMMARY OF THE 5 CHANNEL MUXES/DEMUXES.

Channel/ Port $P_{\lambda n}$	λ [nm]	Band–pass at:		Insertion Losses	Distance to adjacent port (vertical direction, *y*–axis)
		–3dB	–25dB		
$P_{\lambda 1}$	405	30 nm	43 nm	3.9 dB	1.35 mm
$P_{\lambda 2}$	470	35 nm	43 nm	2.6 dB	1.45 mm
$P_{\lambda 3}$	530	38 nm	42 nm	2.8 dB	1.48 mm
$P_{\lambda 4}$	588	37 nm	41 nm	3.1 dB	1.52 mm
$P_{\lambda 5}$	650	37 nm	42 nm	3.5 dB	——

6.4. Experimental Characterization of the Proposed WDM Transmission System

In this section, the experimental characterization of the visible WDM SI−POF transmission system is presented. The generation of the transmitted signals and its recovering are performed using Media Converters boards, specially designed for the transmission of a single channel over SI–POF links. For this reason, the characterization of a single channel link based entirely on the MC boards, as the reported in **[14]** and **[32]**, is first performed. This single channel link is used as the reference for the performance evaluation of the visible WDM system. The objective is to demonstrate that the proposed system can improve the performance, in terms of data rate × length (R×L), of those systems that transmit a single wavelength, in a bidirectional link of up to 50 m. Therefore, the performance of the proposed system will be compared with the reference link in terms of: impulse response, frequency response, data transmission speed, bit error rate, signal to noise ratio and optical power link budget.

6.4.1. Single Channel Link: Reference Link

The single channel link is established and characterized. It is done using two MC evaluation boards as the one reported in **[14]**, but the transceivers are separated from the MCs in order to get access to the transmitted and the received signals, to be used in the proposed WDM system.

MCs are connected to the transceivers using 6–inch coaxial cables, as shown in **Fig. 6.4**. The differential–signals of transmission Tx^+ and Tx^- (*Tx*–signals) are connected from the first MC (client) to the transmitter (*Tx*) and the differential–signals Rx^+ and $Rx^-$are connected from the receiver (*Rx*) to the second MC (server). These interconnections produce a small degradation in the signal to noise ratio of the transmitted and received signals, and in the overall performance of the link compared with its typical characteristics **[14]**. For simplicity, only the uplink loop (client to server) is characterized. The downlink loop is done using coaxial cables, as shown in **Fig. 6.5**.

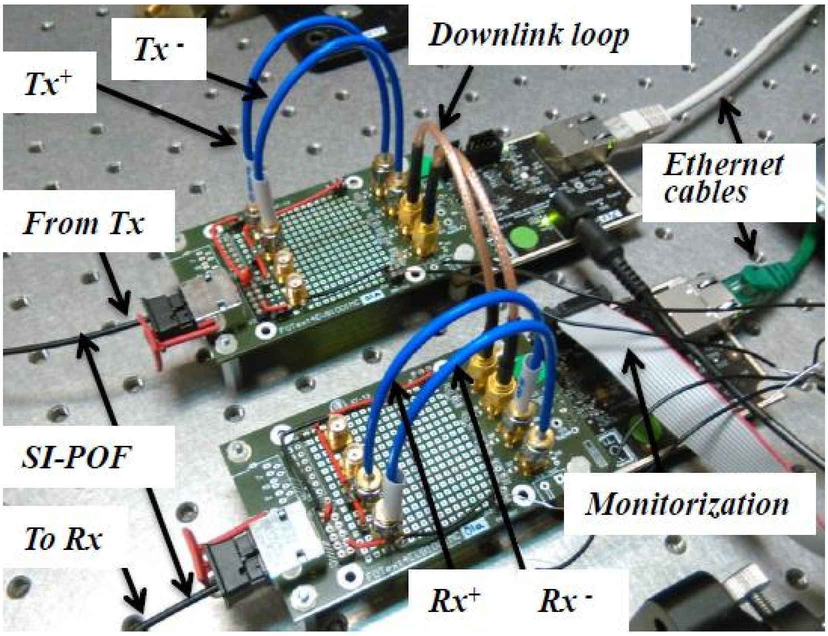

Fig. 6.4: Experimental setup of the single channel SI–POF link.

6.4.1.1. Optical Power Budget

All data links are limited by the optical power budget of the link. The optical power budget is defined as the difference between the output power of the transmitter and the input power requirements of the receiver. All the average optical power measurements are performed using a silica switchable gain detector **[33]**.

The power budget of the reference link is measured using the schematic shown in **Fig. 6.5**. Where P_o is the average power emitted by the LED source, P_{Tx} is the average power coupled to the

SI–POF link, P_{Rx} is the average power at the end of the SI–POF link and P_{PD} is the average power coupled to the receiver photo–detector. A summary of the power link budget is shown in **Table 6.3**. It can be shown that the transmitted power is –3.69 dBm (measured as the average power coupled in 1 m of SI–POF), the total *ILs* are about 10.73 dB, the receiver sensitivity is about –18.85 dBm (measured with a variable attenuator) and that the link margin is about 4.43 dB.

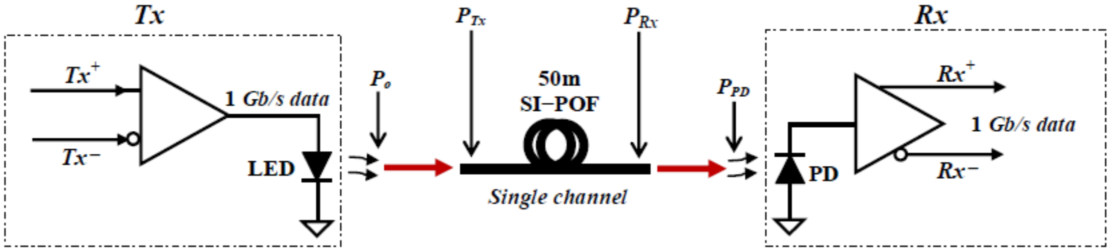

Fig. 6.5: Scheme of the single channel SI–POF link.

TABLE 6.3: SUMMARY OF THE SINGLE CHANNEL LINK POWER BUDGET (1 GBIT/S AT 50 M).

Parameter	$\lambda = 650$ nm
P_{Tx} (dBm)	−3.69
SI–POF attenuation (dB)	8.73
R_x lens coupling loss (dB)	$2^{(1)}$
PD Sensitivity (dBm)	−18.85
Received Power (dBm)	−14.42
Link margin (dB)	4.43

Notes: The LED is encapsulated in special housing for SI–POF coupling so its Po is not measured. (1) The *Rx* lens coupling loss is a mean value taken from [14].

6.4.1.2. Definition of the Link Evaluation Parameters

Media Converter boards offer internal monitoring features that allow estimating the channel response and the link performance before and after Forward Error Correction (FEC) decoding at the receiver. The parameters used for the link performance evaluation are described below:

- **Channel Impulse Response:** Discrete time channel impulse response sampled at symbol rate after timing recovery. The symbol rate at 1 Gbit/s operation is 312.5 MSymbols/s.
- **Channel Frequency Response:** Magnitude of the channel response in the frequency domain. It is defined as the FFT of the Channel Impulse Response. The frequency range is between 0 and the Nyquist frequency (half symbol rate = 156.25 MHz).
- **SNR decod:** Signal to noise ratio measured at the decoding stage after equalization. The minimum required SNR for decoding is 25.4 dB at 1 Gbit/s.
- **BER:** Bit error rate estimation. BER is a precise measurement for low error rates (BER < 10^{-6}).
- **PHDER:** Errored headers rate.

- **Connection speed:** The connection speed is also known as the wire speed, peak bit–rate, useful bit–rate, information rate, data transmission capacity, or digital bandwidth capacity. It is defined as the data transfer rate that the link provides between the physical layer and the data link layer. There are several other factors that determine the final data transfer speed between two devices, as the: Ethernet packets size, the inter packets gap , Hard Drive Speed, Bus Speed, Network Cables, Network Devices and the File Size.

6.4.1.3. Performance Evaluation

SI–POF suffers from high modal dispersion due to its large *NA*, limiting its bandwidth distance product to ~50 MHz×100 m **[12]** and can only provide acceptable attenuation in the visible spectrum (VIS) range (~0.17 dB/m at 650 nm). Therefore, the performance of a SI–POF link is mainly limited by the signal dispersion and the optical power attenuation (link budget).

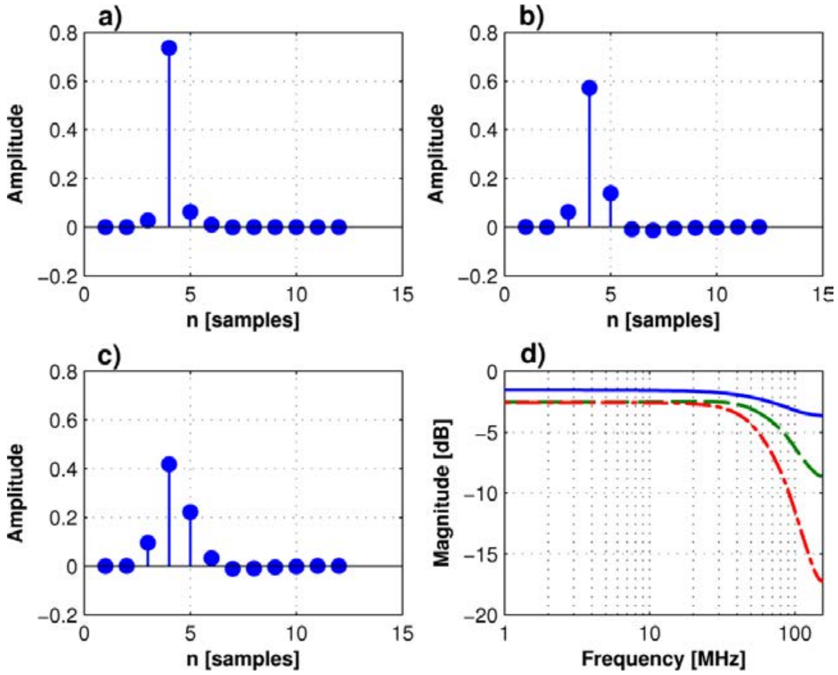

Fig. 6.6: Impulse response of the single channel link using: a) a direct connection between the differential transmission signal (*Tx+* and *Tx–*) and the receiver differential inputs (*Rx*+ and *Rx*-), b) 1 m of SI−POF and c) 50 m of SI−POF. And d) Frequency Response: plot a) (solid line), plot b) (dashed line) and plot c) (dash–dot line).

Fig. 6.6 shows the impulse response of the single channel link under different conditions. **Fig. 6.6a** shows the impulse response of the *Tx*–signal. It is obtained by connecting the differential transmission signal (Tx^+ and Tx^-) to the receiver differential inputs (Rx^+ and Rx^-), similar to the downlink loop connection shown in **Fig. 6.4**. On the other hand, **Fig. 6.6b** shows the impulse response of the link using 1 m of SI–POF. Therefore, impulse response degradation observed is mainly due to the receiver response. The impulse response dispersion is further increased when the signal is transmitted through the 50 m SI–POF link, as shown in **Fig. 6.6c**. The channel dispersion has a direct impact in the channel bandwidth. **Fig. 6.6d** shows the frequency response from the different impulse responses. It can be shown that the power spectral density of the transmitted signal is quite uniform, with a magnitude variation of less than 2 dB between 0 and 156 MHz (solid line). The receiver 3–dB bandwidth is about 100 MHz (dashed line). However, the bandwidth of the link is limited by the SI–POF dispersion. It can be shown that the 50 m of SI–POF reduces the 3–dB bandwidth to about 60 MHz (dash–dot line).

Table 6.4 shows the performance summary of the single channel link. In all three cases analyzed in **Fig. 6.6**, a link with connection speed of 1 Gbit/s between the client and the server is established. It is important to note that the data transfer speed is also limited by the Ethernet connection between the computers and the media converters. The data transfer speed of the Ethernet connection between the client and server is about 980 Mb/s (measured with network traffic analyzer software, connecting the client to the server using a 5 m CAT−5 Ethernet cable). Therefore, it can be shown that the optical link keeps the Ethernet connection data transfer speed (100% of Ethernet data throughput). As expected, the signal to noise ratio decreases as the bandwidth is reduced. **Fig. 6.7** shows the symbols constellations of the three stages decoding at the receiver. The decoding includes the FEC operations and the SNR decod calculation **[31]**. The resulting SNR decod = 25.65 dB, which is enough to establish a 1 Gbit/s link with BER lower than 1×10^{-10}.

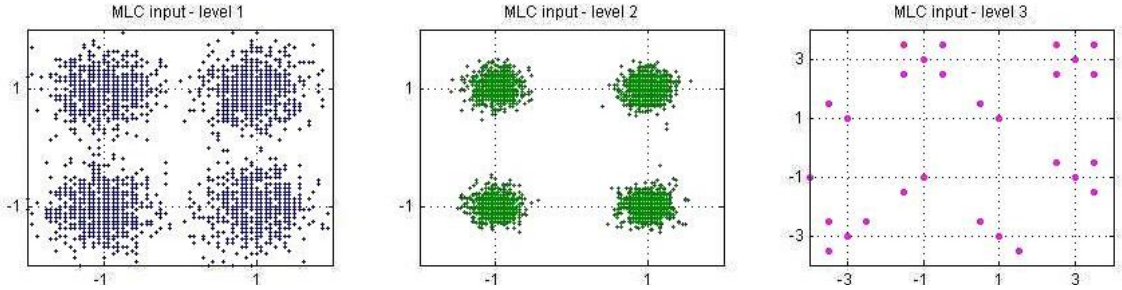

Fig. 6.7: Symbols constellations of the multi level coding input at the reference link receiver after equalization of: level 1 (QPSK), level 2 (QPSK) and level 3 (8−QAM).

TABLE 6.4: PERFORMANCE SUMMARY OF THE SINGLE CHANNEL LINK: REFERENCE LINK.

Link Characteristics	Link with differential Signal (*Tx+* and *Tx–*)	With 1 m of SI–POF	With 50 m of SI–POF
Connection Speed (Gbit/s)	1	1	1
Data transfer speed (Mb/s)	979.8$^{(1)}$	979.8$^{(1)}$	979.5$^{(1)}$
SNR decod (dB)	40.49	31.44	25.65
BER	$<1\times10^{-10}$	$<1\times10^{-10}$	$<1\times10^{-10}$
PHDER	0	0	0

Notes: (1) The data transfer speed that is achieved by connecting the client to the server using an Ethernet cable is about 980 Mb/s.

6.4.2. Transmitters: *Tx*–Signal Conditioning and Modulation of LDs

The *Tx*–signals generated by the MCs are transmitted through the different channels in the visible WDM system. The system performance is tested using the extremes channel (ch_1 = 405 nm and ch_2 = 650 nm) due to the availability of transmitters. These channels allow approximating the link budget of the other channels and the viability of the entire system, as will be discussed on **section 6.4.3**. The blue–violet LD DL–5146–101S and the red LD L650P007 are used for the ch_1 and ch_5 transmission (see **Table 6.1**).

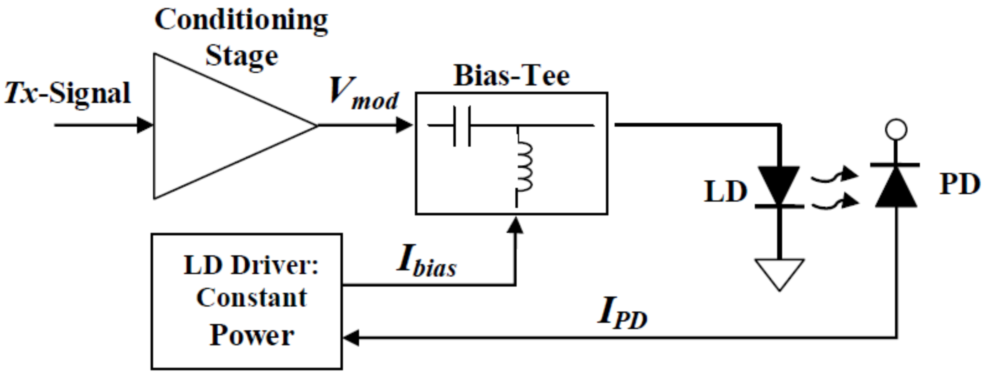

Fig. 6.8: Direct modulation scheme used in the LD based transmitters. PD is the LD internal monitor photodiode.

Each LD is directly modulated by using the modulation scheme shown in **Fig. 6.8**. The LD Driver keeps constant the average power (P_o) by stabilizing the monitor photodiode (PD) current (I_{PD}) through the LD bias current (I_{bias}). The *Tx*–signal is conditioned to generate the modulation voltage (V_{MOD}) and the respective modulation current (I_{MOD}), which is mixed with the I_{bias} through a bias–tee that is directly connected to the LD.

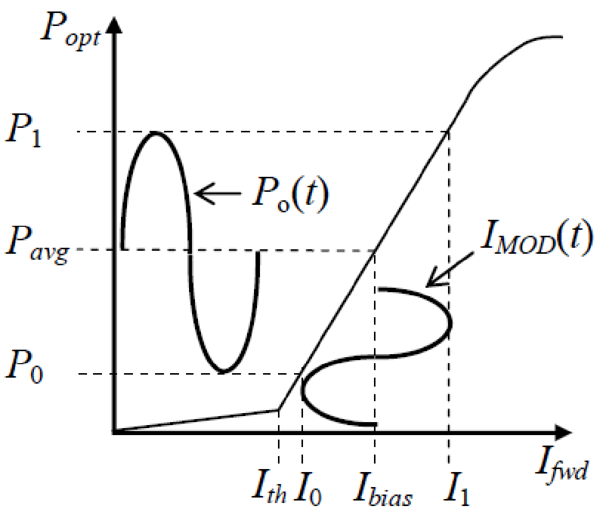

Fig. 6.9: Optical power (P_{opt}) versus the current (I_{fwd}) (*PI* curve) and LD analogue modulation.

The optical power versus the forward current curve (*PI* curve) of a typical LD is shown in **Fig. 6.9**. The linear portion of the *PI* curve defines the transfer function between drive current and light output power. With the LD bias current level established, the modulation current around the bias causes the light output to change according to the linear portion of the *PI* curve. The slope of the curve determines the amplification of drive current to light output. If the laser is overdriven, non–linear effects or clipping will introduce distortions. If the laser is under driven, noise will dominate.

With no input signal, the output optical power is P_{avg}. When the analog signal $I_{MOD}(t)$ is applied, the time−varying (analog) output optical power is: $P_o(t) = P_{avg}[1 + mi\ I_{MOD}(t)]$, where m_i is the optical modulation index **[34]**, defined as:

$$mi = \left(\frac{I_1 - I_{bias}}{I_{bias} - I_{th}} \right) \tag{6.1}$$

The optical modulation index is a measure of how much the modulation signal affects the light output power, and is measured in %. And it is used to set and verify the optimum operating point (light or current bias) that provides the best trade off between noise (under−modulation) and distortions (over−modulation). The optical modulation index is simple to define but often quite difficult to achieve **[34]**.

Table 6.5 shows a summary of the optical equations and the definitions used for the modulation of the LD based transmitters.

TABLE 6.5: OPTICAL EQUATIONS AND DEFINITIONS USED FOR THE LDS MODULATION.

Parameter	Symbol	Relation
Average Optical Power	P_{avg}	$P_{avg} = (P_0 + P_1)/2$
Extinction Ratio	r_e	$r_e = 10 \times \log_{10}(P_1/P_0)$
Optical Amplitude (peak to peak)	$P_{p\text{–}p}$	$P_{p-p} = P_1 - P_0$
Laser Slope Efficiency	η	$\eta = P_{p-p}/I_{MOD}$
Bias Current (AC – Coupled)	I_{bias}	$I_{bias} \geq I_{th} + I_{MOD}/2$
Laser to Monitor Transfer	ρ_{MON}	$\rho_{MON} = I_{PD}/P_{avg}$

Note: P0 and P1 are defined in Fig. 6.9.

In the following, the effects of the conditioning stage over the integrity of the transmission signal (comparison between Tx^+ and V_{MOD}) are presented as well as the modulation parameters used in each LD.

6.4.2.1. *Channel* 1*:* 405 *nm*

The blue−violet LD is directly modulated with the modulation signal V_{MOD1}. V_{MOD1} is obtained by amplifying the single–ended transmission signal Tx^{+} in the conditioning stage, using a general purpose amplifier, with 20 dB power gain and bandwidth from 10 to 500 MHz **[35]**, and fixed attenuators, in order to obtain the desired amplitude, as shown in **Fig. 6.10**.

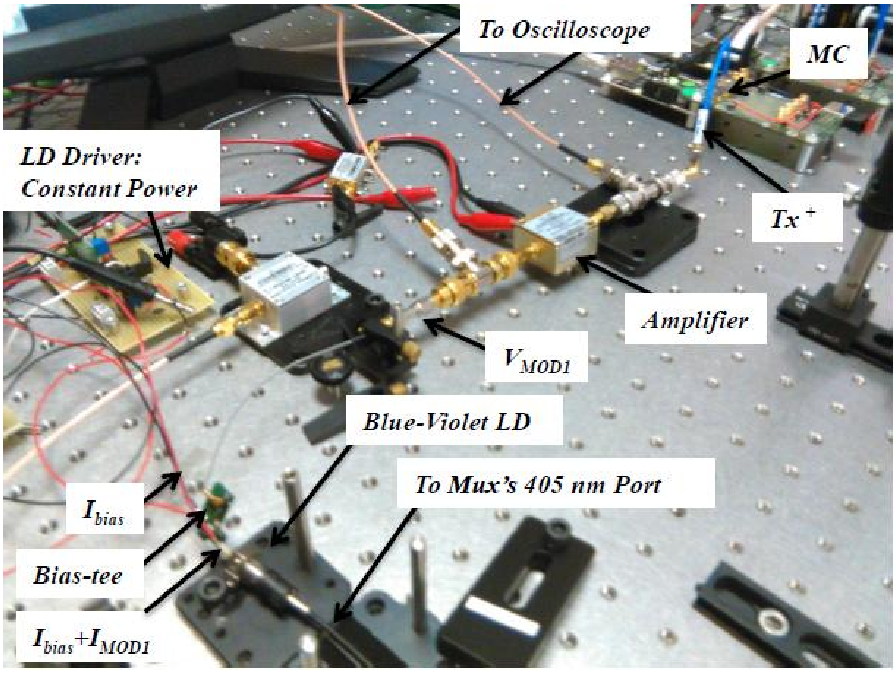

Fig. 6.10: Setup for *Tx*−Signal Conditioning and Modulation of the blue–violet LD DL–5146–101S.

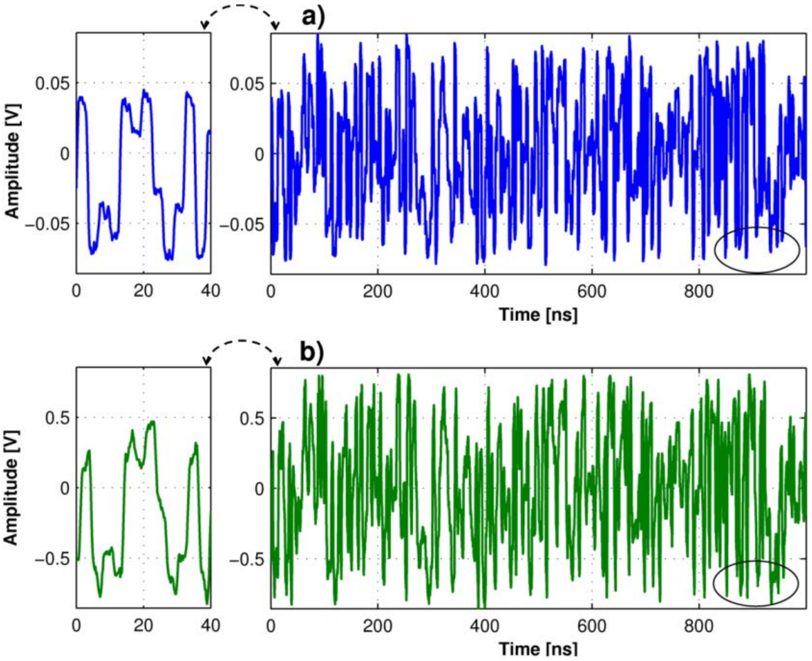

Fig. 6.11: Signal conditioning for the blue−violet laser diode modulation: a) 1000 ns (left) and 50 ns (right) of the $Tx^{+}(t)$ signal, and b) 1000 ns (left) and 50 ns (right) of the conditioned signal, $V_{MOD1}(t)$.

Fig. 6.11 shows a comparison between the single–ended signal Tx^+ (see **Fig. 6.11a**) and the conditioned signal V_{MOD1} (see **Fig. 6.11b**). It can be shown that the amplitude of Tx^+ is about 171 mVpp and that the amplitude of V_{MOD1} is about 1.68 Vpp (Tx^+ is attenuated by an impedance matching network and the oscilloscope probes, see **Fig. 6.10**). It must be noted that the V_{MOD1} envelop has some differences from the Tx^+ envelop (e.g. see circle marks at 875 ns in **Fig. 6.11**) produced by the amplifier in the conditioning stage. The conditioning stage also causes distortion in some pulses, as shown in the left part of **Fig. 6.11a** and **Fig. 6.11b**.

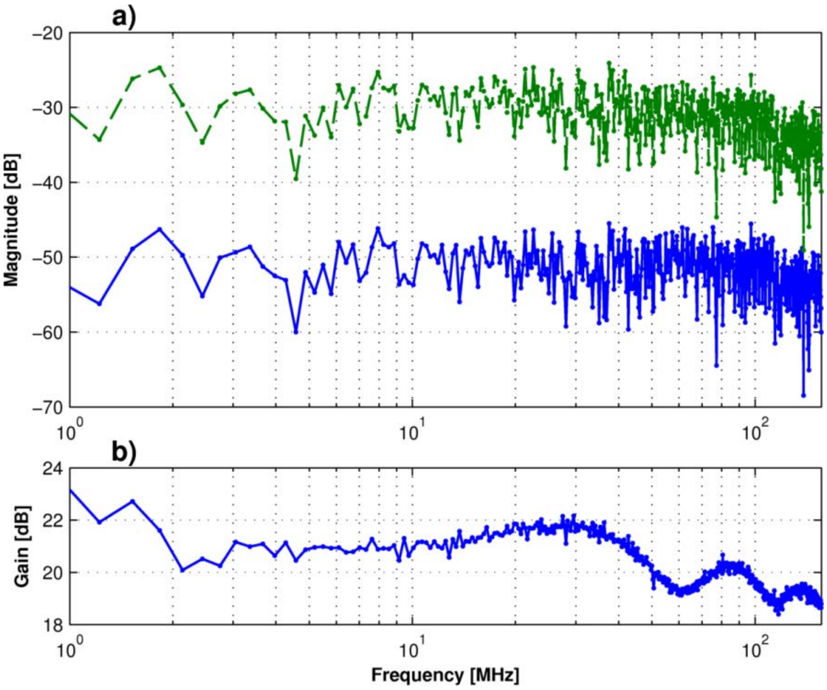

Fig. 6.12: Spectral analysis of the signal conditioning for the blue−violet laser diode modulation: a) Spectral content of the $Tx^+(t)$ signal (solid line) and the conditioned signal, $V_{MOD1}(t)$ (dashed line); and b) Gain = $|V_{MOD1}(f)| - |Tx^+(f)|$.

The spectral analysis of both signals is presented in **Fig. 6.12a.** The spectral content of the Tx^+ signal (solid line) has a quite uniform average magnitude of about –50 dB from 1 to 100 MHz. However, the spectral content of the V_{MOD1} signal is only uniform in the range from 2 MHz to 40 MHz, with average gain of –31 dB. V_{MOD1} signal uniformity can be evaluated better in **Fig. 6.12b** where the gain of the signal conditioning stage is shown. This gain presents variations of up to 3 dB in the range from 40 to 100 MHz. This is due to the amplifier uniformity and may have a significant impact on channel performance, especially in the signal to noise ratio and the bit error rate, as will be analyzed in **section 6.4.4**.

V_{MOD1} produces the modulation current (I_{MOD1}) that is mixed with I_{bias} using a bias–tee with an operation range from 10 kHz to 1 GHz, although the actual frequency range is limited by the impedance network surrounding the LD. The relationship between the V_{MOD1} signal and the modulation current (I_{MOD1}) is defined by the impedance network surrounding the laser diode and is given by:

$$I_{MOD1} = \frac{V_{MOD1}}{100\Omega} \tag{6.2}$$

Then, the amplitude of I_{MOD1} is about 16.8 *mApp* ($I_{MOD} = I_1 - I_0$). Therefore, I_{bias} should be greater than I_{th} + 8.4 mA in order to avoid under driven noise (see **Fig. 6.9** and **Table 6.5**). The blue–violet laser diode used has I_{th} of about 32 mA, so I_{bias} must be greater than 40.4 mA. A summary of the parameters used for the blue–violet laser modulation is shown in **Table 6.6**.

TABLE 6.6: MODULATION PARAMETERS OF THE BLUE–VIOLET LASER DIODE DL–5146–101S (I_{PD} = 400.5 μA, ρ_{MON} = 0.0474 A/W).

I_{th}	I_{bias}	$I_{mod} = I_1 - I_0$	mi	$\Delta P/\Delta I$	P_{avg}	$P_{p\text{–}p} = P_1 - P_0$	r_e
32 mA	42 mA	16.8 mApp	0.84	0.685 W/A	8.45 mW	11.5 mWpp	7.2 dB

6.4.2.2. Channel 5: 650 nm

The red LD is directly modulated with the modulation signal V_{MOD5}. V_{MOD5} is obtained by combining the differential signals Tx^+ and Tx^- in the conditioning stage using a splitter/combiner with an operation range from 1 to 500 MHz, as shown in **Fig. 6.13**. The combiner allows obtaining the required V_{MOD5} amplitude without using amplification stage of **Fig. 6.8**, which reduces the signal distortion.

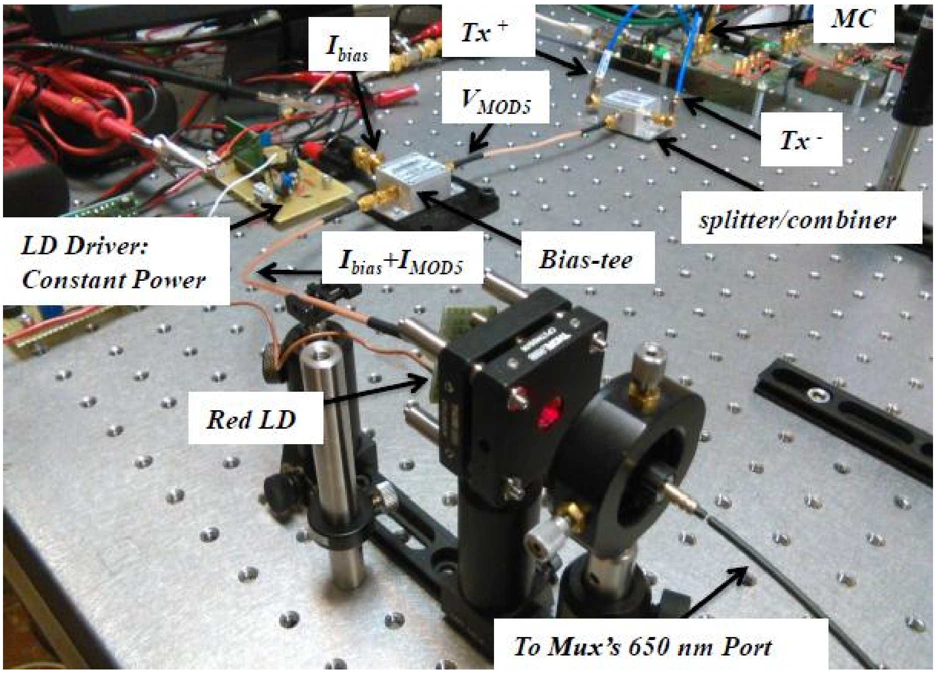

Fig. 6.13: Setup for *Tx*–Signal Conditioning and Modulation of the red LD.

Fig. 6.14 shows a comparison between the single–ended signal Tx^+ (**Fig. 6.14a**) and the conditioned signal V_{MOD5} (**Fig. 6.14b**). It can be shown that the amplitude of Tx^+ is about 276 mVpp and the amplitude of V_{MOD5} is about 357 mVpp. The signals have not been sampled at the same time instant so they cannot be compared in detail. However, the left side of **Fig. 6.14** shows that the pulses shape is quite similar in both signals.

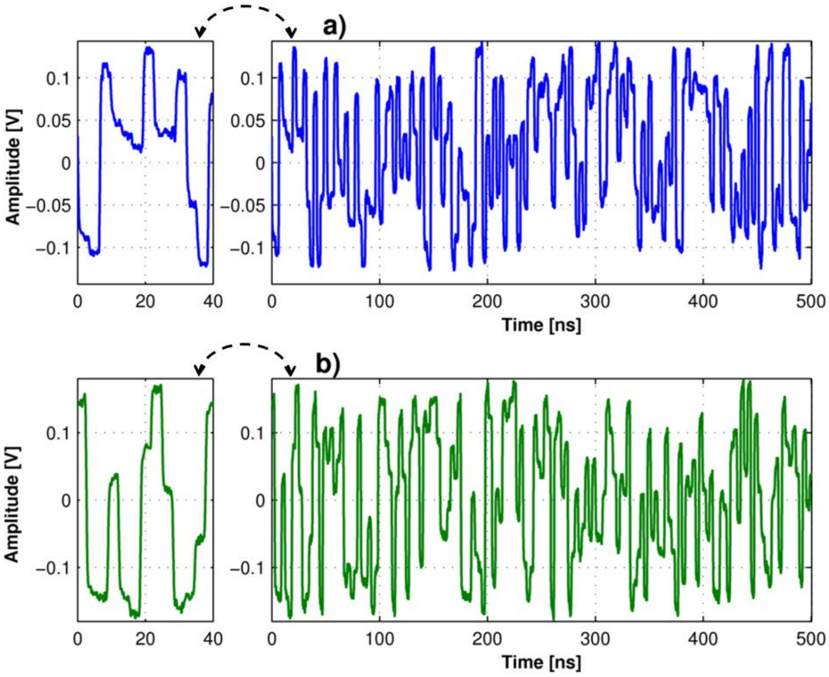

Fig. 6.14: Signal conditioning for the red laser diode modulation: a) 1000 ns (left) and 50 ns (right) of the $Tx^{+}(t)$ signal, and b) 1000 ns (left) and 50 ns (right) of the conditioned signal, $V_{MOD5}(t)$.

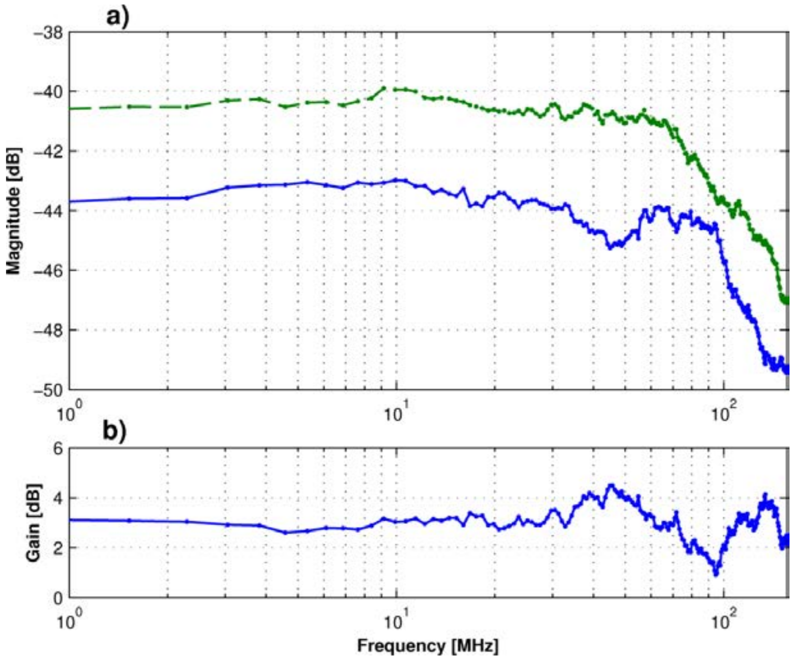

Fig. 6.15: Spectral analysis of the signal conditioning for the red laser diode modulation: a) Spectral content of the $Tx^{+}(t)$ (solid line) and the conditioned signal, $V_{MOD5}(t)$ (dashed line); and b) Gain = $|V_{MOD5}(f)|-|Tx^{+}(f)|$.

The spectral analysis of Tx^+ and V_{MOD5} presented in **Fig. 6.15a** shows that the spectral content of the Tx^+ signal (solid line) has an average magnitude of about –44.2 dB in the range from 1 to 100 MHz, and the spectral density of V_{MOD5} has an average value of –41.3 dB in the same range. This represents a gain of about 2.9 dB, as shown in **Fig. 6.15b**. In this case, the conditioning stage has a very low impact over the spectral content of V_{MOD5}, since the transmission signal is not amplified, the required amplitude is obtained mixing Tx^+ and Tx^-, so it is expected that the signal to noise ratio of the channel 5 will be better than the signal to noise ratio of channel 1.

V_{MOD5} produces the modulation current (I_{MOD5}) that is mixed with I_{bias} using a bias–tee with an operation range from 0.1 to 4200 MHz. The relationship between the V_{MOD5} signal and the modulation current I_{MOD5} is given by:

$$I_{MOD5} = \frac{V_{MOD5}}{100\Omega} \tag{6.3}$$

Then, the amplitude of I_{MOD5} is about 3.57 *mApp* ($I_{MOD} = I_1 - I_0$). Therefore I_{bias} should be greater than I_{th} + 1.79 mA in order to avoid under driven noise (see **Fig. 6.9** and **Table 6.5**). The red laser diode used has I_{th} of about 20.4 mA at 25°C, so I_{bias} must be greater than 21.79 mA. A summary of the parameters used for the red laser modulation is shown in **Table 6.7**.

TABLE 6.7: MODULATION PARAMETERS OF THE RED LASER DIODE L650P007 (I_{PD} = 113 µA, ρ_{MON} = 0.048 A/W).

I_{th}	I_{bias}	$I_{mod} = I_1 - I_0$	*mi*	$\Delta P/\Delta I$	P_{avg}	$P_{p\text{–}p} = P_1 - P_0$	r_e
20.4 mA	23 mA	3.57 mApp	0.69	0.667 W/A	2.35 mW	2.38 mWpp	4.8 dB

6.4.3. Optical Power Budget of the Visible WDM Link

The most important limitation of visible WDM links over SI–POF is the power budget reduction due to the Muxes/DeMuxes insertion losses, limiting the transmission capacity of each channel in comparison with single channel systems. In this section, the comparison between the optical power budget of the visible WDM link and the single channel link (reference link) previously described is presented.

The optical power budget of the WDM system is measured following the schematic shown in **Fig. 6.16** and the experimental setup shown in **Fig. 6.17**. Where P_o is the average power emitted by the LD; P_{Tx} is the average power coupled to the SI–POF; P_{Mux_in} and P_{Mux_out} are the average powers at the input and the output of the multiplexer, respectively; P_{Dem_in} and P_{Dem_out} are the average powers at the input and the output of the demultiplexer, respectively; P_{Rx} is the average power at the end of the SI–POF link; and P_{PD} is the average power at the receiver's photo–detector. The experimental setup used is shown in **Fig. 6.17**. All the average optical power measurements are performed with a silica switchable gain detector **[33]**.

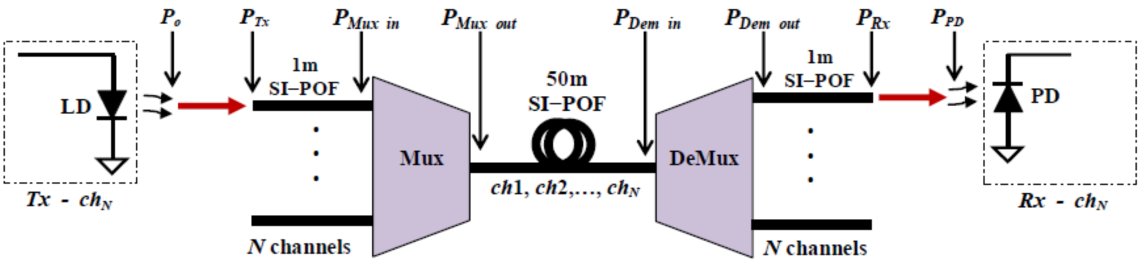

Fig. 6.16: Transmission scheme of the visible WDM SI–POF link.

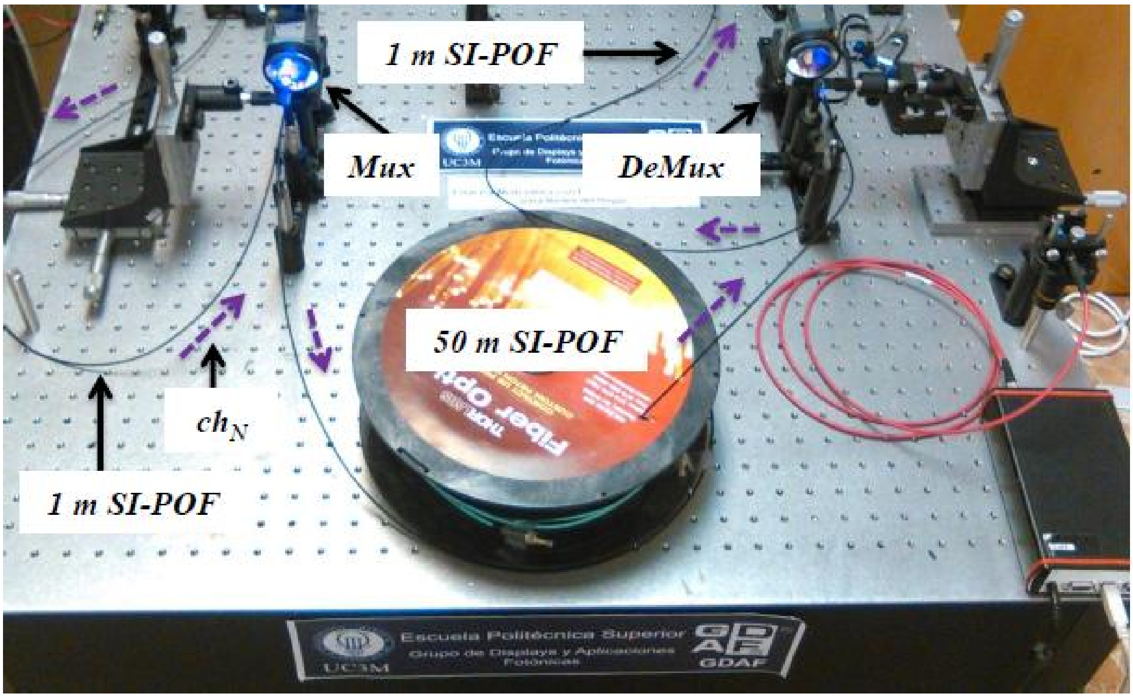

Fig. 6.17: Experimental setup for the power budget characterization of the proposed WDM system.

Fig. 6.18a shows the optical transfer function of the 50 m SI–POF link (solid line). The SI–POF attenuation is ~8.5 dB (0.17 dB/m) at 650 nm. The optical transfer function, average output power to average input power (P_{Rx}/P_{Tx}, see **Fig. 6.16**), of each WDM channel is also observed. Each channel passes through one Mux, 50m of SI–POF and one DeMux. The Muxes/DeMuxes are based on the same design. Therefore, each port can be used as uplink or downlink (reconfigurable bidirectional link). **Fig. 6.18b** shows the *ILs* of each channel in the system due to the Muxes/DeMuxes. The channels ch_1, ch_2, ch_3, ch_4 and ch_5 (405 nm, 470 nm, 520 nm, 590 nm and 650 nm) have an increment of 8.1 dB, 6 dB, 6.1 dB, 6.5 dB and 7.5 dB in their total *ILs* from the simple 50 m link due to multiplexing and demultiplexing.

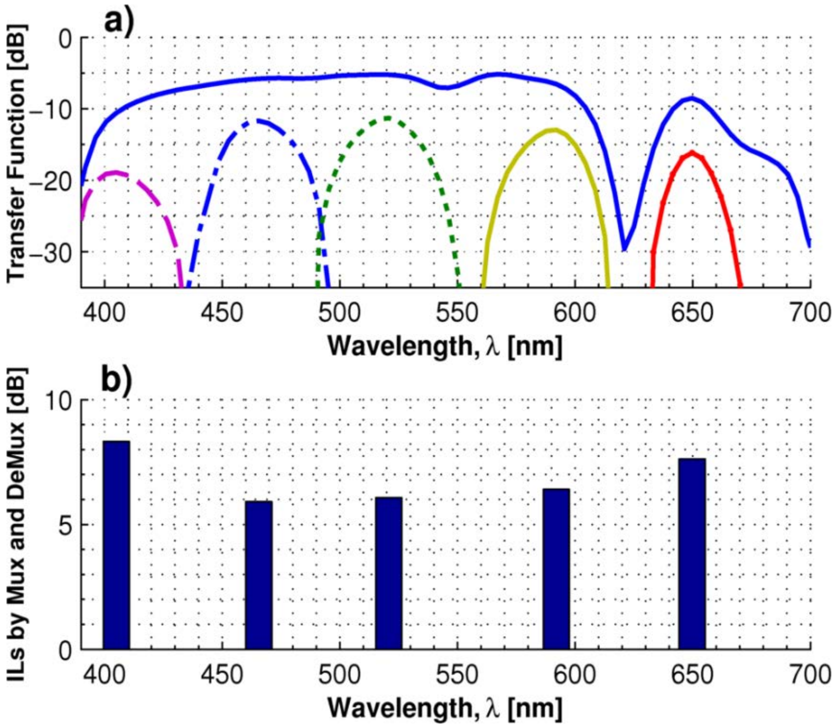

Fig. 6.18: a) Transfer function of each channel in the visible WDM system composed by one Mux, 50 m of SI−POF and one DeMux, and the measured attenuation of 50 m of SI−POF (solid line) b) *ILs* per channel due to the multiplexing and demultiplexing.

6.4.3.1. Receiver Sensitivity Approximation

The power budget of the visible WDM system is directly affected by the receiver sensitivity at the different wavelengths ($S_{Rx\lambda}$). There is no accurate information about the photo–detector spectral responsivity ($\mathcal{R}_\lambda$), so the silicon pin photodiode responsivity, shown in **Fig. 6.19**, is considered **[4]**.

A responsivity decrease can be considered as losses in the power budget of the link or as an increment in the receiver sensitivity at a fixed wavelength. Therefore, the receiver sensitivity at the different wavelengths can be approximated as:

$$S_{Rx\lambda} = S_{Rx|\lambda=650nm} - 10 \times \log_{10}\left[\frac{\Re_\lambda}{\Re_{\lambda=650nm}}\right] \qquad (6.4)$$

From **Fig. 6.19**, it can be shown that the silicon photo−detector responsivity $\mathcal{R}_\lambda$ at $\lambda =$ 405, 470, 520, 590 and 650 nm is about 0.2, 0.26, 0.29, 0.33 and 0.38 A/W, respectively. The receiver sensitivity at 650 nm is –18.85 dBm. This value is measured as the minimum power required at the receiver to obtain a signal to noise ratio (SNR) lower than −25.4 dB, for 1 Gbit/s operation (see **Table 6.3**). Therefore, the receiver sensitivity at $\lambda =$ 405, 470, 520 and 590 nm can be approximated to –16.06, –17.20, –17.68 and –18.24 dBm, which represent variations of 2.79, –1.65, –1.17 and –0.61 dB from the receiver sensitivity at 650 nm, respectively.

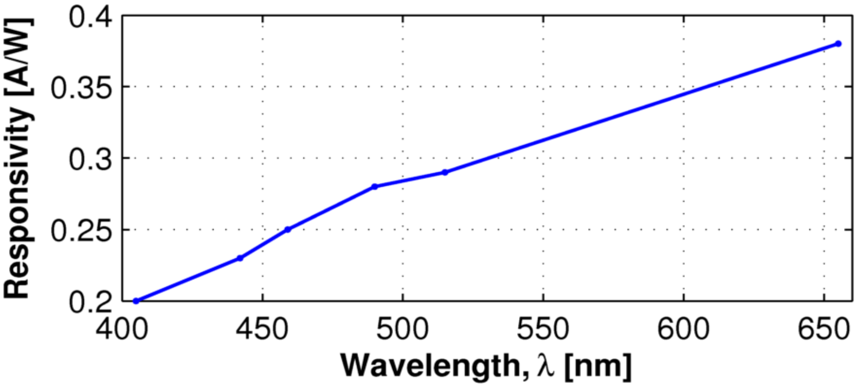

Fig. 6.19: Typical responsivity curve of a silicon pin–photodiode.

6.4.3.2. Approximated power budget of the visible WDM system

Table 6.8 shows the approximated optical power budget of the proposed WDM system, considering the SI–POF attenuation, the multiplexing and demultiplexing losses and the receiver sensitivity variation from sensitivity at 650 nm for 1 Gbit/s operation, see (6.4). It can be shown that the P_{Tx} of each channel (ch_1, ... ch_5) for 1 Gbit/s operation must be greater than 4.84, –3.58, –4.37, –3.67 and 0.7 dBm, respectively.

TABLE 6.8: APPROXIMATED OPTICAL POWER BUDGET OF THE PROPOSED VISIBLE WDM SYSTEM (50 M @ 1 GBIT/S).

Parameter	ch_1 (405nm)	ch_2 (470nm)	ch_3 (520nm)	ch_4 (590nm)	ch_5 (650nm)
P_{Tx} (dBm) (1)	4.84	–3.58	–4.37	–3.67	0.7
SI–POF attenuation (dB)	10.58	5.71	5.24	6.16	8.53
Mux and DeMux attenuation (dB)	8.32	5.91	6.07	6.41	7.62
Rx Sensitivity (dBm) (2)	–16.06	–17.20	–17.68	–18.24	–18.85
Received Power (dBm) (3)	–16.06	–17.20	–17.68	–18.24	–18.85
Link margin (dB)	0	0	0	0	0

Notes: (1) Minimum power required to meet the receiver sensitivity, resulting in a link margin of 0 dB. (2) Calculated as Sensitivity at 650 nm (dBm) − Losses due to photosensitivity variation (dB), see (6.4). (3) A mean *Rx* lens coupling loss of 2 dB is included.

6.4.3.3. Measured power budget of the visible WDM system

The optical power budgets of the extremes channels in the proposed visible WDM SI–POF system have been experimentally tested. **Table 6.9** shows the power measurements performed in the system according to the schematic of **Fig. 6.16**.

THE SUMMARY OF THE POWER LINK BUDGETS OF CHANNELS *CH*1 AND *CH*5 ARE SHOWN IN

Table 6.10. The receiver sensitivity at 650 nm and at 405 nm is –18.85 dBm and –15.79 dBm, respectively. The sensitivity is calculated as the minimum power required at the receiver to obtain a SNR < −25.4 dB. The difference between the sensitivity at 650 nm and at 405 nm is 3 dB, which is close to the 2.79 dB approximation obtained from **Fig. 6.19** and (6.4), see **Table 6.8**. The power transmitted by ch_1 is 9.27 dBm with a resulting link margin of 3.62 dB. And the power transmitted

by ch_5 is 3.72 dBm with a resulting link margin of 7.59 dB. These values are in agreement with the approximations made in the previous section (see **Table 6.8**).

TABLE 6.9: MEASUREMENTS OF OPTICAL POWERS OF THE PROPOSED WDM LINK (50 M @ 1 GBIT/S): CHANNEL 1 AND CHANNEL 5.

Optical Power	ch_1 = 405 nm (I_{PD} = 520µA)		ch_5 = 650 nm (I_{PD} = 254.8µA)	
	mW	dBm	mW	dBm
P_o	8.45	9.27	2.36	3.72
P_{Tx}	6.87	8.37	1.96	2.92
$P_{Mux\_in}^{(1)}$	2.81	4.48	0.84	–0.78
P_{Mux_out}	2.67	4.27	0.80	–0.95
P_{Dem_in}	0.24	–6.27	0.11	–9.45
$P_{Dem\_out}^{(2)}$	0.10	–10.06	0.05	–13.08
PRx	0.09	–10.27	0.05	–13.25
$P_{PD}^{(3)}$	0.06	–12.27	0.03	–15.25

Notes: (1) Calculated as PMux_out + attenuation of 1 m of SI–POF (2) Calculated as *PRx* + attenuation of 1 m of SI–POF (3) Calculated as *PRx* – *Rx* lens coupling loss. The average value of the *Rx* lens coupling loss is 2dB [14].

TABLE 6.10: OPTICAL POWER BUDGET OF THE CHANNELS CH_1 AND CH_5 IN THE PROPOSED VISIBLE WDM LINK (50 M @ 1 GBIT/S).

Parameter	ch_1 = 405 nm	ch_5 = 650 nm
P_{Tx} (dBm)	9.27	3.72
Launching coupling *IL* (dB)	0.90	0.80
Mux attenuation (dB)	4.1$^{(1)}$	3.87$^{(1)}$
SI–POF attenuation (dB)	10.54	8.5
DeMux attenuation (dB)	4.00$^{(2)}$	3.8$^{(2)}$
Rx lens coupling loss (dB)	2.00$^{(3)}$	2.00$^{(3)}$
Sensitivity at PD (dBm)	–15.79	−18.85
Received power (dBm)	–12.27	−15.25
Link margin (dB)	3.52	3.6

Notes: (1) Mux attenuation includes 1 m of SI−POF at the input port. (2) DeMux attenuation includes 1 m of SI−POF at the output port. (3) The *Rx* lens coupling loss is a mean value obtained from [14].

6.4.4. Performance Evaluation of the Visible WDM Transmission System

A 50 m SI–POF visible WDM link has been established and characterized using the extremes channels (ch_1 and ch_5). The WDM system is based on the schematic shown in **Fig. 6.1** and **Fig. 6.16**, the experimental setup is shown in **Fig. 6.20**.

The data transmission is generated in the PC1 (using a traffic generation software), which is called client; the MC1 encodes the Ethernet frames into the 16−PAM signals that are conditioned to directly modulate the LD of the respective channel. All channels are multiplexed, transmitted through 50 m of SI−POF and then demultiplexed at the end of the link to be received and decoded by the respective MC board, which is connected to the PC2, called server. The link performance is analyzed in the server MC board.

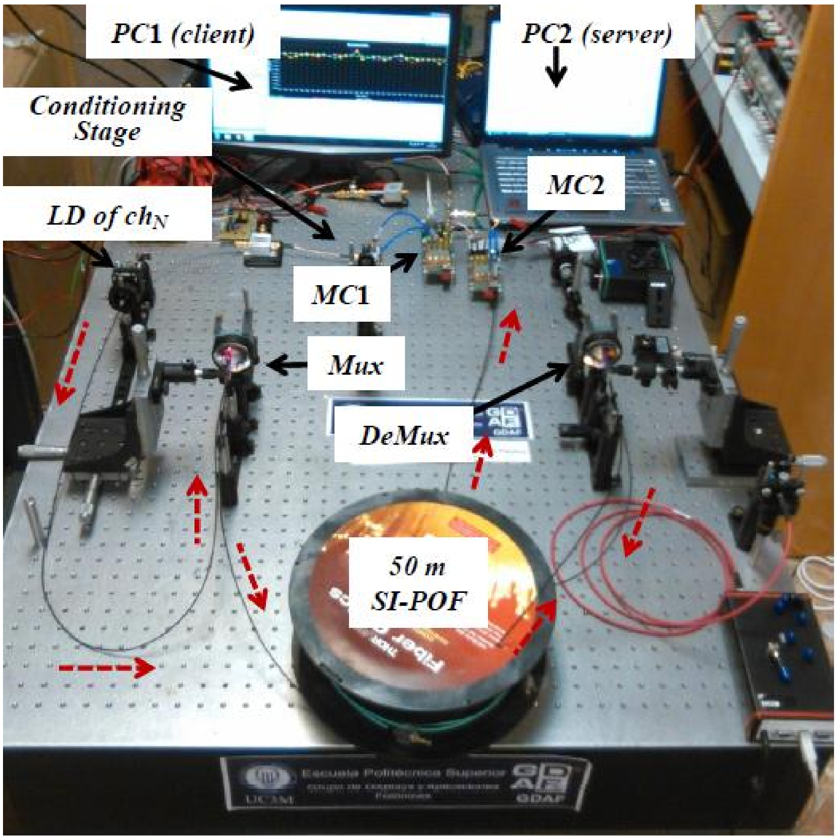

Fig. 6.20: Experimental setup used for the performance evaluation of the visible WDM transmission system.

For simplicity, only the uplink (client to server) is characterized. The downlink loop is done using coaxial cables, as in the case of the reference link (see **Fig. 6.4**). The blue–violet LD DL–5146–101S and the red LD L650P007 are used for the ch_1 and ch_5 transmission. These LDs have threshold currents of about 20 and 35 mA, respectively. Each LD is directly modulated using a V_{MOD} signal (V_{MOD1} and V_{MOD5}), which is obtained from the conditioning the *Tx*–signal (see **section 6.4.2**), with an average transmission power of 9.27 and 3.72 dBm, using bias currents of 23 and 42 mA, respectively (see **Table 6.6** and **Table 6.7**). In the following, the performance evaluation of channels ch_1 and ch_5 is presented.

6.4.4.1. Impulse Response

Fig. 6.21 shows a comparison between the impulse response of the reference link and the impulse response of the channels ch_1 and ch_5 for 3 different conditions: 1) (left column) using 1 m of SI–POF in a single channel configuration (without multiplexing and demultiplexing), 2) (central column) using 50 m of SI–POF in a single channel configuration and 3) (right column) using 50 m of SI–POF with the complete WDM system. Therefore, this comparison shows the difference between the impulse response of the reference link and the impulse response of each channel due to the transmitters (signal conditioning and modulation), the 50 m of fiber and the Multiplexing and Demultiplexing of the complete WDM system.

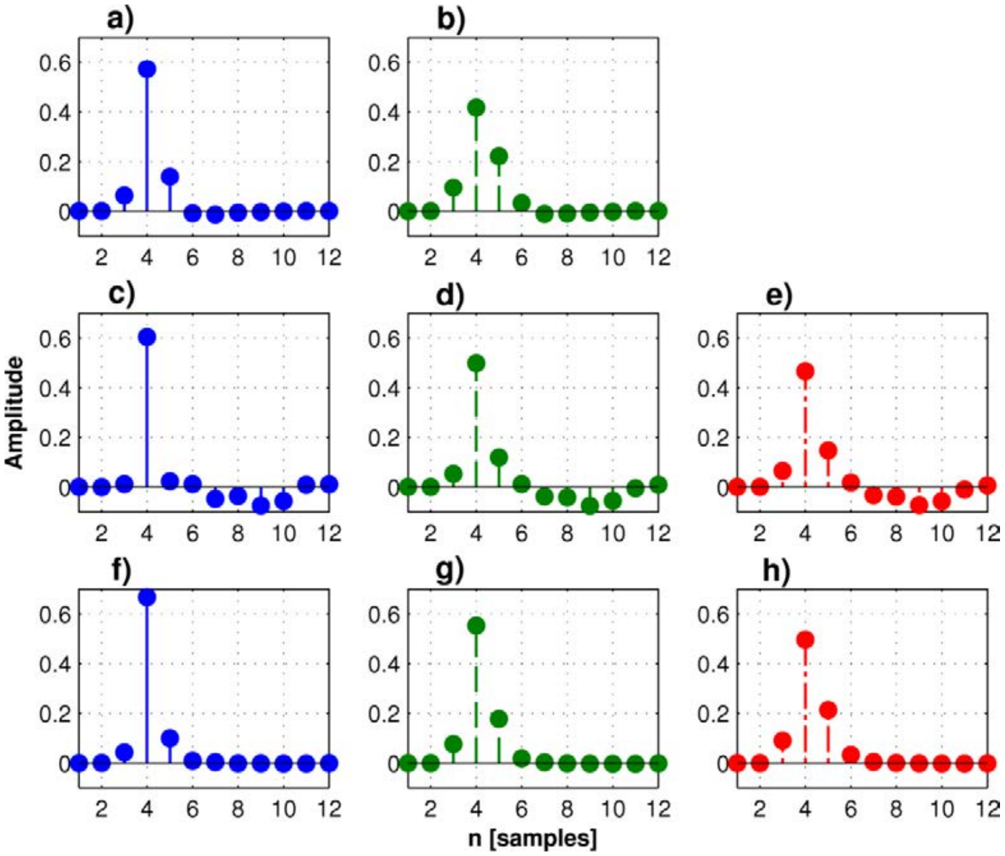

Fig. 6.21: Impulse response of the reference SI−POF link over: a) 1 m and b) 50 m. Impulse response of the SI−POF link using*ch_1* over: c) 1 m, d) 50 m and e) the complete visible WDM system. Impulse response of the SI–POF link using *ch_5* over: f) 1 m, g) 50 m of SI–POF and h) the complete visible WDM link.

The impulse response of the ch_1 transmitter (**Fig. 6.21c**) is the faster one; however, it includes a second order effect, due to the signal distortion produced in V_{MOD1} conditioning (**section 6.4.2.1**). On the other hand, the impulse response of the ch_5 transmitter (**Fig. 6.21f**) is faster than the impulse response of the reference link transmitter (**Fig. 6.21a**, it is a LED transmitter commercial sample) with no second order effects. As expected, the dispersion of the 50 m of SI–POF produce a broadening in the impulse responses, which is greater in the reference link, since its transmitter is based on a LED source with larger spectral bandwidth than the LD based transmitters used in ch_1 and *ch*5. Finally, the effect of the multiplexing and demultiplexing over the ch_1 and *ch*5 performance is shown in **Fig. 6.21e** and **Fig. 6.21h**, respectively. It can be shown that in both cases, the impulse responses are slightly broader.

6.4.4.2. *Frequency Responses*

The impulse response broadening has a direct impact over the channel bandwidth. In the following, the frequency response of the different impulse responses presented in the previous section is analyzed. All the frequency responses are normalized from the transmission signal spectral density (see **Fig. 6.6d**).

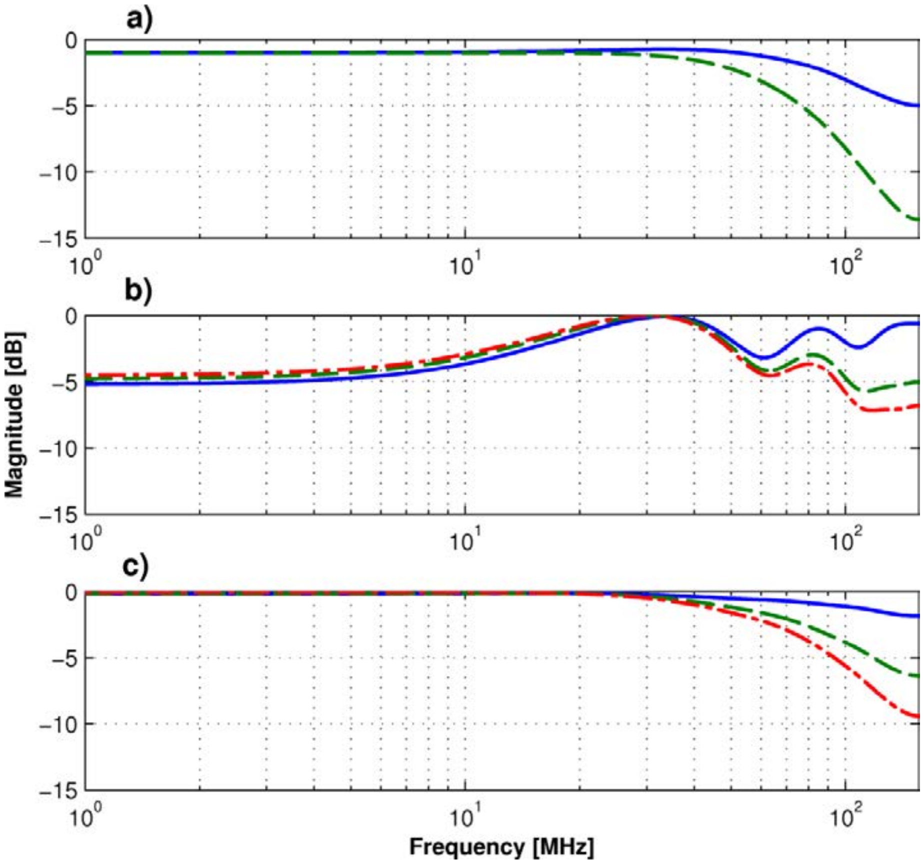

Fig. 6.22: Frequency responses of a) reference link with 1 m (solid line) and 50 m (dashed line) of SI–POF; b) the *ch*$_1$ in a single channel configuration with 1 m (solid line) and 50 m (dashed line) of SI–POF, and the *ch*$_1$ in the complete WDM system of 50 m (dash–dot line); c) the *ch*$_5$ in a single channel configuration with 1 m (solid line) and 50 m (dashed line) of SI–POF, and the *ch*$_5$ in the complete WDM system of 50 m (dash–dot line).

Fig. 6.22a shows the frequency response of the reference link using 1 m (solid line) and 50 m (dashed line) of SI–POF. **Fig. 6.22b** and **Fig. 6.22c** show the frequency response of channels ch_1 and ch_5, respectively, when they are transmitted under different conditions: 1 m of SI–POF in a single channel configuration (solid lines), 50 m of SI–POF in a single channel configuration (dashed lines) and 50 m of SI–POF in the complete WDM system (dash–dot lines). Channel ch_1 has a magnitude attenuation of up to 5 dB for f < 10 MHz and present a ripple effect for f > 60 MHz. This is caused by the distortion produced in conditioning stage over the modulation signal V_{MOD1}. If the modulation signal V_{MOD1} shape (see **Fig. 6.12**) is compared with the shape of the ch_1

frequency response, it can be seen that they are quite similar. However, this is overcome by the equalization in the receiver MC. On the other hand, the frequency responses of the channel ch_5 are as uniform as the frequency responses of the reference link. Comparing the transmission over the 50 m SI–POF link without multiplexing and demultiplexing (dashed lines) with the transmission over the 1 m SI–POF link (solid lines) it can be observed that the fiber dispersion has a lower effect over the frequency responses of the ch_1 and ch_5. But the most important aspect is that the insertion loss of the multiplexer and demultiplexer (dash–dotted lines) has a low impact over the frequency responses of the WDM channels.

6.4.4.3. *Performance Summary*

Table 6.11 shows the performance summary of the channel ch_1. A connection speed of 1 Gbit/s between the client and the server is established in all three cases analyzed in **section 6.4.4.1** and **section 6.4.4.2**. We must remember that the data transfer rate is limited by the Ethernet connection between the computers and the media converters. The Ethernet connection speed between the client and server is about 980 Mb/s (measured with network traffic analyzer software and a direct connection between both PCs using an Ethernet CAT 5 cable). Therefore, it can be shown that the ch_1 keeps the Ethernet connection speed of about 980 Mb/s. **Fig. 6.23** shows the symbols constellations of the three stages decoding at the receiver. The decoding includes the FEC operations and the SNR decod calculation **[31]**. It can be shown that the SNR decod = 26.30 dB in the complete 50 m WDM link, which is quite similar to the SNR decod of the reference link. The BER in all three cases is lower than 1×10^{-10}, which represents a free errors transmission

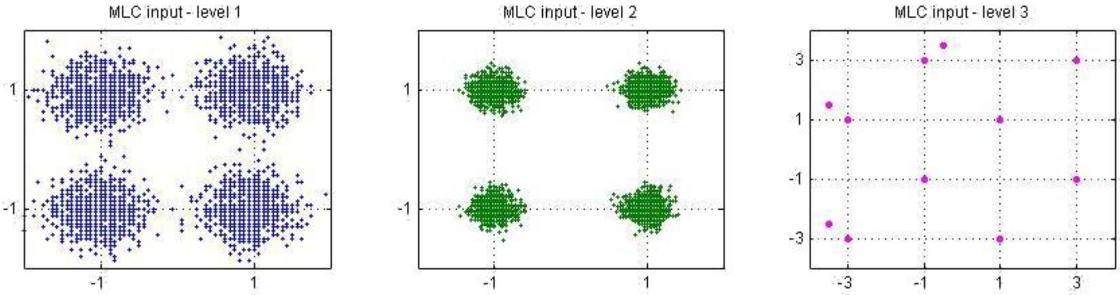

Fig. 6.23: Symbols constellations of the multi level decoding inputs at the *ch*₁ receiver after equalization of: level 1 (QPSK), level 2 (QPSK) and level 3 (8−QAM).

TABLE 6.11: PERFORMANCE EVALUATION SUMMARY OF THE CHANNEL CH_1.

Link Characteristics	1 m of SI–POF	50 m of SI–POF	Complete WDM System
Connection Speed (Gbit/s)	1	1	1
Data transfer speed (Mb/s)	979.4$^{(1)}$	979.96$^{(1)}$	980.03$^{(1)}$
SNR decod	28.75	28.91	26.30
BER	0	0	0
PHDER	0	0	0

Notes: (1) The data transfer speed that is achieved by connecting the client to the server using an Ethernet cable is about 980 Mb/s.

Table 6.12 shows the performance summary of the channel *ch*$_5$. A connection speed of 1 Gbit/s between the client and the server is established in all three cases analyzed in **section 6.4.4.1** and **section 6.4.4.2**. It can be shown that the *ch*$_5$ keeps the Ethernet connection speed of about 980 Mb/s. **Fig. 6.24** shows the symbols constellations of the three stages decoding at the receiver. It can be shown that the SNR decod = 31.75 dB in the complete 50 m WDM link. The BER in all three cases is lower than 1×10^{-10}, which represents a free errors transmission.

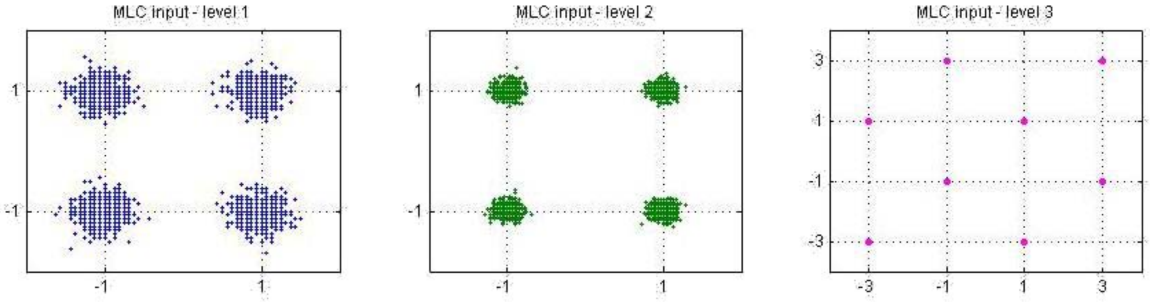

Fig. 6.24: Symbols constellations of the multi level decoding inputs at the *ch*$_5$ receiver after equalization of: level 1 (QPSK), level 2 (QPSK) and level 3 (8−QAM).

TABLE 6.12: PERFORMANCE EVALUATION SUMMARY OF THE *CH*$_5$.

Link Characteristics	1 m of SI–POF	50 m of SI–POF	Complete WDM System
Connection Speed (Gbit/s)	1	1	1
Data transfer speed (Mb/s)	976.18$^{(1)}$	979.46$^{(1)}$	980.15$^{(1)}$
SNR decod	36.96	34.18	31.75
BER	0	0	0
PHDER	0	0	0

Notes: (1) The data transfer speed that is achieved by connecting the client to the server using an Ethernet cable is about 980 Mb/s.

6.5. Energy Efficiency Comparison

Energy conservation is gaining increasing interest in our society in recent years. There is growing consensus on the necessity to put energy conservation at the top of the research agenda, as one of the most compelling and critical. The energy consumption of computers and network equipment is becoming a significant part of the global energy consumption **[36]**. As the coverage of Information and Communications Technology (ICT) is spreading rapidly worldwide, the energy consumption of ICT is also increasing fast, since more equipment and components for networks and communications are being deployed annually **[37]**.

The energy−efficient optical network is a new concept, which is being investigated in recent years. Minimizing energy consumption of optical networks can be generically addressed at four levels: component, transmission, network, and application **[37]**. At the transmission level, efficient optical transmitters and receivers, which improve the energy efficiency of transmission, are required **[38]**.

Previous proposals of SI−POF visible WDM systems use DMT modulation formats **[19]**, **[20]**, while the proposed system uses PAM, which has relatively low power consumption, especially when compared with DMT **[26]**. However, these two systems use directly modulated LDs **[19]**, **[20]**, which are potentially more energy−efficient than externally modulated transmitters. So it is possible to perform a comparison of the power consumption per transmitted bit at the transmitters' level between the proposed system and the previous proposals. The comparison procedure is defined below.

As shown in **Fig. 6.8**, the bias current and the drive signal for the directly modulated LD are combined in a bias−tee (which comprises a dc blocking capacitor and an inductor). Because the LD voltage is approximately constant, its average electrical power consumption is approximately:

$$E_{LD} = I_{bias} \times V_{LD} \tag{6.5}$$

where I_{bias} and V_{LD} are the average LD current and voltage, respectively.

On the other hand, the retransmissions in a TCP/IP network due to the system bit error rate (BER) increases the energy consumption, so it is also considered.

Then, the energy efficiency comparison is done in a first approach with the electrical power consumption per transmitted bit (E_{Tb}), which is defined as the ratio of the average electrical power consumption of the laser (E_{LD}) to the data throughput (T) of a TCP/IP network. E_{Tb} is expressed as:

$$E_{Tb} = E_{LD} / D_T \tag{6.6}$$

6.5.1. Impact of the Bit Error Rate on LAN Throughput

The BER has a direct impact over the data throughput of a TCP/IP network. A fully–loaded Ethernet network interconnected by switches (switched LAN) is considered for the data throughput calculation, where frames (or packets) are separated by the usual 96–bit Inter–Frame Gap (*IFG*). The *IFG* (or Inter−Packet Gap, *IPG*,) is the minimum idle period between transmissions of Ethernet packets that is required by Ethernet devices.

With a switched LAN we can load each connection to almost 100% – it is only the *IFG* that prevents this. The packets throughput is calculated in the worst scenario, where each 1 bit–error provokes a packet–error based on the assumption that bit errors are equally spaced **[39]**. Of course, this is not the case, as bit errors will be statistically distributed. Therefore, the packets throughput (P_T) can be expressed as:

$$P_T = \left(1 - \frac{BER}{Psize + IPG}\right) \tag{6.7}$$

where *Psize* is the Ethernet packets size. Then, the Ethernet data throughput of a TCP/IP network can be expressed as the link data rate by the packets throughput:

$$D_T = R \times P_T \tag{6.8}$$

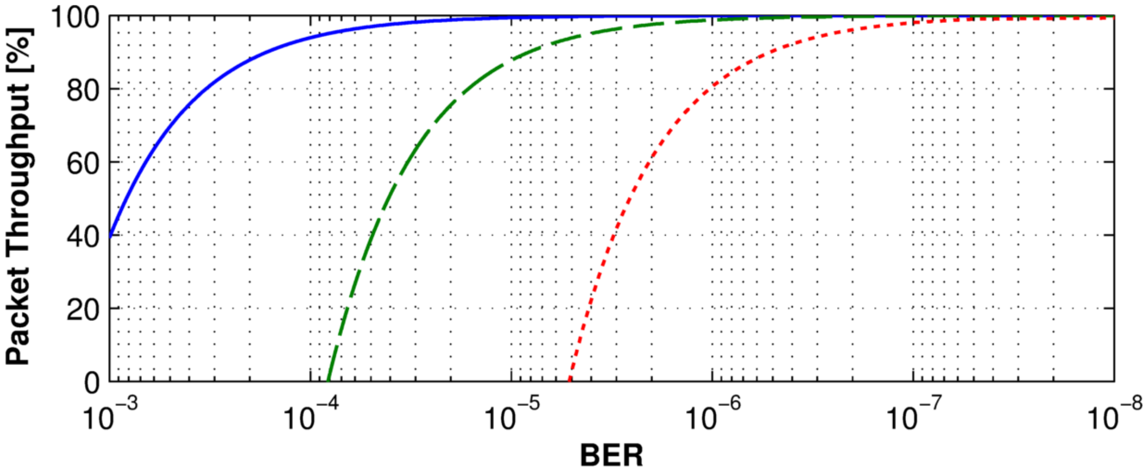

Fig. 6.25: Percentage of Ethernet packets throughput versus the BER considering an *IPG* = 96 bits and packets of 64 Bytes (solid line), 1518 Bytes (dashed line) and big Ethernet frames 1518×16 Bytes (dotted line).

Fig. 6.25 shows the percentage of Ethernet packets throughput for *Psize* = 64 Bytes (minimum *Psize*), 1518 Bytes (maximum *Psize*) and 1518×16 Bytes (big Ethernet packets) **[40]**. It can be seen that: with a BER of 1×10^{-3} the percentage of packets throughput can drop down to 39%; for the maximum *Psize*, a BER lower than 8×10^{-7} is required in order to ensure more than 99% of packets throughput; and for big Ethernet packets, a BER lower than 5×10^{-8} is required in order to ensure more than 99% of packets throughput.

6.5.2. Comparison of Power Consumption per Transmitted bits of Visible WDM Systems

Now that the transmitters' power consumption calculation has been defined, see (6.5) to (6.8). The comparison of the power consumption per transmitted bit at the transmitters' level between the proposed system and two recent proposals of visible WDM SI–POF systems of 50 m is performed. Because each system has a different number of channels, this comparison is done considering the extremes channels of each system.

The results are shown in **Table 6.13**. It can be seen that the energy per transmitted bit in each channel of the proposed system is the lowest one. This is mainly due to the low loss Mux/DeMux devices implemented.

TABLE 6.13: ENERGY EFFICIENCY COMPARISON BETWEEN THE EXTREMES CHANNELS OF RECENTLY REPORTED VISIBLE WDM SI–POF LINKS OF 50 M.

Parameter	This work, 5–ch system		4–ch system **[19]**		6–ch system **[20]**	
	405 nm	650 nm	405 nm	639	405 nm	655 nm
TCP/IP Network Throughput						
Data Rate, R (Gbit/s)	1	1	3.26	3.53	2.35	2.79
BER	$<1\times10^{-10}$	$<1\times10^{-10}$	1×10^{-3}	1×10^{-3}	1×10^{-3}	1×10^{-3}
Data Throughput, D_T (Gbit/s)$^{(1)}$	1.00	1.00	1.27	1.38	0.92	1.09
Energy Efficiency						
I_{bias} (mA)	42	23	80	40	38	36
LD Operation Voltage (V_{LD})	4.8	2.2	5.4	2.3	4.8	2.2
Energy per bit, $E_{Tb,}$ (pJ/b)$^{(2)}$	**201.6**	**50.6**	339.8	66.8	199.0	72.8

Notes: (1) Calculated from (6.7) and (6.8), considering Ethernet packets of 64 Bytes and IPG of 96 bits. (2) Electrical power consumption calculated from Eq (6.6).

6.6. Discussion and Remarks

The performance of the proposed visible WDM link has been evaluated using channels ch_1 and ch_5. In both channels, the transmission speed of the physical layer (PHY rate) is 1035.78 Mb/s, for 1 Gbit/s data rate, with BER < 1×10^{-10}, which represents an error free transmission. The Ethernet data transmission rate achieved was 980 Mb/s (using a traffic generator software), which represents the 100% of the transmission rate achieved with a direct Ethernet cable between the PC1 and PC2 (100% throughput due to the BER < 1×10^{-10}).

Each channel is evaluated in a single channel configuration (without Muxes/DeMuxes) and in the full WDM system. The signal to noise ratio after the decoding (SNR decod) in the single channel configuration is 28.9 and 34.2 dB, and the SNR decod in the full WDM system is 26.3 and 31.8 dB, for channels ch_1 and ch_5, respectively. The lower SNR decod of the ch_1 is due to the amplifier operation range used for V_{MOD1} in the conditioning stage. It is important to note that there is no difference when they are transmitted in the same direction or in opposite directions. The crosstalk attenuation in both situations is higher than 30 dB.

Most important limitation of WDM links over SI–POF is the power budget reduction due to the Muxes/DeMuxes high *ILs*, limiting the transmission capacity of each channel in comparison with single channel systems. **Table 6.14** shows a comparison between the power budget of the proposed system and two recent proposals of WDM SI–POF systems of 50 m. The comparison is done considering the extremes channels of each system. It can be shown that the link margin of the proposed system is greater than 3 dB in both channels, and that the *Po* and the *ILs* due to Mux and DeMux are lower than the *ILs* of recent proposed WDM systems. The total *ILs* in the other 3 available channels in the proposed system are even lower (see **Fig. 6.18** and **Table 6.8**), which demonstrates the possibility of increasing the transmission capacity up to 5 Gbit/s. It is important to note that the *ILs* included by the 2 Mux/DeMux devices are between 6 and 8.3 dB per channel (see

Fig. 6.18). In comparison, the 6−channel diffraction grating demultiplexer implemented in **[20]** includes losses between 7.5 and 10 dB per channel and a simple 1:4 coupler has typical insertion losses of about 8.5 dB **[8]**.

TABLE 6.14: POWER BUDGET COMPARISON BETWEEN THE EXTREMES CHANNELS OF RECENTLY REPORTED VISIBLE WDM SI–POF LINKS OF 50 M.

Parameter	5–ch bidirectional system, this work		4–ch unidirectional system **[19]**		6–ch unidirectional system **[20]**	
	405 nm	650 nm	405 nm	639	405 nm	655 nm
LD output Power, P_o (dBm)	**9.27**	**3.72**	>22.1$^{(1)}$	10$^{(1)\,(2)}$	>12$^{(1)}$	10$^{(2)}$
Launching coupling *IL* (dB)	0.90	0.80	$^{(3)}$	$^{(3)}$	$^{(4)}$	$^{(4)}$
Multiplexing *IL* (dB)	4.00	3.87	5$^{(6)}$	5$^{(6)}$	1.5$^{(6)}$	1.5$^{(6)}$
50 SI–POF (dB)	10.59	8.5	~10.59$^{(4)}$	~8.5$^{(4)}$	10.5	7.5
Demultiplexing *IL* (dB)	4.05	3.8	5.66	3.19	10	9.5
Receiver Lens *IL* (dB)	2.00$^{(5)}$	2.00$^{(5)}$	$^{(4)}$	$^{(4)}$	$^{(4)}$	$^{(4)}$
Sensitivity (dBm)	–15.79	–18.85	$^{(4)}$	$^{(4)}$	$^{(4)}$	$^{(4)}$
Received Power (dBm)	–12.27	–15.25	0.82	–7.04	–10.1	–12.5
Link Margin (dB)	3.52	3.6	$^{(4)}$	$^{(4)}$	$^{(4)}$	$^{(4)}$

Notes: (1) From the total *ILs* and the received power (Link Budget); (2) From the LD datasheet at the *Ibias*; (3) Included in the Multiplexing *IL*; (4) No information is given; (5) Average value taken from manufacturer; (6) Fiber bundle based.

It has been experimentally determined that the receiver sensitivity at 405 nm and 650 nm are approximately –15.79 dBm and –18.85 dBm, and the total power losses are 21.5 dB and 19 dB, respectively, including the launching losses and the losses at the receiver photo−detector lens (∼ 2 B). Thus, two parallel connections at 1 Gbit/s transmitting an average power of 9.27 dBm at ch_1 and 3.72 dBm at ch_5 are established with a link margin of 3.52 dB and 3.6 dB, respectively. In comparison, the single channel reference link has a link margin of about 4.43 dB when transmitting –3.69 dBm (system losses of about 10.73 dB).

The analysis done over the power budget of the proposed WDM system (see 6.4.3.2) shows that the transmitted power in each channel (ch_1, ch_2, ..., ch_5) must be greater than 4.84 dBm, –3.58 dBm, –4.37 dBm, –3.67 dBm and –0.7 dBm, respectively, considering a sensitivity of –18.85 dBm at 650 nm for 1 Gbit/s operation. These values are in accordance with the optical power budget characterization of the channels ch_1 and ch_5.

Previous proposals of SI−POF visible WDM systems report average data rates of about 3.5 Gbit/s per channel with BER of 1×10^{-3} over 50 m. The proposed system presents an average data rate of 1 Gbit/s per channel with BER of 1×10^{-10} over the same distance. BER has a direct impact over the data throughput of a TCP/IP network (and of any network) due to the retransmissions required to keep the data integrity. As it is shown in **section 6.5.1**, the network throughput can drop down to 40% of the transmission rate with BER of 1×10^{-3}, for the minimum Ethernet packet size, and it gets worse when the maximum Ethernet packet size is considered. The product of the average data throughput per channel by the link length (Normalized Data Throughput) is used to locate the proposed system in the current state–of–the–art of SI–POF systems, including single channel and multi−channel systems. The Normalized Data Throughput is expressed as:

$$Normalized\ D_T = \frac{D_T}{ch\#} \times L \tag{6.9}$$

where D_T is de total Ethernet data throughput of the system, from (6.8), *ch#* is the number of channels in the system and L is the link length.

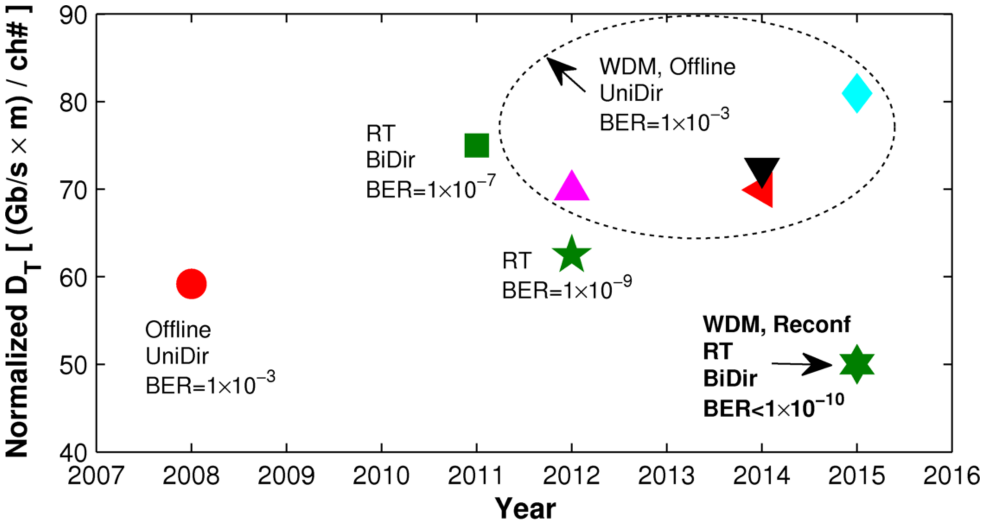

Fig. 6.26: Evolution of the Normalized Ethernet Data Throughput of SI–POF systems. Normalization is done considering a TCP/IP network with the minimum packet size (64 Bytes) and IFG of 96 bits. Offline is used for offline–processing, RT is used for real–time, UniDir is used for unidirectional, Bidir is used for bidirectional, Reconf is used for reconfigurable and WDM indicates that the system transmits more than 1 *ch* over the link. References: Circle [41], Square [23], Pentagram [42], Upward−pointing triangle [43], Downward−pointing triangle [19], Left−pointing triangle [4], Diamond [21] and Hexagram [This work].

As shown in **Fig. 6.26**, the proposed system is the first real time, bidirectional and reconfigurable SI−POF WDM link with BER < 1×10^{-10} with normalized throughput comparable with the current state–of–the–art, with a lower energy consumption than previous WDM proposals. The normalized throughput is lower than in previous WDM proposals, however it should be noted that the data throughput of systems with BER = 1×10^{-3} get much worse when the Ethernet packets size increases and it is even possible that they are not capable of transmitting the maximum packet size of a Ethernet network, see **section 6.5.1**. On the other hand, the normalized throughput of the proposed system is lower than the normalized throughput of recent proposed single channel systems **[23] [41] [42]**. However, it is important to note that the proposed system is able to transmit up to 5 channels, each one with throughput of up to 1 Gb/s over 50 m, which represents a total

Throughput × Length product 3.3 times greater than the total Thoughput × Length product of **[23]** (square marker in **Fig. 6.26**).

In conclusion, the proposed 5–channel visible WDM system can establish a real time bidirectional link at data rates of 2 Gbit/s using 2 channels (1 Gbit/s per channel) with BER < 1×10^{-10} over 50 m of SI−POF. The system has the potential of expanding the transmission data rate up to 5 Gbit/s using 5 channels in longer distances, with better energy efficiency than recent proposals. Each channel can be configured either as uplink or downlink. This represents a real improvement in the performance of commercial and experimental SI−POF transmission systems. The numbers of channels in the system are limited by the Muxes/DeMuxes ports number. Therefore, the number of available channels can be increased up to 8 using the 8–channel Mux/DeMux proposal presented in the discussion section of **Chapter 5**, with similar *ILs* and *CTA*.

6.7. References

[1] A. M. J. Koonen and E. Tangdiongga, "Photonic Home Area Networks," *Journal of Lightwave Technology,* vol. 32, no. 4, pp. 591–604, 2014.

[2] I. Mollers, D. Jager, R. Gaudino, A. Nocivelli, H. Kragl, O. Ziemann, N. Weber, T. Koonen, C. Lezzi, A. Bluschke and S. Randel, "Plastic optical fiber technology for reliable home networking: overview and results of the EU project pof–all," *Communications Magazine, IEEE,* vol. 47, no. 8, pp. 58 – 68, 2009.

[3] Mitsubishi Rayon, "Plastic Optical Fiber (POF) technology for Automotive, Home network systems," in *Presented at IEEE* 802.3 *GEPOF Study Group meeting*, May 2014.

[4] R. Kruglov, J. Vinogradov, S. Loquai, O. Ziemann, C.–A. Bunge, T. Hager and U. Strauss, "21.4 Gb/s discrete multitone transmission over 50–m SI–POF employing 6–channel WDM," in *OFC*, 2014.

[5] E. Dai, "Home Networking bandwidth growth needs and POF," in *Presented at IEEE* 802.3 *GEPOF Study Group Meeting*, October 2014.

[6] KDPOF, "Automotive Applications," [Online]. Available: http://www.kdpof.com/applications/automotive/. [Accessed 29 March 2015].

[7] R. Klos, "MOST in future automotive connectivity," MOST cooperation, 2013.

[8] O. Ziemann, J. Krauser, P. E. Zamzow and W. Daum, POF Handbook: Optical Short Range Transmission Systems, 2nd ed., Springer, 2008.

[9] M. Yaseen, S. D. Walker and R. J. S. Bates, "531–Mbit/s, 100–m all–plastic optical–fiber data link for customer–premises network applications," in *OFC*, San Jose CA, 1993.

[10] J. L. Wei, L. Geng, D. G. Cunningham, R. V. Penty and I. H. White, "Gigabit NRZ, CAP and optical OFDM systems over POF links using LEDs," *Opt. Express,* vol. 20, no. 20, p. 22284−22289, 2012.

[11] O. Ziemman and L. V. Bartkiv, "POF–WDM, theTruth," in *ICPOF*, Bilbao, Spain, 2011.

[12] C. M. Okonkwo, E. Tangdiongga, H. Yang, D. Visani, S. Loquai, R. Kruglov, B. Charbonnier, M. Ouzzif, I. Greiss, O. Ziemann, R. Gaudino and A. M. J. Koonen, "Recent results from the EU POF−PLUS project: multi−Gigabit transmission over 1 mm core diameter plastic optical fibers," *J. Lightwave Technol.,* vol. 29, p. 186–193, 2011.

[13] L. Geng, J. L. Wei, R. V. Penty and I. H. White, "3 Gbit/s LED–Based Step Index Plastic Optical Fiber Link Using Multilevel Pulse Amplitude Modulation," in *OFC/NFOEC*, 2013.

[14] O. Ciordia, C. Esteban, C. Pardo and R. Pérez de Aranda, "Commercial Silicon for Gigabit Communication over SI–POF," in *ICPOF*, Buzios, Brazil, 2013.

[15] M. Jončić, M. Haupt and U. H. P. Fischer, "Investigation on spectral grids for VIS WDM applications over SIPOF," in *ITG Symposium: Photonic Networks*, Leipzing, Germany, 2013.

[16] P. J. Pinzón, K. Heggarty, C. Vázquez and I. Pérez, "Diffraction grating–based Multiplexers for SI–POF networks," in *ICPOF*, Buzios, Brazil, 2013.

[17] U. H. P. Fischer, M. Haupt and M. Joncic, "Optical Transmission Systems Using Polymeric Fibers," in *Optoelectronics – Devices and Applications*, InTech, 2011, Chapter 22.

[18] M. Jončić, M. Haupt and U. Fischer, "Standardization Proposal for Spectral Grid for VIS WDM Applications over SI–POF," in *Proceedings of POF Congress*, Atlanta, 2012.

[19] M. Jončić, R. Kruglov, M. Haupt, R. Caspary, J. Vinogradov and U. H. P. Fischer, "Four–Channel WDM Transmission Over 50 m SI–POF at 14.77 Gb/s Using DMT Modulation," *IEEE Photonics Technology Letter,* vol. 26, pp. 1328–1331, 2014.

[20] R. Kruglov, J. Vinogradov, S. Loquai, O. Ziemann, C.–A. Bunge, T. Hager and U. Strauss, "21.4 Gb/s Discrete Multitone Transmission over 50–m SI–POF employing 6–channel WDM," in *OFC*, San Francisco, California United States, 2014.

[21] U. H. P. Fischer, S. Höll, M. Haupt and M. Joncic, "Polymeric demultiplexer component for wavelength division multiplex communication systems using polymer fibers," in *SPIE* 9368, San Francisco CA, 2015.

[22] P. J. Pinzón, I. Pérez and C. Vázquez, "Efficient Multiplexer/Demultiplexer for Visible WDM Transmission over SI–POF Technology," *IEEE/OSA Journal of Lightwave Technology,* vol. 33, no. 17, pp. 3711–3718, 2015.

[23] A. Antonino, S. Straullu, S. Abrate, A. Nespola, P. Savio, D. Zeolla, J. Molina, R. Gaudino, S. Loquai and J. Vinogradov, "Real–time Gigabit Ethernet bidirectional transmission over a single SI–POF up to 75 meters," in *OFC/NFOEC*, 2011.

[24] S. Abrate, R. Gaudino and G. Perrone, "Step–Index PMMA Fibers and Their Applications," in *Current Developments in Optical Fiber Technology*, InTech, 2013, Chapter 7.

[25] G. Stepniak and J. Siuzdak, "Experimental investigation of PAM, CAP and DMT modulations efficiency over a double–step–index polymer optical fiber," *Optical Fiber Technology,* vol. 20, pp. 369–373, 2014.

[26] R. Kruglov, S. Loquai, C. A. Bunge, M. Schueppert, J. Vinogradov and O. Ziemann, "Comparison of PAM and CAP Modulation Schemes for Data Transmission Over SI–POF," *IEEE Photonics Technology Letters,* vol. 25, no. 23, pp. 2293–2296, 2013.

[27] S. Loquai, R. Kruglov, C.–A. Bunge, O. Ziemann and B. Schmauss, "10 Gbit/s pulse–amplitude modulated transmission over 1 mm large core polymer optical fiber," *IEEE*

Photon. Technol. Lett., vol. 24, no. 10, pp. 851–853, 2012.

[28] M. Wieckowski, J. B. Jensen, I. T. Monroy, J. Siuzdak and J. P. Turkiewicz, "300 Mbps transmission with 4.6 bit/s/Hz spectral efficiency over 50 m PMMA POF link using RC–LED and multilevel carcarrierless amplitude phase modulation," in *OFC/NFOEC*, 2011.

[29] G. Stepniak and J. Siuzdak, "Transmission beyond 2 Gbit/s in a 100 m SI POF with multilevel CAP modulation and digital equalization," in *OFC/NFOEC*, 2013.

[30] K. Zhong, X. Zhou, T. Gui, L. Tao, Y. Gao, W. Chen, J. Man, L. Zeng, A. Lau and C. Lu, "Experimental study of PAM–4, CAP–16, and DMT for 100 Gb/s Short Reach Optical Transmission Systems," *Opt. Express,* vol. 23, pp. 1176–1189, 2015.

[31] KDPOF, "Simple Introduction to Gigabit Communications over POF," 2014. [Online]. Available: http://www.kdpof.com/wp–content/uploads/2012/07/Easy–Introduction–v1.1.pdf. [Accessed 09 September 2015].

[32] KDPOF, "Media Converter Evaluation Kit: KD–EVK10x1B–MC," September 2014. [Online]. Available: http://www.kdpof.com/wp–content/uploads/2012/07/br010__KD_EVK10x1B_MC_Eval_Kit_Brochure__v1_2.pdf. [Accessed 09 April 2015].

[33] Thorlabs, "PDA100A Si Switchable Gain Detector," 8 April 2014. [Online]. Available: http://www.thorlabs.de/thorcat/13000/PDA100A–Manual.pdf. [Accessed 1 April 2015].

[34] M. O. Inc., "Defining Optical Modulation Index," 2010. [Online]. Available: http://www.globalspec.com/m2optics/ref/Defining_OMI.pdf. [Accessed 31 March 2015].

[35] Mini–Circuits, "Low Noise Amplifier: ZFL–500HLN," [Online]. Available: http://www.minicircuits.com/pdfs/ZFL–500HLN.pdf. [Accessed 30 April 2015].

[36] W. Vereecken, L. Deboosere, D. Colle, B. Vermeulen, M. Pickavet, B. Dhoedt and P. Demeester, "Energy efficiency in telecommunication networks," in *European Conference on Networks and Optical Communications & Optical Cabling and Infrastructure (NOC)*, 2008.

[37] Y. Zhang, P. Chowdhury, M. Tornatore and B. Mukherjee, "Energy Efficiency in Telecom Optical Networks," *IEEE Communications Surveys & Tutorials,* vol. 12, no. 4, pp. 441–458, 2010.

[38] R. S. Tucker, "Green Optical Communications—Part I: Energy Limitations in Transport," *IEEE Journal of Selected Topics in Quantum Electronics,* vol. 17, no. 2, pp. 245–260, 2011.

[39] E. Rodriguez–Colina, A. W. Moore, M. Glick, A. Wonfor, I. H. White and R. V. Penty, "BER implication for TCP/IP network throughput over a 10 x 10 Gbps wavelength–striping cascaded SOA–switch," in *London Communications Symposium*, London, 2006.

[40] Band–Rex, "The Impact of Bit Erro Rate on LAN Throughput", [Online]. Available: http://www.pemosa.com/descargar_documento.php?dID=551. [Accessed 09 September

2015].

[41] J. Lee, F. Breyer, S. Randel, H. Boom and T. Koonen, "Gigabit Ethernet over standard step–index polymer optical fiber," in *ICPOF*, Santa Clara, CA, 2008.

[42] M. Atef, R. Swoboda and H. Zimmermann, "Real–Time 1.25–Gb/s Transmission Over 50–m SI–POF Using a Green Laser Diode," *IEEE Photonics Technology Letters,* vol. 24, no. 15, pp. 1331–1333, 2012.

[43] R. Kruglov, J. Vinogradov, O. Ziemann, S. Loquai and C.–A. Bunge, "10.7–Gb/s Discrete Multitone Transmission Over 50–m SI–POF Based on WDM Technology," *IEEE Photonics Technology Letters,* vol. 24, no. 18, pp. 1632 – 1634, 2012.

Chapter VII:

Conclusions and Future Work

7.1. Conclusions

In this research work, different optical devices based on Liquid Crystals and Diffraction Gratings have been proposed. These devices have been specially designed to be implemented on SI–POF sensing and data transmission networks based on visible WDM schemes.

The proposed LC devices such as filters, wavelength selective switches, interleavers and routers are able of including advanced functions into the SI–POF systems such as tuning and reconfiguration in a broadband wavelength range with no optical–to–electrical and electrical–to–optical conversions. However, the insertion losses of these devices are high (> 5 dB), which limits their applicability to systems where the losses are not a limiting factor, e.g. in sensing and data transmission systems of very short range (< 15m). But in general, the insertion losses of these devices can be greatly reduced by using polarization diversity schemes and polarizing devices (linear polarizers and beam splitters) with transmittance optimized for the required operation range.

Through the different simulation results presented in **Chapter 3** and **Chapter 4**, it has been shown that the behaviour of the proposed liquid crystal devices can be successfully modeled by using the Jones formalism and the precise characterization of the LC cells parameters. So the proposed characterization method is a very useful tool for the optimum design of the different LC based devices.

In this work, it has been demonstrated that the Planar Diffraction Gratings are to date an excellent choice for implementing compact Muxes/DeMuxes for SI–POF applications with low–insertion losses and multiple channels. Those characteristics are specially required for implementing efficient Multi–Gbit/s data transmission systems over SI–POF using visible WDM.

The proposed Mux/DeMux designs are on current state–of–the–art due to their low–losses, high crosstalk attenuation and channel counts. These designs have allowed the implementation of a real–time bidirectional Ethernet data transmission system over 50 m of SI–POF using a 5–channels visible WDM system with transmission capacity of up to 5 Gbit/s with error free transmission. This system has better energy efficiency per transmitted bit than similar proposals. So it has been demonstrated that the visible WDM approach used has the potential for increasing the transmission capacity of SI–POF links without an important increment of the transmitted power.

Below is a summary of the most important contributions presented in this research work.

7.2. Research Contributions

In this work, different novel optical devices based on Birefringent and Diffractive elements have been designed and experimentally tested. These devices have been specially designed to be implemented on advanced SI−POF networks based on wavelength division multiplexing (WDM). These kinds of networks are used in self–referenced sensing systems and in Multi−Gbit/s data transmission systems for short range applications, and operate in the visible and near infrared wavelength range.

The proposed birefringent devices based on Liquid Crystal cells have been classified as Wavelength Selective Devices (WSD) and as Optical Routers (OR). These devices give to SI−POF systems advanced functions such as tuning, reconfiguration and low wavelength dependence with no optical to electrical and electrical to optical conversions. Some of them have been designed, tested and successfully simulated using the precise characterization of high birefringence LC cells.

Thus it is reported a novel experimental method for univocal determination of arbitrary nematic LC cells parameters. Unlike previous proposals it uses few angle variations, uses wide searching limits, needs no initial conditions and it can be used for determining the spectral dispersion of the LC birefringence. It is ideal for designing birefringent devices based on staked LC structures for broadband applications. This characterization method can be easily integrated in a precise, fast, and automatic characterization system.

Novel proposals of WSDs, optimized to work in the visible range for SI−POF WDM networks are presented. These devices take advantage of the large aperture, low chromatic dispersion and high reliability that offer the birefringent structures as well as the reconfiguration capability that can be achieved with liquid crystal technology.

The first WSD is a tunable optical filter based on the use of high birefringence nematic LCs (LCTF). The filter parameters have been optimized to work in the VIS−NIR spectrum range. A wavelength tuning range above 200 nm (from 610 to 820nm), with a maximum FWHM of 80 nm has been measured. Low supply voltage (below 1.5 V_{RMS}) has been demonstrated to allow this tuning performance. Additionally, a computer simulation of the filter has been presented. Filter simulations show a good agreement with experimental results.

The second WSD is a reconfigurable 1×2 wavelength selective switch (R−WSS), based on a Lyot filter structure and high birefringence nematic liquid crystal cells. This system allows demultiplexing, switching or blocking any channel through any output port using voltages from 0 to 3 V_{RMS}. Maximum insertion losses of 6 dB (for non−polarized light) and crosstalk attenuation ratios better that 16 dB are obtained.

The performance of the proposed LCTF and the R−WSS can be highly improved by using arbitrary structures, as the one used for designing arbitrary birefringent interleavers, different from the basic Lyot structure. Thus, a flexible and fast synthesis method for designing asymmetric interleavers with flattop, low dispersion, adjustable isolation and bandwidths at both outputs has been proposed. *Z*−transform properties and digital filter design techniques are used for designing interleavers under a set of specifications. At a second level a genetic algorithm optimization approach allows improving the interleaver design adjusting the minimum isolation and/or dispersion, at both outputs. Finally, this synthesis method has been applied for designing an optimized interleaver for SI−POF applications.

Two new proposals for implementing 1×2 reconfigurable LC optical routers (LC–ORs) have also been presented. The first proposal is a reconfigurable 1 × 2 optical router with control of output power level. This router allows blocking or redirecting the input light beam either to only one of the output ports or to both output ports simultaneously. Additionally, the control of the optical power level at each output has also been carried out to prevent damages to the optical receivers caused by irregular input power variations. As the optical input power fluctuates, the output power is monitored and a feedback control loop adjusts the attenuation and maintains constant output power levels. This router may be used in applications like SI−POF local area networks for allowing redundant paths or reconfigurable multicasting in access networks. The second proposal is a broadband 1×2 optical router based on an achromatic LC polarization rotator (PR). The PR design process is simple, fast, and produces results comparable with the current state–of–the–art with more complex designs. The proposed PR design has rotation efficiency $T_y \geq$ 99.28% in the range from 400 to 700 nm. The experimental results show that the proposed router has quite similar values of *IL* and *CTA* in both outputs (OFF and ON states). The router has experimental *CTA* higher than 18.68 dB and average *ILs* lower than 2.74 dB (for polarized light), in both outputs, in the range from 400 to 700 nm. It has been shown that the router performance is quite constant with temperature changes of up to 10 °C. It is also demonstrated that is able to control the split ratio of the output power with good uniformity in the range from 400 to 700 nm. This router is a versatile device that allows routing the multiple broadband channels used in WDM networks and sensor systems based on SI−POF.

On the other hand, new Diffraction Gratings based Muxes/DeMuxes have been reported. First, a 3−channel Mux/DeMux proposal, based on a transmission diffraction grating, with experimental *ILs* from 3.6 to 5.8 dB and adjacent channel *CTA* from 16.4 to 28.6 dB is presented. Then, a 5−channel Mux/DeMux has been designed and experimentally tested. It is based on a reflective blazed diffraction grating and an aspherical lens. It has a length of ~65 mm and height of ~55 mm. The experimental *IL* and *CTA* are found to be less than 4 dB and higher than 30 dB, respectively. It is demonstrated that the central wavelength of each port can be tuned up to 15 nm, in order to accommodate specific channels. It is shown that the Mux/DeMux design can be extended to 8 channels keeping the *ILs* < 4.5 dB and *CTA* > 30 dB in a device with length of ~57 mm and height of ~50 mm. The theoretical analysis presented is in good agreement with experimental results and it can be used to design a compact 5 channel Mux/DeMux with a size reduction factor of 1.75 in length and of 2.2 in height, versus the 5 channel design reported. The Muxes/DeMuxes presented in this work have the best characteristics, in terms of performance, number of channels and size, reported in experimental systems.

Finally, a Multi−Gbit/s data transmission system based on a 5−channel visible WDM scheme over SI−POF technology is demonstrated. This system can establish a real−time bidirectional or unidirectional link at data rates of up to 5 Gbit/s over more than 50 m of SI−POF. The system performance has been experimentally tested using the first and last channels of the 5–channel available grid. The results show that the system can establish a real–time link with connection speed of up to 1 Gbit/s per channel with bit error rate $<1\times10^{-10}$, which represents an error free transmission, with better energy efficiency than recent proposals. Each channel in the system can be independently configured as uplink or downlink. This represents a real improvement in the performance of commercial and experimental SI−POF transmission systems.

7.3. Future Works

Finally, several issues related to the results reported in this work can be considered in further detail as future research. Some of them could be the following:

- To design an automated system for characterization of arbitrary nematic LC cells based in the proposed method. This system can be a useful tool for studying the variation of nematic LC cell's parameters with the temperature and the voltage. These are key issues in commercial applications of optical devices based on staked structures of LC cells.
- To develop new designs of wavelength selective devices based on arbitrary birefringent structures. These designs can be oriented to reduce the insertion losses by eliminating the intermediate linear polarizers required in the Lyot structure implemented, or to improve the crosstalk attenuation.
- To design a control system for improving the switching time of nematic LC cells by applying special driving signals. This can be done based on the fact that the LC cells response time depends on the amplitude change of the applied control voltage.
- To design and to optimize the LDs and/or LED based transmitters of all the channels used in the proposed Multi−Gbit/s Ethernet data transmission system over SI−POF.

- To implement the complete 5−channel Multi−Gbit/s Ethernet data transmission system over SI−POF.
- To study the BER impact over the Ethernet data throughput of a real data transmission system based on SI−POF. This analysis would allow a better comparison of the performance of SI−POF systems with different values of BER.
- To study different distribution topologies for In−Home networks that would enable the implementation the proposed SI−POF visible WDM approach, keeping the optical power that is in contact with the end used near or inside the eye safety limit.

7.4. Publications Related to this Work

The results of this research work have been disseminated through the following publications.

7.4.1. Papers in International Journals and Books

1. **P. J. Pinzón,** I. Pérez, C. Vázquez, J. M. Sánchez Pena,
   "1 × 2 Optical Router with Control of Output Power Level Using Twisted Nematic Liquid Crystal Cells",
   Molecular Crystals and Liquid Crystals , vol. 553, no. 1, pp. 36−43 (January 2012).

2. **P. J. Pinzón,** I. Pérez, C. Vázquez, and J. M. Sánchez Pena,
   "Reconfigurable 1×2 Wavelength Selective Switch using High Birefringence Nematic Liquid Crystals",
   Applied Optics, vol. 51, no. 25, pp. 5960−5965 (September 2012).

3. **P. J. Pinzón,** C. Vázquez, I. Pérez, and J. M. S nc hez−Pena,
   "Synthesis of Asymmetric Flat−Top Birefringent Interleaver Based on Digital Filter Design and Genetic Algorithm",
   ***IEEE Photonics Journal*,** vol. 5, no. 1, pp. 7100113 (February 2013).

4. **P. J. Pinzón**, I. Pérez, J. M. Sánchez−Pena, and Carmen Vázquez,
   "Spectral Method for Fast Measurement of Twisted Nematic Liquid Crystal Cell Parameters",
   Applied Optics, vol. 53, no. 23, pp. 5230−5237 (August 2014).

5. **P. J. Pinzón,** I. Pérez, C. Vázquez, and J. M. Sánchez−Pena,
   “Broadband 1×2 Liquid Crystal Router with Low Thermal Dependence for Polymer Optical Fiber Networks”,
   Optics Communications, vol. 333, pp. 281−287 (December 2014).

6. Co−author of the Book: “Advances in Optical Fiber Technology: Fundamental Optical Phenomena and Applications”,
   D. Sánchez Montero, I. Pérez, C. Vázquez, P. Lallana, A. Tapetado and **P. J. Pinzón**,
   “Recent Advances in Wavelength−Division−Multiplexing Plastic Optical Fiber Technologies”,
   InTech, ISBN: 978−953−51−1742−1, Chapter 12 (February 2015).

7. A. Tapetado, **P. J. Pinzón**, J. Zubia, C. Vázquez,
   “Polymer Optical Fiber Temperature Sensor With Dual−Wavelength Compensation of Power Fluctuations”,
   Journal of Lightwave Technology, vol. 33, no. 13, pp. 2716 – 2723 (July 2015).

8. P. J. Pinzón, I. Pérez, and C. Vázquez
   “Efficient Multiplexer/Demultiplexer for Visible WDM Transmission over SI–POF Technology”,
   Journal of Lightwave Technology, vol. 33, no. 17, pp. 3711 – 3718 (2015),
   DOI: 10.1109/JLT.2015.2455335.

9. P. J. Pinzón, I. Pérez, and C. Vázquez
   “VIS WDM System for Real–Time Multi–Gb/s Bidirectional Transmission over 50–m SI–POF”,
   Photonics Technology Letters, under review (2015).

7.4.2. Papers in National Journals

1. J. F. Algorri, V. Urruchi, **P. J. Pinzón** and J. M. Sánchez−Pena,
   “Modelling Electro−Optical Response of Nematic Liquid Crystals by Numerical Methods”,
   Journal of Optica Pura y Aplicada**,** vol. 46, no. 4, pp. 327−336 (2013).

7.4.3. Contributions in International Conferences

1. **P. J. Pinzón,** I. Pérez, C. Vázquez and J.M.S. Pena,
   “1x2 Optical Router with Control of Output Power Level using Twisted Nematic Liquid Crystal Cells”,
   ***European Conference of Liquid Crystals* 2011 – *ECLC’*11,**
   Poster Presentation, P5−09, Maribor (Slovenia), February 2011.

2. **P. J. Pinzón,** C. Vázquez, I. Pérez and J.M.S. Pena,
   “Reconfigurable Optical Demultiplexer for POF Networks”,
   20*th International Conference on Plastic Optical Fibers – ICPOF´*11,
   Oral Presentation, Proceedings PA1−103, Bilbao (Spain), September 2011.

3. **P. J. Pinzón**, I. Pérez, P. C. Lallana, C. Vázquez and J.M.S. Pena,
   “Reconfigurable Wavelength Selective Switch using High Birefringence Nematic Liquid Crystals”,
   ***XIX Conference on Liquid Crystals – CLC’*11**,
   Oral Presentation, Proceedings O−06, Miedzyzdroje (Poland), September 2011.

4. **P. J. Pinzón,** K. Heggarty, I. Pérez, C. Vázquez,
   “Diffraction Grating−Based deMultiplexers for SI−POF Networks",
   22*th International Conference on Plastic Optical Fibers – ICPOF´*13,
   Oral Presentation, Buzios (Brasil), September 2013.

5. **P. J. Pinzón,** I. ´Pérez, C. Vázquez and J. M. Sánchez Pena,
   “Broadband 1x2 Liquid Crystal Optical Switch with Low Thermal Dependence”,
   22*th International Conference on Plastic Optical Fibers – ICPOF´*13,
   Oral Presentation, Buzios (Brasil), September 2013.

6. **P. J. Pinzón**, I. Pérez, C. Vázquez, J. M. Sánchez Pena,
   “Univocal Determination of Twisted Nematic Liquid Crystal Cells parameters using a sSimple Experimental Approach”,
   12th *European Conference on Liquid Crystals – ECLC´*13,
   Poster Presentation, Rodas (Greece), September 2013.

7. **P. J. Pinzón,** I. Pérez, C. Vázquez, J. M. Sánchez Pena,
   "Broadband 1x2 Optical Switch Based on a Liquid Crystal Polarization Rotator with Optimized Spectral Response",
   XX Conference on Liquid Crystals – CLC'**13**,
   Oral Presentation, Milkojaki (Polonia), September 2013.

8. A. Tapetado, **P. J. Pinzón,** J. Zubia, I. Pérez, C. Vázquez,
   "Self−Referenced Temperature Sensor Based on a Polymer Optical Fiber Macro−Bend",
   23***rd International Conference on Optical Fibre Sensors – OFS'*****14,**
   Oral Presentation, SPIE 9157, pp. 915716, Santander (Cantabria), June 2014.

9. D. S. Montero, **P. J. Pinzón**, A. Tapetado, C. Vázquez, J. Zubia,
   "Performance Evaluation of Short−Range PF−GIOF Links: on Discrete Multi−Tone Transmission and WDM Enhancement",
   23***th International Conference on Plastic Optical Fibers – ICPOF'*****14,**
   Poster Presentation, Hiyoshi (Yokohama), October 2014.

10. **P. J. Pinzón**, C. Vázquez, I. Pérez and P.C. Lallana,
    "Design and Analysis of a WDM System for Multi−Gbit/s Transmission over 50 m of SI−POF",
    23***th International Conference on Plastic Optical Fibers – ICPOF'*****14,**
    Poster Presentation, Hiyoshi (Yokohama), October 2014.

11. C. Vázquez, **P. J. Pinzón** and I. Pérez,
    "Visible WDM System Design for Multi−Gbit/s Transmission over SI−POF",
    Photonics West**,**
    Oral Presentation,
    SPIE 9387, Broadband Access Communication Technologies IX, pp. 93870G,
    San Francisco (California), January 2015.

12. **P. J. Pinzón**, C. Vázquez, I. Pérez and A. López,
    "Efficient Real−Time Multi−Gigabit Ethernet Data Transmission System based on Visible WDM over SI−POF",
    24***th International Conference on Plastic Optical Fibers – ICPOF'*****15,**
    Poster Presentation, Nuremberg (Germany), September 2015.

13. **P. J. Pinzón,** C. Vázquez, I. Pérez and J. Zubia,
    “Low−loss 7−Channel Visible WDM Scheme for Implementing Efficient Data Transmission Systems over SI−POF”
    24th International Conference on Plastic Optical Fibers – ICPOF’15,
    Poster Presentation, Nuremberg (Germany), September 2015.

7.4.4. Contributions in National Conferences

1. **P. J. Pinzón,** I. Pérez, V. Urruchi, C. Vázquez and J.M.S. Pena,
   “Tunable Optical Filter using High Birefringence Nematic Liquid Crystals”,
   VII Reunión Española de Optoelectrónica – Optoel’11,
   Poster Presentation,
   Proceedings S3−111, ISBN 978−84−86116−31−6, Santander (Spain), June 2011.

2. D. Barrios, J. C. Torres, C. Marcos, **P. J. Pinzón,** R. Vergaz, J. M. Sánchez−Pena, A. Viñuales,
   “Dependencia con el espesor y el área de los parámetros del modelo de circuito eléctrico equivalente de dispositivos de cristal líquido disperso en polímero sobre substrato de cristal”,
   VII Reunión Española de Optoelectrónica – Optoel’11,
   Poster Presentation, Proceedings S3−111 ISBN 978−84−86116−31−6, Santander (Spain), June 2011.

3. **P. J. Pinzón,** I. Pérez, C. Vázquez and J.M.S. Pena,
   “Diseño de un Filtro Óptico Sintonizable Basado en Cristal Líquido con Mejora de las Pérdidas de Inserción”,
   XXVI Simposio Nacional de la Unión Científica Internacional de Radio – URSI’11,
   Oral Presentation, Proceedings ISBN 978−84−933934−4−1, Leganés (Spain), September 2011.

4. **P. J. Pinzón,** I. Pérez, C. Vázquez, J.M. Sánchez Pena,
   “Optimization of Polarization Rotators Spectral Response for Broadband Optical Switching Applications",
   VIII Reunión Española de Optoelectrónica – Optoel’13,
   Poster Presentation, Alcalá de Henares (Spain), July 2013.

5. **P. J. Pinzón,** C. Vázquez and I. Pérez,
   “Demonstration of a Data Transmission system With Visible Wavelength Division Multiplexing at 3−Gbit/s over 50−m of Plastic Optical Fiber”
   ***IX Reunión Española de Optoelectrónica – Optoel’*15,**
   Poster Presentation, Salamanca (Spain), July 2015.

6. A. Tapetado, D. Sánchez, J. Montalvo, **P. J. Pinzón** and C. Vázquez,
   “Sistema Permanente de Supervisión de Detección y Localización de Fallos de Fibra Óptica en PONs”
   ***IX Reunión Española de Optoelectrónica – Optoel’*15,**
   Poster Presentation, Salamanca (Spain), July 2015.

7.4.5. Research Stays

- From June 21, to August 23, 2012 **(2 months),**
  Optics Department, Telecom Bretagne, Brest (France),
  Funded by the Mobility Actions of University Carlos III de Madrid 2012,
  Viability study of an optical demultiplexer based on diffraction gratings for separating channels in the visible range, and manufacturing of diffraction grating prototypes,
  Supervised by Professor Kevin Heggarty.

- From June 01, to July 20, 2013 **(1 month),**
  Optics Department, Telecom Bretagne, Brest (France),
  Funded by the Mobility Actions of University Carlos III de Madrid 2013,
  Implementation of an optical demultiplexer based on diffraction gratings for separating channels in the visible range,
  Supervised by Professor Kevin Heggarty.

7.4.6. Other Relevant Information

- Assistance to the theoretical and practical course: **“Técnicas de medida en fibras ópticas”,**
  Organized by: **Comité de Optoelectrónica de la Sociedad Española de Óptica,**
  Sigüenza (Guadalajara), 6−8 October (21 h), 2010.

- Assitance to the advanced curse **“Light Sciences and Technologies for a New World”,**
  Organized by: **Universidad Internacional Menéndez Pelayo – UIM,**
  Santander (Spain), 15−19 June, 2015.

- **Supervisor** of the Bachelor Project: **“Diseño e implementación del controlador de un diodo láser para transmitir datos Ethernet a velocidades de Gbit/s/s sobre fibra óptica de plástico”,**
  Author: Tamara Trillo Gómez,
  Language and Defence: Spanish,
  Department of Electronics Technology,
  September 2014.

- **Supervisor** of the Bachelor Project: **“Sistema Automatizado para la Caracterización Dinámica y Estática de Células de Cristal Líquido Nemático”,**
  Author: Erika Alvarez Pino,
  Language and Defence: English,
  Department of Electronics Technology,
  September 2014.

- María José Pérez, E. Olías, **P. J. Pinzón**,
  “Study of defects in PV generators using image analysis techniques with Matlab”,
  ***International Conference on Renewable Energies and Power Quality−ICREPQ’*14,**
  Cordoba (Spain), April 2014.
  ***Renewable Energy and Power Quality Journal*,** ISSN 2172−038 X, no. 12.

- **Reviewer for two manuscripts submitted to Applied Optics.**

Chapter VIII:

Resumen del Trabajo Realizado

8.1. Motivación

Hoy en día, el volumen de datos transmitidos por las redes de corto alcance, sobre todo por las redes en el Hogar, tanto hacia el proveedor de servicios de Internet (*Internet Service Provider*, ISP) y entre los diferentes terminales, está aumentando más allá del Gbit/s, superando la capacidad de transmisión de las tecnologías de red actuales, como las basadas en cobre y las inalámbricas. Esto se debe al rápido crecimiento de nuevos servicios multimedia tales como: la televisión por internet (IPTV), las configuraciones de multi−visión/multi−habitación, la televisión de alta definición (HDTV), la visualización de imágenes en tres dimensiones, las comunicaciones remotas por videoconferencias y la telepresencia, entre otros.

Por otra parte, el ahorro energético es un tema que está ganando mucho interés en nuestra sociedad en los últimos años. Existe un consenso creciente sobre la necesidad de fijar como prioritario en la agenda de investigación de los países avanzados el desarrollo de tecnologías sostenibles que tengan la eficiencia energética como uno de los parámetros clave de su diseño. El consumo de energía de los ordenadores y equipos de red se está convirtiendo en una parte importante del consumo mundial de energía. A medida que la cobertura de la Tecnología de Información y Comunicaciones (*Information and Communications Technology*, ICT) se extiende rápidamente en todo el mundo, la huella de consumo de energía y de carbono de las ICT también aumentan rápidamente, ya que se despliega más equipos y más componentes en las redes de comunicaciones cada año. Las redes ópticas de alta eficiencia energética son un reto de gran interés. La reducción del consumo energético de las redes ópticas se puede abordar de forma genérica en cuatro niveles: componentes, transmisión, red y aplicaciones.

En los últimos años, se ha propuesto la fibra óptica de plástico (*Polymer Optical Fiber*, POF) como uno de los medios de transmisión más prometedores para la implementación de redes de comunicaciones de corto alcance de bajo coste y de alta velocidad. En concreto, en escenarios tales como redes de área local (*Local Area Networks*, LAN), redes al hogar y de oficina, así como en la industria automotriz, en los buses de información en aplicaciones aviónicas y en la interconexión de centros de datos. Hoy en día, la tecnología POF es una opción excelente para implementar redes de corto alcance de alta velocidad, y está reemplazando paso a paso a las tecnologías basadas en cobre, tales como el cable de par trenzado, el cable coaxial, la red eléctrica y cables Ethernet Cat−5.

Se ha demostrado que las POFs tienen múltiples aplicaciones en sistemas de sensores a un coste bajo o altamente competitivo en comparación con las tecnologías convencionales. Los sensores basados en POF tienen importantes aplicaciones potenciales en la monitorización de la salud estructural de infraestructuras, en biomedicina, medio ambiente y en diferentes áreas bioquímicas.

Las redes de sensores de fibra óptica están evolucionando rápidamente. Esto es debido, entre otros, a la naturaleza inerte de las fibras ópticas que ofrece inmunidad frente a las interferencias electromagnéticas, así como su uso en aplicaciones seguras en atmósferas inflamables. Otras características relevantes son su bajo peso y gran ancho de banda como medio de transmisión. En cualquiera de estos casos, es muy interesante disponer de componentes específicos tales como encaminadores y conmutadores ópticos para la selección de caminos específicos sin necesidad de conversiones óptico−a−eléctrico o eléctrico−a−óptico.

La aplicación de POF en el sector del automóvil ha sido particularmente exitosa. Desde que el estándar de bus de datos para vehículos llamado Sistemas de Medios Orientado al Transporte (*Media Oriented Systems Transport*, MOST) fue introducido por BMW en 2001, la POF ha desplazado al cobre en el habitáculo del automóvil en aplicaciones multimedia. En la actualidad, la tecnología MOST se utiliza por casi todos los principales fabricantes de automóviles en el mundo. Además, también se incluye el uso de POF en los nuevos protocolos de transmisión diseñados para soportar el rápido crecimiento en el número de sensores, actuadores y unidades de control electrónico dentro de los automóviles. Hasta la fecha, se han desarrollado un gran número de redes en el automóvil para aplicaciones multimedia y de seguridad.

Las redes aviónicas también pueden considerarse como un ejemplo de comunicación de corto alcance ya que su tamaño está limitado a una longitud máxima de 100 metros. La necesidad de sistemas de comunicación más rápidos, entre 100 Mbit/s y 1 Gbit/s, inmunes a la radiación electromagnética, motivó en los años noventa la migración de los buses de datos en redes aviónicas de cobre a buses de datos basados en fibra óptica. Los primeros sistemas con fibras de vidrio demostraron una alta fiabilidad, aumentado así de forma considerable el uso de enlaces ópticos en aviones comerciales durante la última década. Gracias a esto, se introduce la tercera generación de redes de comunicaciones ópticas en redes aviónicas con el lanzamiento del avión 787 Dreamliner por la Compañía Boeing. También se introduce los sistemas Lumexis de fibra hasta la pantalla (*Fiber−To−The−Screen*, FTTS) para sistemas de entretenimiento en vuelo (*In flight−entertainment*, IFE) con el lanzamiento del Flydubai B737. La facilidad de instalación y los costes más bajos de las fibras multimodo promueve el interés de la industria aviónica en las fibras de polímero, ya que con este tipo de fibras es posible realizar conexiones de datos de corto alcance y alta velocidad a un coste muy bajo utilizando componentes comerciales. Las fibras de plástico cumplen con los requisitos necesarios para competir en la sustitución por la fibra de las redes de datos de aeronaves que hasta ahora se basan en conexiones de cobre de baja velocidad, en determinadas aplicaciones. El uso de luz visible tiene también ventajas obvias en la detección de fallos y mantenimiento.

Entre los diferentes tipos de POF, la POF de salto de índice (*Step−Index POF*, SI−POF) con diámetro de 980 micras, núcleo de polimetil−metacrilato (PMMA) y apertura numérica (*Numerical Aperture*, *NA*) de ~ 0.5 ofrece varias ventajas, especialmente en los escenarios de corto alcance enumerados anteriormente, debido a su potencial bajo coste asociado con su facilidad de instalación, empalme y conexión. Esto se debe al hecho de que la SI−POF tiene dimensiones más grandes, mayor *NA* y un menor radio de curvatura critico en comparación con otros tipos de POF, como las POF de índice gradual (*Graded Index POF*, GI−POF), y las fibras ópticas de vidrio, o sílice (*Glass Optical Fibers*, GOFs). Por otra parte, la SI−POF es más flexible y dúctil, por lo que es más fácil de manejar, incluso por personas sin formación especializada.

Sin embargo, el ancho de banda de la SI−POF sigue siendo significativamente menor que el de las GI−POFs y GOFs (monomodo y multimodo). Esto es porque la SI−POF sufre de una alta dispersión modal debido a su gran *NA*, lo que limita su producto ancho de banda por distancia a aproximadamente 50 MHz × 100 m. Además, sólo se utiliza en el intervalo del espectro visible (*Visible Spectral Range*, VIS), con una atenuación aceptable (por ejemplo, ~ 0.17 dB/m a 650 nm). El ancho de banda limitado y la alta atenuación obstaculizan la integración deseada de múltiples servicios de banda ancha en un acceso común de SI−POF para redes del hogar y/o en los diferentes escenarios de corto alcance descritos anteriormente.

Para superar las limitaciones de ancho de banda de estas fibras es necesario el desarrollo de técnicas orientadas a ampliar las capacidades de las redes SI−POF, para satisfacer la demanda del consumidor de servicios multimedia en redes de corto alcance. Desde hace algunos años se han propuesto e implementado, con excelentes resultados, diferentes esquemas de modulación y ecualización eficientes para redes SI−POF. Y gracias a esto, la capacidad de los enlaces SI−POF para transmitir a velocidades por encima del Gbit/s ha sido ampliamente demostrada, utilizando sistemas basados en un sólo canal (típicamente a 650 nm).

Pero la capacidad de transmisión de datos de los sistemas SI−POF necesita una mayor explotación para satisfacer las necesidades del usuario, de tasas de datos más alta con un bajo consumo de energía y bajo coste. Esto genera mucho interés en el desarrollo de nuevos sistemas de transmisión con tasas de datos de Multi−Gbit/s sobre tecnología SI−POF, incluyendo nuevos transmisores y receptores, y nuevos estándares.

En este punto, y después de haber explotado las capacidades de transmisión un solo canal sobre SI−POF, se propone la multiplexación por división en longitud de onda (*Wavelength Division Multiplexing*, WDM) visible como una solución prometedora para expandir la capacidad de transmisión de datos de los sistemas basados en SI−POF. La mayoría de los resultados recientes relacionados con sistemas WDM en el visible sobre SI−POF (basados en técnicas de procesamiento posterior) revela el gran potencial de esta tecnología.

Pero hay algunas limitaciones que se deben abordar con el fin de obtener capacidades similares a las soluciones basadas en WDM sobre GOFs. Por ejemplo, las SI−POF se pueden utilizar en el rango visible (400 a 700 nm) que es extremadamente amplio si se compara con las bandas C y L (1530−1565 nm y 1565−1625 nm, respectivamente) utilizadas en los sistemas WDM sobre GOFs. Es por esto que muchos de los dispositivos ópticos, tales como filtros, conmutadores, intercaladores, encaminadores, multiplexores y demultiplexores, que se utilizan en los sistemas WDM sobre GOF no se pueden utilizar en los sistemas basados en SI−POF y los que se podrían utilizar requieren un rediseño completo.

Estos dispositivos ópticos son indispensables para el desarrollo de las futuras redes de comunicaciones de alta velocidad y de corto alcance, así como en muchas aplicaciones de redes de sensores. Sin embargo, las diferentes necesidades y/o requerimientos impuestos por la tecnología SI−POF con WDM en el visible, se deben considerar cuidadosamente en sus diseños. Los dispositivos ópticos necesarios para implementar los sistemas basados en SI−POF deben tener:

- Capacidad de reconfiguración o sintonización, ya que no existen canales definidos.
- Capacidad de manejar canales con gran ancho de banda espectral, ya que se utilizan como transmisores tanto diodos láser (LDs) como diodos emisores de luz (LEDs).
- Capacidad para aceptar haces de luz con alta divergencia, debido a que la SI−POF representa un objeto con 1 mm de altura y apertura numérica de 0.5.
- Pérdidas de inserción (*Insertion Losses*, *ILs*) bajas, con el fin de evitar o reducir la penalización por potencia en la capacidad de transmisión de los sistemas de SI−POF basados en WDM en el visible.

Obviamente, una sola tecnología no puede cumplir todos estos requisitos, la tecnología apropiada para cada dispositivo o aplicación se debe elegir en función del tipo de red, la topología y las necesidades específicas. En este trabajo, se han desarrollado nuevos dispositivos ópticos para aplicaciones sobre SI−POF. Estos se pueden clasificar en dos grandes grupos: dispositivos reconfigurables y dispositivos de bajas pérdidas.

Entre las diferentes tecnologías utilizadas para la implementación de dispositivos ópticos, aquellas basadas en cristales líquidos (*Liquid Crystals*, LC) son una opción muy interesante para el diseño de dispositivos reconfigurables, ya que no necesitan partes móviles para la reconfiguración, utilizan bajos voltajes de excitación y tienen bajo consumo de energía. Las aplicaciones actuales de los dispositivos de cristal líquido en redes WDM basadas en GOF son múltiples (en el rango infrarrojo, IR), pero no en el rango VIS para redes SI−POF con WDM.

El Grupo de Displays y Aplicaciones Fotónicas (GDAF), de la Universidad Carlos III de Madrid (UC3M), ha estado trabajando activamente en el diseño, fabricación y caracterización de dispositivos de cristal líquido para redes de comunicaciones ópticas y en específico para aplicaciones con POF. Debido a esto, a las ventajas que ofrecen las tecnologías de cristal líquido, así como al rápido crecimiento de las redes SI−POF, se ha decidido desarrollar nuevos dispositivos reconfigurables de bajo consumo basados en cristal líquido, específicamente diseñados para implementar redes SI−POF con esquemas de WDM en el visible. Los dispositivos basados en cristal líquido que se presentan en este trabajo han sido clasificados como: dispositivos selectivos en longitud de onda (filtros, intercaladores e interruptores) y encaminadores reconfigurables.

Esos dispositivos de cristal líquido son fundamentales para implementar las futuras redes basadas en WDM visible sobre SI−POF, principalmente debido a su versatilidad y capacidad de reconfiguración, y porque se pueden producir en masa con un bajo coste (principalmente porque son una tecnología madura) y con diseños compactos (incluso utilizando elementos de óptica discreta).

Por otro lado, para implementar sistemas WDM se necesitan dos dispositivos clave, multiplexores (Muxes) y demultiplexores (DeMuxes). Estos dispositivos son necesarios para combinar y separar los canales centrados en diferentes longitudes de onda. Sin embargo, la mayoría de los Muxes/DeMuxes para GOFs, o para GI−POFs con baja *NA* y diámetro pequeño, no son adecuados para redes SI−POFs. Esto se debe al amplio rango espectral utilizado en los sistemas con WDM en el visible sobre SI−POFs, la naturaleza multimodal de la fibra y a sus características físicas, que produce haces en el espacio libre altamente divergentes y con un gran diámetro.

Una limitación importante de los enlaces WDM en el visible sobre SI−POF es la penalización por potencia debido a las altas pérdidas de inserción de los Muxes/DeMuxes actuales, lo que limita la capacidad de transmisión de datos de cada canal en comparación con sistemas de canal único, para la misma potencia óptica de transmisión. La mayoría de los prototipos de Muxes/DeMuxes basados en SI−POF presentes en la literatura se han desarrollado utilizando filtros interferenciales, prismas y rejillas de difracción, con *ILs* muy por encima de los 5 dB. Por lo tanto, para que la implementación de sistemas WDM en el visible sobre SI−POF se convierta en una realidad, se requiere el desarrollo de dispositivos multiplexores y demultiplexores con pérdidas más bajas y múltiples canales. Algunos autores establecen que 5 dB de pérdidas de inserción por canal es un valor razonable para conseguir un aumento real de la capacidad de transmisión de enlaces SI−POF utilizando esquemas WDM en el visible.

Esto ha motivado el diseño e implementación de Muxes/DeMuxes de bajas pérdidas, basados en rejillas de difracción, con *ILs* inferiores a 4.5 dB y con más de 3 canales.

Por último, una de las motivaciones más importantes de este trabajo es demostrar la posibilidad de aumentar la capacidad de transmisión de enlaces SI−POF de canal único utilizando sistemas con WDM en el visible sobre tecnología SI−POF.

8.2. Objetivos

Se necesitan nuevos dispositivos ópticos en el rango visible para el desarrollo de las futuras redes de comunicación de alta velocidad y corto alcance basadas en SI−POF. Estos dispositivos también son de gran utilidad en muchas aplicaciones de sensores basados en POF. Los diseños de estos dispositivos no están bien establecidos hasta la fecha debido a las características físicas y multimodales de la tecnología SI−POF, así como las características de los sistemas WDM en el visible. Por lo tanto, el principal objetivo que se ha establecido para este trabajo de investigación es el desarrollo de nuevos dispositivos ópticos basados principalmente en cristales líquidos y elementos de difracción para aplicaciones en sistemas avanzados de comunicaciones ópticas con fibras ópticas de plástico de salto de índice, lo que garantiza un consumo de energía optimizado para reducir la huella de carbono en esta tecnología en el sector TIC. Este objetivo se aborda a través de los siguientes cuatro objetivos específicos:

Objetivo 1: Diseñar y probar nuevos dispositivos ópticos reconfigurables basados en elementos birrefringentes para la implementación de sistemas SI−POF avanzados con WDM en el visible, incluyendo nuevas técnicas de caracterización. Estos sistemas incluyen esquemas para aplicaciones de protección, recuperación frente a fallos y redes de sensores.

Objetivo 2: Diseñar y probar nuevos dispositivos Multiplexores/Demultiplexores de bajas pérdidas basados en elementos de difracción para implementar sistemas de transmisión de datos basados en WDM en el visible sobre tecnología SI−POF con un consumo energético eficiente.

Objetivo 3: Implementar sistemas de transmisión de datos Ethernet en tiempo real a velocidades de Multi−Gbit/s sobre enlaces bidireccionales de hasta 50 m, libres de errores, con tecnología SI−POF con WDM en el visible, que puedan mejorar el rendimiento, en términos de tasa de transmisión de datos por unidad de longitud, de aquellos sistemas que transmiten sobre un solo canal óptico.

Objetivo 4: Contribuir en la reducción del consumo de energía de las redes ópticas a nivel de componentes y de transmisión, mediante el uso de tecnologías de bajo consumo y dispositivos con bajas pérdidas de inserción.

8.3. Conclusiones

En este trabajo de investigación, se han propuesto diferentes dispositivos ópticos basados en cristales líquidos y rejillas de difracción. Estos dispositivos se han diseñado para su uso en sistemas de sensores ópticos y redes de transmisión de datos basados en esquemas WDM en el visible.

Los dispositivos de cristal líquido propuestos, tales como filtros, conmutadores selectivos en longitud de onda, intercaladores y encaminadores son capaces de incluir funciones avanzadas en muchos sistemas SI−POF tales como sintonización y reconfiguración en un rango espectral muy amplio sin necesidad de conversiones óptico−a−eléctrico y eléctrico−a−óptico. Sin embargo, las pérdidas de inserción de estos dispositivos son altas (> 5 dB), lo que limita su aplicabilidad a sistemas en los que las pérdidas no son un factor limitante, por ejemplo, en sistemas de transmisión de datos y de sensores de muy corto alcance (<15m). Pero, en general, las pérdidas de inserción de estos dispositivos se pueden reducir en gran medida mediante el uso de esquemas de diversidad de polarización y dispositivos sensibles a la polarización (polarizadores lineales y divisores de haz) con una transmitancia optimizada en el rango de operación.

A través de los resultados de las diferentes simulaciones presentadas en el Capítulo 3 y en el Capítulo 4, se ha demostrado que el comportamiento de los dispositivos de cristal líquido propuestos se puede modelar con éxito utilizando el formalismo de las matrices de Jones y la caracterización precisa de los parámetros de las células de cristal líquido. Por lo tanto, se puede afirmar que el método de caracterización propuesto es una herramienta muy útil para el diseño óptimo de los diferentes dispositivos basados en cristal líquido.

En este trabajo, se ha demostrado que las rejillas de difracción planas son hasta la fecha, una excelente opción para la implementación de Muxes/DeMuxes compactos, con bajas pérdidas de inserción y de múltiples canales para aplicaciones de sistemas SI−POF con WDM en el visible. Estas características son especialmente necesarias para implementar sistemas eficientes de transmisión de datos a velocidades de Multi−Gbit/s sobre SI−POF utilizando la multiplexación WDM en el visible.

Los diseños de Muxes/DeMuxes propuestos están al nivel del estado actual de la técnica, debido a sus bajas pérdidas, alta atenuación de diafonía (*Crosstalk Attenuation*, *CTA*) y número de canales. Estos diseños han permitido la implementación de un sistema de transmisión bidireccional de datos Ethernet en tiempo real a través de 50 m de SI−POF utilizando un esquema WDM en el visible de 5 canales, con capacidad de transmisión libre de errores de hasta 5 Gbit/s. Este sistema tiene una mayor eficiencia energética por bit transmitido que otras propuestas. De esta forma se ha demostrado que el enfoque del sistema WDM en el visible propuesto tiene el potencial de aumentar la capacidad de transmisión de datos de los enlaces SI−POF sin un incremento importante de la potencia óptica transmitida.

A continuación se muestra un resumen de las contribuciones más importantes que se presentan en este trabajo de investigación.

8.4. Aportaciones

En este trabajo, se han diseñado y probado experimentalmente diferentes dispositivos ópticos novedosos basados en elementos birrefringentes y rejillas de difracción. Estos dispositivos se han diseñado de forma específica para implementar redes SI−POF avanzadas basadas en multiplexación por división de longitud de onda en el visible (WDM visible). Este tipo de redes se utilizan en sistemas de sensores con esquemas de auto−referencia y en redes de transmisión de datos a velocidades de Multi−Gbit/s para aplicaciones de corto alcance. Además estas redes operan en el rango de longitudes de onda en el rango visible.

Los dispositivos birrefringentes propuestos están basados en células de cristal líquido nemático y han sido clasificados como Dispositivos Selectivos en Longitud de Onda (*Wavelength Selective Devices*, WSD) y Encaminadores Ópticos (*Optical Routers*, OR). Estos dispositivos dan a los sistemas SI−POF funciones avanzadas tales como sintonización, reconfiguración y baja dependencia con la longitud de onda sin necesidad de realizar conversiones óptico−a−eléctrico o eléctrico−a−óptico. Algunos de ellos se han diseñado, probado y simulado con éxito utilizando la caracterización precisa de células de cristal líquido de alta birrefringencia.

Además, se ha desarrollado un nuevo método experimental para la determinación unívoca de los parámetros de las células arbitrarias de cristal líquido nemático. A diferencia de las propuestas anteriores, este método utiliza pocas variaciones del ángulo de azimut de las células, utiliza límites de búsqueda muy amplios (en el ajuste no lineal), no necesita condiciones iniciales y se puede utilizar para determinar la dispersión espectral de la birrefringencia del material de cristal líquido. Este método es ideal para el diseño de dispositivos birrefringentes basados en estructuras de células de cristal líquido en cascada para aplicaciones que requieren de un amplio espectro. Además, se puede integrar fácilmente en un sistema de caracterización preciso, rápido y automático.

Se han propuesto novedosos WSDs, optimizados para trabajar en el rango visible con redes SI−POF. Estos dispositivos se benefician de la gran apertura, de la baja dispersión cromática y alta fiabilidad que ofrecen las estructuras birrefringentes, así como de la capacidad de reconfiguración que se puede lograr con tecnología de cristal líquido.

El primer WSD es un filtro óptico sintonizable basado en células de cristal líquido nemático de alta birrefringencia (*Liquid Crystal Tunable Filter*, LCTF). Los parámetros de este filtro se han optimizado para trabajar en el rango de espectro VIS−NIR. Se ha obtenido un rango de sintonización de la longitud de onda de paso superior a 200 nm (de 610 a 820 nm), con un ancho de banda a mitad de máximo (FWHM) inferior a 80 nm. Se ha demostrado que este rango de sintonización se obtiene con tensiones de alimentación por debajo de 1.5 V_{RMS}. También, se ha presentado los resultados de la simulación del filtro. Estos resultados muestran muy buena concordancia con los resultados experimentales.

El segundo WSD es un conmutador óptico reconfigurable selectivo en longitud de onda (R−WSS), basado en una estructura de filtro Lyot y células de cristal líquido nemático de alta birrefringencia. Este sistema permite funciones de demultiplexación y conmutación, o bloquear cualquier canal a través de cualquier puerto de salida utilizando voltajes de 0 a 3 V_{RMS}. Se obtuvieron pérdidas de inserción máxima de 6 dB (para la luz no polarizada) y relaciones de atenuación de diafonía (*CTA*) superiores a 16 dB.

El rendimiento del LCTF y del R−WSS propuestos se mejora mediante el uso de estructuras birrefringentes arbitrarias como las que se utilizan en el diseño de dispositivos intercaladores birrefringentes, diferentes de la estructura básica de Lyot. Es por este motivo que se ha propuesto un nuevo método de síntesis flexible y rápida para el diseño de dispositivos intercaladores asimétricos de banda de paso plana y baja dispersión, con capacidad de ajustar el rechazo y los anchos de banda en ambas salidas. En este método, se utilizan las propiedades de la transformada Z y las técnicas de diseño de filtros digitales para el diseño de intercaladores ópticos siguiendo un conjunto fijo de especificaciones. En un segundo nivel se emplea un proceso de optimización basado en una implementación del algoritmo genético que permite mejorar las características del intercalador, ajustando el rechazo y/o dispersión, de una o ambas salidas. Este método de síntesis fue utilizado en el diseño de un intercalador óptico optimizado para aplicaciones en SI−POF en el rango visible.

También se han presentado dos nuevas propuestas para la implementación de encaminadores ópticos reconfigurables de cristal líquido (*Liquid Crystal Optical Routers*, LC−OR). La primera propuesta es un encaminador óptico reconfigurable de 1×2 con control del nivel de potencia en ambas salidas. Este encaminador permite bloquear o redirigir el haz de luz de entrada, ya sea sólo a uno de los puertos de salida o a ambos simultáneamente. Además, también se ha llevado a cabo el control del nivel de potencia óptica en cada salida para prevenir posibles daños en los receptores ópticos causados por variaciones irregulares de la potencia de entrada. A medida que la potencia óptica a la entrada fluctúa, un bucle de control de realimentación ajusta la atenuación óptica y mantiene los niveles de potencia de salida constante. Este intercalador se puede utilizar en aplicaciones SI−POF en redes de área local para implementar rutas redundantes o multidifusión reconfigurable en enlaces de acceso. La segunda propuesta es un encaminador óptico 1×2 de amplio rango espectral basado en un rotador de polarización de cristal líquido acromático (*Polarization Rotator*, PR). El proceso de diseño del PR es simple y rápido, y produce resultados comparables con el estado actual de la técnica con diseños más complejos. El diseño del PR propuesto tiene una eficiencia de rotación $Ty \geq 99.28\%$ en el rango espectral de 400 a 700 nm. Los resultados experimentales muestran que este encaminador tiene valores muy similares de *ILs* y *CTA* en ambas salidas (en estados OFF y ON). Tiene medidas experimentales de *CTA* superiores a 18.68 dB e *ILs* inferiores a 2.74 dB (para luz polarizada), en ambas salidas, en el rango espectral de 400 a 700 nm. Además, se ha demostrado que el rendimiento del encaminador es bastante constante frente a cambios de temperatura de hasta 10 °C. También se ha demostrado que este encaminador es capaz de controlar la relación de división de la potencia entre las salidas con una buena uniformidad en el intervalo de 400 a 700 nm. Este es un dispositivo muy versátil que permite encaminar los múltiples canales de amplio espectro utilizados en redes de transmisión de datos con WDM en el visible y en sistemas de sensores con esquemas de auto−referencia basados en SI−POF.

Por otro lado, se han propuesto nuevas configuraciones de Muxes/DeMuxes basadas en rejillas de difracción planas. Primero, se ha propuesto un Mux/DeMux de 3 canales basado en una rejilla de difracción transmisiva, con medidas experimentales de *ILs* de 3.6 a 5.8 dB y de *CTA* entre canales adyacentes de 16.4 a 28.6 dB. Se ha propuesto un proceso de diseño y caracterización de un Mux/DeMux de 5 canales, basado en una rejilla de difracción reflectante y una lente asférica. Este dispositivo tiene una longitud de ~ 65 mm y altura de ~ 55 mm. Las pérdidas de inserción son inferiores a 4 dB y la *CTA* está por encima de 30 dB. Se ha demostrado que se puede sintonizar la longitud de onda central de cada puerto en hasta 15 nm, con el fin de acomodar canales específicos. También se ha demostrado que este diseño de Mux/DeMux se puede extender a unos 8 canales manteniendo la *ILs* < 4.5 dB y la *CTA* > 30 dB en un dispositivo con una longitud de ~ 57 mm y altura de ~ 50 mm. El análisis teórico que se ha presentado muestra que hay una buena concordancia con los resultados experimentales y se ha utilizado para diseñar un Mux/DeMux de 5 canales más compacto, con un factor de reducción de tamaño de 1.75 en longitud y de 2.2 en altura, en comparación con el diseño de 5 canales presentado. Los Muxes/DeMuxes que se han presentado en este trabajo tienen las mejores características en sistemas experimentales que se han publicado hasta la fecha, en términos de rendimiento, número de canales y tamaño.

Finalmente, se han desarrollado un sistema de transmisión de datos a velocidades de Multi−Gbit/s basado en un esquema de WDM en el visible de 5 canales sobre tecnología SI−POF. Este sistema puede establecer un enlace bidireccional (o unidireccional) en tiempo real a velocidades de hasta 5 Gbit/s en longitudes de hasta 50 m de SI−POF. El rendimiento del sistema se ha probado experimentalmente utilizando el primer y el último canal de los 5 canales disponibles. Se ha establecido un enlace en tiempo real con velocidades de conexión de hasta 1 Gbit/s por canal con tasa de bits de error inferior a 1×10^{-10}, lo que representa una transmisión libre de errores, con mejor eficiencia energética que otras propuestas recientes basadas en WDM en el visible sobre SI−POF. Cada canal en el sistema se puede configurar independientemente como enlace ascendente o descendente. Estas características representan mejoras reales en el rendimiento de sistemas de transmisión basados en SI−POF comerciales y experimentales.

Appendices:

A. Phase Delay (Γ) Measurements of High−Birefringence HN Cells

This appendix presents the phase delay characterization and the effective birefringence calculation of three HN cells manufactured with the 1658 LC material. This is an experimental LC material synthesized at the Military University of Technology in Warsaw. Those cells have thicknesses of 5.1 μm and are named 1658−HN1, 1658−HN2 and 1658−HN3. The 1658 is the same high−birefringence material used to fabricate the cell TN2 that has been characterized in **section 2.5.3.4** **[1]** The phase delay, and the birefringence, of the HN cells are determined by using the method reported in **[2]**, with the difference that in this case, multiple wavelengths are measure and analyze simultaneously. Besides, in order to obtain the accurate dispersion profile of the LC material; an automated system is implemented, which is used for applying the voltage sweep required by the method, fast and with good resolution. This allows characterizing high birefringence LC cells avoiding the effect of the room temperature variations during measurements, since it is not stabilized. The procedure presented in this appendix is used for determining the birefringence dispersion of HN cells, for different applied voltages. This information is useful in the design of LC tunable and reconfigurable devices, as the Tunable Filter and the Wavelength Selective Switch presented in **Chapter 3** **[3]**, and the Reconfigurable Routers presented in **Chapter 4** **[4]**, **[5]**.

A.1. Theoretical Basics and Procedure

When a HN cells is placed between parallel and crossed linear polarizers (LPs), with the cell rubbing angle at 45° with respect to the input LP, the optical transmittances ($T_{\parallel}$ and $T_{\perp}$ for parallel and crossed LPs configurations, respectively) of the system LP − HN cell − LP can be obtained using the Jones Formalism (see **section 2.3**), and are given by:

T [redacted] $s^{2}\left(\frac{\Gamma}{2}\right)$ (A.1)

$$T_{\perp} = \sin^{2}\left(\frac{\Gamma}{2}\right) \tag{A.2}$$

From (A.1) and (A.2) it is possible to determine the absolute phase retardation (Γ) of the HN cell, which can be expressed as:

$$\Gamma = \begin{cases} N\pi + ar\cos\left(\dfrac{T_{\|}\text{[redacted]}}{T_{\|}\text{[redacted]}}\right) & for \quad N = 0,2,4,... \\ (N+1)\pi - ar\cos\left(\dfrac{T_{\|}\text{[redacted]}}{T_{\|}\text{[redacted]}}\right) & for \quad N = 1,3,5,... \end{cases} \tag{A.3}$$

N is an integer value that can be determined by analyzing the transmittance curves of $T_{\|}(V)$ and $T_{\perp}(V)$, obtained from the voltage sweep of *V* between 0 and the saturation voltage (V_{sat}), at a fixed λ, as shown in **Fig. A.1**.

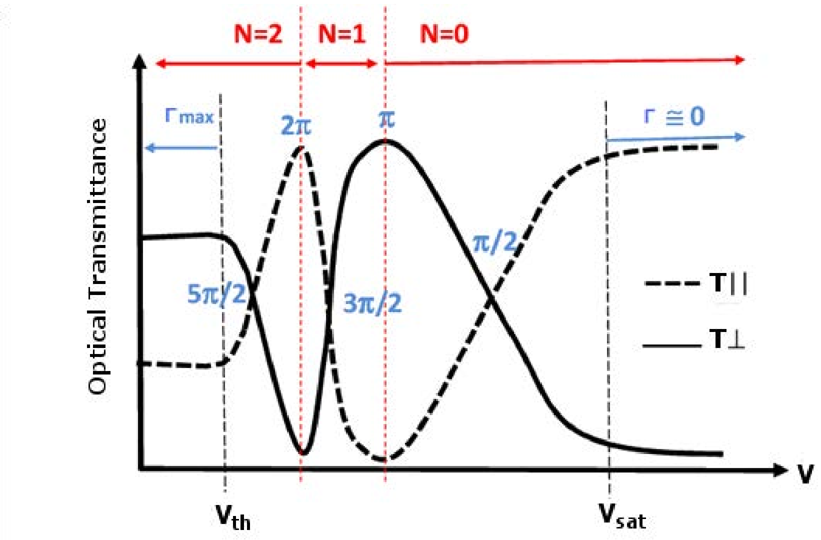

Fig. A.1: Optical transmittance of a HN cell between parallel ($T_{\|}$) and crossed ($T_{\perp}$) LPs as a function of the applied voltage (*V*). The values of *N* are determined by analyzing the inflexion points of the curves.

Finally, if the cell thickness is known (d_H), the effective birefringence $\Delta n_{eff}(V)$ can be determined by using the phase delay definition given in **section 2.2.1.2**:

$$\Gamma = 2\pi \frac{\Delta n_{eff}(V)}{\lambda} \tag{A.4}$$

If the pre–tilt angle of the LC molecules is negligible, the birefringence of the LC material, with which the cell is manufactured, corresponds to the maximum value of Δn_{eff} (at $V<V_{th}$).

A.2. Experimental Set–up

The transmittance curves $T_{\|}$ and $T_{\perp}$ of the 1658–HN cells are measured using the experimental set–up shown in **Fig. A.2**. The input beam is obtained from a halogen light source (Avalight Hall) and the measurements are taken with the spectrometer AvaSpect–128, with spectral range from 360 to 886 nm and 4 nm of spectral resolution. Multimode optical fibers with collimators are used at the input and output ports. The input collimator produces a beam of 5 mm diameter. The LPs (LPVIS050) have a diameter of 12.5 mm and an extinction ration > 10,000:1 in the range from 525 to 1350 nm. Then, transmittance measurements are limited between 525 and 886 nm due the operation range of the LPs and the spectrometer, respectively. The input LP is placed at 45º and the HN cells are places at 0º, while the output LP (analyzer) is placed at 45º (for measuring $T_{\parallel}$) or at 135º (for measuring $T_{\perp}$). The angles are referred from the laboratory *x*−axis.

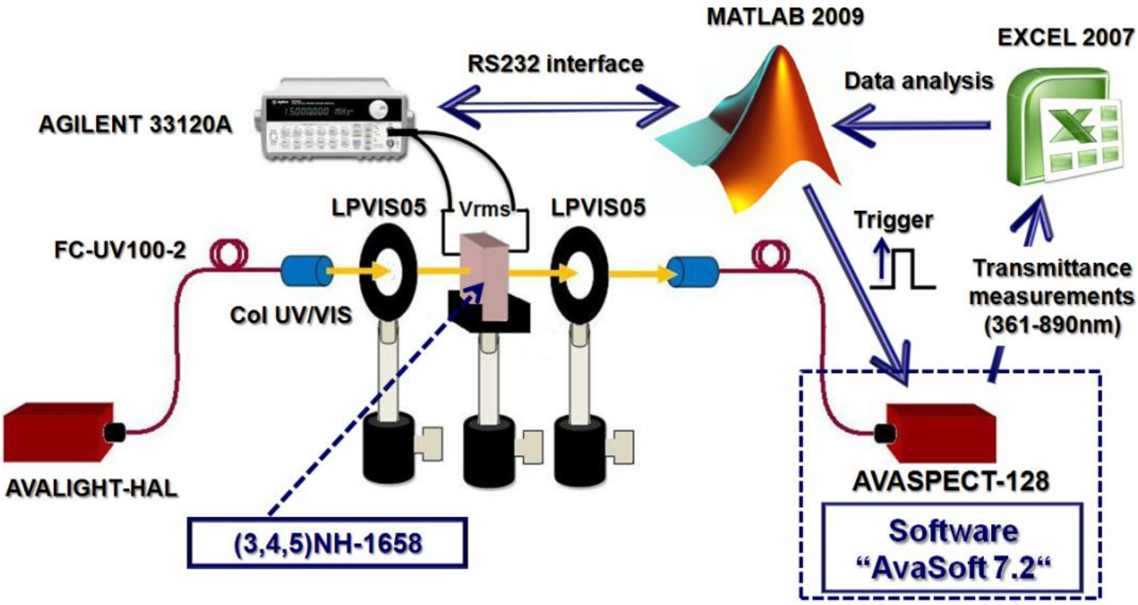

Fig. A.2. Experimental set−up used for the characterization of HN cells and automation scheme.

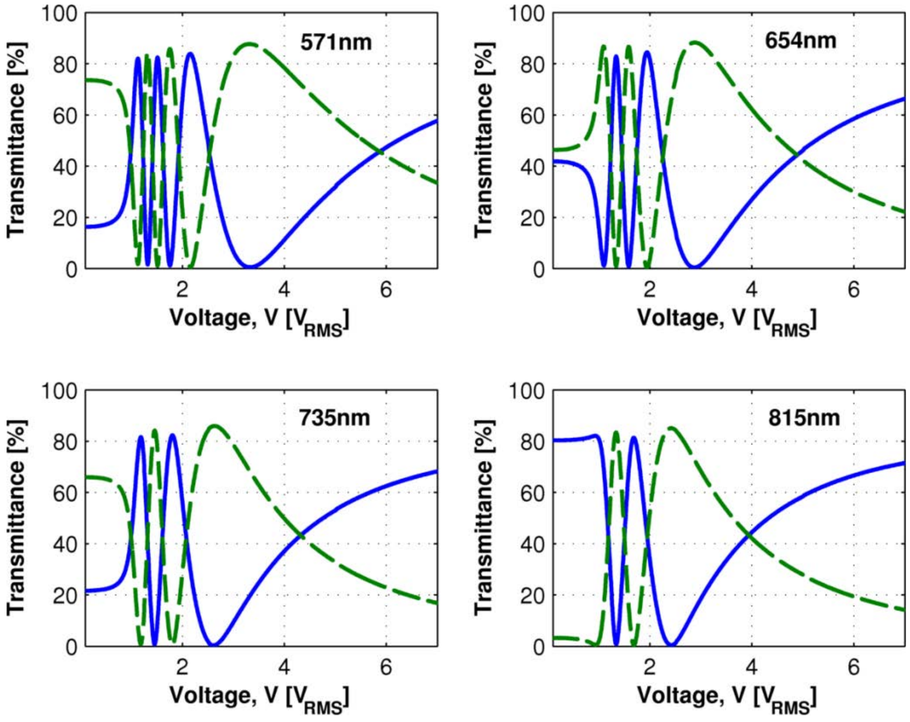

Fig. A.3: Optical transmittance of a HN cell with 1658 LC material and 5.1 *μ*m thickness (1658−HN1) placed between parallel LPs, (solid line) and crossed LPs (dashed line), as a function of the applied voltage (*V*) at four different wavelengths.

The experimental setup that is shown in **Fig. A.2** has been automated as follows. Once the HN cell is placed between the LPs (Parallel or Crossed), the control software (implemented in MATLAB) set the different control voltages ($0 \leq V \leq V_{sat}$) in an arbitrary waveform generator, which is connected to the HN cell. When the specific voltage is set, and the HN cell response is stabilized, the control program send a trigger signal to the spectrometer to perform the transmittance measurements, in the considered spectral range. The transmittance data is saved from the spectrometer in to an Excel file. **Fig. A.3** shows the transmittance curves $T_{\parallel}$ and $T_{\perp}$ of the 1658–HN1 cell at four different wavelengths. The applied voltage is between 0 and 7 V_{RMS} (using a square waveform with frequency of 1 kHz) with resolution of 5 mV_{RMS}.

Finally, the control program analyzes data from the excel file, in order to determine the values of N for different values of V using the procedure shown in **Fig. A.1** (for each λ), and to thus obtain the phase retardation and the birefringence of the HN cell from (A.3) and (A.4).

A.3. Results: Birefringence of 1658–HN Cells

The **Fig. A.4** shows the birefringence results (dots) of the three HN cells of 1658 LC material that have been characterized (1658–HN1, 1658–HN2 and 1658–HN3) at $V = 0 V_{RMS}$.

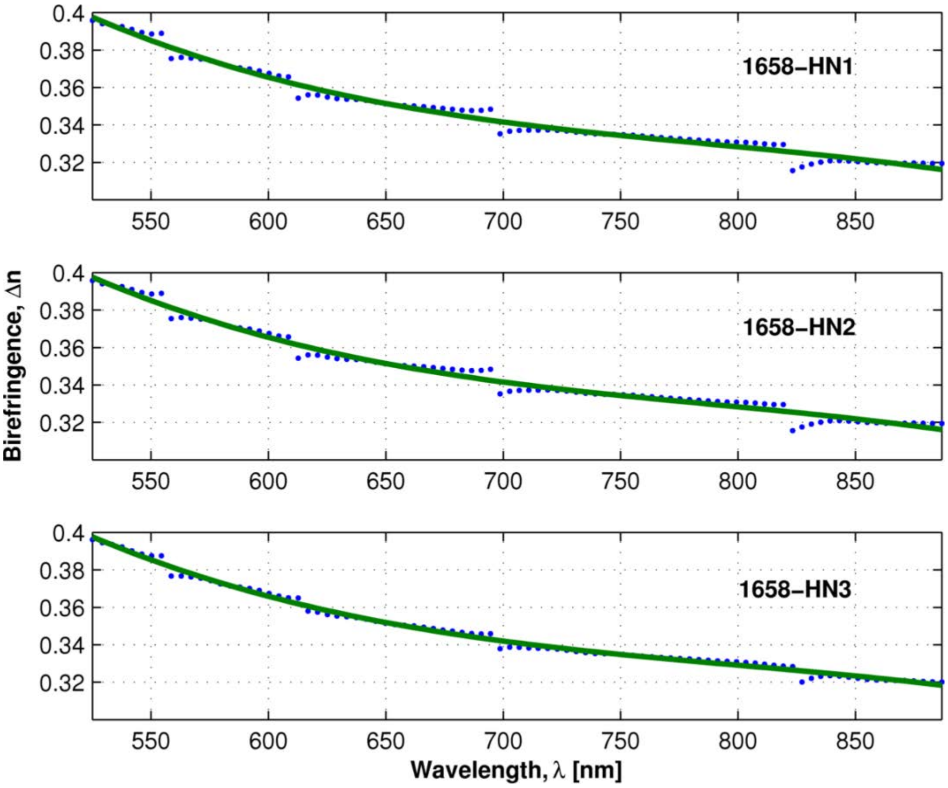

Fig. A.4: Birefringence results of the three HN cells of 1658 LC material and 5.1 thicknesses that have been characterized at $V = 0 V_{RMS}$. Experimental calculations are represented by dots and the polynomial regressions (dispersion profiles) are represented by solid lines.

The discontinuities observed in the birefringence results of **Fig. A.4** appear in the wavelength intervals where N changes from N to $N + 1$. This is the most important disadvantage of this method. The solid lines represent the polynomial regressions from the experimental calculations (dots) and are used in order to overcome the birefringence discontinuities, these curves are names dispersion profiles. The squared error between the different dispersion profiles is less than 1%.

The experimental birefringence (and the respective dispersion profiles) is calculated for each value of V in order to obtain the birefringence of the LC cells as a function of wavelength and the applied voltage, Δn_{eff} (λ, V). **Fig. A.4** shows the birefringence of the LC cell 1658−HN3, as a function V at three different wavelengths.

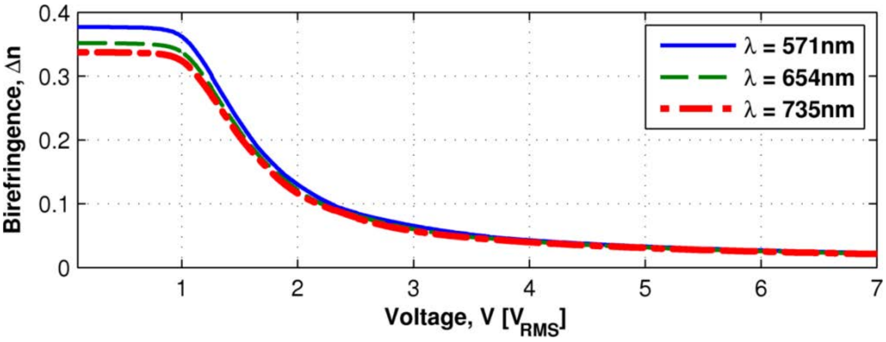

Fig. A.5: Effective birefringence as a function of the applied voltage of the cell 1658−HN1 at three different wavelengths.

Characterization method presented in this appendix is simple, but the discontinuities observed in certain wavelengths ranges represent an important drawback that reduces its accuracy. These discontinuities occur in the ranges of wavelengths where N changes from N to $N + 1$. Let us analyze the transmittance curves of **Fig. A.3** using the scheme shown in **Fig. A.1**. There is uncertainty in the exact value of N at 815 nm and $V = 0$ V_{RMS}. In this case, N may be 3 or 4, since $T_{\parallel}$ is stabilized near its maximum. This is reflected in the discontinuities of the regions near to 825 nm in **Fig. A.4**. On the other hand, transmittance curves at 654 nm and $V = 0$ V_{RMS}, of **Fig. A.3**, have a value close to the mean value (between maximum and minimum), in this case we are certain that $N = 6$. This is reflected in the correlation that exists between the dispersion profiles (solid lines) and the values of birefringence in the regions near to 650 nm in the **Fig. A.4**.

Therefore, the effectiveness of this method has high dependence on the wavelength, so it is necessary to use the procedure presented in this section, by analyzing a wide range of wavelengths at the same time.

Dispersion profiles are obtained by performing a polynomial regression from experimental values of birefringence. It should be noted that this adjustment can be done with a non−linear fitting based on the Cauchy equations. However, the polynomial fit is chosen due to the volume of processed data (polynomial fitting functions are fast). With the procedure used, we have determined the dispersion profiles in a range of 525 nm to 886 nm (with 4 nm resolution) for more than 1300 values of V (between 0 and 7 V_{RMS}) in a time less than 1 minute.

The characterization results obtained in this section are essential for the design of the reconfigurable wavelength selective devices presented in **Chapter 3**, since they are fabricated with the same type of cells.

B. Polarization Converters

LC devices based on polarization management usually require an input linear polarizer (LP) as part of their structures. As a consequence, half of the incoming optical power is filtered, which is translated on intensity power losses of more than 3 dB. The solution for reducing these insertion losses is by using a polarization−diversity method. In a polarization−diversity method the input beam is decomposed into its TE (*s*–polarized light) and TM (*p*–polarized light) components. Both components are treated separately and finally recombined. In this way, the device becomes polarization insensitive, and less insertion losses are expected. This principle can be applied to all the LC devices presented in **Chapter 3** and **Chapter 4**.

B.1 Schematic

The light sources used are typically unpolarized, as the light exiting from SI−POFs. The polarization converter schematic, see **Fig. B.1**, can be used to replace the input polarizer of LC devices that require it. This device allows recovering part of the component that is lost in the input LP. The schematic is composed by two polarization beam splitters (PBS1 and PBS2) and a TN cell, which is acting as polarization rotator **[5]**. The first PBS (PBS1) separates the orthogonal components of the input unpolarized light beam (*s*–polarized component and *p*–polarized component), transmitting the *p*–polarized component while reflecting the *s*–polarized component. LC cell allows rotating 90º the *p*–polarized component transmitted by PBS1, transforming it into a *s*–polarized beam that is reflected by the second PBS (PBS2), which represents a potential improvement of up to 50% of the light transmitted.

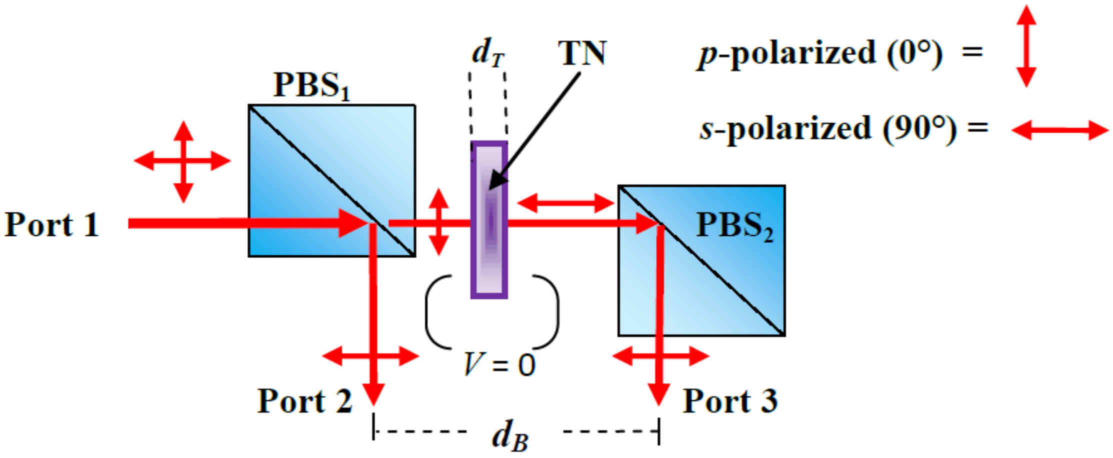

Fig. B.1: Schematic of the polarization converter device.

However, this polarization converter scheme has the disadvantage that transmits two parallel beams with a separation (d_B) that depends on the PBSs separation. This can be overcome using LC cells with large diameter of combining both beams using a lens system.

B.2 Polarization converter performance

The polarization converter, see **Fig. B.1**, has been experimentally tested, using a TN cell of 5CB material and 5μm thickness, and two PBS cubes of 20 × 20 × 20 mm with operation range from 600 to 900 nm. The LC cell transmittance is about 81% in the range from 500 to 900 nm and the PBSs transmittance for the *s*−polarization and *p*−polarization components is about 95% and 90%, respectively.

Results are shown in **Fig. B.2**. When the non−polarized beam is incident on Port 1 (see **Fig. B.1**), approximately 45% of the beam intensity is reflected to the output Port 2 in an *s*−polarized beam (see dashed line in **Fig. B.2**). Approximately 47% of the input beam is transmitted to the TN cell in a *p*−polarized beam. The TN cell transforms part of the *p*−polarized beam into an *s*−polarized beam which is transmitted by PBS2 to the output Port 3. The intensity transmitted through Port 3 is about 29 % of the input beam (dash−dot line in **Fig. B.2**). This percentage depends mainly on the polarization rotation efficiency of the TN cell and on its insertion losses. The total transmittance of the polarization converter is near to 75% from 575 to 900 nm, see solid line on **Fig. B.2**. The *s*−polarized parallel beams are separated a distance of 2 mm.

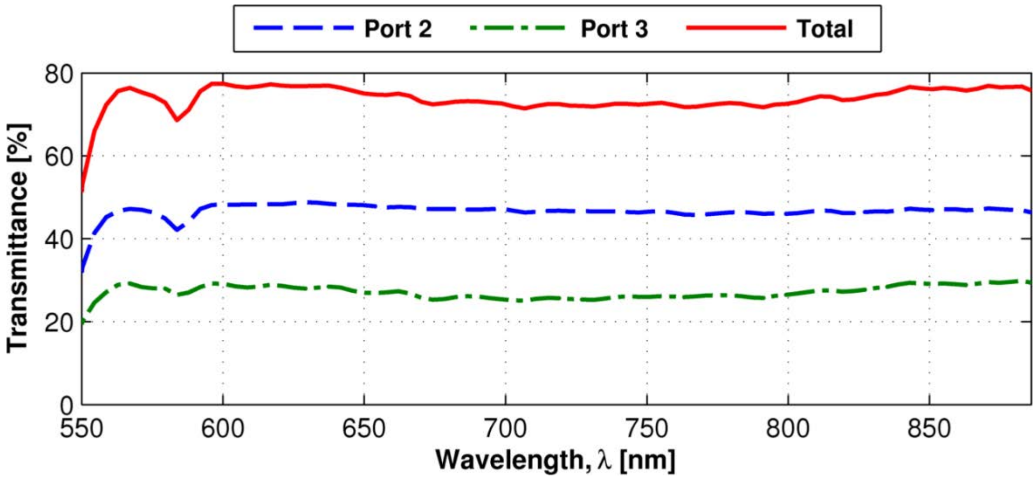

Fig. B.2: Experimental transmittance of the polarization converter device.

The transmittance of the LP used in the LCTF implementation presented in **Chapter 3** is about 35% at 600 nm and 41 % at 900 nm, for non−polarized light. So this polarization converter device can be used to increment in 50% the LCTF transmittance, as reported in **[6]**.

C. Global Optimization using a Genetic Algorithm (GA)

Optimization techniques are used to find a set of design parameters, $x = \{x_1, x_2..., x_n\}$, that can in some way be defined as optimal. In a simple case this might be the minimization or maximization of some system characteristic that is dependent on x. In a more advanced formulation the objective function, $F_{obj}(x)$, to be minimized or maximized, might be subject to constraints in the form of equality constraints, $G_i(x) = 0$ ($i = 1,..., m_e$); inequality constraints, $G_i(x) \leq 0$ ($i = m_e + 1,..., m$); and/or parameter bounds, x_l, x_u.

An efficient and accurate solution to this problem depends not only on the size of the problem in terms of the number of constraints and design variables but also on characteristics of the objective function and constraints. When both the objective function and the constraints are linear functions of the design variable, the problem is known as a Linear Programming (LProg) problem. Quadratic Programming (QProg) concerns the minimization or maximization of a quadratic objective function that is linearly constrained. For both the LProg and QProg problems, reliable solution procedures are readily available. More difficult to solve is the Nonlinear Programming (NProg) problem in which the objective function and constraints can be nonlinear functions of the design variables. A solution of the NProg problem generally requires an iterative procedure to establish a direction of search at each major iteration. This is usually achieved by the solution of an LProg, a QProg, or an unconstrained sub problem.

Usually, optimization is defined as the process of finding the point that minimizes a function. More specifically:

- A local minimum of a function is a point where the function value is smaller than or equal to the value at nearby points, but possibly greater than at a distant point.
- A global minimum is a point where the function value is smaller than or equal to the value at all other feasible points.

C.1 Genetic Algorithm

The genetic algorithm is a method for solving both constrained and unconstrained optimization problems that is based on natural selection, the process that drives biological evolution. The genetic algorithm repeatedly modifies a population of individual solutions. At each step, the genetic algorithm selects individuals at random from the current population to be parents and uses them to produce the children for the next generation. Over successive generations, the population "evolves" towards an optimal solution. Due to its random nature, the genetic algorithm improves the possibility of finding a global solution. The genetic algorithm can be applied to solve a variety of optimization problems that are not well suited for standard optimization algorithms, including problems in which the objective function is discontinuous, non−differentiable, stochastic, or highly nonlinear. The genetic algorithm can also address problems of mixed integer programming, where some components are restricted to be integer−valued.

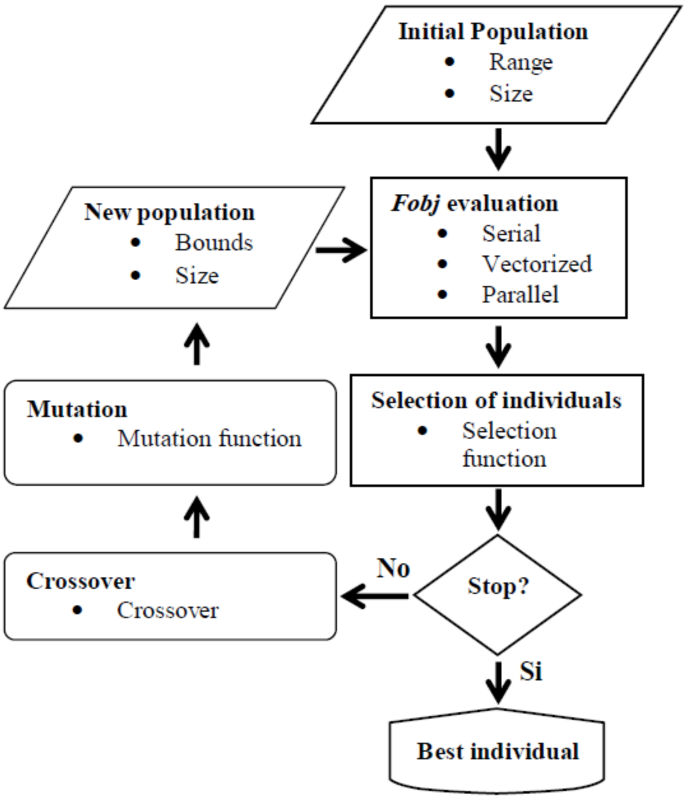

Fig. C.1: Flowchart of the typical implementation of a genetic algorithm.

Fig. C.1 shows the flowchart of a typical implementation of the genetic algorithm. It starts with the initial population of individuals, *x*. There is a finite amount of individuals (Population Size) with characteristics $\{x_1, x_2..., x_n\}$ limited in a specific Range. The actual population is evaluated using the objective function $F_{obj}(x)$. This evaluation can be performed in Serial, where each individual is evaluated separately, one after the other; Vectorized, where all the individuals are evaluated at the same time; and in Parallel, where the complete population is evaluated in parallel by using multiple processors or clusters. Then, the best individuals of the actual population are selected. If the stop condition is not fulfilled (average or minimum value of $F_{obj}(x)$, maximum number of iterations, time, etc...), a new population is produced (next generation). The next generation is obtained at random from by a crossover process between the best individuals of the previous generation, including possible mutations in their characteristics, in order to increase the possibility of finding the global minimum.

C.2 System Requirements

Optimization processes used in **Chapter 2**, **Chapter 3** and **Chapter 4** have been done with an implementation of the genetic algorithm in MATLAB 2012a.

The minimum system requirements for supporting the genetic algorithm implementation used in a Windows Operating System are given on **Table C.1**. In particular, all the results presented in this work are obtained using a personal computer with Operating System Windows XP SP 3, processor Intel® Core™2 Duo E6750 @ 2.66 GHz and RAM of 3.25 GB.

TABLE C.1: GENERAL SYSTEM REQUIREMENTS FOR SUPPORTING THE GENETIC ALGORITHM IMPLEMENTATION.

Operating Systems	Processors	Disk Space	RAM
Windows 8 Windows 7 or SP 1 Windows Vista SP 2 Windows XP SP 3 Windows XP x64 Edition SP 2 Windows Server 2008 SP 2 or R2 Windows Server 2003 R2 SP 2	Any Intel or AMD x86 processor supporting SSE2 instruction set*	1 GB for MATLAB only, 3–4 GB for a typical installation	1024 MB (At least 2048 MB recommended)

Notes: SP for Service Pack

D. Fiber Bundle based SI−POF Multiplexer

Most of SI−POF WDM systems developed to date use couplers as multiplexers, since they are relatively simple and cheap to produce **[7]**, **[8]**. So the need for couplers for large core fibers, such as SI−POF, is increasing. In recent years, there have been various proposals for the construction of 1:2 and 1:4 couplers based on direct joint **[7]**, wave guide elements **[7]**, **[9]** and fused−tapers **[10]**, with good results. But the minimal insertion loss (*IL*) of a Y−coupler (2:1 coupler) based on these fabrication techniques is 3 dB. This is independent of its use as a splitter or a coupler **[7]**. Additionally, a Y−coupler includes excess losses between 1 dB and 2 dB, so they have total *IL* of about 4.5 dB **[11]**. In the same way, a 4:1 coupler has *IL* of about 9 dB **[8]**. On the other hand, different Mux/DeMux devices for SI−POF based networks have been reported. They are mainly based on thin−film filters and diffraction gratings, with *ILs* between 3 dB and 6 dB **[12]**. Besides, in all the multiplexing solutions it should be also considered the losses from coupling the transmitters to the input fibers. Then, the most interesting solution for an efficient multiplexing it is to couple the transmitters directly to the SI−POF, taking advantage of its large core, as in the scheme proposed in 1999 **[13]** for graded−index POF (GI−POF). However, this type of configurations has not been implemented so far.

This appendix presents the design of a multiplexer system that can transmit up to 7 channels over a single SI−POF. The multiplexer is based on a lens system which couples the light from 7 input fibers into a single SI−POF. Its design and efficiency analysis are carried out by using a sequential ray tracing software, considering all possible losses as well as commercial devices or devices easy to manufacture with current technology. The overall multiplexing system has an efficiency between 60% and 74%, for wavelengths between 405 nm and 660 nm, which represents insertion losses lower than 2.5 dB per channel.

D.1 Multiplexing Scheme

The proposed multiplexing scheme is shown in **Fig. D.1**. It consists of three main sections. First, the light from each transmitter (e.g. a laser diode, LD) is injected into different input fibers, through coupling lenses. Then, the input fibers are joined to form a fiber bundle. And finally, all the input fibers are multiplexed into a single SI−POF using a lens system.

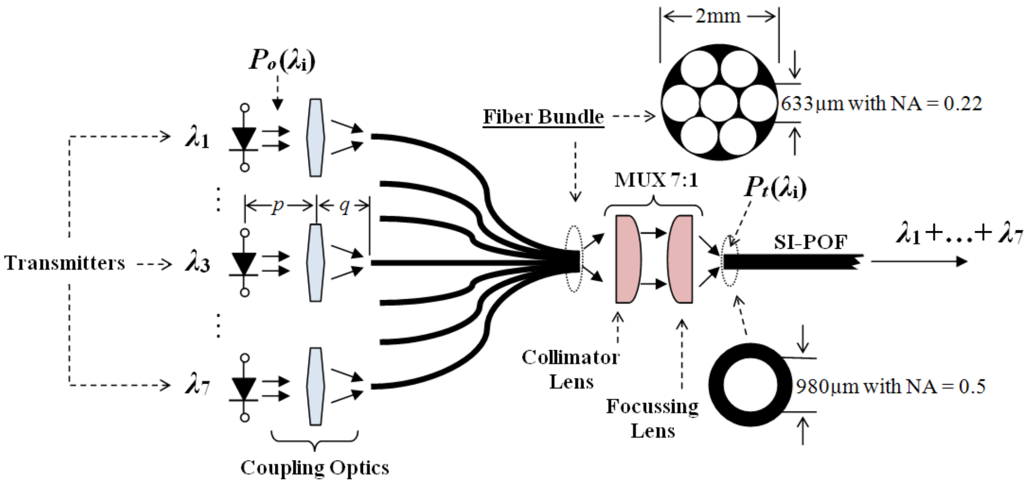

Fig. D.1: Proposed 7:1 multiplexing scheme for multi–wavelength transmission over SI–POF networks.

- **Fiber Bundle**

The *NA* and core diameter of the input fibers are determinant factors in the overall system efficiency. A small core diameter and a small *NA* simplify the multiplexer setting up. However, they can greatly increase the transmitters (laser diodes, LDs) coupling losses. In the proposed design, the fiber bundle BF20HSMA from Thorlabs is considered. This bundle is made of seven step–index silica multimode fibers; each one has 550 µm core diameter, 600 µm cladding diameter, 630 µm buffer diameter and 0.22 *NA*. The fibers attenuation is about 30 dB/Km, 15 dB/Km and 8 dB/Km at 405nm, 520 nm and 660 nm, respectively.

- **Optical Coupling between the transmitter and the optical fiber**

The system is capable of multiplexing up to 7 wavelengths (or channels). The coupling of each LD to the respective input fibers is done using the aspheric lens 352440 from LightPath. The optimal distances *p* and *q* (see **Fig. D.1**) of each LD are found by optimizing the coupled power in the input fiber. The parallel and perpendicular beam divergence of commercial LDs and the glass window of a typical TO56 package are considered.

- **Multiplexing optical system**

The multiplexing optical system must be able to couple the beam from each input fiber on the SI–POF. This is not a difficult task since the *NA* of the input fibers is less than half of the *NA* of the SI–POF. So the object, of 2 mm diameter and *NA* of 0.22 (fiber bundle), can be focused into an image smaller than 1 mm diameter with *NA* less than 0.5. The multiplexing system is made up of a collimator lens and a focusing lens as shown in **Fig. D.1**. **Fig. D.2** shows the multiplexing system layout and its specifications are described on **Table D.1**. These lenses are not commercial, but are simple biconvex lenses and are easy to manufacture with the actual injection molding technology.

The decenter coordinate is used to simulate the position of the input fibers in the bundle. The six outer fibers are at the same distance from the center, so they can be represented by the decenter value (0.630, 0.000) since the system is symmetric. The system has been designed so that the outer fibers have the best possible coupling.

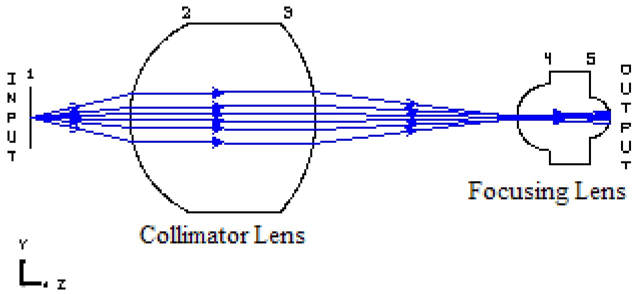

Fig. D.2: Multiplexing lens system layout

TABLE D.1: MULTIPLEXING LENS SYSTEM DATA. THE LENS SURFACES INCLUDE AN AR COATING. ALL DIMENSIONS ARE IN MM.

Surface	Comments	Radius	Thickness	Glass	Semi−Diameter	Decenter (X, Y)
Input	Input fiber end−face	Infinity	0.000	SILICA	0.630	(0.630, 0.000)
1	Dummy surface 1	Infinity	7.091	−−−	2.260	−−−
2	Collimator lens front face	7.404	13.058	N−LASF43	6.600	
3	Collimator lens rear face	−10.141	14.162	−−−	6.600	
4	Focusing lens front face	2.337	6.552	N−LAK12	3.324	
5	Focusing lens rear face	−1.441	0.028	−−−	2.389	
Output	SI−POF end−face	Infinity	−−−	PMMA	0.500	

D.2 Efficiency Analysis

The coupling efficiency (from the LD to the input fiber) is highly dependent on the transmitters' wavelength and divergence. Therefore, it will be tested using the characteristics of three commercial laser diodes, covering the visible spectrum. The laser diodes used in the simulations are the DL−5146−101S from SANYO, the PL 520 from OSRAM and the HL6544FM from OPNEXT. The typical central wavelength and divergence of each LD are presented on **Table D.2**. The coupling efficiency is calculated considering the central wavelength and the beam divergence (perpendicular and parallel to the diode junction) of each LD. The results are also shown on **Table D.2**.

The multiplexing lens system allows that more than 99% of rays fall on the end−face of the SI−POF with a *NA* lower than 0.5. So the multiplexing efficiency is determined by the Fresnel losses, scattering, the material absorption (air, fiber and glasses) and the imperfections of the fibers.

These phenomena, except for the fiber imperfections, are considered in the efficiency calculations. It is also considered that the beams at the output of the fiber bundle have a diameter of 0.55 mm and *NA* of 0.22 with Gaussian profile. **Fig. D.3** shows the multiplexing efficiency and the profile of a beam coming from the fiber bundle focused at the end face of the SI−POF. The 520 nm beam comes from an input fiber that is decentered 0.630 mm (this position represents the six outer fibers). It can be seen that the efficiency is 89% and that the beam is focused almost in the center of the SI−POF. The multiplexing efficiency for each wavelength is shown on **Table D.2**. In the case of the central input fiber, the multiplexing efficiency is 90% at 520 nm.

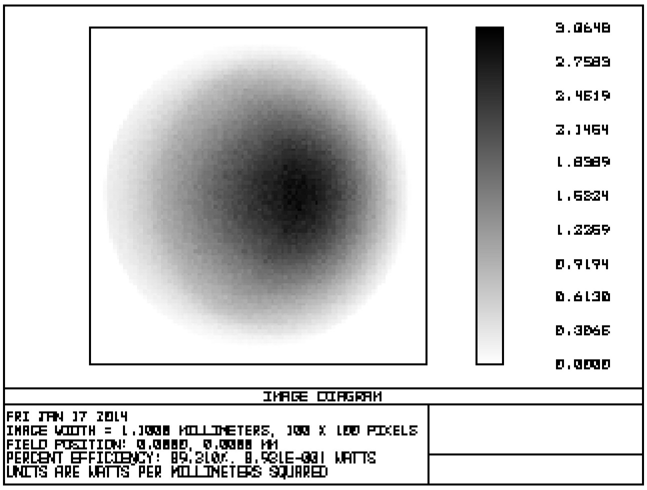

```
FRI JAN 17 2014
IMAGE WIDTH = 1.1000 MILLIMETERS, 100 X 100 PIXELS
FIELD POSITION: 0.0000, 0.0000 MM
PERCENT EFFICIENCY: 89.210%. 8.921E-001 WATTS
UNITS ARE WATTS PER MILLIMETERS SQUARED
```

Fig. D.3: Profile and multiplexing efficiency of a beam from the fiber bundle focused at the end face of the SI−POF.

It has been shown that the proposed system allows multiplexing up to 7 input channels with insertion losses lower than 2.5 dB. The lowest coupling efficiency is achieved for the laser diode PL 520. This is due to the large difference between the parallel and perpendicular divergence. In general, the laser diodes coupling efficiency can be increased up to 90% using specific lenses **[14]**. In this case the total *IL* can be less than 1 dB.

TABLE D.2: TRANSMITTERS CHARACTERISTICS AND EFFICIENCY OF THE PROPOSED MULTIPLEXING OPTICAL SYSTEM. THE TOTAL EFFICIENCY INCLUDES THE COUPLING AND THE MULTIPLEXING EFFICIENCIES AND THE ATTENUATION OF THE INPUT FIBER (1 M).

LD	Wavelength	Beam Divergence		Efficiency % (Eff)			*IL* = −10log(Total Eff)
		Perpendicular	Parallel	Coupling	Multiplexing	Total	
DL−5146−101S	405 nm	19º	8º	0.74	0.82	0.60	2.22 dB
PL 520	520 nm	22º	7º	0.69	0.89	0.61	2.15 dB
HL6544FM	660 nm	17º	10º	0.83	0.89	0.74	1.31 dB

References of Appendices

[1] P. J. Pinzón, I. Pérez, J. M. Sánchez–Pena and C. Vázquez, "Spectral method for fast measurement of twisted nematic liquid crystal cell parameters," *Applied Optics,* vol. 53, no. 23, pp. 5230–5237, 2014.

[2] V. Urruchi, I. Pérez, N. Gaona and J. M. Sánchez–Pena, "Phase Modulation and Optical Anisotropy of High Birefringence Liquid Crystals," *Molecular Crystals and Liquid Crystals,* vol. 502, no. 1, pp. 207–219, 2009.

[3] P. J. Pinzón, I. Pérez, C. Vázquez and J. M. Sánchez–Pena, "Reconfigurable 1×2 wavelength selective switch using high birefringence nematic liquid crystals," *Applied Optics,* vol. 51, no. 25, pp. 5960–5965, 2012.

[4] P. J. Pinzón, I. Pérez, C. Vázquez and J. M. Sanchez–Pena, "1 × 2 Optical RouterWith Control of Output Power Level Using Twisted Nematic Liquid Crystal Cells," *Molecular Crystals and Liquid Crystals,* vol. 533, no. 1, pp. 36–43, 2012.

[5] P. J. Pinzón, I. Pérez, C. V zquez and J. M. S nc hez−Pena, “Broadband 1×2 Liquid Crystal Router with Low Thermal Dependence for Polymer Optical Fiber Networks,” *Optics Communications,* 2014.

[6] P. J. Pinzón, I. Pérez, C. Vázquez and J. M. S. Pena, "Diseño de un Filtro Óptico Sintonizable Basado en Cristal Líquido con Mejora de las Pérdidas de Inserción," in *XXVI Simposio Nacional de la Unión Científica Internacional de Radio – URSI'*11, Leganés (España), 2011.

[7] O. Ziemann, J. Krauser, P. E. Zamzow and W. Daum, POF Handbook: Optical Short Range Transmission Systems, 2nd ed., Springer, 2008.

[8] M. Joncic, S. Höll, M. Haupt, R. Caspary and U. H. P. Fischer, "Development status of a four–channel CWDM system for multi_GBit/s data links over SI–POF," in *ICPOF*, Buzios, 2013.

[9] V. Prajzler, M. Neruda and J. Spirková, "Planar large core polymer optical 1×2 and 1×4 splitters connectable to plastic optical fiber," *Radioengineering,* vol. 22, no. 3, pp. 751–757 , 2013.

[10] M. S. Ab–Raham, H. Guna, M. H. Harun, S. D. Zan and K. Jumari, "Cost–effective fabrication of self–made 1×12 polymer optical fiber–based optical splitters for automotive applications," *American. J. of Engineering and Applied Sciences,* vol. 2, no. 2, pp. 252–259, 2009.

[11] I. Industrial Fiber Optics, "Plastic Plastic Fiber Couplers (Splitters)," 2014.

[12] P. J. Pinzón, I. Pérez and C. Vázquez, "Efficient Multiplexer/Demultiplexer for Visible WDM

Transmission over SI–POF Technology," *IEEE/OSA Journal of Lightwave Technology,* 2015.

[13] J. Mizusawa, "Advantages of POF WDM System Design," in *ICPOF*, 1999.

[14] L. Technologies, "Aplication Notes: Using precision molded aspheres," 2014.